Large Volume Reconstruction and Analysis of Directionally Solidified Aluminium Copper Dendritic Forests

Author:

Joshua Ethan Miller

Supervisors:

Dr. Nils Warnken

Dr Martin Strangwood



UNIVERSITY OF BIRMINGHAM

Department of Metallurgy and Materials

College of Engineering and Physical Sciences

University of Birmingham

March 2019

Wordcount: 47,000

UNIVERSITY OF
BIRMINGHAM

University of Birmingham Research Archive

e-theses repository

This unpublished thesis/dissertation is copyright of the author and/or third parties. The intellectual property rights of the author or third parties in respect of this work are as defined by The Copyright Designs and Patents Act 1988 or as modified by any successor legislation.

Any use made of information contained in this thesis/dissertation must be in accordance with that legislation and must be properly acknowledged. Further distribution or reproduction in any format is prohibited without the permission of the copyright holder.

"The time you enjoyed wasting is not wasted time."

Bertrand Russell

UNIVERSITY OF BIRMINGHAM

Abstract

School of Metallurgy and Materials

PhD Materials Science

Large Volume Reconstruction and Analysis of Directionally Solidified Aluminium Copper Dendritic Forests

by Joshua Ethan Miller

The analysis of solidification in three dimensions is a very novel area in materials science. As a result there are few current methodologies to analyse directionally solidified samples in three dimensions. This thesis forms the basis for further projects within the **MI**crostructure evolution in **CAST**ing of technical aluminium alloys under diffusive and controlled convective conditions (**MICAST**) framework providing image analysis methodologies for use on samples solidified under varying gravitational conditions.

Methods are put forward for analysing large Computerised Tomography (**CT**) volumes of Al-10 wt% Cu alloy. This includes the trialling and comparing of a number of novel centre finding techniques to ones obtained from the literature. This was tested on samples directionally solidified under varying withdrawal rates. Information on the cellular spacing and dendritic interaction along the length of the samples was obtained. The results showed that the cellular array adapts over a distance which is dependent upon the diffusion length and therefore the velocity also.

Acknowledgements

Thanks to the European Space Agency, German Space Agency and University of Birmingham for sponsoring this work.

Thanks to Jake Brooks from the University of Warwick for providing the MRI brain scans.

Gerhard Zimmernann and Laszlo Sturz of Access, Aachen RWTH for the invaluable discussions and for their help in the production of the SG18 paper in the append Chapter 11 [1]. And to Christoph Pickmann at Access for help with running the Bridgman furnace.

Sonja Steinbach for helping me undertake the computerised tomography work at the German Space Agency and for her help in the production of the SP17 and SG18 papers in Chapters 10 and 11 [1, 2]. And also for including parts of this work in [3] presented by Sonja at **ESA**.

Thanks to Amanda and Sam at the University of Birmingham for help with the EDM machine when cutting samples this for research.

Thanks to the M^3 group at the University of Birmingham, Eric, Mohammad, Seb, and especially Vanessa for help with this Thesis and her help with creating the aerogel furnace model in Chapter 9.

Thanks to Martin Strangwood and especially Nils Warnken for their supervision during this project and help with researching and the appendices and papers in Chapters 9 to 11 [1, 2].

Preface

Parts of this thesis have appeared in and/or at the conferences or journals indicated. Unless otherwise indicated in the text all the experimentation and analysis on each paper was undertaken by the main author. Other authors provided guidance with the research, supervision and help with editing the papers.

Conferences:

J. E. Miller, M. Strangwood, S. Steinbach, and N. Warnken. Skeletonisation to find the centre of dendrites traced from a 2d microstructural image. In Z. Fan, editor, *Solidification Processing 2017*, 2017

S. Steinbach, J. Drescher, J. E. Miller, N. Warnken, L. Sturz, and G. Zimmermann. Furnace technology for experiments on sounding rockets: Directional solidification of al-cast alloys in artex. In J. J. W. A. van Loon, editor, *Hypergravity Workshop January 2018*, 2018

J. E. Miller, L. Sturz, G. Zimmermann, S. Steinbach, and N. Warnken. A large-scale 3d computer tomography analysis of primary dendrite arm spacing response to withdrawal velocity change using dendrite centre tracking. In *Solidification and Gravity 2018*, 2018

To be submitted:

J. E. Miller, V. Indrizzi, M. Strangwood, and N. Warnken. Simulation and design for directional solidification experiments of al-20wt *To be submitted*, TBC

J. E. Miller and N. Warnken. Grain orientation from optical images. *To be submitted*, TBC

Contents

Abstract ii

Acknowledgements iii

Preface iv

Contents iv

List of Figures ix

List of Tables xxi

Abbreviations xxiii

Nomenclature xxiv

Dedication 1

1 Introduction 1
- 1.1 Motivation . . . 1
- 1.2 Introduction . . . 3
- 1.3 Thesis Structure . . . 5
  - 1.3.1 Appendices . . . 7

2 Literature Review 9
- 2.1 Binary Alloy Solidification . . . 15
- 2.2 JMAK and Avrami Equations . . . 25
- 2.3 Microstructural growth and morphology . . . 28
- 2.4 Furnace Design: Directional Solidification . . . 36
- 2.5 Estimating Primary and Secondary Dendrite Arm Spacing, **PDAS** λ_1 . . . 39
  - 2.5.1 Primary Dendrite Arm Spacing . . . 41
  - 2.5.2 Effect of Gravity Level on **PDAS** . . . 46
  - 2.5.3 Changing v^* and/or ∇T and the Effect on **PDAS** . . . 48
  - 2.5.4 Secondary Dendrite Arm Spacing . . . 50

2.6 Pseudo-2-Dimensional Experiments . . . 52
2.7 Image Analysis of Directionally Solidified Samples . . . 53
2.7.1 Binarisation . . . 55
2.7.2 Finding the Centre of a Dendrite . . . 56
2.8 Calculating the Bulk and Local **PDAS** . . . 59
2.9 Tracking Dendrite Centres Through the Sample . . . 61
2.10 Grain Orientation . . . 63
2.11 Gaps Identified Within the Literature . . . 64

3 Experimental **66**
3.1 Experimental Equipment . . . 69
3.2 Experimental Methodology . . . 72
3.3 Constant and Varying Withdrawal Rate Experiments . . . 74

4 Image Analysis Techniques **81**
4.1 Image Acquisition and Pre-Processing . . . 82
4.1.1 Tophat image filtering . . . 83
4.1.2 Binarising Images . . . 85
4.1.3 Active contours method . . . 89
4.1.4 Watershed Segmentation . . . 91
4.1.5 Removal of small shapes and holes . . . 96
4.2 Finding the 'True' Centre of a Dendrite . . . 96
4.2.1 Hand Assigning the Centre Point . . . 97
4.2.2 Centre of Geometry . . . 97
4.2.3 Skeleton Centre . . . 99
4.2.4 Combined Skeleton-Centre of Geometry . . . 100
4.2.5 Intercept Centre . . . 100
4.2.6 Centre of Curvature . . . 103
4.2.7 Gradient Across a Blurred Interface (Gaussian Centre) . . . 103
4.2.8 Symmetry-Based Feature Extraction . . . 105
4.2.9 Convolutional Neural Network Centre Finding . . . 106
4.2.10 Dendrite centre finding comparison . . . 106
4.2.11 Trialling Methods on a Binarised Al-10 wt% Cu Slice . . . 121
4.3 Primary Dendrite Arm Spacing Calculations . . . 123
4.3.1 Minimum Spanning Tree . . . 133
4.3.2 Warnken-Reed Primary Dendrite Arm Spacing . . . 137
4.3.3 Voronoi Primary Dendrite Arm Spacing . . . 139
4.3.4 Warnken-Reed-Voronoi Primary Dendrite Arm Spacing . . . 139
4.3.5 Local PDAS Calculations on Hand-Assigned and Skeleton-Geometry Dendrite Centres . . . 139
4.4 Tracking Centres Along the Length of a Sample . . . 148
4.5 Finding Initiation and Termination of Dendrites . . . 150
4.6 Finding Misorientation of Dendrites . . . 150
4.7 3D Isosurface of Individual Dendrites . . . 152

4.8 Grain Orientation Finding From Optical Images 153
4.8.1 Grain Orientation Finding Method 154
4.8.2 Skeletonisation 158
4.8.3 EBSD measurements 158
4.8.4 Results of the Grain Orientation Technique 158
4.8.5 Analysis of the Grain Orientation Method 163
4.8.6 Analysing the Grain Orientation Method for Use with Aluminium-Copper Dendrites 169

5 Experimental Analysis Results 172
5.1 Primary Dendrite Arm Spacing 175
5.1.1 Constant Withdrawal Rate 175
5.1.2 Increasing Withdrawal Rate 179
5.1.3 Increasing Withdrawal PDAS Rates of Change 181
5.2 Number of Nearest Neighbours Along the Length of the Samples . . 220
5.3 JMAK and Avrami 220
5.4 Porosity Within the Samples and Location of Newly Initiated and Outcompeted Dendrites 221
5.5 Misorientation of the Dendrites to the Z-Axis 221
5.6 Minimum-Spanning-Tree Packing Factor 223
5.7 PDAS for All samples 223
5.8 Comparison of Warnken Reed PDAS Calculation Method with Theoretical Methods 230
5.9 Experimental Results Against Relative Velocity Change 230
5.10 Three Dimensional Dendrite Forests 236
5.11 Tracking Dendrite Initiations and Terminations 239
5.12 Isosurface Plots of Dendrites 239

6 Discussion 244
6.1 Accumulation of Error Through Analysis 245
6.2 Constant Withdrawal rate 247
6.3 Varying Withdrawal rate 251
6.3.1 40-60-100 μms^{-1} Sample 256
6.4 Stabilisation Length in Terms of Diffusion Lengths 256
6.5 PDAS Calculation Comparison 258
6.6 JMAK Analysis of Samples 261
6.7 Number of Nearest Neighbours 262
6.8 Minimum-Spanning-Tree Packing Factor 265
6.9 Experimental Results Against Relative Velocity Change 266
6.10 Misorientation of Dendrites in the Samples 267
6.11 3D Dendrite Forests 270
6.12 3D Dendritic Isosurface Comparison 271

7 Conclusions 273
7.1 Image Analysis Techniques and Centre Finding Methods 273

7.2 Dendritic Centre Finding Methods . . . 275
7.3 Local and Bulk PDAS Calculation Methods . . . 275
7.4 Effect on PDAS with Changing Withdrawal Rate . . . 276
7.5 Visualisation of Individual Dendrites and Dendritic forest . . . 277
7.6 Whole Sample Analysis . . . 277

8 Future Works 279

9 Appendix A: Aerogel Furnace Modelling 282
9.1 Introduction . . . 282
9.2 Methodology . . . 286
9.2.1 Governing Equations . . . 287
9.2.2 Maintaining a Constant v^* and d . . . 291
9.3 Model Validation . . . 292
9.3.1 Model Methodology . . . 292
9.3.2 Validation Results . . . 295
9.3.3 Validation Discussion . . . 299
9.4 Simulation of Al-20wt%Cu Temperature Profiles for Sounding Rocket Experiments . . . 302
9.4.1 Materials and Simulation Parameters . . . 302
9.5 Results . . . 304
9.6 Discussion . . . 309
9.7 Conclusions . . . 315
9.8 Further Work . . . 316
9.8.1 Fluid flow in the melt . . . 316
9.8.2 Rayleigh number based fragmentation . . . 320

10 Appendix B 324

11 Appendix C 330

Bibliography 339

List of Figures

2.1 Photograph of a snowflake which grows with a branching dendritic structure [6] . . . 10
2.2 Slice of a Ni-superalloy directionally solidified 10 mm cross-section sample. . . . 10
2.3 Example relationship between tip velocity and tip radius of a growing dendrite for a fixed undercooling. . . . 12
2.4 European Space Agency's Large Diameter Centrifuge based in Noordwijk, Netherlands. Reproduced under creative commons license [7]. . . . 16
2.5 Mushy depth, d, of different aluminium-copper alloys dependent upon the thermal gradient, ∇T. Calculated using Equation (2.2) and the equilibrium solidus temperature for each alloy. . . . 18
2.6 Aluminium copper phase diagram, reproduced under creative commons. [8] . . . 20
2.7 Concentration profile for a solidified ingot for various values of the solidification partition coefficient k. . . . 22
2.8 Concentration profile for a solidified 1D bar with three zones, an initial transient region, a steady state region and a final transient region. The final solidified concentration is shown by the thick black line and the dotted line shows the advancing bow-wave like interface. 24
2.9 Characteristic sigmoidal shape of the Avrami equation describing phase change [9] . . . 30
2.10 log-log plot of the Avrami equation used to find the Avrami exponent n [9] . . . 30
2.11 Solid-liquid evolution morphology with increasing interface velocity, v^*. a) Planar interface for very slow solidification times. b-c) Cellular interface. d) Dendritic structures. e) Cellular interface. f) Planar interface from rapid solidification. . . . 31
2.12 Schematic of the competition between columnar and equiaxed dendrites occurring during a columnar to equiaxed transition. a) Purely columnar. b) Equiaxed grains form ahead of the columnar dendrites. c) Equiaxed dendrites out compete the columnar dendrites. . 32
2.13 Solidification map of an aluminium 10 wt% copper alloy. The primary dendrite arm spacing are displayed as contours and the changing microstructural regions are labeled. . . . 35

2.14 Schematic of a two heater Bridgman furnace of the type used in this thesis. The sample is withdrawn downwards through the two heaters and the baffle. 37
2.15 **PDAS** calculations for 40 to 100 μms^{-1} using Equations (2.23) to (2.26) with a thermal gradient of ∇T = 10 000 Km^{-1} and the parameters in Table 9.3 and from [10]. 44
2.16 Calculated effect of the primary dendrite arm spacing λ as a function of the acceleration due to gravity, g, calculated using Equations (2.26) and (9.3). Below and above 1g equation Equation (9.3) is used to modify the expected **PDAS** using the factor $\frac{g}{g_E}^{-0.125}$. The standard deviation of the mean is overlain on the graph for the calculated λ at $0g$. 47
2.17 a) A decrease in **PDAS** due to an increase in v^* or ∇T. A new primary dendrite arm is formed by the means of tertiary arm stabilisation. b) An increase in **PDAS** due to a decrease in v^* or ∇T. The central dendrite is outcompeted by the dendrites to either side of it. 49
2.18 MRI scan of a human brain [11] 57
2.19 Section from a **CT** scan of a constant withdrawal rate 40 μms^{-1} directionally solidified Al-10wt% Cu sample cast as part of this thesis. 57

3.1 Schematic diagram of a Bridgman furnace and schematic of the nominal and actual thermal gradient along the sample during solidification. 70
3.2 Schematic diagram of different mushy zone morphologies at different locations within the Bridgman furnace and a nominal and actual temperature gradient in the sample. 71
3.3 Schematic of the sample dimensions. a) is the 50 mm of the sample which is held in place by the sample holder. b) is the 20 mm which is melted back prior to the experiment beginning. c) is the 90 mm over which the experiment is conducted. d) is the 40 mm of the sample which was treated as waste. 75
3.4 Lab scale Bridgman furnace at Access, Aachen RWTH. 76
3.5 Normal distribution of local **PDAS** distributions for each average **PDAS** using the minimum and maximum stable **PDAS** values put forward by Ma [12, 13]. 78
3.6 Solidification map for an Al 10 wt% Cu alloy. Experimental withdrawal velocities shown as yellow dots in the columnar-dendritic region of the map. 80

4.1 Image analysis process flow chart. 84
4.2 A single slice of the raw reconstructed CT volume slice with the line showing where the intensity profile was taken from. 86
4.3 The intensity profile along the line shown in figure Figure 4.2 86
4.4 A single slice of the top-hat filtered CT volume with the line showing where the intensity profile was taken from. 87

4.5 The intensity profile along the line shown in figure Figure 4.4 87
4.6 a) **CT** slice of a Al-10 wt% Cu sample. b) Active contours thresholding. c) Histogram based thresholding. d) Otsu thresholding. . . . 88
4.7 a) **CT** slice of a Al-10 wt% Cu sample. b) Active contours thresholding. 90
4.8 Final binarised image of a **CT** slice of a constant withdrawal 100 μm^{-1} Al-10wt%Cu sample. 92
4.9 Conjoined dendrites 93
4.10 Distance transform 94
4.11 Segmented dendrites 95
4.12 Schematic of the true centre of a dendrite growing into an undercooled melt. 98
4.13 Steps of the skeletonisation operation, a, b, and c are some of the erosion steps which lead to the one pixel thickness skeleton seen in image d. This image subsequently has any spurs removed giving image e. Finally the cross points are found where two lines intersect i.e. the *branching points* in f which are one pixel in size. 101
4.14 Extreme points centre assigning. a), branch points found from skeletonisation (Points have been artificially enlarged for ease of viewing). b), perimeter of the shape. c), find longest line in approximately perpendicular direction. d), assigning the centre closest to the intercept of the two lines as the centre of the dendrite. 104
4.15 Example traced directionally solidified nickel superalloy micrograph used to test the various centre finding techniques. 108
4.16 Distance between the hand assigned centre and the centres assigned using the different methods against the area in pixels of each dendrite. The black circles are the inner dendrites and the blue the edge ones. 113
4.17 Distance between the hand assigned centre and the centres assigned using the different methods against the aspect ratio of each dendrite. The black circles are the inner dendrites and the blue the edge ones. 114
4.18 Distance between the hand assigned centre and the centres assigned using the different methods against the circularity of each dendrite. The black circles are the inner dendrites and the blue the edge ones. 115
4.19 Distance between the hand assigned centre and the centres assigned using the different methods against the compactness of each dendrite. The black circles are the inner dendrites and the blue the edge ones. 116
4.20 Distance between the hand assigned centre and the centres assigned using the different methods against the convexity of each dendrite. The black circles are the inner dendrites and the blue the edge ones. 117
4.21 Distance between the hand assigned centre and the centres assigned using the different methods against the eccentricity of each dendrite. The black circles are the inner dendrites and the blue the edge ones. 118

4.22 Distance between the hand assigned centre and the centres assigned using the different methods against the elongation of each dendrite. The black circles are the inner dendrites and the blue the edge ones. 119
4.23 Distance between the hand assigned centre and the centres assigned using the different methods against the roundness of each dendrite. The black circles are the inner dendrites and the blue the edge ones. 120
4.24 Histograms of the distances between the three chosen methods and the hand-assigned centre of gravities for the aluminium 10 wt% copper **CT**'d slice shown in Figure 4.8 124
4.25 Distance between the hand assigned centre and the centres assigned using the different methods against the area in pixels of each dendrite for the aluminium-copper **CT**'d slice. The black circles are the inner dendrites and the blue the edge ones. 125
4.26 Distance between the hand assigned centre and the centres assigned using the different methods against the aspect ratio of each dendrite for the aluminium-copper **CT**'d slice. The black circles are the inner dendrites and the blue the edge ones. 126
4.27 Distance between the hand assigned centre and the centres assigned using the different methods against the circularity of each dendrite for the aluminium-copper **CT**'d slice. The black circles are the inner dendrites and the blue the edge ones. 127
4.28 Distance between the hand assigned centre and the centres assigned using the different methods against the compactness of each dendrite for the aluminium-copper **CT**'d slice. The black circles are the inner dendrites and the blue the edge ones. 128
4.29 Distance between the hand assigned centre and the centres assigned using the different methods against the convexity of each dendrite for the aluminium-copper **CT**'d slice. The black circles are the inner dendrites and the blue the edge ones. 129
4.30 Distance between the hand assigned centre and the centres assigned using the different methods against the eccentricity of each dendrite for the aluminium-copper **CT**'d slice. The black circles are the inner dendrites and the blue the edge ones. 130
4.31 Distance between the hand assigned centre and the centres assigned using the different methods against the elongation of each dendrite for the aluminium-copper **CT**'d slice. The black circles are the inner dendrites and the blue the edge ones. 131
4.32 Distance between the hand assigned centre and the centres assigned using the different methods against the roundness of each dendrite for the aluminium-copper **CT**'d slice. The black circles are the inner dendrites and the blue the edge ones. 132
4.33 Comparison of different packing arrangements in Table 4.5 with varying levels of noise added. 136

4.34 Step-by-step of the Warnken-Reed *PDAS* assigning technique. a) the dendrite centre to be examined. b) the calculation of the average distance $\bar{x}_1$ using the first three nearest neighbour centres. c) is the checking stage to see if the fourth furthest dendrite centre fits within the threshold distance $\bar{x}_1+\alpha\sigma_x$. d) as it falls within the search radius a new search radius is created. However the fifth nearest centre does not fit within this search radius and as a result the technique stops here. 138

4.35 A step-by-step guide of the Voronoi technique to calculate local *PDAS*. a) is the dendrite centre to be examined and the surrounding microstructure. b) is the Voronoi tessellation. c) shows which other centres would be used to calculate the average distance for the local *PDAS*, i.e. only the ones with touching edges to the tessellation and not those that share vertices. 140

4.36 A step-by-step guide of the Warnken-Reed-Voronoi technique to calculate local *PDAS*. a) is the dendrite centre to be examined and the surrounding microstructure. b) is the Voronoi tessellation. c) is the calculation of the average distance $\bar{x}_1$ using the first three nearest neighbour centres. d) is the checking to see if the fourth furthest dendrite centre fits within the threshold distance $\bar{x}_1 + \alpha\sigma_x$. e) As the fourth value fits within the threshold then it is used to calculate the new search radius $\bar{x}_2 + \alpha\sigma_x$. However even though the fifth nearest point falls within the search radius as it does not share a tessellation edge with the central point being observed– only a vertex–the Warnken-Reed-Voronoi method does not count it. Therefore the *PDAS* is $\bar{x}_1$ and the central point has four nearest neighbours. 141

4.37 Histograms showing the a) Warnken-Reed **PDAS** of the hand assigned centres, b) the Warnken-Reed **PDAS** of the skeleton-geometry centres. Figure c) shows the percentage difference between the local PDAS calculated using the hand centres and the local PDAS calculated using the skeleton-geometry centres. 144

4.38 Histograms showing the a) Voronoi **PDAS** of the hand assigned centres, b) the Voronoi **PDAS** of the skeleton-geometry centres. Figure c) shows the percentage difference between the local PDAS calculated using the hand centres and the local PDAS calculated using the skeleton-geometry centres. 145

4.39 Histograms showing the a) Warnken-Reed-Voronoi **PDAS** of the hand assigned centres, b) the Warnken-Reed-Voronoi **PDAS** of the skeleton-geometry centres. Figure c) shows the percentage difference between the local PDAS calculated using the hand centres and the local PDAS calculated using the skeleton-geometry centres. . . . 146

4.40 Histograms showing the a) minimum-spanning-tree **PDAS** of the hand assigned centres, b) the minimum-spanning-tree **PDAS** of the skeleton-geometry centres. Figure c) shows the percentage difference between the local PDAS calculated using the hand centres and the local PDAS calculated using the skeleton-geometry centres. . . . 147
4.41 The distance search method of tracking the dendrite centres between slices. Method shown on a random data set of points. 151
4.42 Process flow chart for finding the orientation of an input shape or dendrite. 155
4.43 ai) Square with its four principle directions overlain, with no skeletonisation. bi) The four principle angles of the square test shape which are shown in ai. aii) Square with its four principle directions overlain, with skeletonisation. bii) The four principle angles of the square test shape which are shown in aii. 160
4.44 ai) Dendrite 1 with its four principle directions overlain, with no skeletonisation. bi) The four principle angles of the dendrite test shape which are shown in ai. aii) Dendrite 1 with its four principle directions overlain, with skeletonisation. bii) The four principle angles of the square test shape which are shown in aii. 161
4.45 ai) Dendrite 2 with its four principle directions overlain, with no skeletonisation. bi) The four principle angles of the dendrite test shape which are shown in ai. aii) Dendrite 2 with its four principle directions overlain, with skeletonisation. bii) The four principle angles of the square test shape which are shown in aii. 162
4.46 ai and aii give the result of the technique without and with skeletonisation respectively on the microstructure. bi and bii show the DBSCAN sorting without and with the skeletonisatoin. ci and cii show the resulting sorted grain structure without and with the skeletonisation. 164
4.47 a) The four principle angles overlain on the dendrites. b) The result of the DBSCAN sorting. c) The dendrites sorted into grains. 165
4.48 a) *EBSD* map of the polycrystalline nickel superalloy sample. b) *EBSD* map overlain on the result of the dendrite sorting. 166
4.49 Results of the orientation based grain assigning resulting in erroneous results. a) N = 5, $\epsilon = 0.1$, b) N = 10, $\epsilon = 0.1$, c) N = 5, $\epsilon = 0.7$, d) N = 10, $\epsilon = 0.7$ 170

5.1 Transverse section of the constant withdrawal rate 100 μms^{-1} sample **CT** volume. $\lambda_{avg} = 260$ μm. 174
5.2 Side view section of the constant withdrawal rate 100 μms^{-1} sample **CT** volume. 174
5.3 Transverse section of the 40-60-80 μms^{-1} sample in the 40 μms^{-1} region. $\lambda_{avg} = 300$ μm. 176
5.4 Transverse section of the 40-60-80 μms^{-1} sample in the 60 μms^{-1} region. $\lambda_{avg} = 250$ μm. 176

5.5 Transverse section of the 40-60-80 μms^{-1} sample in the 80 μms^{-1} region. $\lambda_{avg} = 230$ μm. 176
5.6 Transverse section of the 40-60-100 μms^{-1} sample in the 40 μms^{-1} region. $\lambda_{avg} = 295$ μm. 177
5.7 Transverse section of the 40-60-100 μms^{-1} sample in the 60 μms^{-1} region. $\lambda_{avg} = 270$ μm. 177
5.8 Transverse section of the 40-60-100 μms^{-1} sample in the 100 μms^{-1} region. $\lambda_{avg} = 240$ μm. 177
5.9 Dendrite forest of centres traced along the length of the 40 μms^{-1} sample. 182
5.10 Primary dendrite arm spacing along the length of the 40 μms^{-1} continuously withdrawn sample. 183
5.11 Number of nearest neighbours along the 40 μms^{-1} sample. 183
5.12 a) Schematic showing location of porosity within the 40 μms^{-1} continuously withdrawn sample. b) Location of new dendrites and outcompeted dendrites in the sample when viewed side on. c) Cumulative number of new and outcompeted dendrites with a linear fit. 184
5.13 Orientation of the constant withdrawal rate 40 μms^{-1} sample for all dendrite primary trunks, outcompeted dendrites and newly created dendrites. 185
5.14 Dendrite forest of centres traced along the length of the 60 μms^{-1} sample. 186
5.15 Primary dendrite arm spacing along the length of the 60 μms^{-1} continuously withdrawn sample. The average **PDAS** has an error of approximately 1 μm, whilst this is shown on the curve it is not clearly visible at this scale. 187
5.16 Number of nearest neighbours along the 60 μms^{-1} sample. 187
5.17 a) Schematic showing location of porosity within the 60 μms^{-1} continuously withdrawn sample. b) Location of new dendrites and outcompeted dendrites in the sample when viewed side on. c) Cumulative number of new and outcompeted dendrites with a third order polynomial fit. 188
5.18 Orientation of the constant withdrawal rate 60 μms^{-1} sample for all dendrite primary trunks, outcompeted dendrites and newly created dendrites. 189
5.19 Dendrite forest of centres traced along the length of the 80 μms^{-1} sample. 190
5.20 Primary dendrite arm spacing along the length of the 80 μms^{-1} continuously withdrawn sample. 191
5.21 Number of nearest neighbours along the 80 μms^{-1} sample. 191
5.22 a) Schematic showing location of porosity within the 80 μms^{-1} continuously withdrawn sample. b) Location of new dendrites and outcompeted dendrites in the sample when viewed side on. c) Cumulative number of new and outcompeted dendrites with a third order polynomial fit. 192

5.23 Orientation of the constant withdrawal rate 80 μms^{-1} sample for all dendrite primary trunks, outcompeted dendrites and newly created dendrites. 193
5.24 Dendrite forest of centres traced along the length of the 100 μms^{-1} sample. 194
5.25 Primary dendrite arm spacing along the length of the 100 μms^{-1} continuously withdrawn sample. The average **PDAS** has an error of approximately 1 μm, whilst this is shown on the curve it is not clearly visible at this scale. 195
5.26 Number of nearest neighbours along the 100 μms^{-1} sample. 195
5.27 a) Schematic showing location of porosity within the 100 μms^{-1} continuously withdrawn sample. b) Location of new dendrites and outcompeted dendrites in the sample when viewed side on. c) Cumulative number of new and outcompeted dendrites with a third order polynomial fit. 196
5.28 Orientation of the constant withdrawal rate 100 μms^{-1} sample for all dendrite primary trunks, outcompeted dendrites and newly created dendrites. 197
5.29 Dendrite forest of centres traced along the length of the 40-80 μms^{-1} changing withdrawal rate sample. 198
5.30 Primary dendrite arm spacing along the length of the changing withdrawal rate 40-80 μms^{-1} sample. 199
5.31 Number of nearest neighbours along the 40 to 80 μms^{-1} changing withdrawal rate sample. 199
5.32 Primary dendrite arm spacing along the length of the changing withdrawal rate 40-80 μms^{-1} sample. 200
5.33 JMAK analysis of the change in **PDAS** after the withdrawal rate change from 40 μms^{-1} to 80 μms^{-1}. The inset shows a zoomed in portion of the graph showing an indication of the incubation time after the transition. 201
5.34 Results of Avrami analysis for the different **PDAS** calculation methods in the 40 - 80 μms^{-1} changing withdrawal rate sample after the withdrawal rate change from 40 μms^{-1} to 80 μms^{-1}. a) Average **PDAS**, b) MST **PDAS**, c) Voronoi **PDAS**, d) WR **PDAS**, e) WRV **PDAS**. 202
5.35 a) Schematic showing location of porosity within the 40-80 μms^{-1} changing withdrawal rate sample. b) Location of new dendrites and outcompeted dendrites in the sample when viewed side on. c) Cumulative number of new and outcompeted dendrites with a third order polynomial fit. 203
5.36 Orientation of the varying withdrawal rate 40-80 μms^{-1} sample for all dendrite primary trunks, outcompeted dendrites and newly created dendrites. 204
5.37 Dendrite forest of centres traced along the length of the 40-60-80 μms^{-1} changing withdrawal rate sample. 205

5.38 Primary dendrite arm spacing along the length of the changing withdrawal rate 40-60-80 μms^{-1} sample. 206
5.39 Number of nearest neighbours along the 40-60-80 μms^{-1} varying withdrawal rate sample. 206
5.40 Primary dendrite arm spacing along the length of the changing withdrawal rate 40-60-80 μms^{-1} sample after the first withdrawal change from 40 μms^{-1} to 60 μms^{-1} 207
5.41 JMAK analysis of the change each of calculated **PDAS** after the withdrawal rate change from 40 μms^{-1} to 60 μms^{-1} in the 40-60-80 μms^{-1} sample. 208
5.42 Results of Avrami analysis for the different **PDAS** calculation methods in the 40 - 60 - 80 μms^{-1} changing withdrawal rate sample after the withdrawal rate change from 40 μms^{-1} to 60 μms^{-1}. a) Average **PDAS**, b) MST **PDAS**, c) Voronoi **PDAS**, d) WR **PDAS**, e) WRV **PDAS**. 209
5.43 Primary dendrite arm spacing along the length of the changing withdrawal rate 40-60-80 μms^{-1} sample after the second withdrawal change from 60 μms^{-1} to 80 μms^{-1} 210
5.44 JMAK analysis of the change in each calculated **PDAS** after the withdrawal rate change from 60 μms^{-1} to 80 μms^{-1} in the 40-60-80 μms^{-1} sample. 211
5.45 Results of Avrami analysis for the different **PDAS** calculation methods in the 40 - 60 - 80 μms^{-1} changing withdrawal rate sample after the withdrawal rate change from 60 μms^{-1} to 80 μms^{-1}. a) Average **PDAS**, b) MST **PDAS**, c) Voronoi **PDAS**, d) WR **PDAS**, e) WRV **PDAS**. 212
5.46 a) Schematic showing location of porosity within the 40-60-80 μms^{-1} changing withdrawal rate sample. b) Location of new dendrites and outcompeted dendrites in the sample when viewed side on. c) Cumulative number of and outcompeted dendrites with a linear fit for all the dendrites. 213
5.47 a) Schematic showing location of porosity within the 40-60-80 μms^{-1} changing withdrawal rate sample. b) Cumulative number of and outcompeted dendrites with a linear fit for the 40 μms^{-1} section. c) Cumulative number of and outcompeted dendrites with a linear fit for all the dendrites for the 60 μms^{-1} section. 214
5.48 a) Schematic showing location of porosity within the 40-60-80 μms^{-1} changing withdrawal rate sample. b) Cumulative number of and outcompeted dendrites with a linear fit for all the dendrites for the 80 μms^{-1} section. 215
5.49 Orientation of the varying withdrawal rate 40-60-80 μms^{-1} sample for all dendrite primary trunks, outcompeted dendrites and newly created dendrites. 216
5.50 Primary dendrite arm spacing along the length of the changing withdrawal rate 40-60-100 μms^{-1} sample. 217

5.51 Number of nearest neighbours along the 40-60-100 μms^{-1} varying withdrawal rate sample. 217
5.52 a) Schematic showing location of porosity within the 40 μms^{-1} section of the 40-60-100 μms^{-1} changing withdrawal rate sample. b) Location of new dendrites and outcompeted dendrites in the sample when viewed side on. c) Cumulative number of and outcompeted dendrites with a third order polynomial fit for the 40 μms^{-1} section. 218
5.53 a) Schematic showing location of porosity within the 60 μms^{-1} section of the 40-60-100 μms^{-1} changing withdrawal rate sample. b) Location of new dendrites and outcompeted dendrites in the sample when viewed side on. c) Cumulative number of and outcompeted dendrites with a third order polynomial fit for the 60 μms^{-1} section. 219
5.54 a) The $\bar{m}^*$, $\bar{sigma}^*$ pairing for each slice along the length of the 40 μms^{-1} sample. b) The $\bar{m}^*$, $\bar{sigma}^*$ pairing for each slice along the length of the 60 μms^{-1} sample. c) The $\bar{m}^*$, $\bar{sigma}^*$ pairing for each slice along the length of the 80 μms^{-1} sample. d) The $\bar{m}^*$, $\bar{sigma}^*$ pairing for each slice along the length of the 100 μms^{-1} sample. . . 224
5.55 The $\bar{m}^*$ $\bar{sigma}^*$ pairing for each slice along the length of the 40-80 μms^{-1} changing withdrawal rate sample. 225
5.56 The $\bar{m}^*$ $\bar{sigma}^*$ pairing for each slice along the length of the 40-60-80 μms^{-1} changing withdrawal rate sample. 226
5.57 Collation of the average Warnken-Reed **PDAS** values for each of the samples. The calculated **PDAS** for the Hunt, Trivedi, Kurz-Fisher and Bouchard-Kirkaldy given in Equations (2.23) to (2.26) . 228
5.58 a) The mean average **PDAS** for each of the constant withdrawal rate samples and the sections of the varying withdrawal rate samples. b) The mean minimum-spanning-tree **PDAS** for each of the constant withdrawal rate samples and the sections of the varying withdrawal rate samples. c) The mean Voronoi **PDAS** for each of the constant withdrawal rate samples and the sections of the varying withdrawal rate samples. d) The mean Warnken-Reed-Voronoi **PDAS** for each of the constant withdrawal rate samples and the sections of the varying withdrawal rate samples. 229
5.59 Results of theoretical **PDAS** models of Equations (2.23) to (2.26) compared to the average **WR PDAS**. Figure shows all samples. . . 232
5.60 Results of theoretical **PDAS** models of Equations (2.23) to (2.26) compared to the average **WR PDAS**. Figure shows only changing withdrawal rate samples. 232
5.61 a) Incubation time against relative velocity change for the 40 - 80 and 40 - 60 - 80 μms^{-1} samples. b) Time until transition is completed against relative velocity change for the 40 - 80 and 40 - 60 - 80 μms^{-1} samples. c) Transition length against relative velocity change for the 40 - 80 and 40 - 60 - 80 μms^{-1} samples with an exponential fit. d) Diffusion length against relative velocity change for the 40 - 80 and 40 - 60 - 80 μms^{-1} samples. 233

5.62 a) Transition length over diffusion length against relative velocity change for the 40 - 80 and 40 - 60 - 80 μms^{-1} samples. b) Change in **PDAS** before and after the transition against relative velocity change for each of the changing withdrawal rate samples. c) Change in **PDAS** over transition length before velocity change and after the array stabilises post transition against relative velocity change for each of the changing withdrawal rate samples. d) Change in **PDAS** over diffusion length before velocity change and after the array stabilises post transition against relative velocity change for each of the changing withdrawal rate samples. 234
5.63 a) Rate of change in **PDAS** for each relative velocity change. b) JMAK n exponent against relative velocity change. c) Change in the number of nearest neighbours for the Warnken-Reed, Voronoi and Warnken-Reed-Voronoi **PDAS** methods before and after the transition for each of the changing withdrawal rate samples. 235
5.64 Zoomed in view of some dendrite centres traced from the 40 μms^{-1} sample. 237
5.65 Zoomed in view of some dendrite centres traced from the 60 μms^{-1} sample. Two instances of dendritic branching can be seen. The single dendritic trunk at the bottom of the **CT** volume splits twice to form three primary dendrites. The two branching points are highlighted in green. 238
5.66 Isosurface of dendrite taken from 40 μms^{-1} constant withdrawal rate sample. 241
5.67 Isosurface of dendrite taken from 40 μms^{-1} constant withdrawal rate sample. 241
5.68 Isosurface of dendrite taken from 40 μms^{-1} constant withdrawal rate sample. 241
5.69 Isosurface with skeleton centres overlain 242
5.70 Isosurface with skeleton centres overlain. 242
5.71 Isosurface with skeleton centres overlain. 242
5.72 a) Isosurface with skeleton centres overlain and thresholded. b) Isosurface with skeleton centres overlain and thresholded. c)Side view of the isosurface with skeleton centres overlain and thresholded. Also shown is the centre of gravity for each slice along the length of the dendrite. d) Side view of the isosurface with skeleton centres overlain and thresholded. Also shown is the centre of gravity for each slice along the length of the dendrite. e) Plan view of the isosurface with skeleton centres overlain and thresholded. Also shown is the centre of gravity for each slice along the length of the dendrite. 243

6.1 Schematic view of dendrites at an angle to the [001] direction (upwards to top of the page). The red line indicates a plane taken across the **CT** volume corresponding to an individual slice of the sample. 264

9.1 Schematic design of the aerogel furnace manufactured by the German Space Agency[14] (not to scale). 283
9.2 Schematic of the simulated furnace volume (not to scale). 290
9.3 Temperature-time profiles for the validation simulation of the cool down of an Al-4 wt%Cu alloy in microgravity. The markers are temperatures taken from the experimental work and the lines are temperature readings obtained from the simulation. 296
9.4 Relative error in composition against sample length for the simulated alloy compared to the composition readings obtained by Cahoon et al [15] for an Al-4wt% Cu alloy in microgravity. 297
9.5 Composition of the minimum and maximum composition at the end of the experiment against the mesh density. 298
9.6 Relative error of the mushy depth with time obtained from the simulation of the aerogel furnace. The initial transient ended at 15 s. The standard deviation was calculated from the complete data set. 305
9.7 Relative error in thermal gradient with time calculated using the values given in fig. 9.6, the ΔT_0 from table 9.4 and eq. (9.1). The initial transient ended at 15 s. The standard deviation was calculated from the complete data set. 306
9.8 Relative error in solidification front velocity with time obtained from the simulation of the aerogel furnace in terms of percentage area from the input value of 12×10^{-5}. The initial transient ended at 15 s. The standard deviation was calculated from the complete data set. 307
9.9 Relative error in primary dendrite arm spacing ($PDAS$) with time. The initial transient ended at 15 s. The standard deviation was calculated from the complete data set. 308
9.10 Temperature time profiles for the top and bottom heaters. 310
9.11 Calculated effect of the primary dendrite arm spacing λ as a function of the acceleration due to gravity, g, calculated using eqs. (9.2) and (9.3). The results of the simulation at $0g$ or when there was no flow are used in eq. (9.3). The standard deviation of the mean is overlain on the graph for the calculated λ at $0g$. 311
9.12 Composition profile for the Al-20wt%Cu rod after solidification . . 312
9.13 The affect of gravity on the buoyancy source term described in eq. (9.23) 319
9.14 The effect of gravity on the interdendritic velocity where λ_1 is also a function of g as described in the text above. 321

List of Tables

2.1 Avrami exponents, n [16, 17, 18, 19, 20] 29

3.1 Bridgman furnace parameters 73
3.2 Constant withdrawal rate Bridgman furnace experiments. Expected **PDAS** calculated using Equation (2.26) 78
3.3 Changing withdrawal rate solidification experiments. 79

4.1 Table of shape factors for different regular, irregular and dendritic shapes. 111
4.2 Table showing the mean, standard deviation and variance values for the different dendrites obtained from the traced nickel superalloy sample and from the binarised aluminium-copper **CT** volume. . . . 112
4.3 Table showing the mean, standard deviation and variance values for the scaled distance between the hand assigned centres and the centres assigned by each of the different methods. Included are subsets of the data containing the values for only the inner or edge dendrites from the microstructures. 112
4.4 Table showing the mean, standard deviation and variance values for the scaled distance between the hand assigned centres and the centres assigned by the centre of geometry, skeleton-geometry and symmetry-based methods tested on the Al-10 wt% Cu **CT** slice. Included are subsets of the data containing the values for only the inner or edge dendrites from the microstructures. 124
4.5 Normalised average edge lengths, m^*, for select packing orientations. 135
4.6 Comparison of the local **PDAS** calculation methods undertaken on the 'perfect' hand-assigned centres and the skeleton-geometry centres obtained from Figure 4.8. The statistics in this table are taken from Figures 4.37 to 4.40 a) and b). 149
4.7 Statistics for percentage error, δ between the hand and skeleton-geometry local **PDAS** calculations. The local **PDAS** calculation methods undertaken on the 'perfect' hand-assigned centres and the skeleton-geometry centres obtained from Figure 4.8. The statistics in this table are taken from Figures 4.37 to 4.40 c). 149
4.8 Principle orientation of test shapes, without and with skeletonisation included 163

5.1 Equations for each linear fit of each calculated **PDAS** as a function of distance from velocity change ($\lambda(d_{\Delta v})$) in Figure 5.32 and the goodness of each fit. 200
5.2 Equations for each linear fit of **PDAS** as a function of distance from velocity change ($\lambda(d_{\Delta v})$) in Figure 5.40 and the goodness of each fit. 207
5.3 Equations for each linear fit of **PDAS** as a function of distance from velocity change ($\lambda(d_{\Delta v})$) in Figure 5.43 and the goodness of each fit. 210
5.4 Avrami equations fitted for the Warnken-Reed calculated **PDAS** for the changing withdrawal rate samples. 222
5.5 The mean Warnken-Reed **PDAS** for each of the constant withdrawal rate samples and the sections of the varying withdrawal rate samples. 228
5.6 The rate of change in **PDAS** for each of the changing withdrawal rate experiments for the Warnken-Reed calculations 231
5.7 The incubation and the end of transition for the changing withdrawal rate samples after the changing withdrawal rates for the Warnken-Reed **PDAS** calculations obtained from the JMAK analysis. The error is associated with a possible measurement error when marking the location of the transition on the sample with a ruler. 231

9.1 Thermocouple location in the graphite crucible wall [15] 293
9.2 Simulation parameters for the model validation. † h is the distance between the top and bottom thermocouple rather than the entire casting as explained in the model validation methodology. 294
9.3 Materials Parameters for Al-4 $wt\%$Cu[15] 294
9.4 Materials parameters for Al 20 wt% Cu. An approximate value for latent heat was used, in this instance for a Al 6.2$wt\%$ Cu alloy.[21] . 303
9.5 Simulation parameters 304
9.6 Results of the simulations with differing solidification rates and mushy depth requirements and the average values obtained. 323
9.7 Parameters used to evaluate the $\Delta\rho$ during the Aerogel furnace simulation using the Boussinesq equation in eq. (9.20) 323

Abbreviations

CET	**C**olumnar to **E**quiaxed **T**ransition
CNN	**C**onvolutional **N**eural **N**etwork
CT	**C**omputerised **T**omography
DBSCAN	**D**ensity **B**ased **S**pacial **C**lustering
DLR	**D**eutsches Zentrum für **L**uft und **R**aumfahrt
DRM	**D**irectional **R**eflectance **M**icroscopy
EBSD	**E**lectron **B**ack **S**cattered **D**iffraction
ESA	**E**uropean **S**pace **A**gency
ISS	**I**nternational **S**pace **S**tation
JMAK	**J**ohnson-**M**ehl-**A**vrami-**K**olmogorov
LDC	**L**arge **D**iameter **C**entrifuge
MICAST	**MI**crostructure evolution in **CAST**ing of technical Aluminium alloys under diffusive and controlled convective conditions
MRI	**M**agnetic **R**esonance **I**maging
MSL	**M**aterials **S**cience **L**ab
MST	**M**inimum **S**panning **T**ree
PDAS	**P**rimary **D**endrite **A**rm **S**pacing
SDAS	**S**econdary **D**endrite **A**rm **S**pacing

Nomenclature

Latin Symbols

$\bar{x}$ Average distance, m

$\dot{G}$ Growth rate, ms^{-1}

$\dot{N}$ Nucleation rate, m^3s^{-1}

$\vec{AB}$ Vector

$\vec{AM}$ Vector

$\vec{BM}$ Vector

$\vec{MM}$ Vector

A Area, m^2; Materials coefficient

a Primary dendrite arm coarsening constant, $K^{\frac{1}{2}}m^{-\frac{1}{2}}$; Equation exponent

a_1 Primary dendrite arm calibrating factor

A_c Constant of proportionality

A_p Area of porosity in a slice, m^2

A_R Aspect ratio

A_{bound} Area of a shapes minimum bounding circle, m^2 or pixels.

b Equation exponent

C Concentration, wt%

c	Equation exponent; Temperature adjustment scaling parameter
$\bar{C}$	Total or mixed concentration, wt%
C_0	Bulk Composition, wt%
C_l	Liquid Composition, wt%
c_p	Heat capacity, $\mathrm{Jkg^{-1}K^{-1}}$
C_s	Solid Composition, wt%
D	Diffusion coefficient, $\mathrm{m^2\ s^{-1}}$
d	Diffusion length, m; Mushy zone depth, m; Distance between two points, pixels, voxels or m
d_0	Capillary length, m
d_h	Distance between the hot and cold zone of the furnace, m
D_l	Diffusion coefficient in liquid, $m^2 s^{-1}$
$d_{\Delta v}$	Distance from velocity change, mm
f	Number of faces of the convex hull; Shape factor
f_C	Circularity shape factor
f_E	Elongation shape factor
f_l	Fraction liquid
f_s	Fraction solid
f_w	Convexity or waveiness shape factor
f_{comp}	Compactness shape factor
f_{ecc}	Eccentricity shape factor
G	Gaussian distribution

g	Acceleration due to gravity, ms^{-2}
g_E	Unit Acceleration due to gravity on Earth, 1g = 9.81, $\mathrm{m}s^{-2}$
H	Area of the convex hull, m^2; Enthalpy, Jkg^{-1}
h	Heat transfer coefficient, $\mathrm{Wm}^{-2}\mathrm{K}^{-1}$; Sample height, m
h_{ref}	Sensitive enthalpy at reference condition, Jkg^{-1}
I	Image
I_0	Original Image
K	Curvature, m^{-1}; Permeability of a medium, m^2
k	Partition coefficient; Reaction coefficient, s^{-1}
L	Boundary layer thickness, m; Characteristic length, m; Latent heat, JK^{-1}; Constant dependent on harmonic perturbations
L_c	Characteristic length, m
L_d	Diffusion length scale, m
l_d	Solute diffusion length, m
l_{ref}	Reference length, m
l_T	Thermal diffusion length, m
M	Point on dendrite perimeter
m	Liquidus slope, K/wt%
m^*	Normalised edge length
N	Number of dendrites; Minimum number of points in **DBSCAN**
n	Avrami parameter
N_0	Nucleant density, m^{-3}

P	Perimeter length, m; Pressure, Pa
P_c	Convex hull perimeter length, m
Q	Energy, J
R	Thermal resistance, KW^{-1}; Dendrite tip Radius, m
r	Radius, m; Magnitude of the normal
S	Source term
s	Structuring element
T	Temperature, K
t	Time, s
$\dot{T}$	Cooling rate, Ks^{-1}
T_e	Eutectic temperature, K
T_F	Fusion temperature of the solvent, K
T_l	Liquidus temperature, K
T_m	Melting temperature of pure material, K
T_s	Solidus temperature, K
T_{Al}	Melting temperature of pure Al, K
u	Vector component; Liquid velocity, ms^{-1}
v	Vector component; Velocity, $\mathrm{m}s^{-1}$
v^*	Solidification front velocity, ms^{-1}
V_f^β	Volume fraction of β phase
V_{C-D}	Critical cellular-dendritic limit, ms^{-1}
V_C	Critical planar velocity limit, ms^{-1}

w width, m

x' Distance ahead of the moving interface, m

X_B Atomic fraction of solute

X_{Cu} Atomic fraction of copper

z Height, m, Length, m

Greek Symbols

α Warnken-Reed parameter

$\bar{\lambda}$ Mean Primary Dendrite Arm Spacing, μm

β_C Expansion coefficient, $\text{kgm}^{-3}\text{wt}\%^{-1}$

β_T Coefficient of thermal expansion, $\text{kgm}^{-3}\text{wt}\%^{-1}$

ΔA Mesh size, m^2

Δr Radial step, m

ΔS Entropy of fusion per unit volume, $\text{JK}^{-1}m^{-3}$

Δt Time step, s

ΔT_0 Liquidus-solidus range at C_0, K

ΔT_c Solute undercooling of dendrite tip, K

ΔT_N Nucleation undercooling, K

Δv Change in velocity, ms^{-1}

Δz Axial step, m

δz Solid-liquid interfacial thickness, m

δ Bow wave length, m; Percentage error, %

ϵ Emissivity; Distance between values in the **DBSCAN**; Interfacial energy anisotropy parameter; Surface tension scaling factor

Γ Gibbs-Thomson Coefficient, Km

γ_{sl} Solid-liquid interfacial energy, Jm^{-2}

κ Thermal conductivity, $\mathrm{Wm}^{-1}\mathrm{K}^{-1}$

λ Primary Dendrite Arm Spacing, μm

λ_1 Primary Dendrite Arm Spacing, μm

λ_2 Secondary Dendrite Arm Spacing, μm

∇C Concentration gradient, $\mathrm{wt\%m}^{-1}$

∇P Pressure gradient, Pam^{-1}

∇T Thermal gradient, Km^{-1}

ν Kinematic viscosity, m^2s^{-1}

Ω_0 Active contour interface

Ω_1 Active contour foreground image

Ω_2 Active contour background image

ϕ Extended volume fraction of equiaxed grains, %; Level set result; Pixel intensity

ϕ_E Extended volume fraction of equiaxed grains, %

ρ Density, kgm^{-3}

σ Standard deviation; Stefan-Boltamann Constant, $\mathrm{Wm}^{-2}\mathrm{K}^{-4}$; liquid-solid surface energy, erg m^{-2}

σ^* Marginal stability criterion

$\sigma_{\bar{\lambda}}$ Standard deviation of the mean primary dendrite arm spacing, μm

$\sigma_{\bar{d}}$ Standard deviation of the mean mushy depth, m

$\sigma_{\bar{v^*}}$ Standard deviation of the mean velocity, ms^{-1}

θ Angle, ^{o}

ξ Function of the solute Peclet number

Subscripts

$1g$ At 1g

adj Temperature adjustment

atm Atmosphere

avg Average

b Bouyancy

bot Bottom heater

E Earth; East

e Eutectic

f Final

$flow$ Fluid flow

HS Heat shield

i Array pointer

j Array pointer

l Liquid

max Maximum

min Minimum

MST Minimum spanning tree PDAS

$mushy$ Mushy width

N North

rad Radiation

ref Reference

req Required

S South

s Solid

$surf$ Sample surface

top Top heater

V Voronoi PDAS

W West

WR Warnken-Reed PDAS

WRV Warnken-Reed-Voronoi PDAS

Superscripts

$*$ Interface; Normalised value

$corr$ Corrected

p Time step

Dimensionless Numbers

Bi Biot number, $\frac{hl_{ref}}{\kappa}$

Fo Finite difference form of the Fourier number

Pe Péclet number, $\frac{v^* L}{D_l}$

Pe_i Interfacial Péclet number, $\frac{v^* d}{2D_l}$

$Var(x)$ Variance of data set x

To my Parents and Sister

Chapter 1

Introduction

1.1 Motivation

Understanding solidification and the processes that occur during solidification is one of the main goals of materials science. Almost all of a components mechanical properties come about as a direct result of the processing history [22]. A material's microstructure formed during solidification is therefore very important for obtaining desired properties in engineering materials. Once solidification has been achieved it is a costly and often time-inefficient process to correct any defects that occur during this initial step, for example heat treating nickel superalloys is time intensive [22, 23]. Moreover in directional solidification it is extremely costly to alter the primary dendrite arm spacing (**PDAS**) once solidification has occurred, if possible to do at all. The **PDAS** is an extremely important parameter in aerospace applications as decreasing it increases the fatigue life and Young's modulus of nickel-superalloy turbine blades [22]. The prediction of microstructures is also very important to prevent any defects from forming in the first instance.

In order to predict final microstructures the following knowledge of the material and how it is processed is needed [22, 24, 25, 26, 27, 28, 29]:

- the processing conditions;
- mass, and solute transport within the liquid;
- kinetics of new phase formation within the melt;
- thermodynamics of the material to determine new phases formed.

These different phenomena all play a vital part in the solidification of metals and are complexly linked together so that any change in one parameter can alter many others dramatically.

One factor that affects the final microstructure dramatically is the extent of solute transport within the melt. Fluid flow causes the phenomena of macrosegregation. Macrosegregation is a problem in large scale castings where there is a density difference between the evolving solid and the liquid. This problem can be further exacerbated at higher gravity levels (g) when density differences (Δp) become even greater resulting in faster solute movement within the melt (v_{mush}). This is described by Darcy's law in Equation (1.1):

$$v_{mush} = \frac{\Delta \rho g K}{\nu f_l} \tag{1.1}$$

Where: K is the permeability, f_l is the fraction of liquid and ν is the kinematic viscosity. Moreover the extent of fluid flow has a large effect upon the packing of the dendrites, *i.e.* the **PDAS**. Increasing the magnitude of fluid flow causes the dendrites to become more closely packed together and thus decreasing the **PDAS** [30]. The converse is also true, decreasing fluid flow increases **PDAS** [30].

Traditionally work has focused on examining the **PDAS** in 2D by taking transverse slices of directionally cast alloys [15, 22, 23, 31, 32, 33, 34, 35, 36]. However with the advent of computerised tomography (**CT**) analysis can now be obtained quickly

and easily over whole components, rather than just a few select slices of a material (often taken at random points along the length of the sample) which is the case in traditional metalographic methods.

In order to investigate the affect of macrosegregation and microstructural evolution along the length of a sample this work, as part of the wider **MICAST** project funded by the European Space Agency (**ESA**), aims to investigate the effect of **PDAS** and dendrite packing along the length of aluminium 10 wt% copper rods in 3D. The alloy was chosen due to the simplistic nature of the binary alloy and the wealth of research that has been conducted on it and similar alloys [15, 31, 37, 38, 39, 39, 40, 41, 42, 43, 44, 45, 46, 47, 48, 49].

This work will be ground based, *i.e.* at $1g$, but forms preparatory work that is to be continued by **MICAST** project as a whole. As such this body of work places emphasis upon the analysis of metallographic specimens in 3D and the creation and examination of novel image analysis methods trialled on samples produced under differing withdrawal velocities (v^*) but identical thermal gradients (∇T).

1.2 Introduction

As the need for stronger and more reliable components has increased, so too has the need to understand the complicated process that go into making them. By increasing knowledge of the underlying physics, *a priori* assumptions can be made prior to the production of a new metal component. Therefore resulting in better, lighter, and more cost effective components.

An example of this is the production of turbine blades which have over the last half century been a product of many incremental and iterative changes to the design, composition, and processing parameters [22]. By altering processing parameters–such as the thermal gradient and withdrawal velocity (∇T, v^*) during

solidification–there can be vast differences in the resulting mechanical properties of a component [22]. This is as a result of changing crystal–in this instance dendritic–structure within the resulting material.

Commonly the primary dendrite arm spacing (**PDAS**, λ) is altered in order to give more favourable mechanical properties by changing these two solidification parameters [10, 22, 24, 25, 31, 32, 50, 51, 52, 53, 54, 55, 56, 57, 58, 59, 60] (∇T and v^*). Moreover by solidifying material under varying gravity levels (where 1g $= 9.81$ ms^{-1}) from microgravity to hyper-gravity, one can further alter the **PDAS** [33, 61, 62].

The effect of changing solidification parameters has been studied here. Namely the effect of a changing withdrawal rate as a sample wast cast using a Bridgman furnace at Access, Aachen RWTH. To this end novel image analysis techniques have been produced and trialled on **CT**'ed volumes of the Bridgman furnace samples. These techniques have been compared and contrasted with commonly available ones (in Chapter 4) in order to obtain information on the **PDAS** along the length of these samples and how it changes after an increase in the withdrawal velocity in three dimensions.

The project in collaboration with the European Space Agency (**ESA**), forms part of the **MICAST** project exploring the solidification of technical aluminium alloys in controlled convective conditions. The **MICAST** project aims to better understand how the dendritic growth and the resulting microstructure can be impacted by changing solidification conditions. The project was supported by Access, Aachen RWTH, and the German Space Agency (**DLR**) where the castings were produced and then imaged respectively.

The aim of this thesis is to act as a starting point for further works undertaken on the Materials Science Lab (**MSL**) of the International Space Station (**ISS**) and ground based experiments at 1g and hyper-gravity experiments within the Large

Diameter Centrifuge (**LDC**). The thesis aims to produce schemes for analysing large numbers of samples in a reasonable length of time. The throughput and number of samples examined here is drastically increased over conventional methods by incorporating new image analysis techniques. In particular, attention is paid to accuracy of techniques for finding the centre of a dendrite which have often been relatively simplistic (*e.g.* assigning the centre by hand) and how local dendrite arm spacing changes along the length of sample as compared to predictions from classical **PDAS** calculation equations. Analysis is made to examine how errors propagate through the analysis from initial CT scan through to the final coordinate matrix.

1.3 Thesis Structure

The thesis begins with an overview in Chapter 2 of the relevant solidification theory of binary alloys and dendritic solidification in particular. Classical models to describe the shape and growth of dendrites are described, in particular the chemistry and microstructure of aluminium copper alloys are described. Furthermore, the effect that processing conditions have on the resulting microstructure is explored with classical equations for the **PDAS**. Subsequently in Chapter 2 the effect that different image analysis techniques play in data-mining large samples is explored with respect to classical techniques.

Chapter 3 details the methodology of experiments undertaken at 1g in a Bridgman furnace at Access, Aachen RWTH. A range of constant withdrawal velocities were trialled (40, 60, 80 and 100 μms^{-1}) as well as three experiments into the effect of changing withdrawal velocity (40-80 μms^{-1}, 40-60-80 μms^{-1}, and 40-60-100 μms^{-1}). These velocities were chosen as they: a) did not result in a columnar to equiaxed transition; and b) they were calculated to result in a **PDAS** which was greater than 2/3 of the previous **PDAS**.

The material produced as a result of the experiments detailed in Chapter 3 are examined using novel image analysis techniques which are outlined within Chapter 4. The chapter details the image acquisition by means of **CT** of the Al 10wt% Cu samples. Subsequently the methods to analyse these images are detailed and examined, including methods for binarising of images. Different methods for finding the centre of a dendrite are compared and contrasted. Shape factors are used to compare the different methods for a large number of dendrites taken from Ni-superalloy and Al-10wt% Cu samples. Finally a number of different **PDAS** calculation techniques from the literature are explained briefly which will be used to analyse the results of the **CT** scans. By comparing all of these image analysis techniques the most reliable methods are trialled on the larger data.

Chapter 4 gives a detailed review of current image analysis finding techniques. Emphasis is given to methods of **CT** volumes in 3D. Novel methods are put forward and compared to existing methods of dendritic analysis. Skeletonisation and the use of neural networks for finding the centre of a dendrite is explored. A skeletonisation based technique was found to be the best method for finding the centre of aluminium-copper dendrites compared to all methods tested. This technique was chosen for the large scale analysis of the **CT** volumes.

The chosen image analysis techniques are trialled on the **CT** data from the experiments presented in Chapter 3. The results of which are given in Chapter 5 and discussed. In this chapter the three dimensional nature of the solidification is reported in terms of how the **PDAS** changes along the length of the sample as well as the array packing and number of nearest neighbours.

Chapter 6 gives a detailed discussion of the results presented in Chapter 5 in light of prior research. The experiments showed that restructuring does occur in three dimensions when a change in withdrawal velocity occurs. Further the results

showed that this dendritic restructuring is not an instantaneous process but one that takes place over many mm and is dependent upon the diffusion length, L.

Chapter 7 reports the main conclusions of the thesis. For example a summary of the analysis techniques explored within this thesis and the results presented from examining the Al-10 wt%Cu samples in three dimensions.

Chapter 8 makes suggestions for future works and developments for the techniques and methods put forward in this thesis.

1.3.1 Appendices

Further work undertaken as part of this PhD thesis is provided in the following appendices in Chapters 9 to 11. The work provided in these appendices is supportive in nature and provided to give greater understanding to the reader of solidification of aluminium copper alloys (Chapters 9 and 11) and image analysis techniques for quantification of dendritic materials (Chapters 10 and 11).

An aerogel furnace model is presented in Chapter 9 in the form of a brief introduction and a subsequent text on the topic. A supplementary section is presented after the text to further clarify the chapter within the scope of solidification science. The text details the governing equations, for simulating an aerogel furnace (with a constant v^* and ∇T) as well as a brief review of similar methods to simulate the internal workings of an aerogel furnace. The model acts as a basis for the production of cooling curves for the top and bottom furnace heaters present in an aerogel furnace which is being commissioned and produced by **DLR**. This furnace will be used in the future in 0-20g research in sounding rocket, lab and centrifuge based experiments. The validation and results of the model are presented. The contribution of the other authors are presented in the acknowledgments section.

Chapter 10 is a paper detailing a novel image analysis technique used in this PhD thesis presented at the Soldification Processing 2017 Conference. This paper is included to provided further context for the image analysis techniques discussed herein for the reader. The contributions of the other authors are acknowledged before the paper.

Chapter 11 includes a conference paper which formed part of a plenary presentation at SG18. The paper and presentation detail analysis of the 40 to 80 μms^{-1} changing withdrawal rate sample. Chapter 11 provides more detail on this specific sample. The contributions of the other authors are acknowledged before the paper.

Chapter 2

Literature Review

Dendritic growth patterns are some of the most frequently observed structures in solidification. These structures are seen in the formation of natural structures such as: snowflakes (Figure 2.1) [63, 64], minerals like moss agate [65], and in technically relevant engineering alloys: nickel-superalloys [66] (Figure 2.2) and aluminium alloys [67] to name two. The growth of dendrites is characterised by their rather beautiful morphology as can be shown in Figure 2.1 and Figure 2.2. The solidification mechanisms of dendrites are complex due to the underlying dynamics controlling a dendrites' evolution, and as such there is still great debate around the topic.

Beginning with Papapetrou [68] there have over the last century been a number of models put forward that can describe dendritic growth, however they have all–for one reason or another–not been able to completely describe it. This is in part due to the fact that many models do not take into account the effect of convection on dendritic growth [25, 50, 51, 52, 53, 54]. This is a problem, as in reality convection almost always occurs at the solidification front [57, 69] apart from in some very specific occasions. One example of this being solidification in microgravity [57].

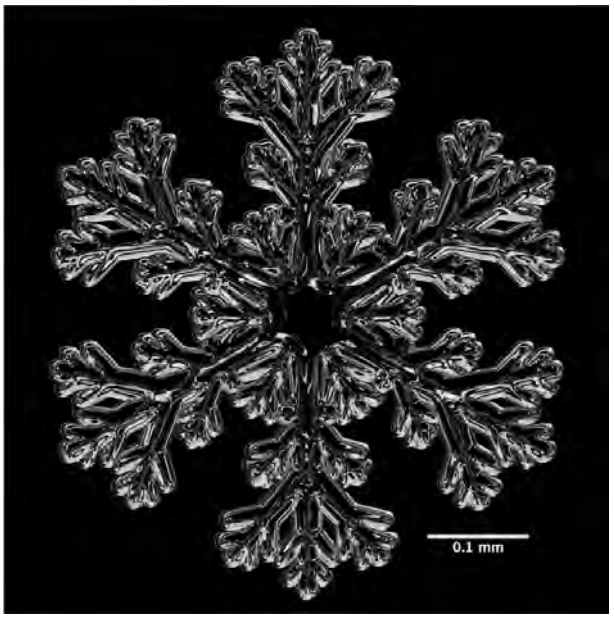


FIGURE 2.1: Photograph of a snowflake which grows with a branching dendritic structure [6]

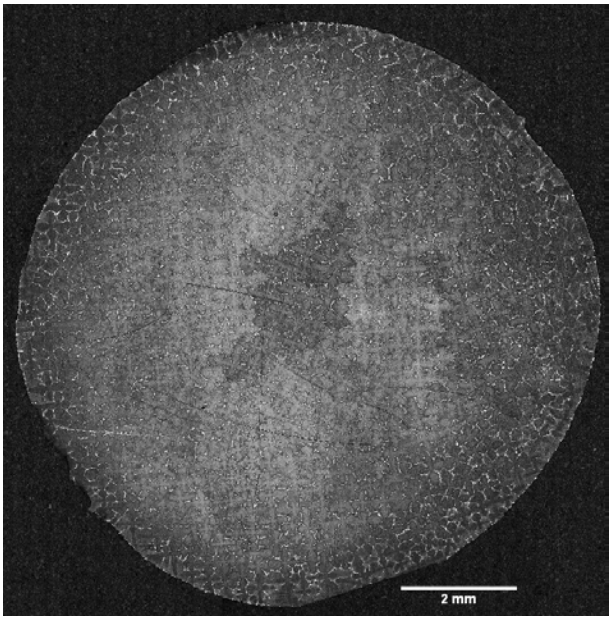


FIGURE 2.2: Slice of a Ni-superalloy directionally solidified 10 mm cross-section sample.

In microgravity the effect of convection is practically negligable resulting in purely diffusive mass transportation.

Classical models–such as the Ivanstov solution to 2-dimensional and 3-dimensional paraboidal dendritic growth–have been used to model microstructural evolution at the dendritic tip. They have been used to solve the Stefan problem (a boundary value problem involving a partial differential equation) for the liquid to solid phase transition [50, 51]. However the result of this analysis leads to the calculation of the Péclet (Pe) number as a function of the dendrite tip velocity (v_{tip}) multiplied by the radius of curvature of the tip (R_{tip}) i.e. $v_{tip}\, R_{tip}$, as such the analysis leads to the curious result whereby the system can either be solved as a very sharp quickly growing dendrite or as slowly growing broad dendrite [25, 53]. In fact Ivanstov's model predicts that there are in-fact an infinite number of possible values of R_{tip} and v_{tip} for a valid Stefan number (Ste). This is shown graphically in Figure 2.3. As a result the Ivanstov model has been widely disproven within the literature and is not commonly used [25].

The Ivanstov method does not constrain the dendrite tip to a single parameter. As such, it must be modified to constrain it. The effect of interfacial energy and attachment kinetics are coupled into the equation to modify it. This adaption resulted in the modified Ivanstov technique [25, 53].

The modified Ivanstov method relates the tip undercooling with the bulk undercooling, the tip undercooling and the capillary effect. This results in a curve, as seen in Figure 2.3, which gives a value for a vR pair. This value is the maximum of the modified Ivanstov curve. This allows for a single value to be calculated for both tip velocity and tip radius offering a clear advantage over the unmodified Ivanstov solution which gives infinite solutions. However, this is only for very small radii. It was originally believed that this maxima on the modified Ivanstov curve

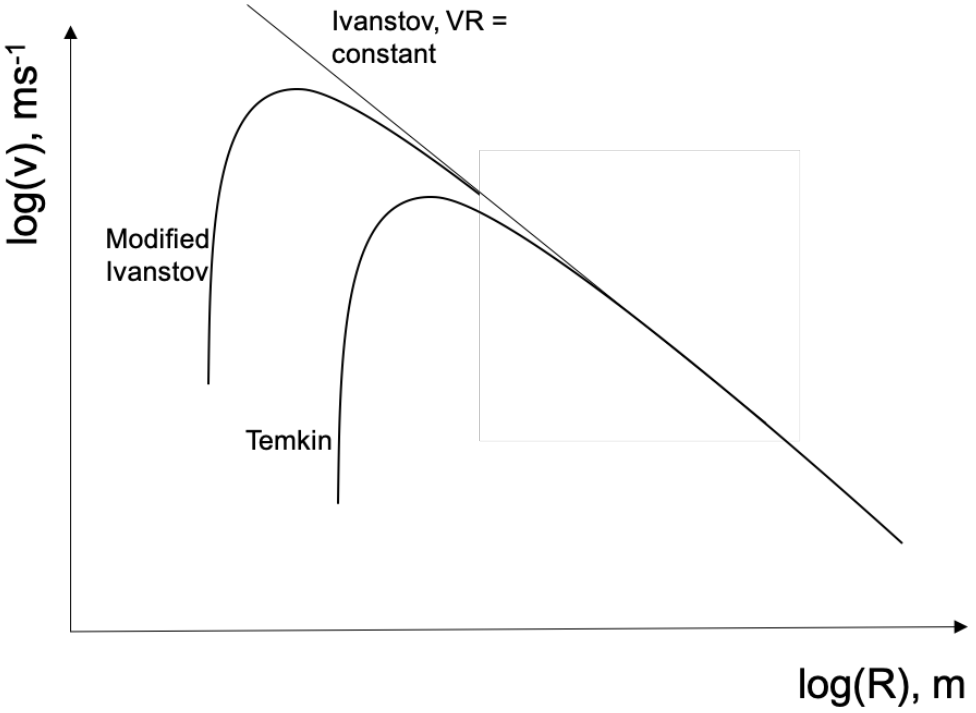


FIGURE 2.3: Example relationship between tip velocity and tip radius of a growing dendrite for a fixed undercooling.

was the selection point for the dendrite tip radius. This has since been disproven [25, 53].

A number of further models have been presented over the years developing approximate solutions to this problem. Temkin [52] proposed a solution which applied the Gibbs-Thomson condition to the parabolic shape of the growing dendrite. As such a maximum value of v_{tip} and R_{tip} can be obtained from the analysis. This minimum was believed to be a system self-selecting operating value for the dendritic growth [70]. Analysis of this method by Nash and Glicksman [54] concluded that the solution did not consistently satisfy the Gibbs-Thompson condition. Subsequently, Horvay and Cahn [51] provided a more general solution to the growth problem which included the special cases of both dendritic platelets and circular cross-sectioned dendrites.

A general expression for the tip selection for an alloy can be given by [25]:

$$m\nabla C\xi - \nabla T = \frac{1}{\sigma^*}\frac{\Gamma}{R^2} \tag{2.1}$$

Where: m is the slope of the liquidus, ∇C is the concentration gradient at a dendrite tip, ξ is a function of the solute Peclet number, ∇T is the temperature gradient, R is the tip radius and σ^* is a constant.

Finally Langer and Muller-Krumbhaar developed the marginal stability theory which interpreted σ^* [25, 53, 71, 72]. They proposed that dendrite tip radii smaller than the value of the extreme are all unstable and that dendrite radii larger than a maximum critical value are also unstable. This second instability was due to the capillary effect becoming so small that a dendrite tip was likely to split, for example into two new dendrite tips each with a new tip radius. Langer and Muller-Krumbhaar theorised that a dendrite would thus select the largest stable radii that

did not lie in these instabilities [25, 53, 71, 72]. They called this selection criteria the marginal stability theory [25, 53, 71, 72].

This theory came about after Langer and Muller-Krumbhaar undertook a linear stability analysis of the dendritic tip of an Ivanstov dendrite, with the inclusion of an interfacial energy effect. It resulted in the selection of a value of σ^* of 0.025 which gives good agreement with many experimental results [25, 53, 71, 72].

Even though Langer and Muller-Krumbhaar obtained relatively good agreement with experimental results and their definition of σ^* as 0.025 the definition of σ^* is still hotly debated within the literature [25, 53]. For instance with the introduction of the microsolvability criterion which defines σ^* as a function of the interfacial energy anisotropy parameter, ϵ rather than a constant [73]. The microsolvabilty approach gives a discrete set of shape preserving solutions [73].

These models briefly summarised above are expanded, compared, and contrasted with other models in the seminal literature review by Trivedi and Kurz [25]. What is clear however is that there is still ongoing debate around prediction of dendritic growth.

One drawback of all these classical models however, is that they do not take into account the effect of convection on the shape of the evolving microstructure. As such they cannot accurately portray evolving dendritic microstructure as convection can very dramatically influence an evolving microstructure [25, 55, 56].

Therefore, whilst these models are useful for benchmark or estimation exercises they cannot accurately portray real life dendritic solidification under nominal (1g) or higher gravity conditions (>1g). However these methods have been shown to be effective in describing the evolution of succinonitrile in microgravity, i.e. where natural convection does not take place due to the lack of buoyancy effects in the melt. Strong agreement was observed between observed velocity and calculated Ivanstov parabola by Glicksman [57]. One draw back within the literature is

the lack of information regarding dendritic growth in hypergravity (larger than $1g$) conditions. Mostly this is due to the lack of locations where hypergravity experiments can be undertaken. In 2010 the European Space Agency's (**ESA**) large diameter centrifuge came online (see Figure 2.4) which has greatly increased the number of hypergravity experiments in recent years. However, there is still a lack of current literature on the topic, with most experiments undertaken on the **LDC** related to life sciences [74, 75, 76, 77]. Although there have been a number of experiments looking into the effect of the the Columnar to Equiaxed Transition (**CET**) under higher gravity conditions on the **LDC** [78, 79, 80], and also under low gravity conditions [81], there is as such is a gap in the literature regarding higher gravity solidification.

Furthermore models which can predict the complexities of real growth scenarios involving dendrites–for a range of gravitational strengths–are needed to optimise parameters for solidification. This will allow for quicker research and bring about stronger, lighter and greener materials. This literature review aims to give a brief background of dendritic growth.

2.1 Binary Alloy Solidification

The vast majority of metallic materials used for engineering applications are alloys. Alloys are made up of a constituent metallic element, such as aluminium, and one or more metallic such as copper or non-metallic alloying elements such as carbon. These alloys are usually cast from a molten liquid mixture of the components. When an alloy is solidifying there will be two (or more) phases present, a solid and liquid phase. Solidification leads to the creation of a mushy zone which is a mixture of both solid and liquid, which can be described as the distance over which solid and liquid phases coexist during the solidification [26].



FIGURE 2.4: European Space Agency's Large Diameter Centrifuge based in Noordwijk, Netherlands. Reproduced under creative commons license [7].

The mushy depth, d, can be calculated for a solidifying alloy if the composition and thermal gradient, ∇T, of the solidification is known, as well as the liquidus temperature, T_l, and solidus temperature T_s.

$$d = \frac{T_l - T_s}{\nabla T} \tag{2.2}$$

Where the liquidus temperature T_l at the alloy composition can be given by:

$$T_l = T_m + mC_0 \tag{2.3}$$

with T_m the melting temperature of the pure material; m the slope of the liquidus line; and C_0 the bulk composition of the alloy. This expression is true for dilute alloys.

It is clear that depth of the mushy zone, d, is dependent upon the concentration of the alloy itself, as shown in Figure 2.5.

As the solid grows there is concentration and solute redistribution within the evolving microstructure. The extent of which can be conveniently defined by the equilibrium partition coefficient k which is a ratio of the composition of the solid and liquid [18, 26, 82, 83], C_s and C_l respectively:

$$k = \frac{C_s}{C_l} \tag{2.4}$$

The value of k can be obtained for each temperature during the solidification but is commonly assumed to be a constant value. This simplification is made when assuming that the lines of a phase diagram are straight (shown in Figure 2.6). When k is less than 1 there will be an increase in the liquid concentration as the solidification progresses. This enrichment can lead to microsegregation within

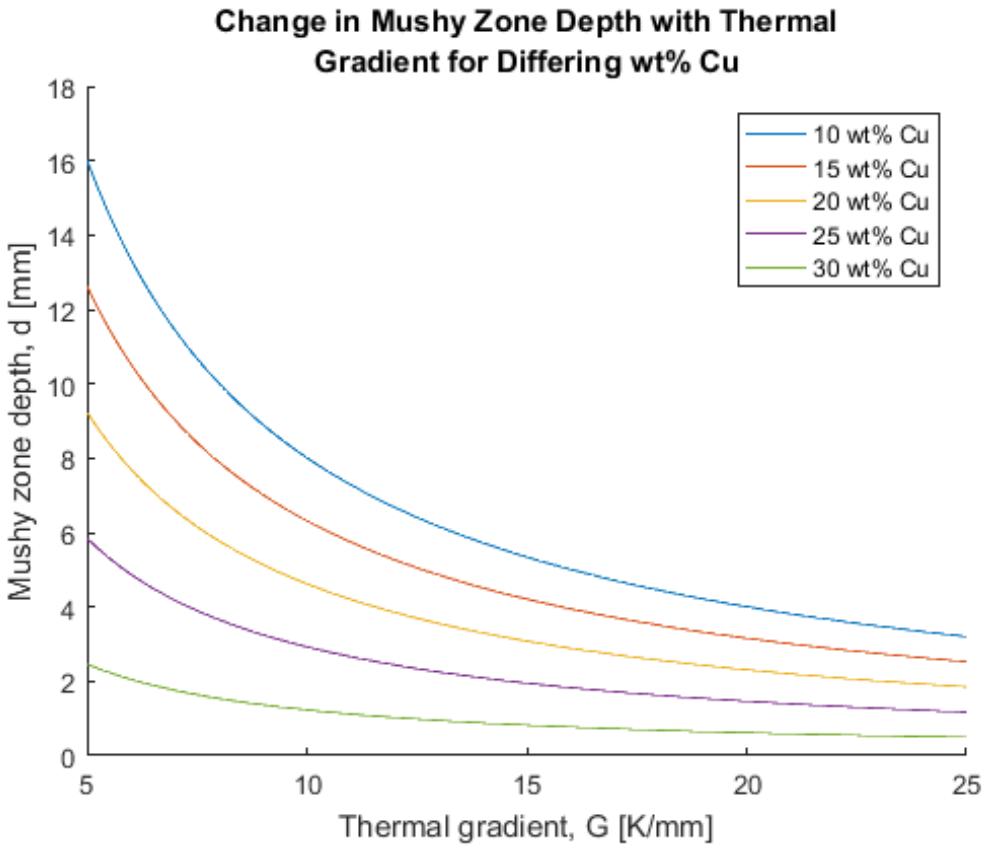


FIGURE 2.5: Mushy depth, d, of different aluminium-copper alloys dependent upon the thermal gradient, ∇T. Calculated using Equation (2.2) and the equilibrium solidus temperature for each alloy.

crystals or casting defects such as macrosegregation over greater distances along the length of a casting.

As a solid front advances at a velocity (v^*) and solute becomes more concentrated within the liquid ($k < 1$) there is a flux towards the liquid across this concentration gradient which can be described by [18, 26, 53, 82, 83]:

$$- D_l \Big(\frac{\partial C}{\partial z}\Big)^* = C_l^*(1-k)v^* \tag{2.5}$$

This flux can be used to calculate the unknown liquid composition at the solid-liquid boundary, C_l^*. The boundary has a characteristic thickness, L, equal to [18, 53, 82, 83]:

$$L = \frac{D_l}{v^*} \tag{2.6}$$

Where D_l is the diffusivity in liquid. This equation holds true in diffusive conditions but not where convection is present within the liquid. Generally convection is present within the liquid melt. One simplifying assumption to deal with this is to assume that there is complete mixing within the liquid [18, 26, 83]. This will give a uniform concentration within the liquid. Therefore when a sample is completely molten it will have a concentration equal to the bulk composition of the alloy, C_0. Another simplifying assumption is that once solidification has taken place there is no diffusion within it, *i.e.* $D_s = 0$. This assumption holds true if the characteristic diffusion length, d, is much lower than the length of the sample, $d \ll L$.

Once solidification has begun the composition of the initial solid (C_s) will have a concentration as given by Equation (2.8) [18, 26, 83]:

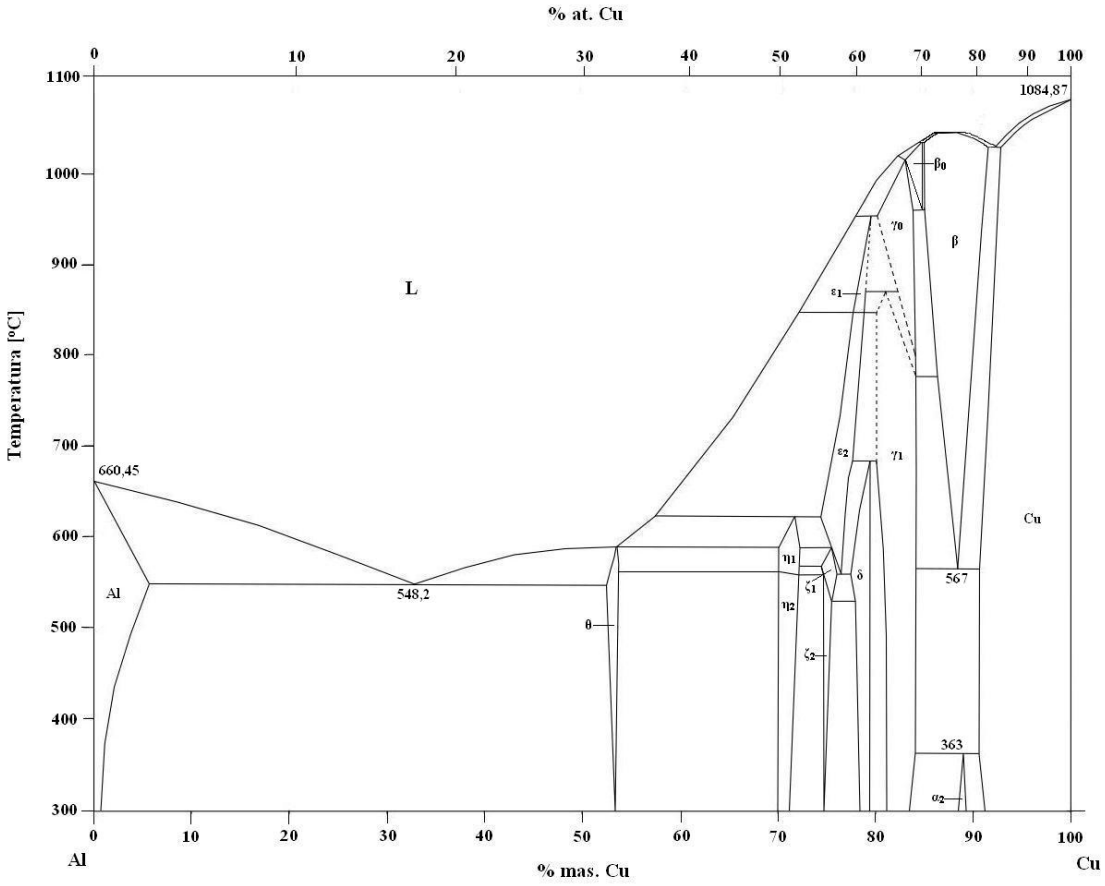


FIGURE 2.6: Aluminium copper phase diagram, reproduced under creative commons. [8]

$$C_s = kC_0 \tag{2.7}$$

Where C_0 is the bulk composition. Thereafter the solid concentration (C_s) will have a composition as a function of the liquid concentration (C_l):

$$C_s = kC_l \tag{2.8}$$

Which as $C_l = C_0(f_l)^{k-1}$ and $f_l = 1 - f_s$ gives the Scheil equation:

$$C_s = kC_0(1 - f_s)^{k-1} \tag{2.9}$$

This equation describes the concentration of the evolving solid as a function of the fraction solid, f_s, and the solute partition coefficient, k (Equation (2.4)). The value of k plays a major part in the final concentration of the evolving solid as can be seen in Figure 2.7. A $k < 1$ causes an enrichment in the liquid as solidification progress causing an upwards trend in the final solid concentration along the length of the sample. The opposite is true for a $k > 1$, resulting in a downwards trend in solute concentration along the length of the sample.

The logical conclusion of Scheil type solidification is that the final fraction of the solid solidified will either have an infinite concentration, or a concentration approaching 0 for any non-unity value of k. However, this is not realistic. In reality once a steady state is reached after an initial transient the concentration remains constant until a final transient phase at the end of solidification. This results in a concentration curve similar to the one shown in Figure 2.8.

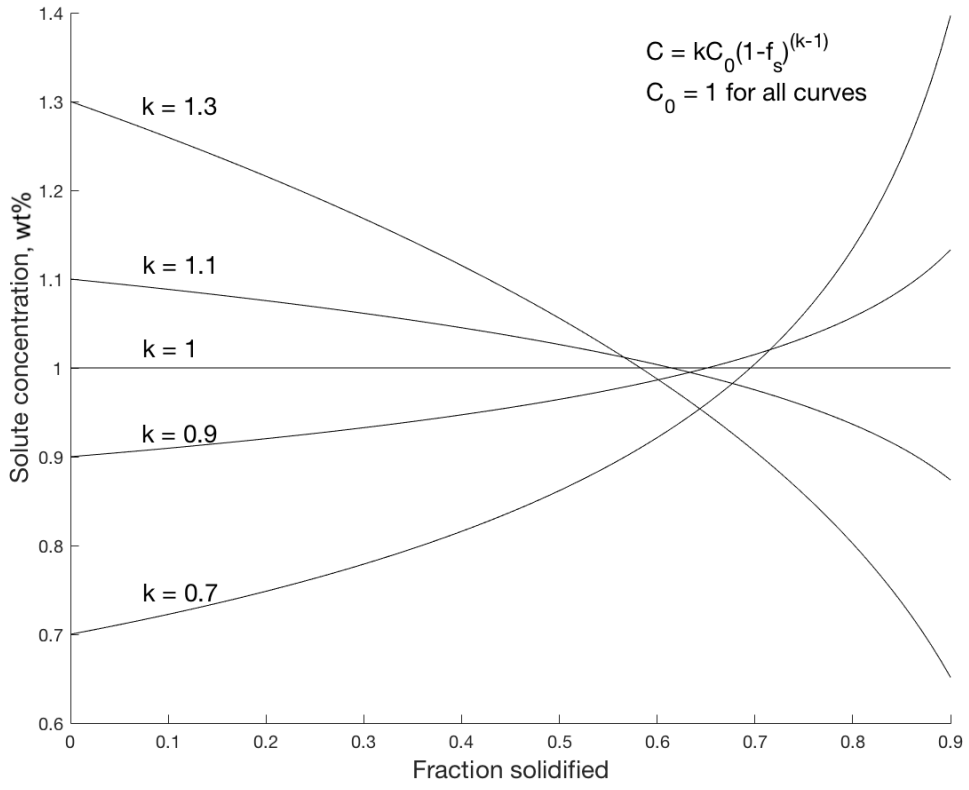


FIGURE 2.7: Concentration profile for a solidified ingot for various values of the solidification partition coefficient k.

This curve can be described using a steady state method based on Ficks second law and assumes no diffusion in the solid but diffusional diffusional mixing in the liquid [18, 83].

$$C_l = C_0 + \frac{C_0(1-k)}{k} exp\left(\frac{-x'}{D_l/v^*}\right) \tag{2.10}$$

This model describes the solute profile ahead of the advancing solid-liquid interface in steady state solidification where x' is the distance ahead of the moving interface along a 1D bar. The initial concentration is kC_0 when $x' = 0$ and as solidification progresses there is an increase in the composition of the solid formed until it reaches the bulk composition C_0. This region is the initial transient. This liquid adjacent to the advancing solid has a composition of C_0/k and the solid has the bulk composition of C_0. The model describes the enrichment of the liquid composition ahead of interface during steady state which forms a bow-wave of solute [18, 83]. This is shown graphically in Figure 2.8.

The bow-wave has a characteristic thickness of δ. Where δ is equal to D_l/v^*. This bow-wave thickness is equivalent to the solid-liquid interface length described in Equation (2.6). When the bow wave approaches the end of the bar it causes the solute to 'pile up' giving a rapid increase in the solute concentration. This region is known as the final transient [18, 83]. This is shown graphically in Figure 2.8.

Neither of these methods however take into account movement of solute within the liquid. They can simulate the effect of convection in microgravity situations (as has been studied previously [15]), but in usual processing there will be some natural convection within the liquid redistributing solute. For a similar reason they cannot be used in scenarios where there is forced fluid flow within the melt. Examples of which involve stirring of the liquid by mechanical or magnetic means. More complex methods are required to simulate concentration profiles in these situations. One example, not discussed here, is the Burton-Prim-Schlichter (BPS)

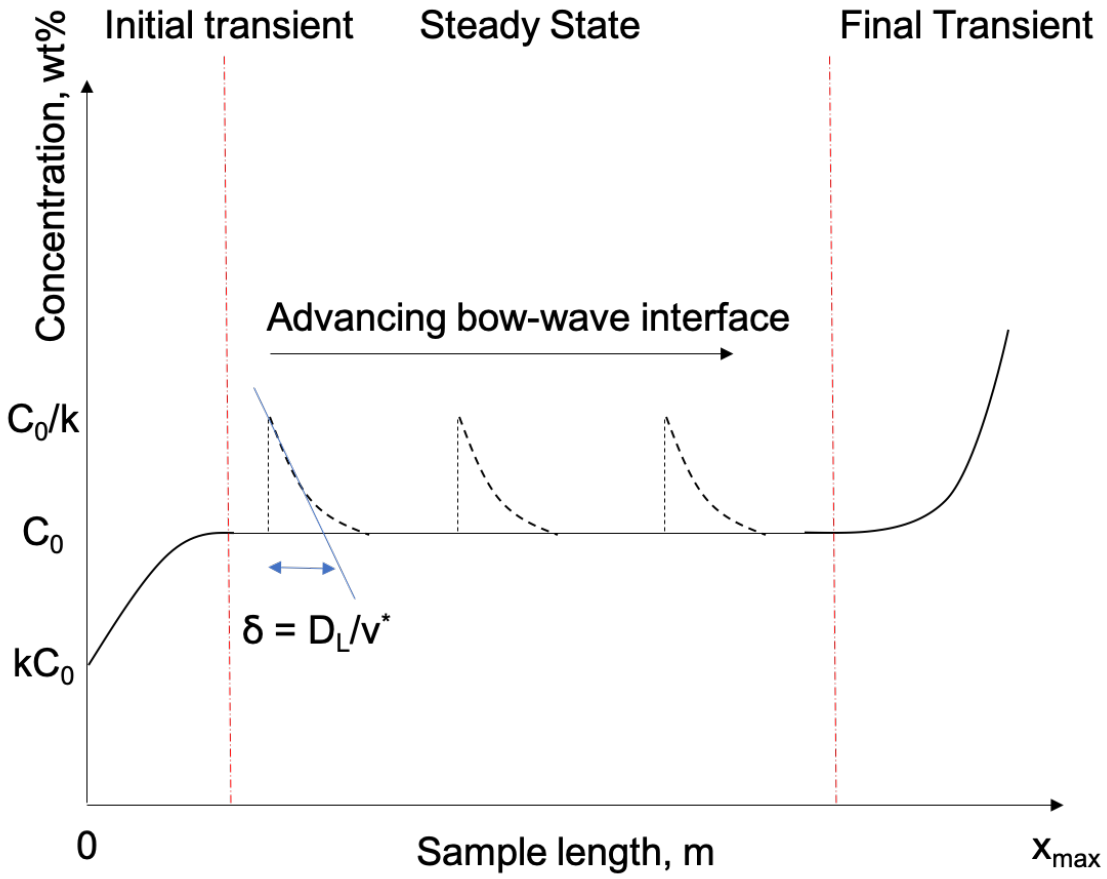


FIGURE 2.8: Concentration profile for a solidified 1D bar with three zones, an initial transient region, a steady state region and a final transient region. The final solidified concentration is shown by the thick black line and the dotted line shows the advancing bow-wave like interface.

control theory [83]. The BPS theory allows for the calculation of concentration profiles under natural or forced convection [83].

Moreover, neither the Scheil method nor the steady state method take into account the effect of diffusion within the solid. In both theories the solid concentration is fixed [18, 83]. In reality there will still be diffusion within the solid. Solid diffusion is an important parameter to include for castings of dendritic materials. Not only can the solute at the solid interface diffuse into the solid away from the interface, it can also diffuse into the liquid for an example of which being the remelting of secondary dendrite arms during Ni-superalloy solidification [22, 83].

2.2 JMAK and Avrami Equations

The Johnson-Mehl-Avrami-Kolmogorov (or JMAK) equation is a model which combines both nucleation and growth kinetics [16, 17, 18, 19, 84]. It has been used widely within metallurgy and materials science over the last half century, as such, it will only be given a brief overview here. The JMAK equation describes crystallisation and can be generally applied to phase changes. The equation makes a number of assumptions and simplifications when simulating growth from one phase to another [16, 17, 18, 19, 84]:

- Nucleation occurs randomly and homogeneously in the untransformed material;
- The growth rate does not depend on the extent of transformation;
- Growth occurs in all directions at the same rate.

The result of the JMAK analysis is the general solution Avrami equation which calculates the volume fraction (V_f^{β}) of a second β phase nucleating from an α phase [16, 17, 18, 19]:

$$V_f^\beta = 1 - exp\Big(- kt^n \Big) \tag{2.11}$$

where k is a reaction constant dependent on the nucleation rate and growth rate. $k = \pi \dot{N} \dot{G}^3/3$, when n = 4. n is the Avrami exponent which gives an indication of the type of phase transformation. Different values of n and their meaning are given in Table 2.1. The Avrami equation gives a substantially sigmoidal curve describing phase change from initiation of new crystals through to impingement as shown in Figure 2.9 [16, 17, 18, 19, 84].

In order to find the values of n and k for a system undergoing a phase change values of V_f^β at a time t must be known. Then by plotting $lnln(1/(1 - V_f^\beta))$ against ln(t), as in Figure 2.10, a straight line is obtained.

This straight line has the equation:

$$lnln\left(\frac{1}{1 - V_f^\beta}\right) = nln(t) + ln(k) \tag{2.12}$$

The values of n and k can be easily obtained by finding the gradient and y-intercept of the line.

Whilst JMAK and the Avrami equation has been used substantially over the last 50 years in materials science [16, 17, 18, 19, 20, 84], it has not yet been used to calculate rates of change in the **PDAS** of dendritic materials when a change in withdrawal velocity occurs. In this example the α-phase would be the dendrite array prior to a withdrawal change from v_1 to v_2. The β-phase would be the array after the withdrawal change, at a time t after the change to v_2. Therefore V_f^β would relate to the extent of the array reordering from $V_f^\beta = 0$ at v_1 (just before the transition) and $V_f^\beta = 1$ at the fully impinged state at time t after the change to v_2.

Dendritic growth is diffusion controlled [20, 25, 85]. It would therefore be reasonable to assume that the result of any Avrami analysis would lead to an n value of 1.5 - 2.5 (Table 2.1). These values correspond to parabolic, or diffusion, controlled growth [16, 17, 18, 19, 20].

2.3 Microstructural growth and morphology

Planar growth for directional solidification occurs in situations where the gradient $\nabla T > 0$. A planar growth front is stable at very low velocities and for very high velocities (see Figure 2.11) [25, 27, 53]:

$$\frac{\nabla T D_l}{\Delta T_0} \leq v^* \leq \frac{D_l \Delta T_0}{k\Gamma} \tag{2.13}$$

The lower limit (left hand side of Equation (2.13)) is the critical velocity V_c and the upper limit (right hand side of Equation (2.13)) is the absolute stability limit, V_a. ΔT_0 is the liquidus-solidus range at the bulk composition. Γ is the Gibbs-Thomson coefficient. D_l is the diffusivity of liquid. Once a planar front destabilises when V_c is reached it reorganises into a cellular structure (Figure 2.11 a-b).

As the interfacial velocity, v^*, increases further beyond V_c the cellular structure will begin to breakdown and dendrites will form (Figure 2.11 c-d). This transition occurs at the critical cellular-dendritic growth rate, V_{C-D}:

$$V_{C-D} = \frac{\nabla T D_l}{k\Delta T_0} \tag{2.14}$$

This equation holds true for solidification at low velocities and at very small Péclet numbers as proposed by Kurz and Fisher [25]. This transformation occurs once the thermal length $k\Delta T_0/\nabla T$ becomes greater than the solute diffusion length, d [25].

Of further interest to the current work is the Columnar to Equiaxed Transition **CET**. The **CET** is to be avoided in order to produce columnar microstructures. This transition is characterised by the change from a purely columnar structure to an equiaxed dendritic structure as shown in Figure 2.12 [26, 86, 87, 88].

TABLE 2.1: Avrami exponents, n [16, 17, 18, 19, 20]

n	
1	Constant nucleation rate
1.5	Decreasing nucleation rate, 3D parabolic growth
2	Constant nucleation rate, 2D parabolic growth
2.5	Constant nucleation rate, 3D parabolic growth
3	Decreasing nucleation rate, 3D linear growth
4	Constant nucleation, 3D linear growth

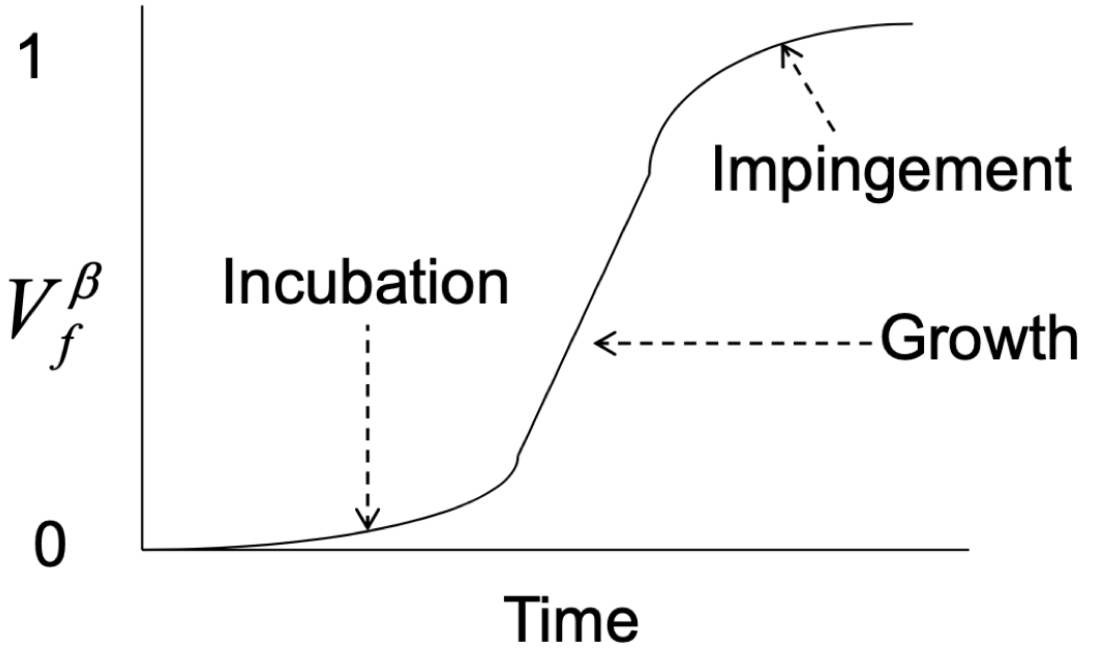


FIGURE 2.9: Characteristic sigmoidal shape of the Avrami equation describing phase change [9]

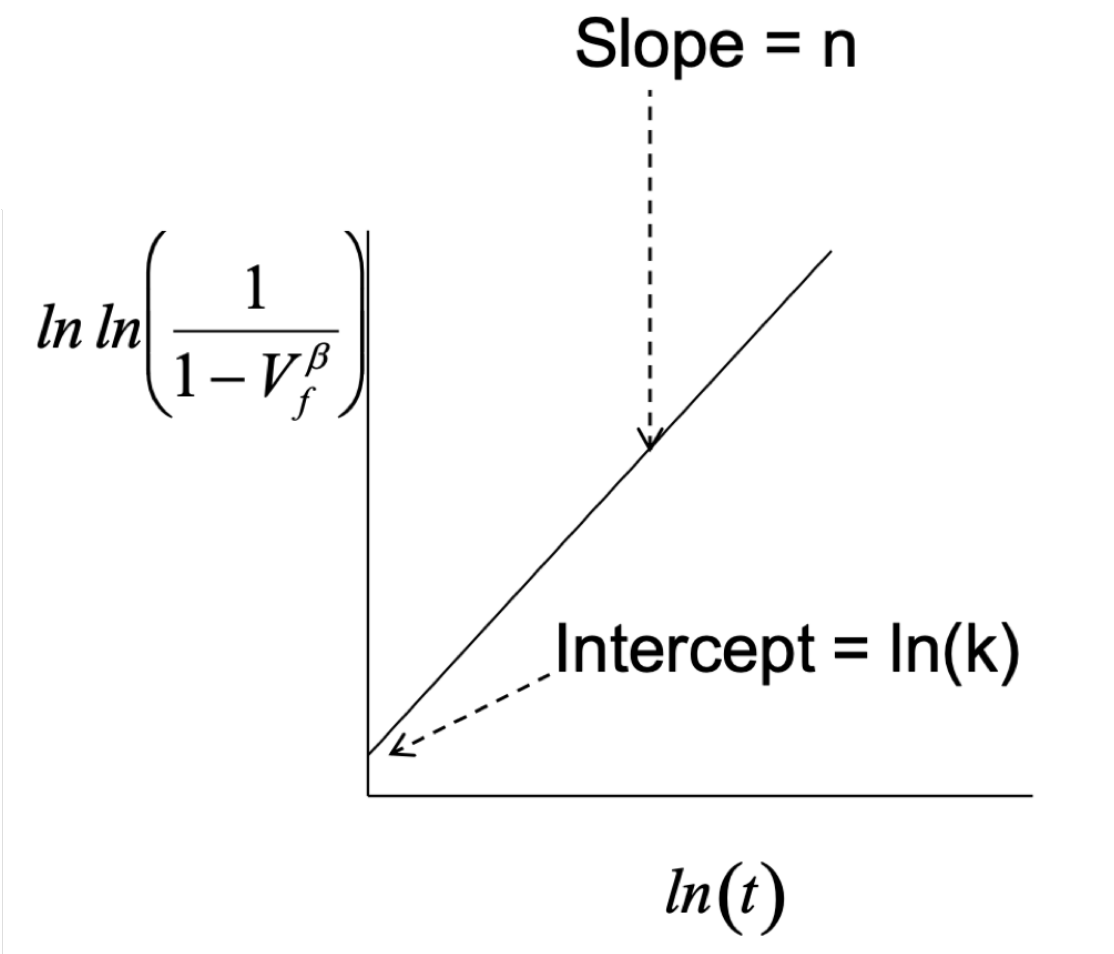


FIGURE 2.10: log-log plot of the Avrami equation used to find the Avrami exponent n [9]

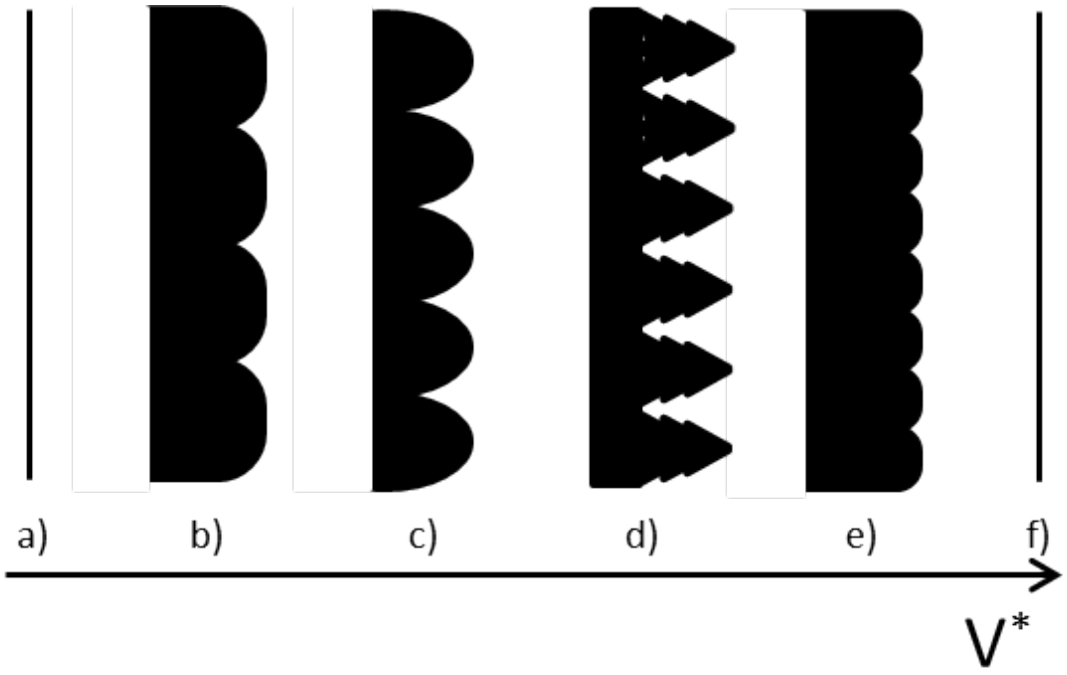


FIGURE 2.11: Solid-liquid evolution morphology with increasing interface velocity, v^*. a) Planar interface for very slow solidification times. b-c) Cellular interface. d) Dendritic structures. e) Cellular interface. f) Planar interface from rapid solidification.

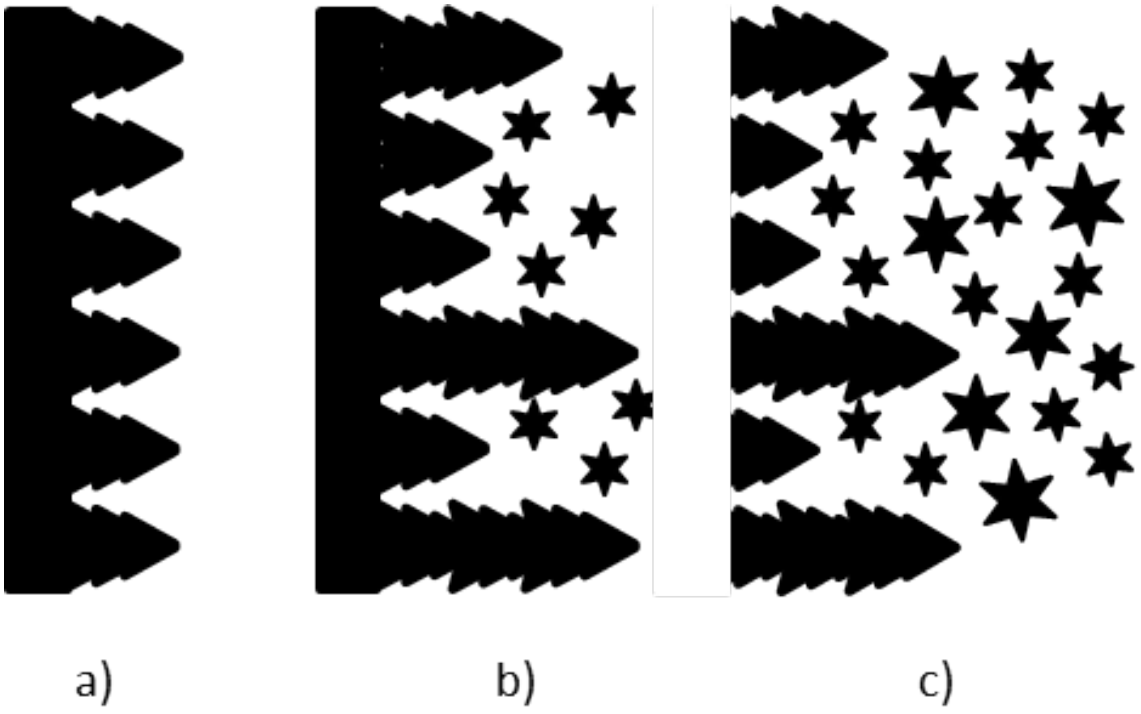


FIGURE 2.12: Schematic of the competition between columnar and equiaxed dendrites occurring during a columnar to equiaxed transition. a) Purely columnar. b) Equiaxed grains form ahead of the columnar dendrites. c) Equiaxed dendrites out compete the columnar dendrites.

Hunt [88] first put forward an analytical solution for steady state columnar and equiaxed growth based on the work by Avrami [16, 17, 89]. Hunt's analytical model allows for the calculation of a transition from columnar growth, to mixed columnar and equiaxed, and through to fully equiaxed growth (as shown in Figure 2.13). Mathematically this transition can be described by [86, 88]:

$$\nabla T < 2.9 N_0^{1/3} \Delta T_c \left(1 - \frac{\Delta T_N^3}{\Delta T_c^3} \right) : \phi < 0.0066 \tag{2.15}$$

and

$$\nabla T < 0.6 N_0^{1/3} \Delta T_c \left(1 - \frac{\Delta T_N^3}{\Delta T_c^3} \right) : \phi > 0.49 \tag{2.16}$$

Where N_0 is the nucleant density, ΔT_c is the solute undercooling of a dendrite tip and ΔT_N is the nucleation undercooling.

For an equiaxed microstructure the volume fraction ϕ (also known as the mechanical blocking fraction) is greater than 0.49 [88], this corresponds to an extended volume fraction, ϕ_E of 0.66 [88]. The extended volume fraction of $\phi_E = 0.66$ is assumed to be a critical value, above which the growth of equiaxed crystals 'blocks' any columnar dendrites. The volume fraction ϕ and the extended volume fraction ϕ_E are related by the expression [88]:

$$\phi = 1 - e^{-\phi_E} \tag{2.17}$$

It is assumed that a fully columnar microstructure is present when ϕ is less than 0.0066 [88]. This corresponds to a value of 1% of the critical extended volume fraction ϕ_E.

In situations where $0.0066 < \phi < 0.49$ there exists a state of mixed columnar and equiaxed growth [88]. That is to say growth as shown in Figure 2.12b, columnar growth with some equiaxed growth between and competing with columnar dendrites.

Using data provided by Equations (2.13) to (2.16) a map of all the different crystal structures that can be built up. An example of which is given in Figure 2.13.

Maps such as this one (Figure 2.13) are extremely useful for determining the final microstructure of a directionally solidified metal so long as the processing conditions (*i.e.* the v^* and ∇T) are kept constant [27, 90, 91]. A great deal of work has been undertaken by Kurz and his colleagues to produce and validate solidification maps of aluminium-copper binary systems [27, 90, 91]. These solidification maps however only give an idea of the microstructural region that the solidification will take place in, be it planar, cellular, dendritic, equiaxed, or some mixture of them. In order to get a more accurate idea of the final microstructure a value for the primary dendrite arm spacing or **PDAS**, λ_1 should also be calculated for each value of v and ∇T. This results in the contour map of the type shown in Figure 2.13 [27, 90, 91]. The **PDAS** has a large effect upon the final mechanical properties of a directionally solidified component and therefore is an important parameter to estimate. A decrease in the **PDAS** increases the mechanical strength of materials, it is also an important parameter to control in order to decrease time needed for post solidification heat treatments [22]. This parameter will be discussed in more detail below in Section 2.5

Another parameter which is very useful for evaluating the mechanical properties of alloys is the secondary dendrite arm spacing (**SDAS**) [10, 22, 25, 31, 92]. The **SDAS** is the average spacing between the secondary arms along the length of the dendrites in the sample [10, 22, 25, 31, 92]. The **SDAS** is linked to the strength and hardness of dendritic materials in a way analogous to grain size in wrought

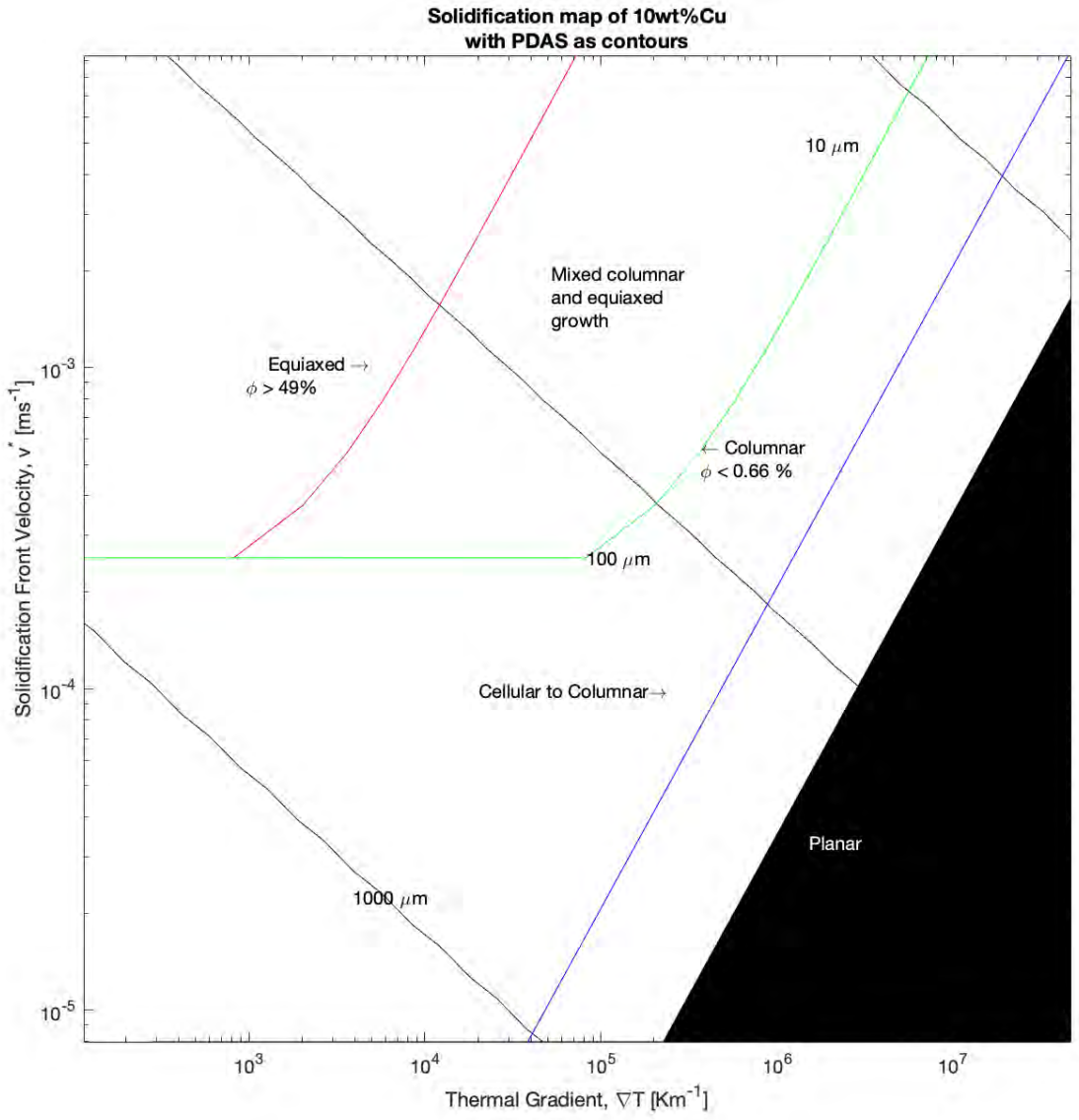


FIGURE 2.13: Solidification map of an aluminium 10 wt% copper alloy. The primary dendrite arm spacing are displayed as contours and the changing microstructural regions are labeled.

structures [92]. Decreasing the **SDAS** will increase the strength of a material [10, 18, 22]. The **SDAS** is also linked to interdendritic porosities and has an influence on electrical and thermal conductivity of materials [92]. The estimation of **SDAS** will be briefly discussed in Section 2.5.

2.4 Furnace Design: Directional Solidification

For the directional solidification of an alloy to take place (as mentioned in Section 2.1) a thermal gradient (∇T) in one direction needs to be set up in a direction anti-parallel to the growth direction of the crystals. One simple method for achieving this is using a Bridgman furnace [22, 31, 93, 94, 95]. A Bridgman furnace has a hot and cold zone which can be set to have the ∇T between them (where T_1 and T_2 are the top and bottom zones temperatures respectively and d_h the distance between them). The sample is then withdrawn downwards between the two heaters under a withdrawal velocity, v. This withdrawal speed can be set to a constant value or a changing one if required. A schematic diagram of a Bridgman furnace is shown in Figure 2.14.

The advantage of a small lab scale Bridgman furnaces is their ability to provide a constant withdrawal velocity and thermal gradient. However these furnaces can be very large with even small scale lab furnaces being around 2 m in height. Industrial furnaces are much larger and can fill a large room. The larger the furnace the harder it is to achieve a constant unidirectional thermal gradient.

In situations where weight and size needs to be minimised–for example in micro or hypergravity research on rockets or centrifuges–Bridgman furnaces are not the ideal choice. This is due in part to their large size. Moreover as the withdrawal is undertaken using moving components this adds to operational complexity. The

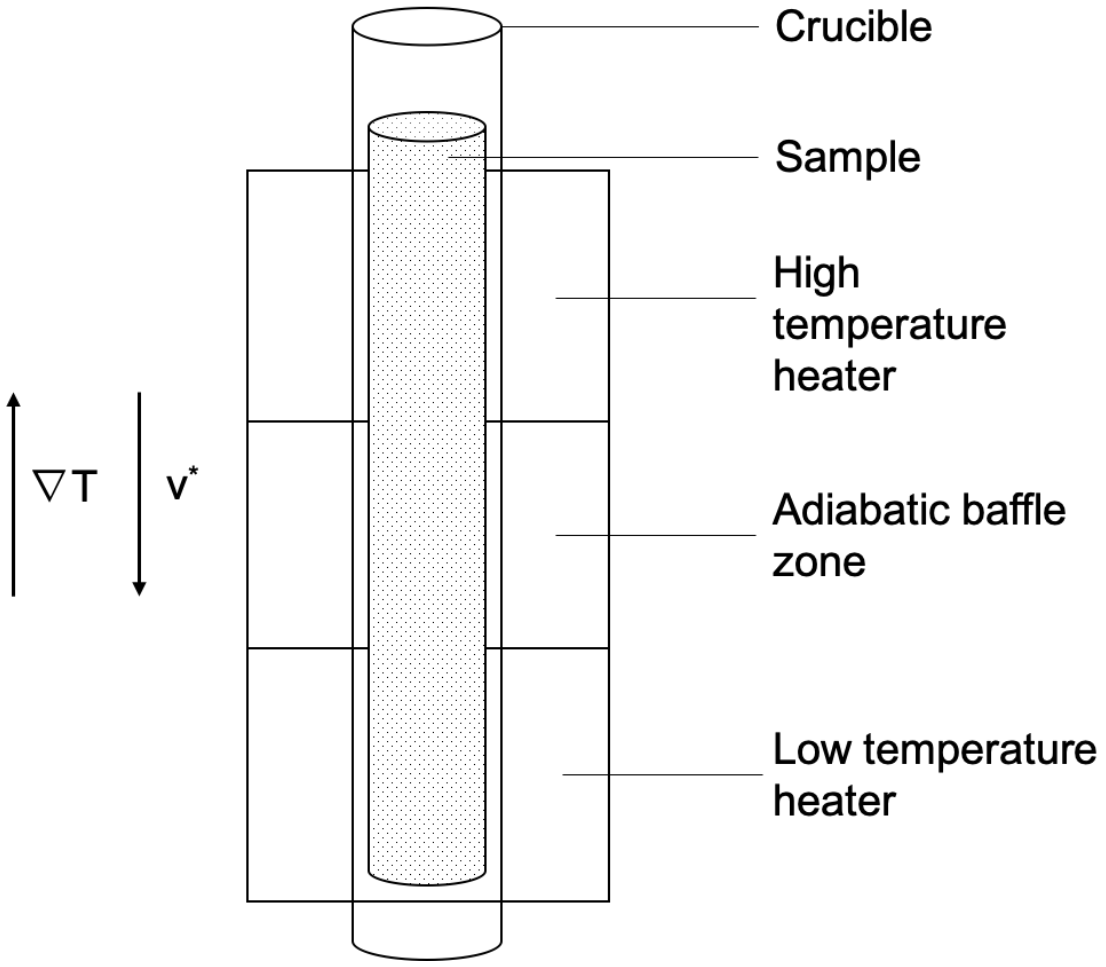


FIGURE 2.14: Schematic of a two heater Bridgman furnace of the type used in this thesis. The sample is withdrawn downwards through the two heaters and the baffle.

more complex a component is the more potential issues or problems that could arise from using it in practice.

Therefore for these highly specific and complex applications power down furnaces are often used [3, 15, 37, 96, 97]. These furnaces, like Bridgman furnaces, have their advantages and disadvantages. They are much more compact and as a result, lighter weight. They have no moving parts so operational complexity is also reduced. However the only way to control v^* and ∇T is by controlling the cool down of the furnace heater(s) which are usually placed at the top of the furnace with a chill plate at the bottom. Or, in furnaces with a top and bottom heater, the heaters are placed at the top and bottom of the crucible. Controlling and maintaining a constant v^* and ∇T in this way is something which can be hard to achieve.

In recent years there has been an increase in the use of aerogel furnaces [37, 96, 97] especially for microgravity research undertaken at the German Space Agency (Deutsches Zentrum für Luft und Raumfahrt, **DLR**). Aerogel furnaces offer some exceptional properties which are not otherwise available from other furnaces for solidification research. As aerogel is an optically transparent material it allows for thermal and optical imaging of a sample whilst it solidifies. Moreover aerogel is an extremely good insulator (thermal conductivity is approximately 0.04 $\mathrm{Wm^{-1}K^{-1}}$ [96]) and has a very low density whilst still having good mechanical properties when under compression. As such, less material is needed for an aerogel crucible furnace than when using more conventional crucible materials such as graphite. The main drawback to aerogel however is it's relative difficulty to manufacture. With only a few small scale producers of the material it can be a difficult and expensive material to get ahold of.

It is with these points in mind the present work aims (in the Appendix of Chapter 9) to put forward a method for producing cool-down regimes for twin-heater

furnaces (heating elements on the top and bottom of the crucible) in order to produce continuous solidification front velocities and thermal gradients. This is something to the authors knowledge has not been trialled before. Experiments have previously been undertaken on producing cool-down regimes in aerogel furnaces with a constant velocity, cooling rate, and a constant solidification front acceleration [37]. The method presented will in subsequent work be trialled on an aerogel furnace produced and commissioned by the **DLR**. Whilst this method does not form part of the main body of the thesis it is included in the appendices in Chapter 9 for completeness.

2.5 Estimating Primary and Secondary Dendrite Arm Spacing, PDAS λ_1

Three characteristic length scales control the growth of solidifing materials [25, 85]:

- Thermal diffusion length, l_T;
- Solute diffusion length, l_d;
- Capillary length, d_0.

The thermal diffusion length is given by:

$$l_T = \frac{D_l}{v^*} \tag{2.18}$$

The solute diffusion length for an alloy [25, 85] is given by:

$$l_d = \frac{\Delta T_0}{\nabla T} \tag{2.19}$$

The capillary length for an alloy [25, 85] is given by:

$$d_0 = \frac{\Gamma}{\Delta T_0} \tag{2.20}$$

where ΔT_0 is the liquidus solidus range at bulk composition, ∇T is the thermal gradient, D_l is the diffusivity of liquid, v^* is the tip velocity and Γ is the Gibbs-Thompson coefficient. The thermal diffusion coefficient may be on the centimetre to meter scale, the solute diffusion length may be on the micro to a millimetre scale, and the capillary length on the nanometer scale [25, 85].

Solidifying structures, such as dendrites, can also be affected significantly by convection [22, 25, 31, 85].

For directionally solidified materials the processing parameters affect the characteristic length scales. For example during Bridgman solidification the withdrawal rate v and the applied thermal gradient ∇T will affect the thermal and solutal diffusion lengths respectively.

The relationship between these three length scales and a characteristic length scale L_c can be described the microstructural scaling equation [25, 85]:

$$L_c = A_c[l_d]^a[l_T]^b[d_0]^c \tag{2.21}$$

where A_c is a constant of proportionality, and a, b and c are constants whose sum equals 1 [25, 85].

In situations where the thermal diffusion length does not influence the microstructural length, such as in columnar dendritic tip radius, the value of b can be set as 0. Therefore the values of a and c are set to 0.5. This sets the tip radius $R \propto \sqrt{l_d d_0}$ [25, 85].

For primary dendrite arm spacing the value of $a = c = 0.25$ and $b = 0.5$ [10, 18, 22, 24, 25, 31, 58, 60, 85, 98]. This can also be expressed in relation to the tip radius, R, by $\lambda_1 \propto \sqrt{l_T R}$ [25, 85].

2.5.1 Primary Dendrite Arm Spacing

As the **PDAS** decreases the strength of a dendritic material increases [22, 99], it also decreases levels of microporosity [100] and it increases microhardness [101] in the final structure. The **PDAS** is an important parameter to obtain as it is the controlling factor in post solidification heat treatments, for example in Ni-superalloys [22]. A greater **PDAS** means a longer length that particles must diffuse across in heat treatments to obtain the desired materials properties. As some of the elements in Ni-superalloys are very slowly diffusing elements, for example tungsten, if the **PDAS** is too great heat treatment may become too cost prohibitive to perform due to increased energy and time required to homogenise the sample [22, 102].

The **PDAS** is affected by the physical properties of a material, *e.g.* composition, the biggest factors are the withdrawal rate, v^*, and the thermal gradient, ∇T, whilst the sample is being directionally solidified (Figure 2.13). Much analysis into accurately calculating the **PDAS** has been undertaken over the last 50 years [10, 18, 22, 24, 31, 58, 59, 60, 98]. For the calculating the **PDAS** Equation (2.21) can be rewritten into the form:

$$\lambda_1 = A^a (v^*)^{-b} (\nabla T)^{-c} \tag{2.22}$$

Where λ_1 is the **PDAS** and A is a constant dependent upon the materials composition, physical properties and the model used. The exponents are set at $a = c = 0.25$ and $b = 0.5$ [10, 18, 22, 24, 25, 31, 58, 60, 85, 98]. The most

commonly used and well established methods are the ones put forward by Hunt [58], Kurz and Fisher [24], and Trivedi [59], shown in Figure 2.15. These equations can all be used to describe steady state directional growth for uniformly spaced cells or dendrites. In each equation the **PDAS** is assumed to be uniform across the sample with each dendrite spaced equidistant from their surrounding dendrites.

Hunt's model was among the first to calculate a spherical dendrite front taking into account the diffusion field between the dendrites or cells. By calculating for the minimum possible undercooling the primary dendrite arm spacing can be calculated using the formula [58]:

$$\lambda_1 = 2.83\big[m(k-1)D_L\Gamma C_0\big]^{0.25}(v^*)^{-0.25}\nabla T^{-0.5} \tag{2.23}$$

Where m is the liquidus slope, k is the partition coefficient, D_L is the diffusion coefficient, Γ is the Gibbs-Thomson coefficient, C_0 is the bulk composition, v^* is the velocity, ∇T is the thermal gradient.

This method was expanded by Trivedi to include the marginal stability criterion resulting in the following equation [59]:

$$\lambda_1 = 2.83\big[m(k-1)D_L\Gamma LC_0\big]^{0.25}(v^*)^{-0.25}\nabla T^{-0.5} \tag{2.24}$$

Where L is a constant that depends upon harmonic perturbations which Trivedi set to 28 [59, 103]. Using the marginal stability criterion and the assumption that growing dendrites and cells can be approximated by an ellipsoid Kurz and Fisher produced the following equation [24]:

$$\lambda_1 = 4.3\left[\frac{m(k-1)D_L\Gamma C_0}{k^2}\right]^{0.25}(v^*)^{-0.25}\nabla T^{-0.5} \tag{2.25}$$

Which is valid when the interface velocity v^* is greater than the ratio of the critical velocity at which a planar interface becomes unstable (v_p) to the partition coefficient, k, *i.e.* when $v^* > \frac{v_p}{k}$.

Of the three methods it was put forward by Günduz and Cidrili [31] that the Trivedi method is the best for estimating the **PDAS** of low weight percent aluminium-copper alloys. The other methods either over or under-estimated the value of **PDAS**.

These above models can be used to estimate the **PDAS** in a directionally cast material and are commonly used to do so in samples under directional solidification. These methods however only work under steady-state solidification [10, 31], when there is no change in the processing conditions. As a result an empirically derived formula based upon previous work by Kirkaldy and Venugopalan [104] was put forward by Bouchard and Kirkaldy [10] to overcome this problem, shown in Figure 2.16. Kirkaldy and Venugopalan [104] derived an analytical model which predicted spacing for cells in 2D. Bouchard and Kirkaldy [10] expanded this expression to cover 3D dendrites.

$$\lambda_1 = a_1 \left[\frac{16 X_B^{1/2} \nabla T_0 (\epsilon\sigma) T_m D_L}{(1-k) m H \rho \nabla T R} \right]^{\frac{1}{2}} \tag{2.26}$$

Where: a_1 is a calibrating factor, X_B is atomic fraction of solute, $\nabla T/\nabla T_0$ is a normalised temperature gradient, ϵ is a surface tension scaling factor, σ is the liquid-solid surface energy, T_m is the melting point of pure solvent, D_L is the diffusivity of the solute in the liquid, k is the partition coefficient, m is the liquidus slope, H is the enthalpy, ρ is the density and R is the dendrite tip radius.

One draw back to this method is its use of the primary dendrite calibrating factor a_1, which takes into account diffusion relaxations, the contribution of solid diffusion and coring reduction that is not included in the rest of the equation [41]. It was

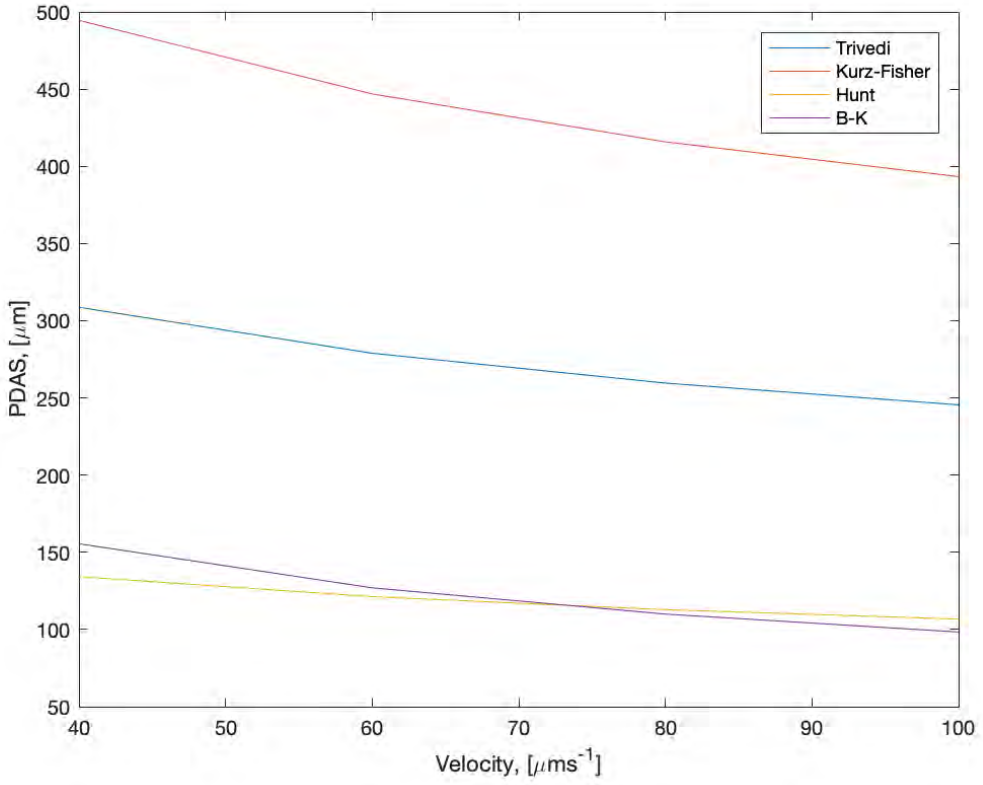


FIGURE 2.15: **PDAS** calculations for 40 to 100 μms^{-1} using Equations (2.23) to (2.26) with a thermal gradient of ∇T = 10 000 Km^{-1} and the parameters in Table 9.3 and from [10].

found to differ between alloy systems and vary by around a factor of 5. Bouchard and Kirkaldy tentatively put forward a general form of this equation where a_1 was given as 120 [10] which would give a prediction for the **PDAS** within a factor of two for material with no experimental data as of yet. This value was used as a_1 varies from 50 (Sn alloys) to 250 (Al alloys) in the initial experimental work undertaken using this equation [10, 15, 105]. However the values given for a_1 can result in an over estimation of **PDAS** as found by Canté et al when they analysed Al-Ni alloys which had been directionally solidified [105].

The method has since seen much use within the literature in computational simulations of unsteady state directional solidification [15, 41, 105, 106]. However as mentioned previously the use of the fitting factor a_1 has caused some disagreement and as such more analysis is needed to examine the role it plays on calculating a value for the primary dendrite arm spacing and what physical parameters of the material or casting process it represents.

One issue with all of these methods is that they assume a uniform distribution of dendrites in the array. None of the equations take into account local spacing distributions which cause a decrease in the actual **PDAS** of an experimental sample [10, 18, 22, 24, 25, 31, 58, 60, 85, 98, 107].

The above equations Equations (2.23) to (2.26) have basis in 0-1g experiments but not however in hypergravity. Hypergravity research is undertaken in centrifuges [33, 61, 62]. Centrifuges allow for an increased simulated gravity level due to the acceleration experienced by rotating gondola containing the experimental apparatus. As Darcy's law states (Equation (1.1)) the velocity of the solute within the melt is proportional to gravity level and solidification under increased gravity conditions will experience an increased level of convection.

The increased convection within the melt has the affect of reducing the **PDAS** [33, 61, 62]. Diepers and Steinbach put forward an analytical expression for this

effect:

$$\lambda_{flow} = \lambda_{1g} \frac{g}{g_E}^{-\frac{1}{8}} \tag{2.27}$$

Where λ_{flow} is the **PDAS** as a function of **PDAS** at 1g (λ_{1g}), gravity of the experiment (g) and Earths gravity (g_E).

This expression fitted well with experimental work undertaken by Chen [61] and Battaile [33]. However there has been a lack of further research into this phenomenon. An example of how the **PDAS** alters with gravity level is given in Figure 2.16. With the advent of the Large Diameter Centrifuge **LDC** at **ESA** Nordwijk there has been renewed interest into undertaking experiments at larger simulated gravity levels. This thesis acts as a starting point for these experiments into a solidification at a range of gravity levels from micro-to-hypergravity (μg to 20g). Image analysis techniques and methodology required for a complete analysis of the samples to be undertaken by subsequent researchers is also provided.

2.5.2 Effect of Gravity Level on PDAS

The equations presented above (Equations (2.23) to (2.26)) are extremely useful for obtaining the **PDAS** at uniform gravity level (*i.e.* 1g = 9.81 ms^{-2}). It is at this gravity level that the vast majority of research into solidification has been undertaken due to the costly and complex nature of undertaking micro or hypergravity research.

Microgravity solidification research can be undertaken using a number of different methods (in order of increasing microgravity time): drop-test, parabolic flight, sounding rocket experiment, and aboard the International Space Station materials science lab. Each of these different methods have their advantages and disadvantages however only sounding rocket experiments and experiments aboard the

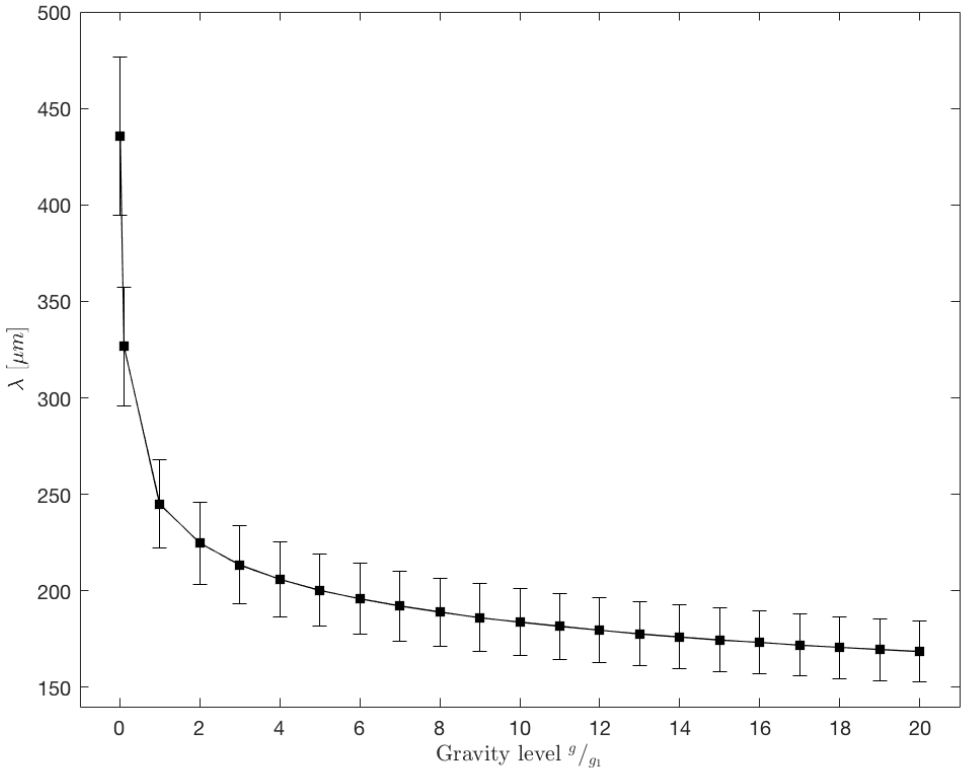


FIGURE 2.16: Calculated effect of the primary dendrite arm spacing λ as a function of the acceleration due to gravity, g, calculated using Equations (2.26) and (9.3). Below and above 1g equation Equation (9.3) is used to modify the expected **PDAS** using the factor $\frac{g}{g_E}^{-0.125}$. The standard deviation of the mean is overlain on the graph for the calculated λ at $0g$.

materials science lab have the required length of microgravity time needed for directional solidification experiments on a longer time scale (*i.e.* longer samples which require longer time for solidification).

2.5.3 Changing v^* and/or ∇T and the Effect on PDAS

It is well established fact that if ∇T or v^* remain constant or relatively unchanged then the **PDAS** will remain relatively constant between a maximum and minimum stable spacing. This spacing for the dendrites to the left and right of the dendrite being observed Ma [12, 13, 60] was found to be within the range of $\lambda_{min} = \frac{2}{3}\lambda_1$ to $\lambda_{max} = \frac{4}{3}\lambda_1$.

If however either ∇T or v^* (or both) change during the directional solidification of a component then there will be a change in the **PDAS** to compensate for this [12, 13, 108, 109] if the new spacing lies outside the stable range given by Ma [12, 13]. As this occurs new dendrites will be created or outcompeted and 'killed' off. The mechanism for this has been researched in two dimensions however not to the same extent in three dimensions [12, 13, 60, 108, 109]. These researchers found that when either ∇T or v^* changed resulting in a decrease of the **PDAS** then a tertiary arm of the dendrites would stabilise and form a new primary trunk in a gap between its neighbours. Conversely, if the change results in an increase in the **PDAS** then one or more of the primary trunks will become outcompeted by its neighbours and it will 'die' off. This is restructuring is shown schematically in Figure 2.17.

This effect has been explored in pseudo two dimensional microstructures [12, 13, 60, 108, 109] where an array of growing dendrites which are one dendrite thick have been subjected to changing ∇T or v^*. However this has not been explored within three dimensions. In 3D there is an extra dimension which affects the array packing as the dendrites restructure when a sample is solidified, rather than

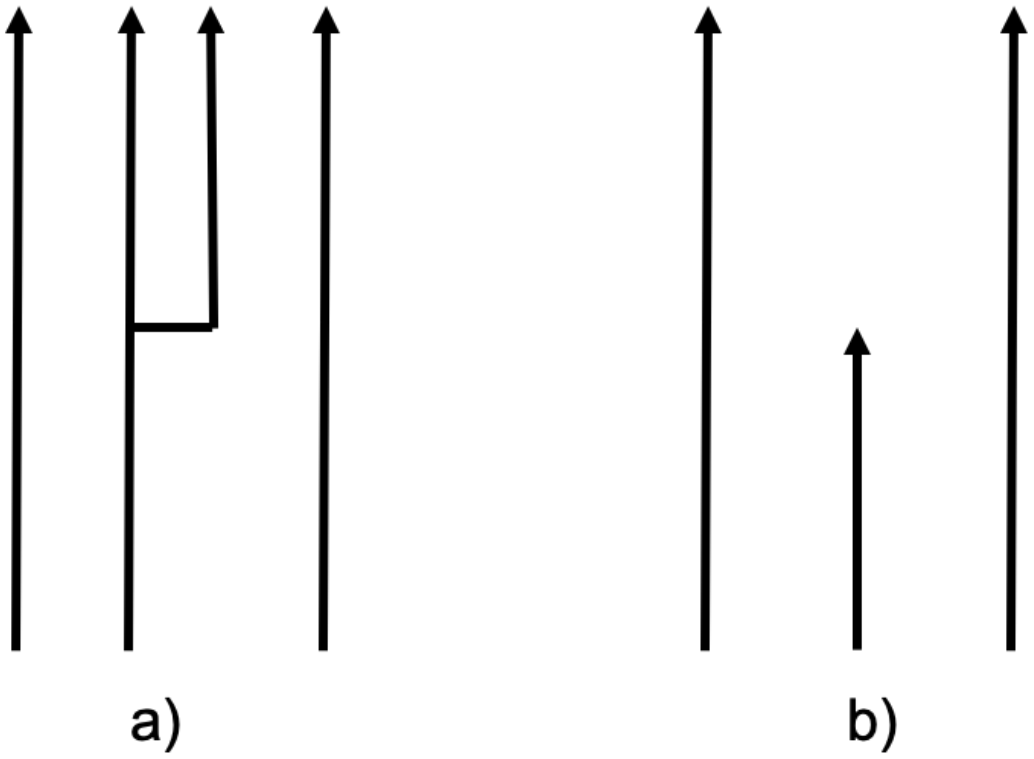


FIGURE 2.17: a) A decrease in **PDAS** due to an increase in v^* or ∇T. A new primary dendrite arm is formed by the means of tertiary arm stabilisation. b) An increase in **PDAS** due to a decrease in v^* or ∇T. The central dendrite is outcompeted by the dendrites to either side of it.

in the more simplistic case in 2D [12, 13, 60]. The suitability of 3D experiments to analyse array spacing selections will be examined in greater detail here.

2.5.4 Secondary Dendrite Arm Spacing

The **SDAS** is an important parameter to estimate as it controls many important properties of the resulting microstructure [10, 18, 22, 25, 31, 92, 110]. As **SDAS** decreases the strength and hardness of a dendritic material increases [92]. The **SDAS** has also been shown to affect the corrosion resistance of aluminium alloys [110], with lower **SDAS** giving better corrosion resistance of Al-10wt %Sn alloys [110]. Due to its importance in a number of materials properties it is a very important parameter to control.

Similar to the primary dendrite arm spacing the secondary arm spacing can be described by adapting Equation (2.21) [25, 85]. In this case the initial secondary arm spacing can be calculated using coefficients a = 0.5 and c = 0.5 [25, 85]. The final secondary dendrite arm spacing, for example as obtained from coarsening models, uses coefficients of a = b = c = 1/3 [25, 85].

A method of calculating the **SDAS** under steady state conditions was put forward by Trivedi and Somboonsuk [111] which defined the **SDAS** with a scaling law $\lambda_2/R = 2$ and for small Peclet numbers.

$$\lambda_2 = \left(\frac{8\Gamma D_l L}{k v^* \Delta T_0} \right)^{0.5} \tag{2.28}$$

Where λ_2 is the **SDAS**, Γ is the Gibbs-Thomson coefficient, D_l is the diffusivity of solute in the liquid, L is a constant dependent on harmonic perturbations, k is the partition coefficient, v^* is the tip velocity and ΔT_0 is the difference between the solidus and liquidus temperatures.

This method has seen much use within the literature [31, 112, 113, 114]. However it is only relevant for samples solidifying under steady state conditions.

Bouchard and Kirkaldy put forward a semi-empirical general model for estimation of **SDAS** under non-steady state growth [10, 114].

$$\lambda_2 = 12\pi \left(\frac{4\Gamma}{C_0(1-k)^2 T_F} \left(\frac{D}{v^*} \right) \right)^{1/3} \tag{2.29}$$

Where C_0 is the bulk composition and T_F is the fusion temperature of the solvent.

The exponential in this equation is equal to 1/3. Bouchard and Kirkaldy chose this value of the exponential after reviewing experimental data compiled from the literature. They found that the average value for the exponent from a number of different alloys, including Al-10 wt% Cu, was 0.34 ± 0.04. This value corresponds closely to the theoretical value of 1/3 for the exponents a, b and c for final secondary dendrite arm spacing after coarsening. This is to be expected as the semi-empirical formula of Equation (2.29) is based on experimental data. The experimental data is all obtained post solidification and therefore after any secondary dendrite arm coarsening has happened [10]. The non-steady state equation of Bouchard and Kirkaldy has proven itself to be adapt at calculating values of **SDAS** in both steady and non-steady state heat flows [10, 15, 114] at 1g and also in microgravity conditions.

The effect of changing withdrawal rate on the **SDAS** will not be explored further within this thesis. The inclusion of equations and literature on **SDAS** is included for completeness and as background information for the reader.

2.6 Pseudo-2-Dimensional Experiments

Experiments to analyse the changing dendrite structure such as those undertaken by Ma, Shevchenko and others has generally been undertaken in pseudo-2D samples [12, 13, 44, 55, 60, 109, 115]. Pseudo-2D (or 2.5D) experiments are undertaken on very thin samples. Essentially the experimental samples are so thin, on the order of a single dendrite thick, that they can be treated as 2-dimensional. Unlike solidification in 3D there is essentially no fluid flow around growing dendrites. There is only fluid flow between the growing dendrites. It is often assumed that pseudo-2D analysis can be used to accurately simulate 3D growth of materials [12, 13, 44, 55, 60, 109, 115].

The pseudo-2D experiments of Ma [12, 13] showed that dendritic spacing changes upon changing thermal gradient and the dendrites which are outcompeted or 'born' is dependent upon the local spacing along the width of the sample. This essentially reduces the criteria down to a 1-dimensional spacing between dendrites. This 1D array spacing has not as-of-yet been compared with a 2D array spacing which is present in 3D samples. In a 2D sample there are only two distances controlling whether a new dendrite is formed or outcompeted. One on the left hand side and another on the right hand side of the dendrite being examined. In a 3D array there is, for a square array of dendrites (four nearest neighbours), not only a 'left' and 'right' spacing but also a 'front' and 'rear' spacing to the closest dendrites. This would increase to six different distances for a hexagonal-close-packed array (six nearest neighbours for each dendrite). It is clear that 3D solidification is inherently more complex than a pseudo-2D solidification.

Currently however, there is a lack of data to check that the assumptions of pseudo-2D scale to 3D solidification. The lack of this data is due to the extreme difficulty of analysing dendritic growth in 3D, especially on non-transparent alloys. 3D samples, unlike psuedo-2D ones, cannot often be analysed in-situ using X-rays to

show dendritic growth due to alloy densities and their differences [44, 55]. As a result analysis must be taken ex-situ after the experiment has taken place. This must be done on samples either by serial sectioning or using a CT scanner. Both of these techniques have their downsides as will be explained in further detail below.

A method for analysing 3D data is needed to confirm that the assumptions made when undertaking pseudo-2D experiments are valid and that pseudo-2D analysis can in-fact capture the complexity of truly 3D growth.

2.7 Image Analysis of Directionally Solidified Samples

In order to check that the values output from these equations are correct (Equations (2.23) to (2.26)) and how the dendritic array corrects itself with changing stimulus, directionally solidified samples must be cast under known values of ∇T and v^*. The castings then need to be sectioned and examined to find the **PDAS** along the sample. The classical method of this is standard metallography preparation. This is simply taking a transverse section of a sample, mounting it, then polishing and etching in order to reveal the underlying microstructure. This sample preparation method has been used within the field of metallurgy and materials science as a whole since the inception of the field.

This method of sample preparation has some obvious advantages: it is cheap; has a low learning curve; and is a very well understood and established technique. Moreover it requires no specialised equipment other than a microscope and etchants, which in some cases are not needed. For example aluminium copper alloys do not require etchants in order to reveal their dendritic microstructure.

The major disadvantage of standard metallography preparation is that it is a two dimensional analysis method. If a three dimensional picture of the sample is to be built up many sections of a sample need to be prepared and examined individually layer by layer. This takes a substantial amount of time to prepare and analyse each layer and it can be very difficult to manually control the volume of sample removed between each analysis layer [35, 36, 116, 117, 118, 119, 120].

In recent years there have been a number of machines that have been used to automate and speed up the process. One example of which being the ROBOMET machine [119, 120]. This sample preparation machine serially sections and images microstructures of a sample that is input into it. However the technique like classical sample preparation is a destructive process. Material is removed from the surface meaning any analysis cannot be repeated which is an obvious disadvantage. Moreover whilst serial sectioning using a Robomet is much quicker than manual sectioning, it is still a relatively slow process.

A non-destructive technique which is becoming much more popular in recent years is tomography. Tomography has been used to observe the internal structures of a sample [47, 55, 118, 119, 121, 122, 123, 124]. Tomography uses high energy X-ray beams to penetrate a volume and image a cross-section. The object is rotated and many cross-sections are built up to give a three dimensional virtual volume which can be analysed using software packages such as Avizo [125] or ones programmed by the user in Matlab or any other computation language.

For researchers there are two options for undertaking 3D tomography analysis, using a synchrotron facility or a lab-scale computerised tomography (**CT**) scanner. Both methods have their advantages and disadvantages. A synchrotron based tomography scanner is able to produce much higher energy x-rays and therefore able to penetrate and image much denser or larger diameter objects. However

getting time on a synchrotron can be very difficult with competition for beam-time being very stiff.

Lab based computerised tomography machines allow for small scale imaging of the internal structures of a component without the difficulty of getting access to a synchrotron site. The maximum energy of the x-ray beam as well as the size of the sample chamber is often much smaller than that for a synchrotron. The speed and relative ease of use of a lab scale tomography machine is an obvious advantage allowing for quick analysis of samples. In the present work a lab-scale **CT** was used to produce all of the volumes needed for the analysis.

One potential problem however with using a **CT** scanner, either lab scale or at a synchrotron is that imaging solidification of large samples in-situ introduces axial flow into the sample. Larger samples must be imaged by rotating them, then the images are stitched together after a full 360^o scan has been produced. If a sample is solidifying on the tomography table there will be forced fluid flow introduced which will affect the final microstructure. The introduced shear forces may cause fragmentation at the dendrite tips causing a columnar to equiaxed transition. For this reason in-situ scans of samples are currently only done on very thin samples, which do not need to be rotated, for example pseudo-2D samples [55, 124].

2.7.1 Binarisation

In order to reduce the **CT** volumes down to only the required information various image analysis methods need to be undertaken. As the volumes in question can be on the order of several 1000 slices in size it would be impossible for them to be manually analysed. As such in recent years several novel techniques have been put forward for the analysis of microstructures in order to reduce the input data down to a manageable size.

Firstly a **CT** volume must be binarised so that only the dendrites are present within the volume and any other data is removed completely from the analysis. There are several common methods which have been used to 'threshold' out the unwanted information. Some common binarisation methods are: Otsu's, histogram based, entropy based, spatial, local, and clustering based thresholding methods [126, 127]. These methods work to varying degrees in differing situations. The more complex methods often revealing the best results. In recent years there has been an abundance of research into image analysis methods for use in medical imaging (as shown in Figure 2.18). Especially in the area of neuroscience and brain imaging using **CT** scanners (see Section 2.7.1) [127, 128, 129, 130, 131]. These advances have slowly moved into materials science where some of the same issues are a problem. Namely, the automatic selecting of the correct point or area in an image and subtracting it from the unwanted background.

It is for this reason that active contour segmentation has become exceedingly popular in areas where image segmentation is needed [127]. This technique is an entropy based method for subtracting the required foreground–whether it is a dendrite or grey matter in a brain scan–from the unwanted background (Figures 2.18 and 2.19). This method has proved very successful in separating features which have proved too complex for other more simplistic segmentation methods such as Otsu's method. Therefore it, and other methods like it, warrant more analysis for use in materials science applications.

2.7.2 Finding the Centre of a Dendrite

Once a **CT** volume has been binarised each slice can be examined and analysed in detail. This allows the researcher to find the number of the dendrites which is needed in order to calculate a value for the **PDAS** using:

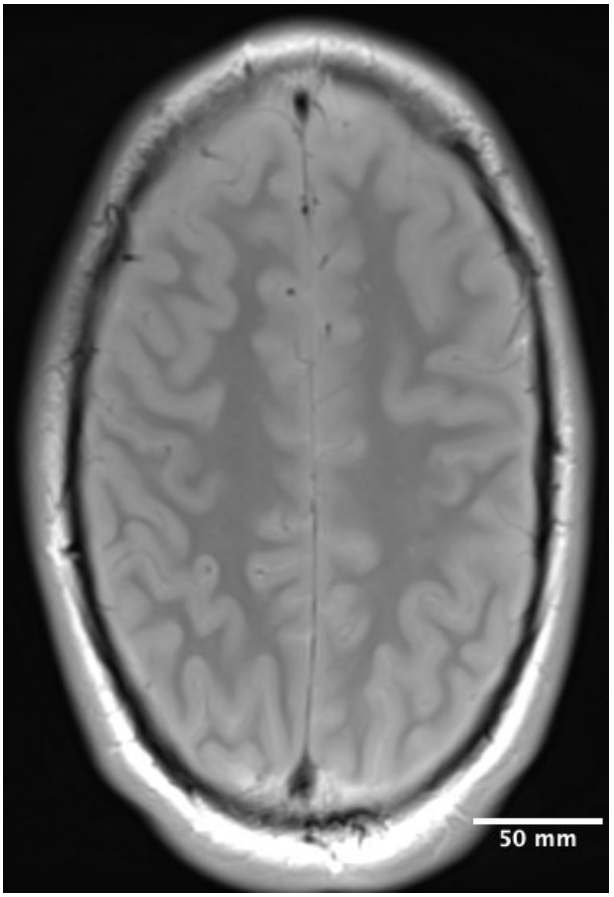


FIGURE 2.18: MRI scan of a human brain [11]

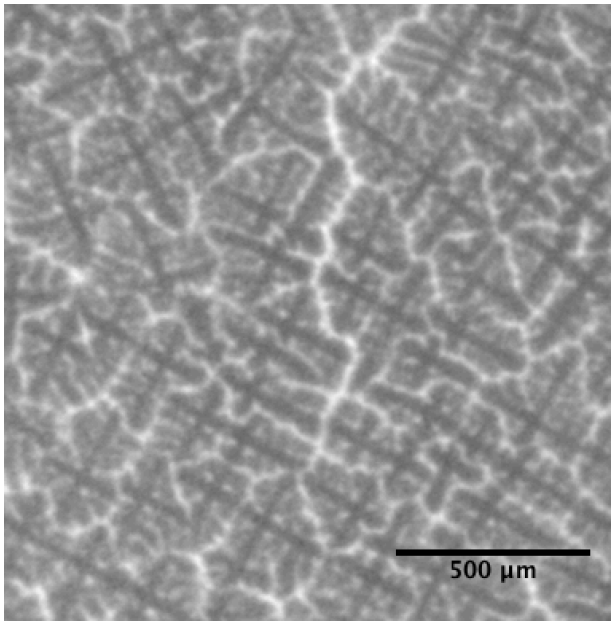


FIGURE 2.19: Section from a **CT** scan of a constant withdrawal rate 40 μms^{-1} directionally solidified Al-10wt% Cu sample cast as part of this thesis.

$$\lambda_1 = c\sqrt{\frac{A}{N}} \tag{2.30}$$

Where c is a coefficient that depends on microstructure (c is 0.5 for a random array, 1 for a square array, and 1.075 for a hexagonal array [107]), A is area of the sample (in this case the cross-sectional area of the volume) and N is the number of dendrites present within the area. This equation gives the average value for the **PDAS**. However it does not give information on how the local **PDAS** changes across the sample or the range of **PDAS** in the sample itself. This value is simply the average distance between all of the dendrite centres if they were set out on a grid with each point being equidistant from its surrounding points.

More complex methods of **PDAS** calculation have been put forward over the years including: minimum spanning tree; Voronoi tessellation; Warnken-Reed; and the combined Voronoi-Warnken-Reed method. Each of these techniques have various advantages and disadvantages, but in each case they allow for the statistical analysis of the bulk and local **PDAS** to be undertaken. These varying methods will be compared and contrasted subsequently within this text.

Paramount to finding an accurate local or bulk **PDAS** is accurately finding the centre of a dendrite. It is important to find this point as an incorrectly assigned centre will affect the local **PDAS** calculation as each of the locations of the centres are used to calculate a local displacement.

In order for the accurate obtaining of a centre of a dendrite a definition of what this centre is needed. The 'centre of a dendrite' is not the centre of a shape *i.e.* the geometric centre or centre of gravity but it is meant as the point from which nucleation or growth of the dendrite occurred from in this plane [2]. This 'centre' is therefore the point of a plane at which the tip of the dendrite first passed through when it grew through a two dimensional transverse slice of a microstructure.

As a result of this a number of novel techniques have been put forward which can be used to find the centre of a dendrite within this thesis. These techniques rely upon the shape of the dendrite itself like the centre of geometry method however they do so in various different ways. The methods are based upon using: skeletonisation (as in the appendix in Chapter 10 [2]); finding the intercept of the two primary axis obtained from the points furthest away from each other; gradient across a blurred interface; symmetry-based feature extraction [34, 36]; curvature of the dendrite; and finding the centre by means of a convolutional neural network. They will be compared and contrasted with the commonly used centre of geometry and hand assigned centre techniques in terms of accuracy, precision, and time taken for completion of the routine.

2.8 Calculating the Bulk and Local PDAS

As stated in Section 2.7.2 there are a number of methods for calculating the **PDAS**. For calculating the bulk **PDAS** Equation (6.1) can be used for a dendritic microstructure. However this equation only gives the 'average' **PDAS** and as a result no information on the spread of values across the microstructure. Other methods however, such as the minimum-spanning-tree, Warnken-Reed, Voronoi, and Warnken-Reed-Voronoi techniques can give information on how the **PDAS** changes across a microstructure [32, 107, 132, 133]. The value of all these methods are generally lower than the bulk **PDAS**. These methods are explored in more detail in Chapter 4.

These methods can all be used to capture information on the local **PDAS** for a dendrite. However each of them does it in different ways.

As a brief summary of the techniques:

- the minimum spanning tree finds the minimum 'path' length connecting all the dendrites in an array in one continuous line and averages this value;
- the Voronoi method uses a Voronoi tessellation to calculate the average distance between a dendrite and the dendrites surrounding it in adjacent Voronoi cells which share a common edge;
- the Warnken-Reed method uses an iterative search radius method to find local neighbouring dendrites which fit within the search radius. The local spacing is the average distance between the examined dendrite and all the neighbours. The method uses an user input parameter α which changes the size of the search radius;
- the Warnken-Reed-Voronoi method is a combination of the Warnken-Reed and Voronoi techniques. The search radius however can only 'find' dendrites which are in adjacent Voronoi cells which share a common edge with the dendrite being examined.

As a result of the different ways the local **PDAS** is calculated there are inherently different results output. The work undertaken on single slices of directionally solidified samples by Tschopp *et al* [133] showed that generally the local **PDAS** output went from largest to smallest in the following order, Voronoi, Warnken-Reed-Voronoi, Warnken-Reed and then the minimum-spanning-tree method. The bulk, or average, **PDAS** was larger than all of these calculated values.

Whilst these methods are fairly well established, they have not as yet been used to examine the spacings along an entire sample. Nor have they been used to give an accurate picture of which dendrites affect each other. It is well known that the solute field of dendrites affect each other. The solute field around a dendrite is much smaller than, for instance, the thermal field. It is very likely that only the very closest neighbouring dendrites surrounding a dendrite affect its growth. Thus

by using the local **PDAS** calculation techniques the local neighbouring dendrites can be found [32, 107, 132, 133].

The Warnken-Reed method is likely to be the best candidate for finding the number of neighbouring dendrites with solute fields effecting a dendrite and the local spacing which actual affects the dendrite. The search radius method of the Warnken-Reed technique can limit this to finding only the closest dendrites which would have affected the solute field of the examined dendrite during growth. The Voronoi method has an inherent flaw in comparison. As the Voronoi method finds the average spacing between all neighbouring Voronoi cells which share a common edge 'neighbouring' dendrites could be included in the search that are in fact no where near the dendrite being examined. It is only by a quirk of geometry that the two dendrites share a common Voronoi edge between cells. This method is also a problem for the Warnken-Reed-Voronoi method as it takes the Voronoi tessellation into consideration when calculating the local **PDAS**. However, as this technique also includes a search radius criteria it is not effect the results to the same degree. Finally as the minimum-spanning-tree method finds only the shortest distance between dendrites it arguably will only ever find one neighbouring dendrite. This neighbouring dendrite being the one in the closest proximity to the dendrite being examined.

2.9 Tracking Dendrite Centres Through the Sample

In order to see the effect that gravity and changing solidification conditions have on an evolving microstructure the dendrites need to be tracked through a sample. This is a fairly trivial exercise in two dimensions especially when using an optically transparent organic model alloy such as succonitrile or other similar material which

can be imaged either as a thin two dimensional sample [12, 13, 46, 60, 134, 135] or from above for a solidifying three dimensional sample [132]. Or when using thin metallic sample which can be imaged using in-situ x-ray radiography [44, 55].

However in all of these cases the tracking of dendrites is done in-situ, that is to say whilst the microstructure is evolving [12, 13, 44, 46, 55, 60, 132, 134, 135]. In order to analyse three dimensional metallic samples the classical route has been to section a sample transversely–at approximately 90° to the growth direction–then polishing and etch revealing the underlying dendritic microstructure. As a result it is much more difficult to 'track' the growth of a dendrite after a sample has solidified. Moreover information such as the dendrite tip radius and the tip velocity cannot be obtained after solidification has occurred as they cannot be obtained after the fact.

There has been limited research into methods of tracking the primary arms through a solidified volume. However in neuroscience there has been great advances in finding and fitting splines to 'dendron' these are dendrite like cells within the brain which have a tree like branching structure [136]. Lessons can be drawn and adapted from this field due to the many overlapping similarities with the problems in investigating dendrites in three dimensions. In both cases the dendrons and dendrites are presented as 3D volumes from a CT image, as such they are both greyscale; they also have a similar branching morphology with a primary arm or spine with branching side arms.

If the dendrites can be traced through a solidified sample then it will be possible to gather information on an individual dendrite, *e.g.*, to find where the secondary and tertiary arms are; or if a tertiary arm stabilised and became a new primary arm. Once this can be obtained for a single dendrite all of the individual dendrites which make up a sample can be tracked and traced leading to information on the **PDAS** and the array structure itself in 3D.

2.10 Grain Orientation

In order to gather information on the crystal structure and grain orientation of a sample Electron Back Scatter Detection analysis (**EBSD**) should be undertaken [137, 138, 139, 140, 141, 142]. **EBSD** works by characterising the materials inherent diffraction pattern. This pattern which is unique to the crystal structure gives information on: the grain orientation, phase, grain boundaries, and the morphology of grains [117, 137, 138, 139, 140, 141, 142].

The issue however with **EBSD** is that it requires an electron microscope with an **EBSD** detector which can be very expensive. Moreover the time taken to undertake the analysis is very long and increases exponentially when making a 3D **EBSD** volume [117]. A further drawback of this method is that it is generally only used on small areas again due to its time intensive nature [117, 137, 138, 139, 140, 141, 142]. The issue therefore with combining serial sectioning and **EBSD** is that they are both extremely time intensive processes and thus expensive.

As a result of this long timescale methods are needed that can quickly and accurately find the grain orientation of whole microstructures in 3D. Methods using optical microscopy such as the one put forward by Seita *et al* [139] are one such option. By optically imaging whole microstructure using light at different incident angles Seita *et al* [139] was able to separate the different grains in the polycrystalline structure.

Other methods such as using specific etches can reveal information on grain orientation [143]. However this method only works in a number of cases with etchants only reacting with specific materials.

A method is needed to easily analyse and evaluate the orientation of grains within a microstructure and separate them. In this work specifically dendritic microstructures are analysed. A technique is needed that can quickly find their orientation

in three dimensions.

A method put forward here utilising the skeleton of binarised dendrites which can be used quickly and efficiently to separate grains in dendrites. This technique provides a starting point for further research on this topic.

2.11 Gaps Identified Within the Literature

Whilst undertaking this literature review it has come to the attention of the author that there are some gaps within the literature that are needed to be addressed. In most instances it is only because of recent advances in computational power and breakthroughs in the field of metallographic image analysis that have made these avenues of research viable.

- Production of cool down regimes for bridgman style directional solidification using a two heater furnace to give constant v^* and ∇T;
- Three dimensional analysis of dendrite array restructuring;
- Initiation and termination of dendrites along length of directionally solidified sample;
- Analysis of dendrite initiation and termination within grains of a polycrystalline directionally solidified sample;
- Affect of increased convection levels on the initiation and termination of dendrites;
- Array packing changes within grains;
- Change in array packing with varying crucible diameter;
- Length of **PDAS** restructuring 'lag' after v^* or ∇T change;

A number of these items will be explored as part of this current work however some are beyond the scope of the current work and as such are questions to be answered in future works (Chapter 8).

Chapter 3

Experimental

Two dimensional metallurgical analysis has for over a century pushed forward the field of materials science. With much knowledge being gathered into the way crystals grow. Examples of only a handful of many researchers are Bouchard, Fisher, Glicksmann, Kirkaldy, Kurz, and Trivedi [10, 24, 25, 83]. All of whom have all made great advances to the field of metallurgy with their work on primary dendrite arm spacing and dendrite array packing.

One example of the investigation into **PDAS** is the work undertaken by Bouchard and Kirkaldy (Equation (2.26)) [10] under non-steady-state conditions. This empirical formula given in Equation (2.26) in Chapter 2 builds upon work by Kurz, Fisher, Trivedi and others [10, 24, 25, 83] who had previously put forward formulas for the *PDAS* under steady-state conditions.

Equations such as this have long been used to compare with the result of solidification experiments in order to and make better predictions for future castings [10, 24, 25, 83, 144]. These experiments are often undertaken using Bridgman furnaces. A Bridgman furnace allows for greater control of solidification processes

than more simplistic casting methods such as power down or die casting. Bridgman furnaces allow control of both the thermal gradient and the withdrawal rate (and thus the solidification front velocity) [94, 145].

Bridgman furnaces have a top and bottom heater separated by an adiabatic baffle. A thermal gradient, ∇T, is applied across the baffle between the two heaters. Generally the top heater is at a higher temperature than the bottom heater. The sample is heated so that the top of the sample is molten in the hotter end and solid at the colder end. During alloy solidification a mushy zone forms between the completely molten liquid and solid. This mushy zone is a mixture of solid and liquid coexisting together [94, 145] which is aimed to be kept within the adiabatic region of the furnace. A schematic diagram of a Bridgman furnace is shown in Figure 3.1.

The imposed (or nominal) thermal gradient ∇T generally cannot be taken as the actual thermal gradient across the mush zone of an evolving microstructure [94]. During solidification latent heat is released which causes an increase in temperature in the mush zone. The effect of latent heat can have a significant effect on the heat transfer within the system as it solidifies [94]. A schematic showing examples of the imposed and actual temperature profile across the mushy zone is given in Figure 3.1. For this work it was assumed that the latent heat did not affect the thermal gradient substantially.

During steady state solidification in a Bridgman furnace it is important to understand the morphology of the mushy zone. To reduce any other unwanted effects it is important to maintain a uniform and flat solidification interface. The morphology and shape of the solidification interface can depend upon the location of the interface in a Bridgman furnace [94, 145, 146]. The location of the solidification interface can be controlled by controlling the location of the alloy's melting temperature T_m by control of ∇T and the temperature of the hot and cold regions

of the furnace. The mushy zone morphology can be affected, for example, by radial temperature gradients which can result in a U-shaped or curved solid-liquid interface [94, 145, 146], as shown in Figure 3.2.

The dimensionless Biot number can be used to understand the morphology of the solid-liquid interface itself [94, 145, 146, 147]. The Biot number (Bi) gives a ratio of the heat transfer resistances inside a body and at the surface of the body.

$$Bi = \frac{hl_{ref}}{\kappa} \tag{3.1}$$

For a cylindrical sample the reference length, l_{ref} is the set to half the radius of the sample, $r/2$. The value of $r/2$ equates to the ratio between the volume of a cylinder and the surface area of the curved cylindrical face. h is the heat transfer coefficient and κ is the thermal conductivity.

During solidification the interface can be assumed to have a flat morphology if the Bi<0.1. In this situation it can be assumed that the temperature at the centre of the body is equal to the temperature at the interface [147]. This is due to the axial heat transfer being much faster than the radial heat transfer. If a flat interface is required, it is thus important to prevent radial heat transfer.

This can be achieved, in practice in Bridgman solidification, by placing an insulating material between the hot and cold regions of the Bridgman furnace and keeping the solidification front in the this insulated region. The insulating region is known as a baffle zone [146], as shown in Figures 3.1 and 3.2. The baffle is a substantially adiabatic region with a radial heat flux of approximately zero (or as close to zero as possible) [94]. In an adiabatic region there is only axial conduction during solidification [94], therefore resulting in a Bi<0.1.

The further from this baffle zone that the solidification front is the more pronounced and curved the solidification front can be [146]. Outside of the adiabatic

baffle zone there is a radial heat flux. In the hot zone this is a positive heat flux which results in a curved interface of an upside-down U-shaped parabola, as shown in Figure 3.2. As there is a positive radial heat flux into the sample the edges of the sample will be hotter than the inner part of the sample. The result is that axial conduction cools the sample much quicker than the radial conduction giving a curved interface.

If the solidification front is located in the cool region of the sample then the interface takes a U-shaped form [94, 146], as shown in Figure 3.2. In this instance there is a negative heat flux radially. The result is that the parts of the sample near the radial surface will cool much quicker than the parts of the sample located along the centreline.

In this work a flat interface was assumed to be maintained throughout the solidification. Maintaining a flat interface prevents any curvature of the evolving solidification front which may affect the array packing. There is a lack of current research is into the understanding of array packing of dendrites and the history dependence of the arrays in three dimensions [144, 148]. As such a number directional solidification experiments conducted using a Bridgman furnace are detailed in this chapter are used as the basis for three dimensional analysis of dendritic arrays with a **CT** scanner.

3.1 Experimental Equipment

A series of directional solidification experiments were undertaken at a 10 K/mm under a series of different withdrawal rates. The cast samples were then analysed using a **CT** scanner and novel image analysis techniques performed on them.

A master alloy of Al-10 wt% Cu was mixed and gravity cold die cast into a large diameter billet. Subsequently it was machined down using wire-cut Electrical

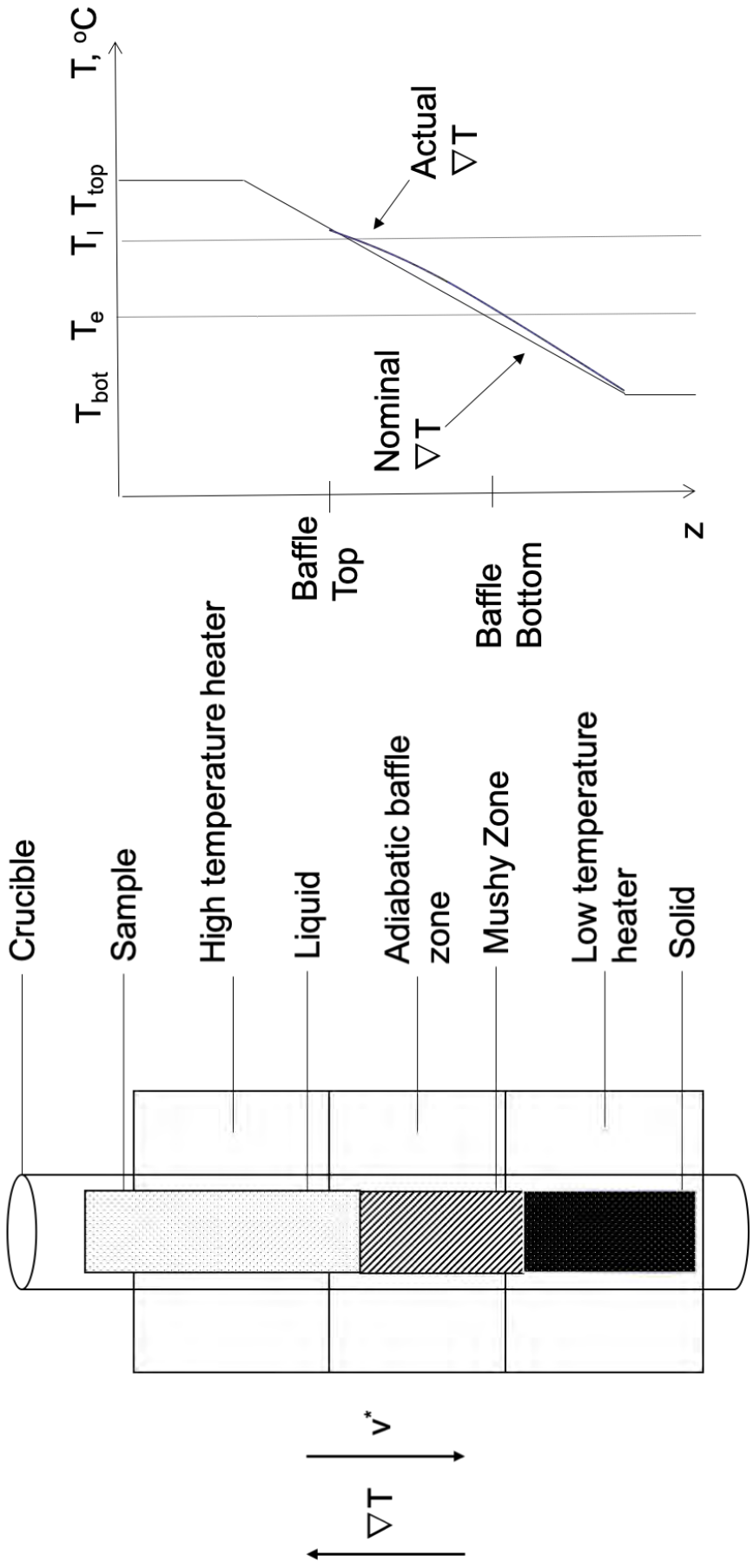


FIGURE 3.1: Schematic diagram of a Bridgman furnace and schematic of the nominal and actual thermal gradient along the sample during solidification.

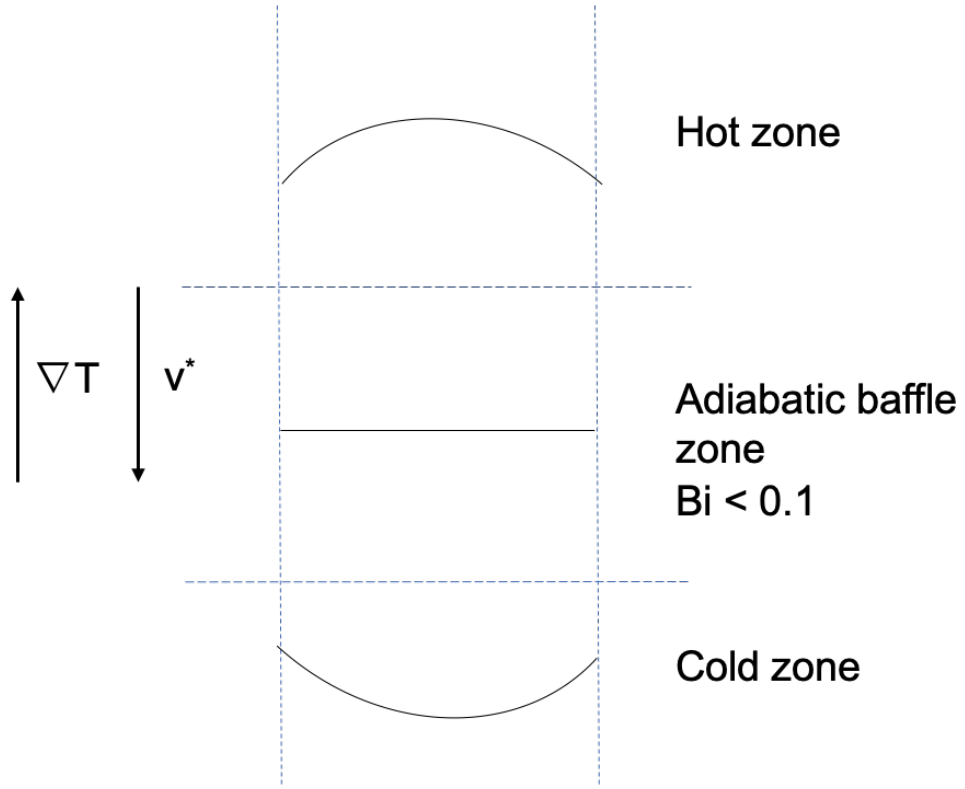


FIGURE 3.2: Schematic diagram of different mushy zone morphologies at different locations within the Bridgman furnace and a nominal and actual temperature gradient in the sample.

Discharge Machining (**EDM**) into a series of 6 mm diameter by 210 mm length rods. These rods were then recast using a Bridgman furnace at Access, University of Aachen RWTH (Figure 3.4) under varying withdrawal rates with an identical thermal gradient of 10 K/mm applied across the 35 mm baffle. The withdrawal rates were controlled by a programmable stepper motor.

The top of the baffle was maintained at approximately 1165 K (T_1) throughout and the bottom of the baffle was held at approximately 815 K (T_2). The furnace parameters are given in Table 3.1. The experiments were carried out in an argon atmosphere. The thermal insulation is a hard graphite felt with graphite foil wrapped around the hot side of the baffle and heater. The hard graphite felt has a thermal conductivity of 0.3 $Wm^{-1}K^{-1}$ in an Argon atmosphere [149]. Alumina crucibles were used to directionally cast the samples. A schematic of the internal workings of the Bridgman furnace is given in Figure 3.1 for the lab-scale Bridgman furnace shown in Figure 3.4.

The solidification front for the castings will be located in the adiabatic baffle as the location of T_m is between the top and bottom temperatures at the top and bottom of the baffle respectively. Furthermore, as the thermal conductivity of the adiabatic baffle is low it can be assumed that the solidification front morphology will be flat. The low thermal conductivity means that there is a negligible radial heat flux in the adiabatic baffle region.

3.2 Experimental Methodology

The test sample was 210 mm long and is shown schematically in Figure 3.3. The bottom 50 mm of the sample acted to hold the sample in place. The following 20 mm was held within the furnace baffle and was melted back and held until remelting of the sample and a mushy zone had formed. The following 160 mm

TABLE 3.1: Bridgman furnace parameters

Furnace Parameter	Value
Baffle height	35 mm
T_1	1165 K
T_2	815 K
∇T	10 K/mm
κ	0.3 $\mathrm{Wm^{-1}K^{-1}}$ [149]

of the samples were used to conduct the experiments as described in Tables 3.2 and 3.3.

The first 30 mm of the 160 mm was used to allow for the dendritic array to stabilise and become steady state. The subsequent 90 mm were used in the experiments themselves. The 90 mm section was either held at a constant withdrawal rate or varied accordingly to whichever varying withdrawal rate experiment was to be analysed (Table 3.3). The last and top 40 mm of the sample was not used and treated as waste. This was to prevent any affects of macrosegregation effecting the results of the analysis.

3.3 Constant and Varying Withdrawal Rate Experiments

The Bridgman experiments were split into two categories, the first being constant withdrawal rates (of which the experiments' parameters are described in Table 3.2). For these samples the entire length was withdrawn at a constant rate as described in Table 3.2.

The second category of experiments are the varying withdrawal rate experiments. In these cases the withdrawal rate was changed by means of an instantaneous acceleration from the previous to the new velocity. Three experiments were undertaken with changing velocities. The length of sample held under each velocity was scaled in terms of the diffusion length at each of the speeds using Equation (2.6). This was done so that each section had the same number of diffusion lengths within it as a function of the velocity. Furthermore for experiments 2 and 3 in Table 3.3 the values of velocity were chosen so that each subsequent stable **PDAS** corresponded to a value that is greater than $\frac{2}{3}\lambda$ of the previous velocity. This was done to test the theory that there would be no **PDAS** change when the new 'stable' **PDAS**

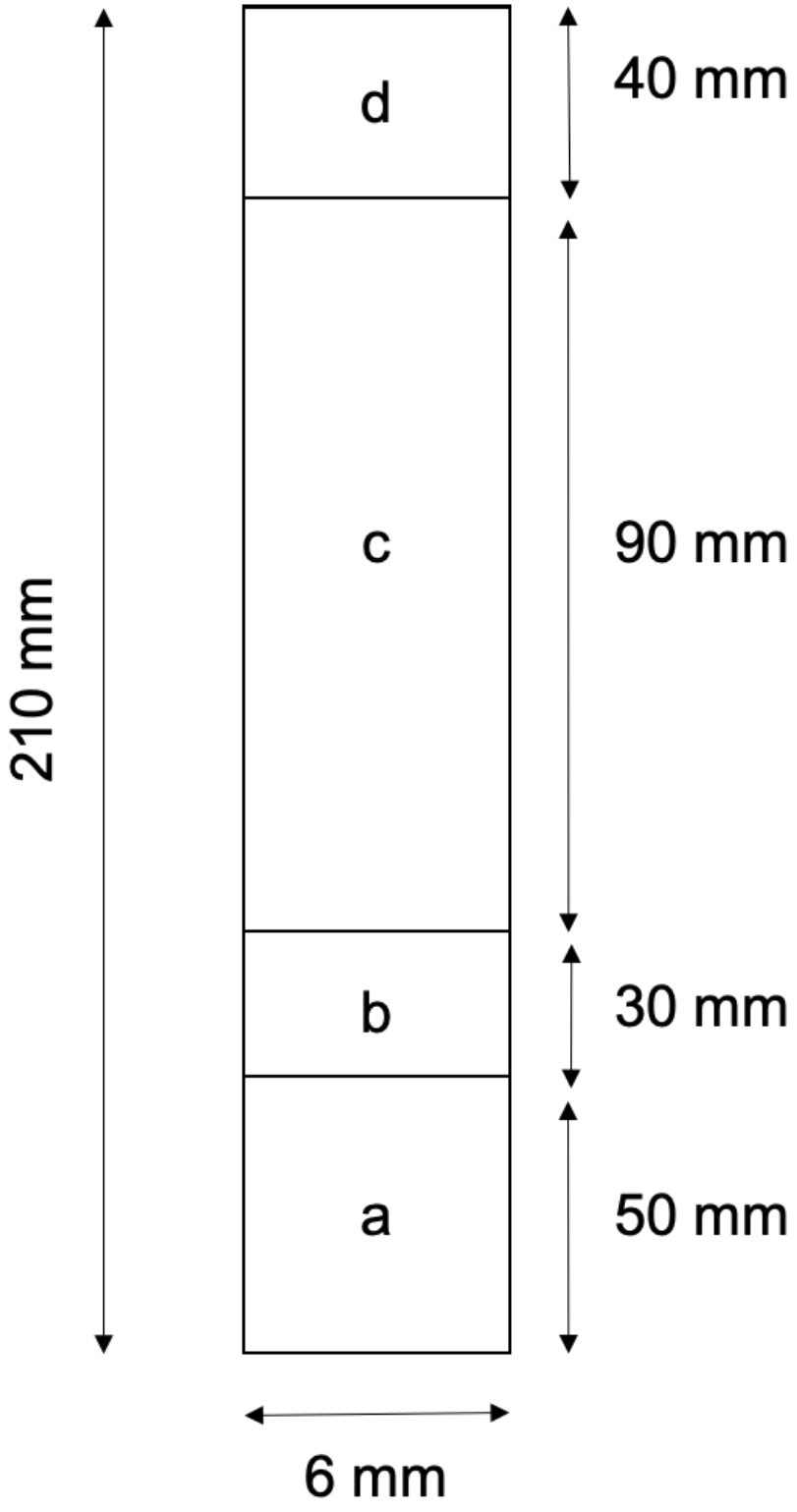


FIGURE 3.3: Schematic of the sample dimensions. a) is the 50 mm of the sample which is held in place by the sample holder. b) is the 20 mm which is melted back prior to the experiment beginning. c) is the 90 mm over which the experiment is conducted. d) is the 40 mm of the sample which was treated as waste.

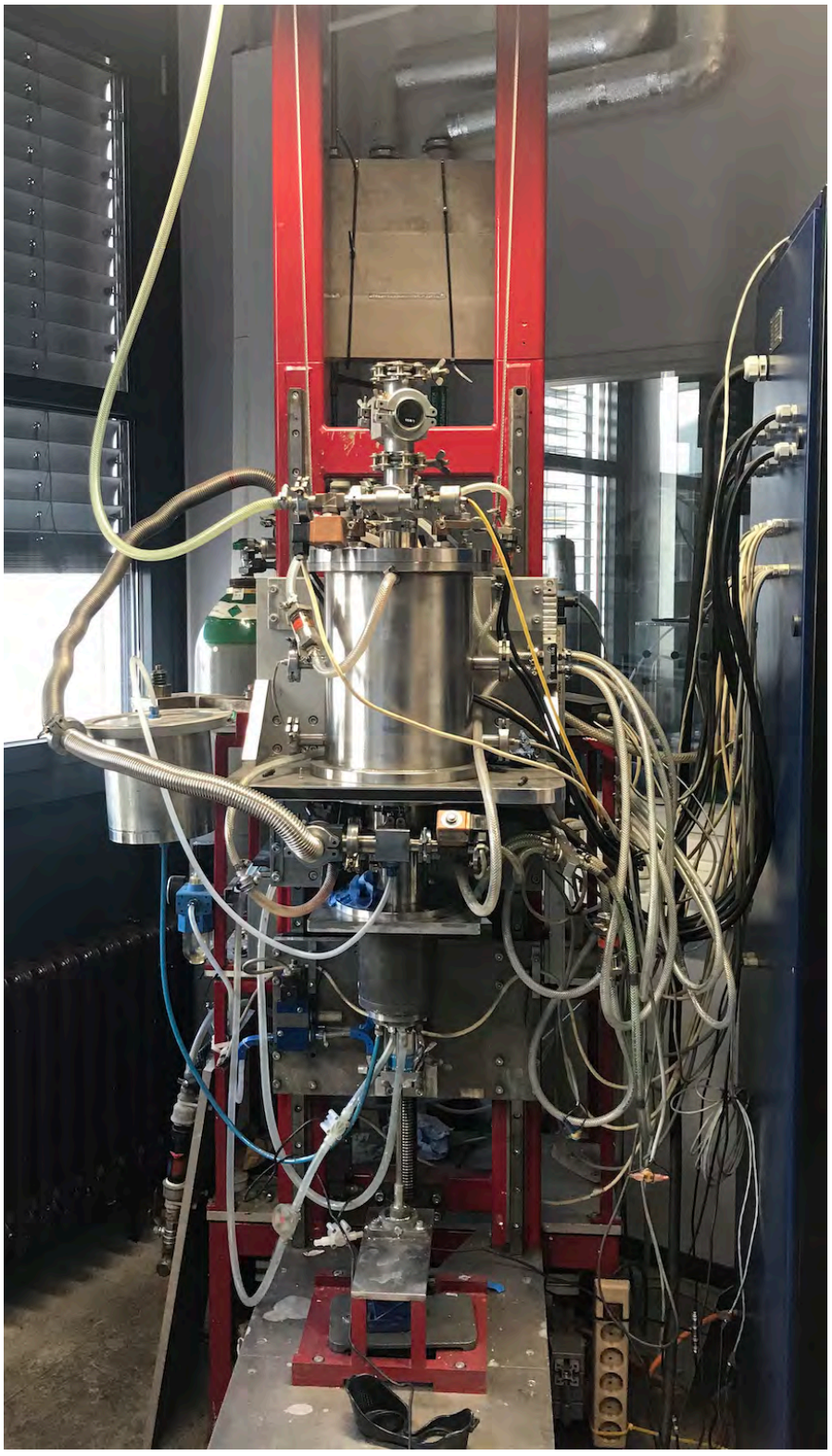


FIGURE 3.4: Lab scale Bridgman furnace at Access, Aachen RWTH.

is above this value as theorised by Ma [12, 13]. This distribution put forward by Ma [12, 13] for each velocity is shown in Figure 3.5.

These velocities were chosen as they were all within the columnar dendritic region of the solidification map. Shown in Figure 3.6. As such there will be no occurrence of a columnar to equiaxed transition (**CET**). This is important as this effect is wanted to be avoided in the experiments so that only dendritic array restructuring is wanted to be analysed. Further work could look into the effect that equiaxed crystals disrupting the structure of the dendritic array, but this is beyond the scope of the current work.

The experiments were cast successfully and subsequently removed from the alumina crucibles. However upon removal from the crucible experiment 3 (Table 3.3) became slightly bent. As such a full scan of the length of sample was not possible within the **CT** scanner.

These experiments form the precursor for further work to be undertaken with the European Space Agency, German Space Agency and the **MICAST** project.

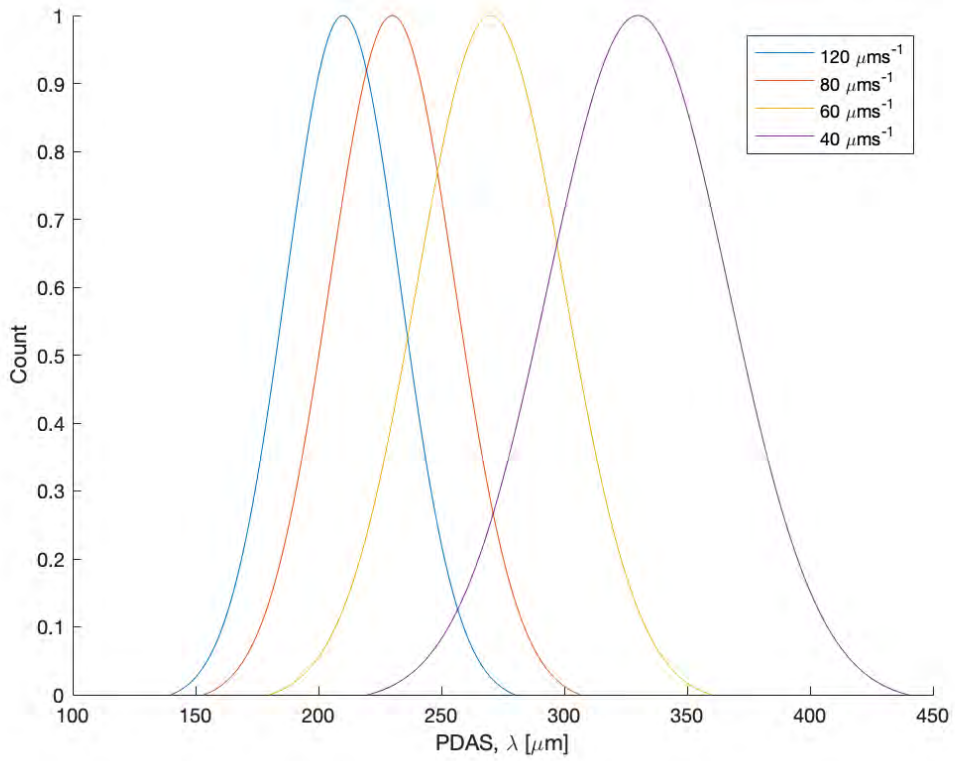


FIGURE 3.5: Normal distribution of local **PDAS** distributions for each average **PDAS** using the minimum and maximum stable **PDAS** values put forward by Ma [12, 13].

TABLE 3.2: Constant withdrawal rate Bridgman furnace experiments. Expected **PDAS** calculated using Equation (2.26)

G, K/mm	V, μms^{-1}	L_d, μm	λ, μm
10	40	75.0	330
10	60	50.0	270
10	80	37.5	230
10	100	30	210

TABLE 3.3: Changing withdrawal rate solidification experiments.

Exp. no.	Step	G, K/mm	V, $\mu m s^{-1}$	L_d, μm	Distance, μm	λ, μm
1	1	10	40	75.0	60 000	330
	2	10	80	37.5	30 000	230
2	1	10	40	75.0	41 538	330
	2	10	60	50.0	27 692	270
	3	10	80	37.5	20 769	230
3	1	10	40	75.0	43 560	330
	2	10	60	50.0	29 070	270
	3	10	100	30.0	17 460	210

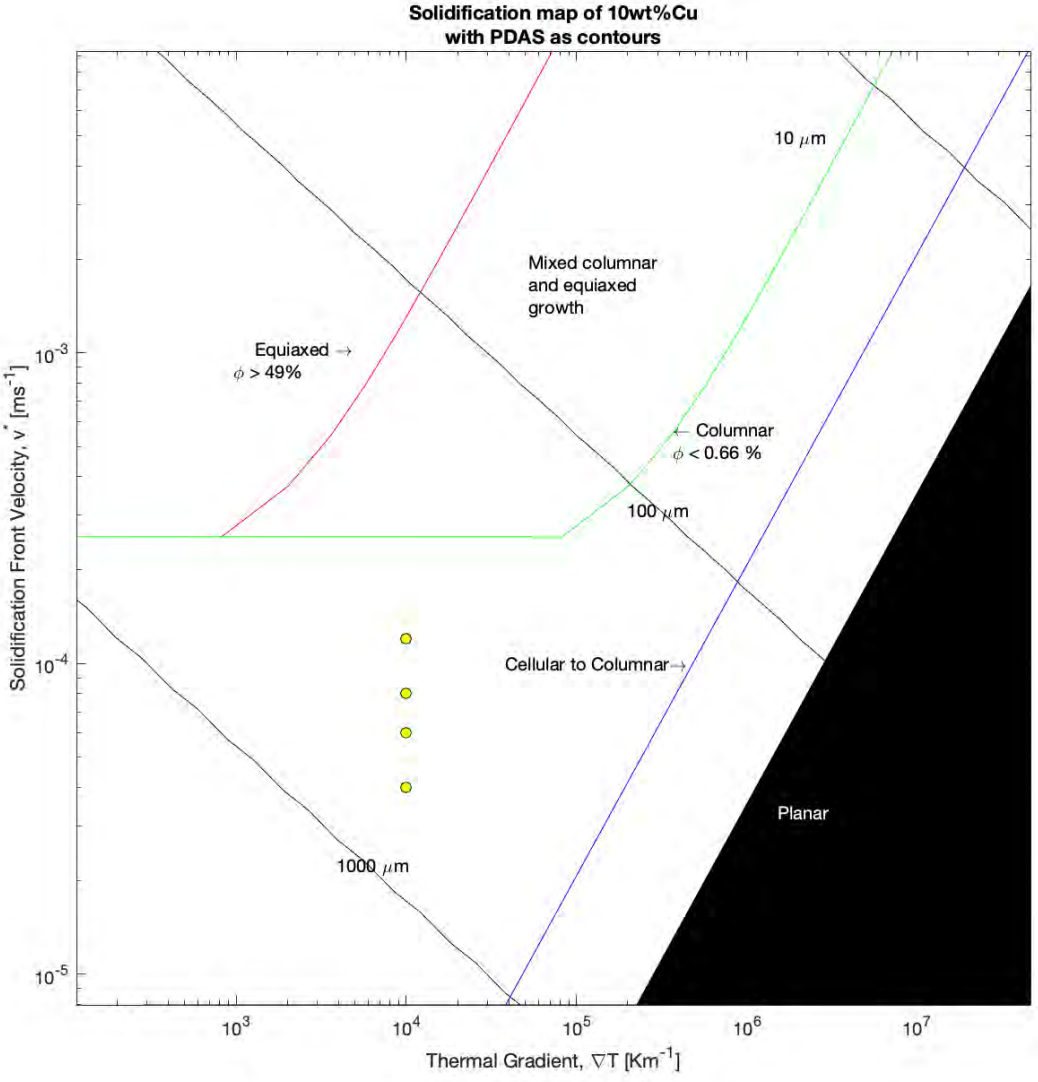


FIGURE 3.6: Solidification map for an Al 10 wt% Cu alloy. Experimental withdrawal velocities shown as yellow dots in the columnar-dendritic region of the map.

Chapter 4

Image Analysis Techniques

As solidification is a three dimensional problem it is paramount that analysis be conducted in three dimensions. Whilst work has been done on this previously [12, 13, 44, 46, 55, 60, 132, 134, 135] the work generally compromises the tracking of pseudo-two dimensional dendritic growth. That is across thin samples rather than along the entire length of a casting. However when work has been undertaken in three dimensions, as was done by Spanos *et al* [117] to obtain **EBSD** maps, it takes an extremely long time due to the repetitive nature of the sample preparation techniques employed. In this case classical metallographic methods of grinding, polishing, then etching.

In order to increase the speed at which large volumes of microstructural data can be obtained the present experiments were analysed using a Computerised Tomography (**CT**) machine. A **CT** scanner allowed the acquisition of volumes containing 2000 slices with a voxel size of approximately 2 μm in 2-4 hours per volume. If an equivalent number of slices were obtained by means of classical metallography the time taken would have been astronomical. To prepare and optically image the whole surface of a microstructure would have taken approximately 2 hours per slice. Moreover adding to this obvious disadvantage is the fact that it is nigh

impossible to consistently remove a set depth each time the sample is polished. For these reasons **CT** was the preferred option to image the samples.

In order to analyse the vast stacks of data obtained from the **CT** image acquisition novel image analysis techniques needed to be created so that large quantities of data could be analysed swiftly. The **CT** stacks compromised of between 2 000 to 24 000 images, with each image approximately 2000x2000 pixels. These image stacks could reach volumes equating to several hundred Gb and in the instances of larger volumes approximately a Tb. Therefore it was paramount that a parallel computing based image analysis scheme be created to analyse all of the information to speed up analysis. A scheme is outlined below for the manipulation of **CT** images which gives a binarised microstructure which can subsequently used to find the local primary dendrite arm spacing. Done by first finding the 'true' centre of each dendrite as defined in Chapter 2.

A number of methods are put forward below for the finding of the centre of a dendrite. This must be accurately obtained in order to get precise information on the local primary dendrite arm spacing. These methods were trialled and tested on a single crystal Ni-superalloy sample which consisted of dendrites with regular morphology. These methods were then tested on more complex dendrites present in the aluminium-copper samples.

4.1 Image Acquisition and Pre-Processing

The images of the samples described in the experimental section above were collected using two differing methods. The first was via conventional metallography and optical microscopy. The second was using a computerised tomography **CT** to collect the images. The **CT** images were processed and made into a 3D volume. Slices of this volume were then taken perpendicular to the z-axis of the

volume. The **CT** slices and the optical microscopy images were then analysed in the same manner. This method shall be outlined in more detail below but briefly it compromises of:

- Input image
- Crop to leave only region of interest
- Subtract background
- Active contours image segmentation
- Binarisation
- Remove small features
- Watershed segmentation
- Find the dendrites in the image
- Run analysis on each dendrite
- Find the centre of the dendrite

This methodology is briefly summarised in Figure 4.1.

4.1.1 Tophat image filtering

The top hat transformation is used to remove any contrast variation which is inherent in the **CT** scanning process. As can be seen in figures Figure 4.2 and Figure 4.3 there is a clear variation in intensity across the sample with a higher value being reported at the edge rather than in the centre. This removal of contrast variation is achieved by opening the image, I_0, using a structuring element, s, in order to give a new image I.

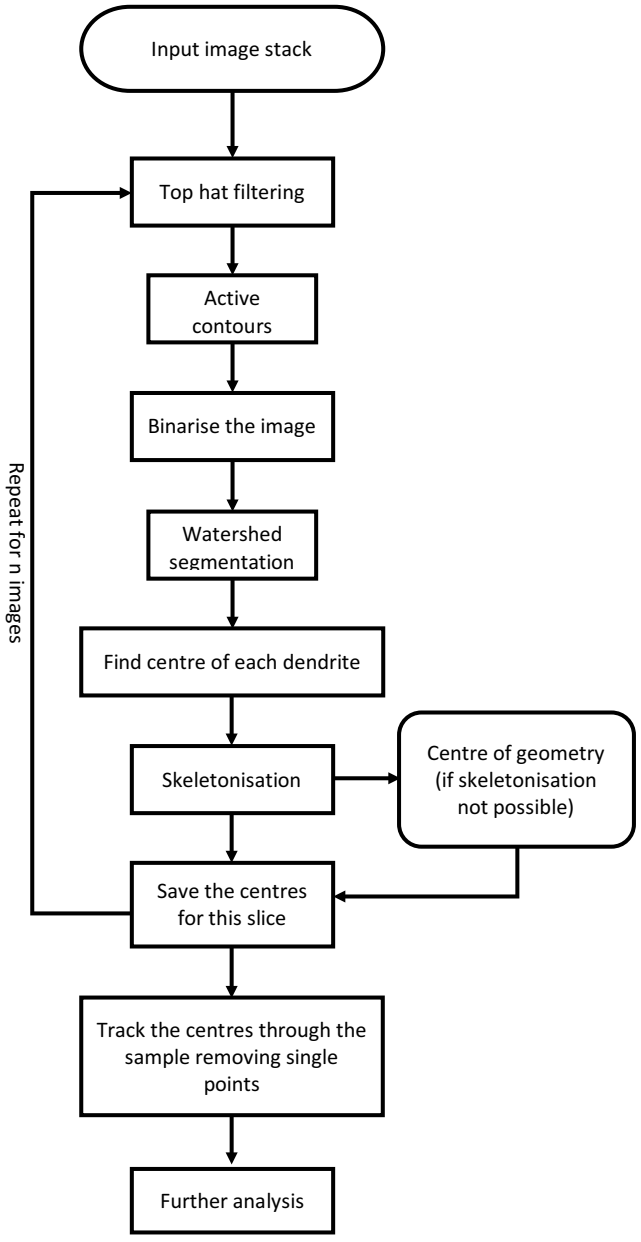


FIGURE 4.1: Image analysis process flow chart.

$$I = I_0 - \big(I_0 \circ s\big) \tag{4.1}$$

As a result by comparing figures Figure 4.2 and Figure 4.4 with the two post top hat filtering (figures Figure 4.3 and Figure 4.5) shows that there is much more even contrast across the surface. With no high intensity regions on the circumference of the sample itself.

4.1.2 Binarising Images

One of the most important parts of image analysis is using a correct binarisation technique. If an incorrect method is used then an image may become over or under-segmented which will effect the results of any further data-mining taking place on the image. A comparison of three different techniques on a slice of an Al 10 wt% Cu sample is given in Figure 4.6. As can be seen the thresholding methods have a great effect on the final image quality. Images Figure 4.6 c) and d) have under-segmented the image and over-segmented respectively. The under-segmentation seen in Figure 4.6 c) is characterised by the conjoined nature of the dendrites within the image. Moreover each of these segmented dendrites have a large area of the surrounding dendritic envelope which is not wanted. In comparison in Figure 4.6 b) the dendrites are largely separated and only the region of interest (the 'spines') of the dendrites are obtained.

Over-segmentation as seen in Figure 4.6 d) is characterised by dendrites which are very thin and often have been erroneously segmented resulting in disjointed sections which should be whole. By comparing Figure 4.6 a-b) and Figure 4.6 d) it is clear that in some instances this over-segmentation has resulted in dendrites with tertiary arms to become disconnected from the dendrite.

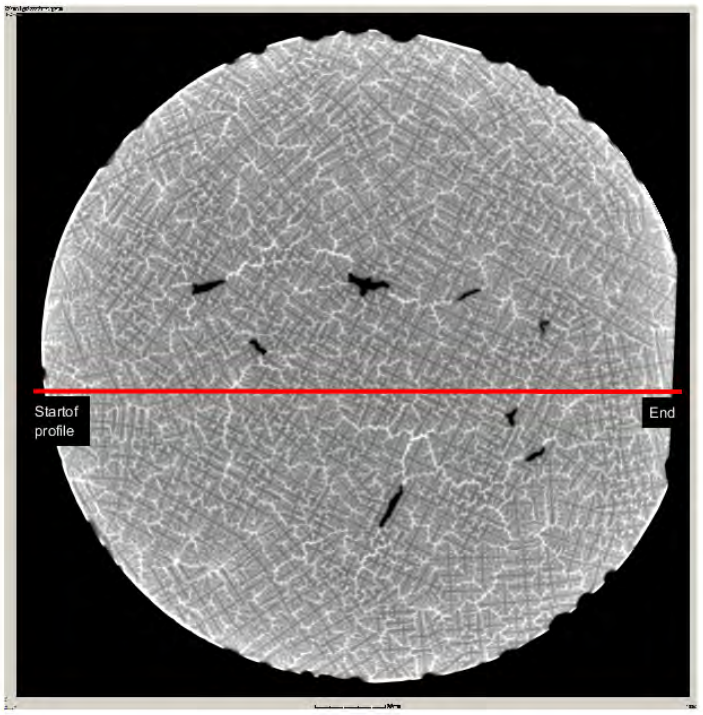


FIGURE 4.2: A single slice of the raw reconstructed CT volume slice with the line showing where the intensity profile was taken from.

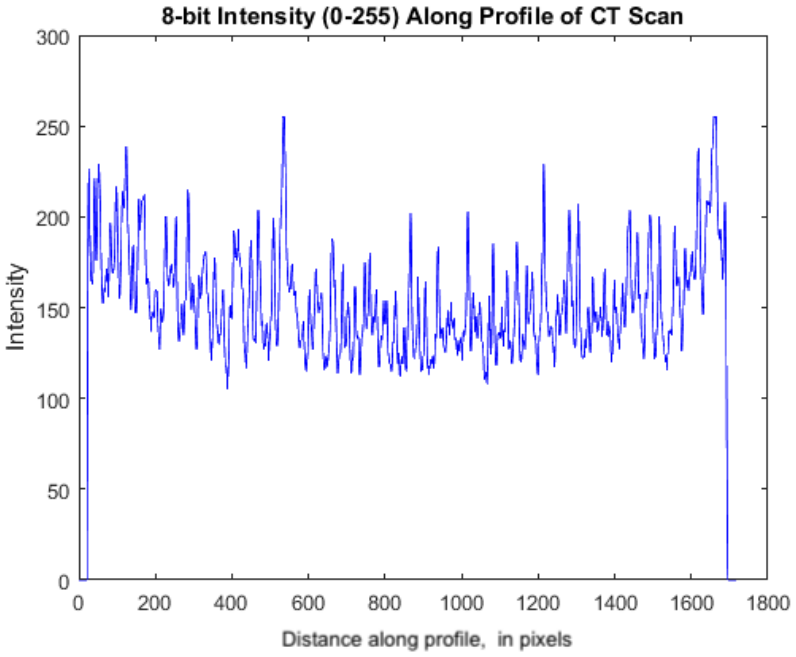


FIGURE 4.3: The intensity profile along the line shown in figure Figure 4.2

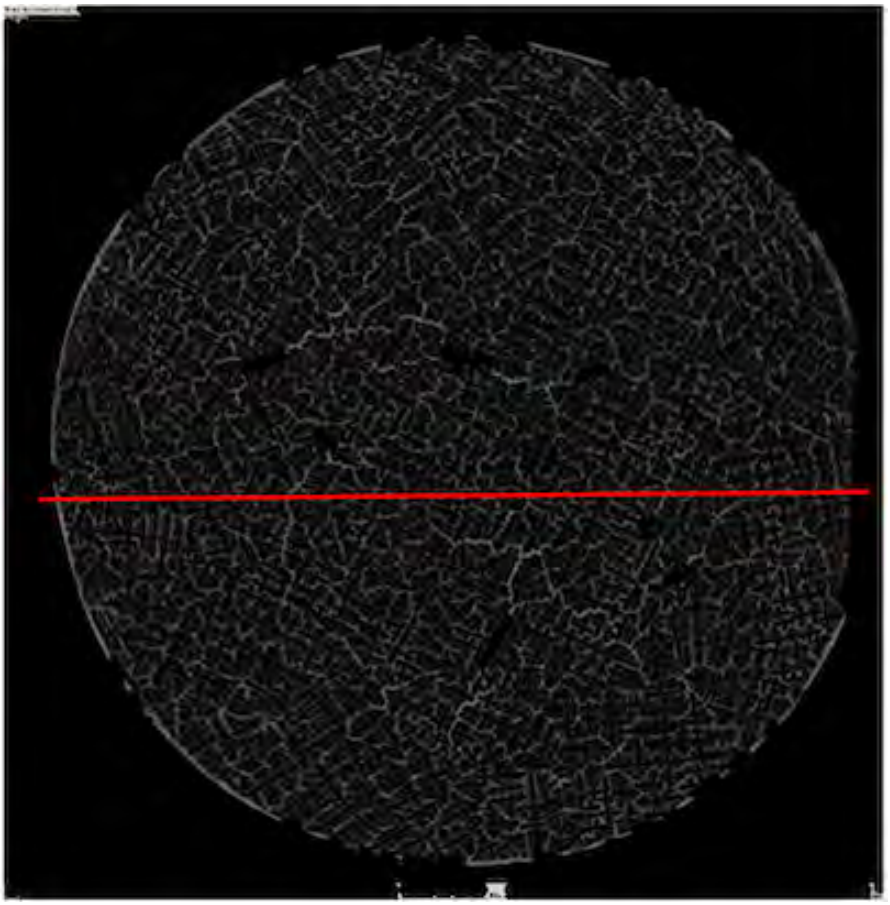


FIGURE 4.4: A single slice of the top-hat filtered CT volume with the line showing where the intensity profile was taken from.

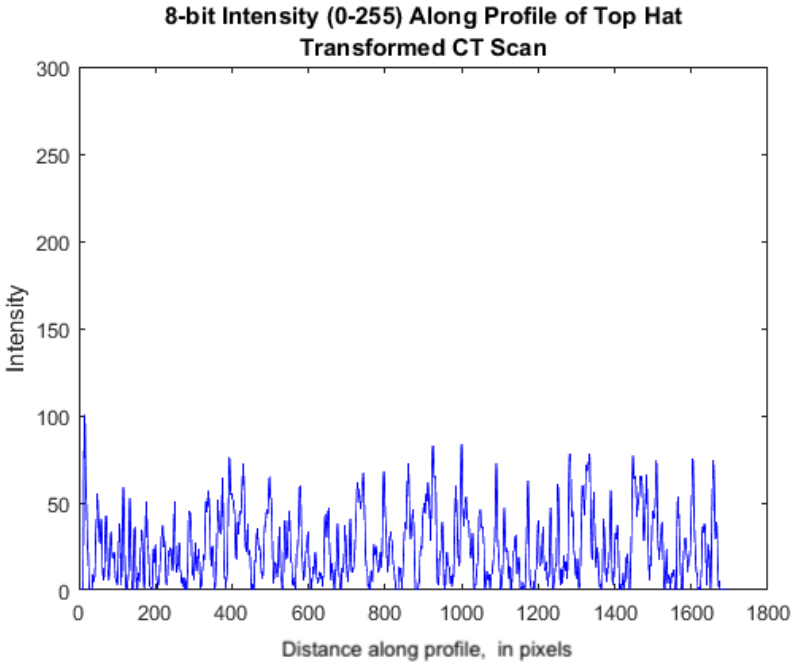


FIGURE 4.5: The intensity profile along the line shown in figure Figure 4.4

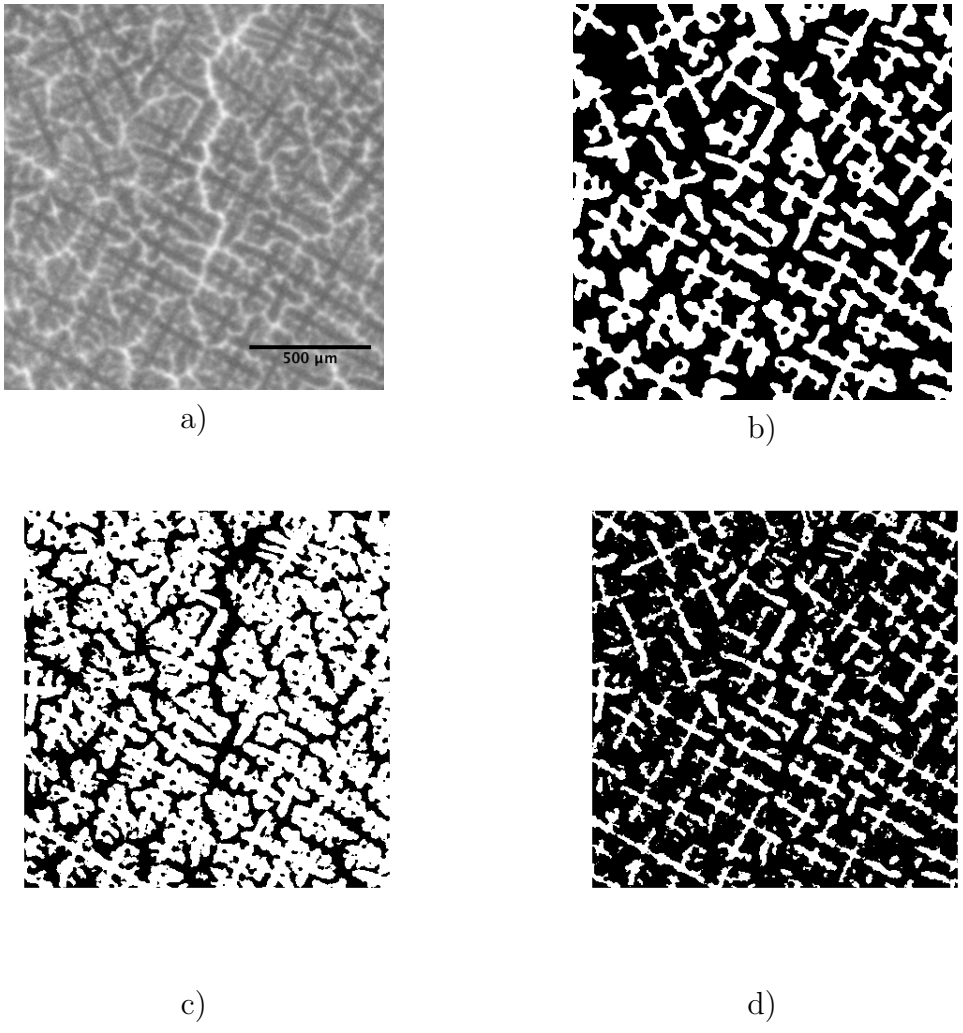


FIGURE 4.6: a) **CT** slice of a Al-10 wt% Cu sample. b) Active contours thresholding. c) Histogram based thresholding. d) Otsu thresholding.

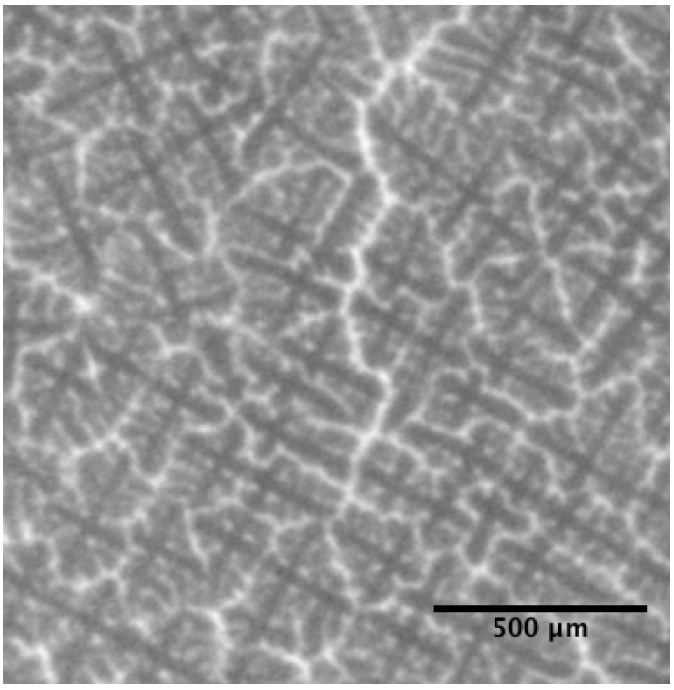
The method which can most closely and accurately represent the binarised form of a dendrite is the manual tracing of the shape from the micrograph. By doing this the 'true' dendrite shape can be obtained. However the obvious drawback of this technique is that it is very time consuming and dependent upon the person doing the manual tracing of the shape. Two different researchers may have two different ideas as to what the outline of a dendrite is. Thus giving two alternate results.

It is for this reason that a binarisation scheme involving active contours was employed in this work. This method captured the relevant microstructural information needed to analyse the samples, without over or under-segmenting the input images. As such the method will be described briefly in more detail.

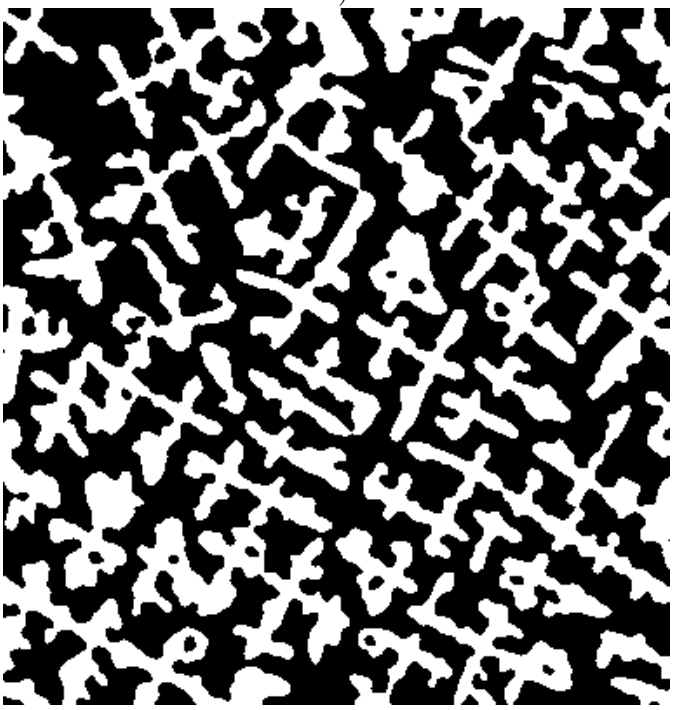
4.1.3 Active contours method

Use of an active contour method is driven by the fitting of Gaussian distributions to find and characterise local intensity variations. These local intensity variations are sorted and segmented into a foreground and background image [127].

The technique uses a variational level set framework to partition the image into two regions, a foreground and background, denoted by Ω_1 and Ω_2 respectively. The two regions are defined as above or below the zero level set function. That is the internal region (the dendrites)–which is in this case the foreground image– is defined by $\Omega_1 = \{\phi > 0\}$ (where ϕ is the result of the level set method for each pixel in the image). Conversely the background is given by $\Omega_2 = \{\phi < 0\}$. Therefore the interface–that is the dendritic to interdendritic boundary–is where $\Omega_0 = \{\phi = 0\}$. A more detailed explanation of this method is given by Wang *et al* [127].



a)



b)

FIGURE 4.7: a) **CT** slice of a Al-10 wt% Cu sample. b) Active contours thresholding.

The result of the active contour segmentation is then binarised making the image into a logical array. This is achieved by assigning the interface and foreground, Ω_0 and Ω_1 respectively a value of one and all the other points within the image a value of zero. This is shown below in figure Figure 4.7a and b, giving the original microstructural image and the output of the active contours method. A whole binarised microstructure is shown in Figure 4.8. Some artefacts are left over from the technique, such as the regions of porosity in the sample, but it is fairly trivial to remove these by adapting the image analysis regime slightly. For example by finding and subtracting these holes from the image prior to any further analysis being undertaken.

4.1.4 Watershed Segmentation

Whilst the majority of the dendrites have now become separated due to the active contours segmentation some of them may still be conjoined. This is due to small variations in the interface that separates the two dendrites being smaller than resolution of the **CT** image. This can be seen on some dendrites in Figure 4.9.

A watershed segmentation works by performing a distance transform across the whole of the image. That is computing the minimum distance to the closest non-zero valued pixel for every pixel within the image. This leads to an image for each dendrite similar to the one shown in Figure 4.10 for the conjoined dendrites in Figure 4.9.

This effectively gives a 3-dimensional surface to the 2-dimensional dendrites with peaks and troughs that correspond to the magnitude of the distances. A watershed segmentation then segments the image along these low lying regions or catchment basins in order to separate the touching dendrites. The segmentation line between the two conjoined dendrites is shown in Figure 4.11 which corresponds to the trough on Figure 4.10.

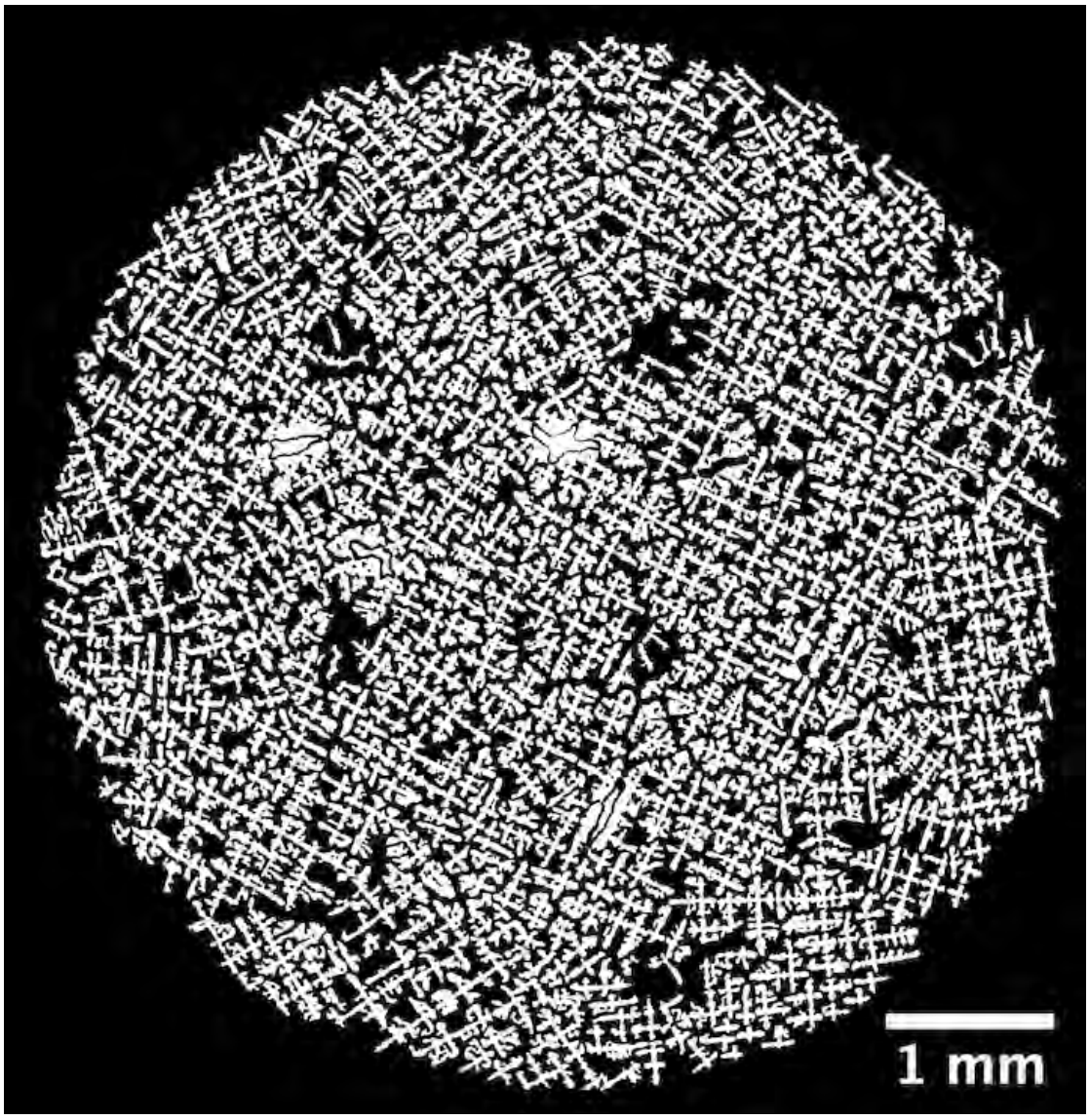


FIGURE 4.8: Final binarised image of a **CT** slice of a constant withdrawal 100 μm^{-1} Al-10wt%Cu sample.

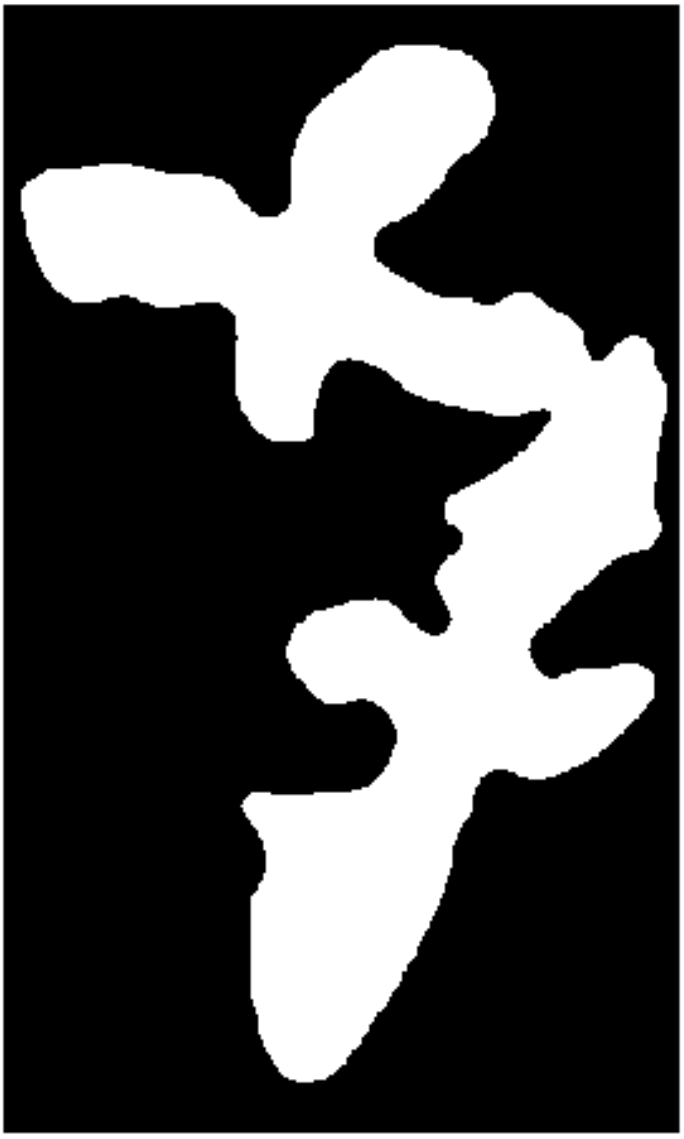


FIGURE 4.9: Conjoined dendrites

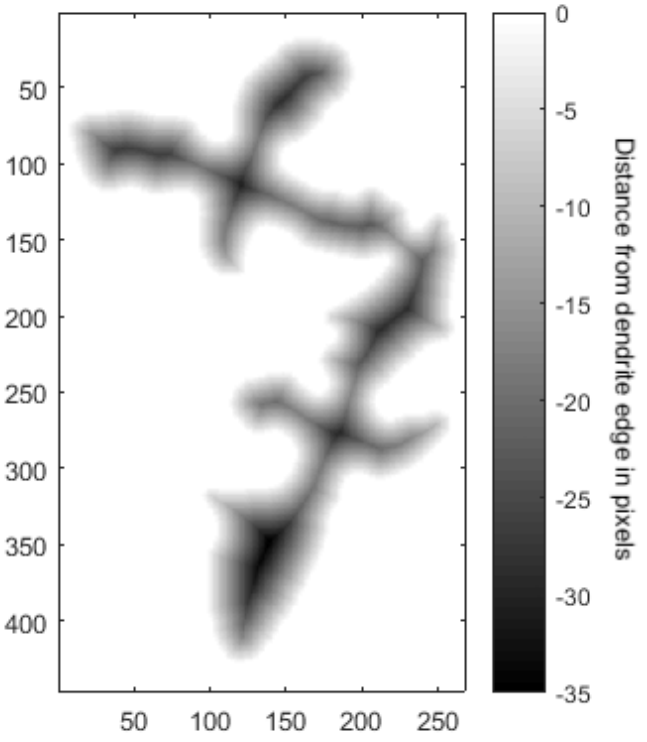


FIGURE 4.10: Distance transform



FIGURE 4.11: Segmented dendrites

4.1.5 Removal of small shapes and holes

Small unconnected shapes below a threshold size, approximately 100 pixels, were removed from the final image. This prevents any analysis of small areas which are not dendrites themselves. A function taking into account the area of each dendrite across each slice could be used to delete any shapes with an area at the smaller end of the area distribution. For this work a simplistic threshold was used however.

4.2 Finding the 'True' Centre of a Dendrite

For further analysis of a the **CT**'ed image stack accurate methods of finding the 'true' centre of a dendrite must be used. Here we define the 'true' centre not as the geometrical centre of the shape but rather the point at which the dendrite tip first passed through on a plane whilst it was growing (see Figure 4.12 for a schematic example). There are various methods within the literature which have been put forward over the years to try to solve this problem [31, 34, 36, 107, 150]. A number of them will be trialled and compared below. These methods are:

- Hand assigning the centre
- Centre of geometry
- Skeletonisation*
- Skeletonisation-geometry centre*
- Intercept of perpendicular bisectors*
- Centre of curvature*
- Gradient*
- Symmetry-based feature extraction

- Convolutional neural-network centre*

The starred (*) methods are techniques which have been put forward by the author. The methods without stars are ones taken from the literature [31, 34, 36, 107, 150]. The hand assigned centre, and centre of geometry however are methods which are commonly found throughout the literature. All of the different techniques will be trialled on traced and binarised dendrites taken from sections of a single crystal nickel superalloy. A number of common parameters of shape factors for each of the binarised shapes will be used to compare each technique.

4.2.1 Hand Assigning the Centre Point

Manual point assigning by hand is by far the easiest of the methods as it is simply finding the centre of the dendrite by hand along with its coordinates. This method is also one of the most commonly seen within the literature [107, 133]. For this work the multipoint clicker and analyser tool in the software Fiji (a variant of ImageJ) was used. For the comparison of the techniques it is assumed that the hand assigned dendrite centres are the 'correct' and 'perfect' centres of the dendrite (even if in reality the points are slightly away from the true centre of the dendrite).

4.2.2 Centre of Geometry

The centre of gravity method–like the manual assigning method–is rather simplistic and works on the principle of finding the 'average' position of all the points within a shape whilst assuming that the shape has uniform density and is within a uniform 'gravitational' field. This 'average' position can be within the shape or outside of it [2].

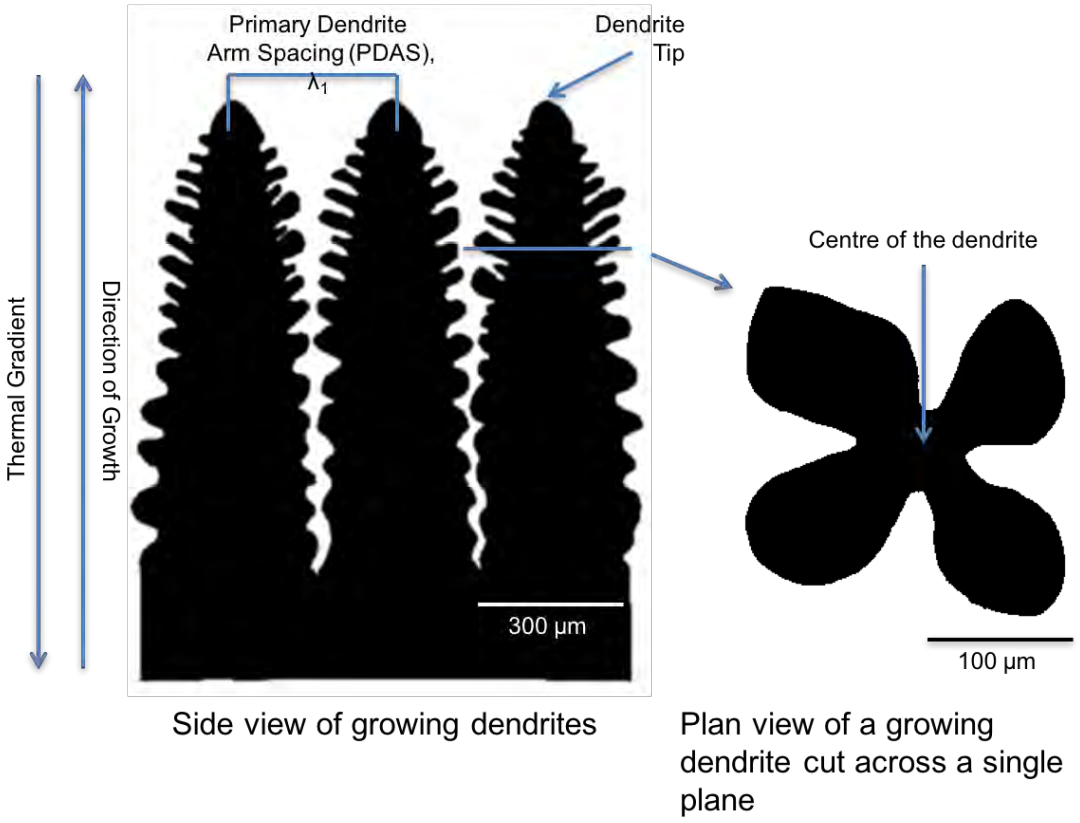


FIGURE 4.12: Schematic of the true centre of a dendrite growing into an undercooled melt.

4.2.3 Skeleton Centre

The skeleton centre method obtains the location of the centre of the dendrite by first obtaining the dendrites 'skeleton'. The skeleton is the medial transform of a shape. In other words the skeleton is an erosion of the perimeter of the shape pixel by pixel until it is eroded away leaving a one pixel thick line. This line provides sufficient information that if it were to be dilated back by adding a pixel onto the edge of the perimeter the number of steps taken for the initial skeletonisation it would reform the original shape [151]. A mathematical explanation of the skeletonisation technique can be found in reference [151].

The skeleton of a cross, such as a dendrite, will be a one pixel thick cross. As such, it is hypothesised that the true centre of the dendrite would be this point where the two lines of the one pixel thick line of the cross' skeleton intercept. That point being the *branching point* where the 'arms' of the skeleton intersect. This point can be easily found as it is simply in the locations where the binary matrices

$$\begin{bmatrix} 0 & 1 & 0 \\ 1 & 1 & 1 \\ 0 & 1 & 0 \end{bmatrix} \quad or \quad \begin{bmatrix} 1 & 0 & 1 \\ 0 & 1 & 0 \\ 1 & 0 & 1 \end{bmatrix}$$

occur. At these points the central pixel in the cross is then assigned as the centre of the dendrite. These points are referred to as the *branching points*. These *branching points* are shown in Figure 4.13f.

However as can be seen in figure Figure 4.13f the skeletonisation method results in$\sim$10 different points to choose from for the actual centre of the dendrite. The 'correct' centre of the dendrite is chosen as the *branching point* which is at the intersection of the two longest skeleton lines. The assumption is that the *branching point* connected to the longest arms is likely to be the one at the centre of the dendrite itself.

This method is described in greater detail in Chapter 10. Chapter 10 includes a comparison of the skeletonisation technique and the centre of geometry method as applied to several different regular and irregular shapes.

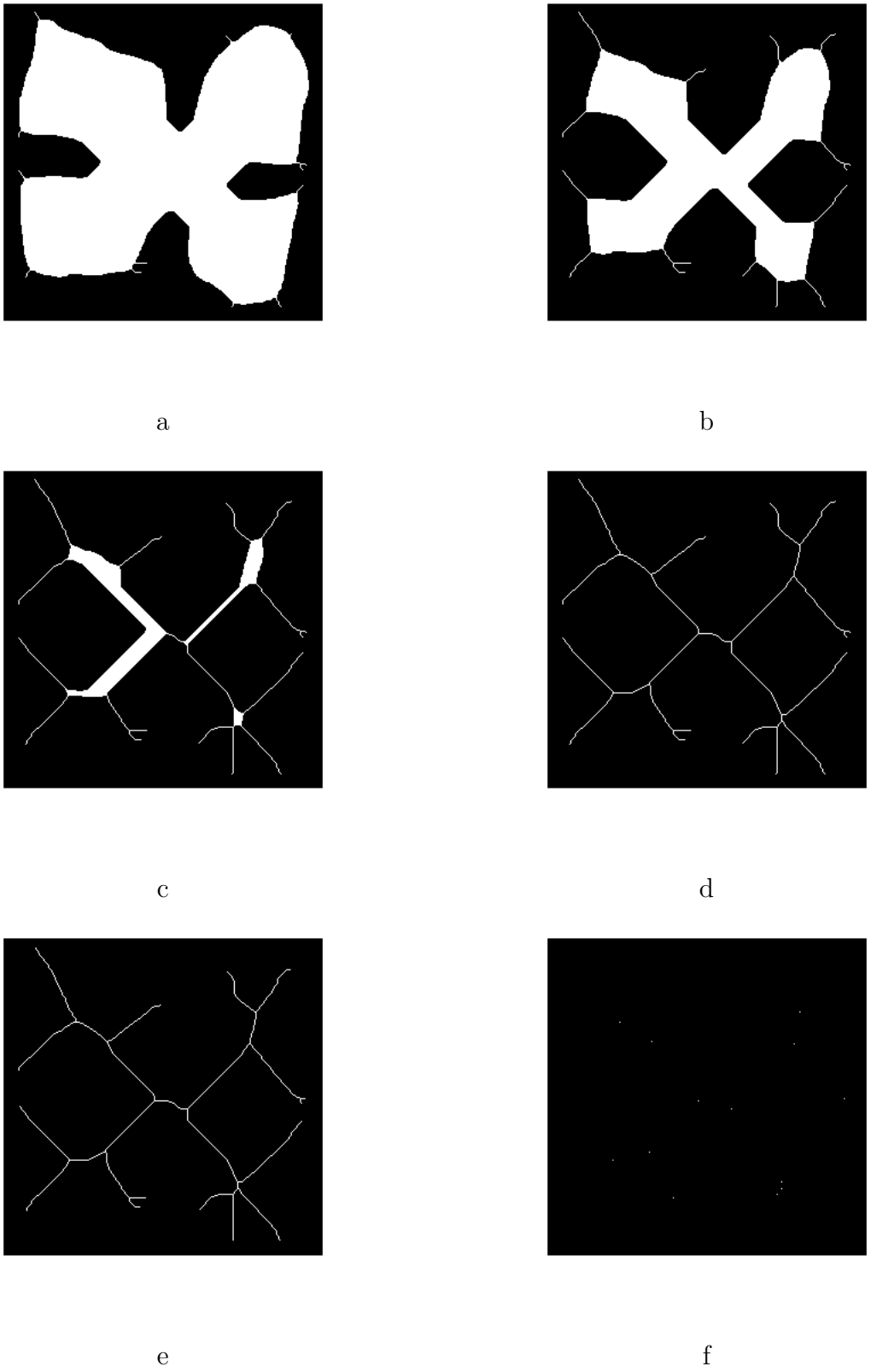
4.2.4 Combined Skeleton-Centre of Geometry

When multiple branching points are obtained using the method described here in (and also in the Appendix of Chapter 10) only one of them can be chosen as the actual centre of the dendrite. In order to choose only one of a multiple branching points an algorithm is needed to pick one of these branching points. The centre of geometry is the deciding factor in choosing one of the different skeleton branching points. The skeleton branch point closest to the centre of geometry is chosen as the 'correct' centre.

This method combines the two methods described previously (skeletonisation and centre of geometry in Chapter 10) in order to remove the possibility of erroneous centres being assigned which can occur for dendrites showing tertiary arm growth. This can be a problem due to the large number of branching points which may be present within the final skeletonised image (see Figure 4.13 and Figure 4.14a).

4.2.5 Intercept Centre

A further method similar to the skeleton-geometry method is to find the interception of the two longest lines which are approximately perpendicular to each other. This is done by finding four points along the perimeter of the binary shape which are furthest apart then find the intercept of these two lines obtained by joining the opposite points together (see figure Figure 4.14). This method takes advantage of the fact that generally the two longest lines are the 'diagonals' across



a b c d e f

FIGURE 4.13: Steps of the skeletonisation operation, a, b, and c are some of the erosion steps which lead to the one pixel thickness skeleton seen in image d. This image subsequently has any spurs removed giving image e. Finally the cross points are found where two lines intersect i.e. the *branching points* in f which are one pixel in size.

a dendrite. The dendrite centre will be the *branching point* which is closest to this point (figure Figure 4.14d).

In order to do this the perimeter of the shape must first be found (figure Figure 4.14b). This is a relatively easy operation for a binary shape as it is just the point where the 1s are adjacent to 0s. Subsequently the longest line between two points along the perimeter is found by computing the lengths between each point and each other point using the equation:

$$d = \sqrt{(x_1 - x_2)^2 + (y_1 - y_2)^2} \tag{4.2}$$

All of these values are sorted to find the largest distance distance. This value of distance corresponds to the vector $\overrightarrow{AB}$ where point A has co-ordinates (x_1, y_1) and point B has co-ordinates (x_2, y_2) (figure Figure 4.14c). Then in order to find the longest line which is in an approximately perpendicular direction to the vector $\overrightarrow{AB}$ one finds the determinant det of the vectors $\overrightarrow{AM}$ and $\overrightarrow{BM}$ where $M(x_m, y_m)$ is a point along the perimeter. This is done using the equation:

$$D = (x_2 - x_1)(y_m - y_1) - (y_2 - y_1)(x_m - x_1) \tag{4.3}$$

Where D is the determinant. The magnitude of the value determines how far away from the line $\overrightarrow{AB}$ the point M is. If the value is negative the point M lies on one side of the line and conversely if it is positive it lies on the other side of the line. If the value of D is 0 then the point M lies on the line itself. The locations of M_1 and M_2 are found by computing the determinant of each point along the perimeter.

Subsequently a new line is drawn between M_1 and M_2, where M_1 and M_2 have the largest positive and negative values of D (figure Figure 4.14c). The point which

intercepts the two vectors $\overrightarrow{AB}$ and $\overrightarrow{M_1M_2}$ is then used to find the closed branching point from the skeletonisation analysis achieved earlier (Figure 4.14d).

4.2.6 Centre of Curvature

The centre of curvature finds the curvature at each point along the perimeter of a dendrite by fitting a circle to each point and the 5 points either side of it. The smaller the radius (r) of this circle the greater the curvature (K) of each point.

$$K = \frac{1}{r} \tag{4.4}$$

Points with high curvature occur at the base of the secondary arm as they attach to the primary truck. As a result it can be assumed that if four of these regions of high curvature can be found then the coordinates of these points can be averaged out in order to find the central point between them and therefore the centre of the dendrite itself.

4.2.7 Gradient Across a Blurred Interface (Gaussian Centre)

A Gaussian filter can be used to smooth the interface of a binarised dendrite and find the centre of a dendrite. This smoothed interface gives a sigmoidal change in intensity across the boundary. The steeper this transition in the sigmoidal curve the greater the curvature along this boundary at this point.

The greatest curvature along the perimeter of a dendrite is at the base of the arms as they connect to the primary trunk of the dendrite. As such the transition will have the steepest gradient at these points. Four points along the perimeter of

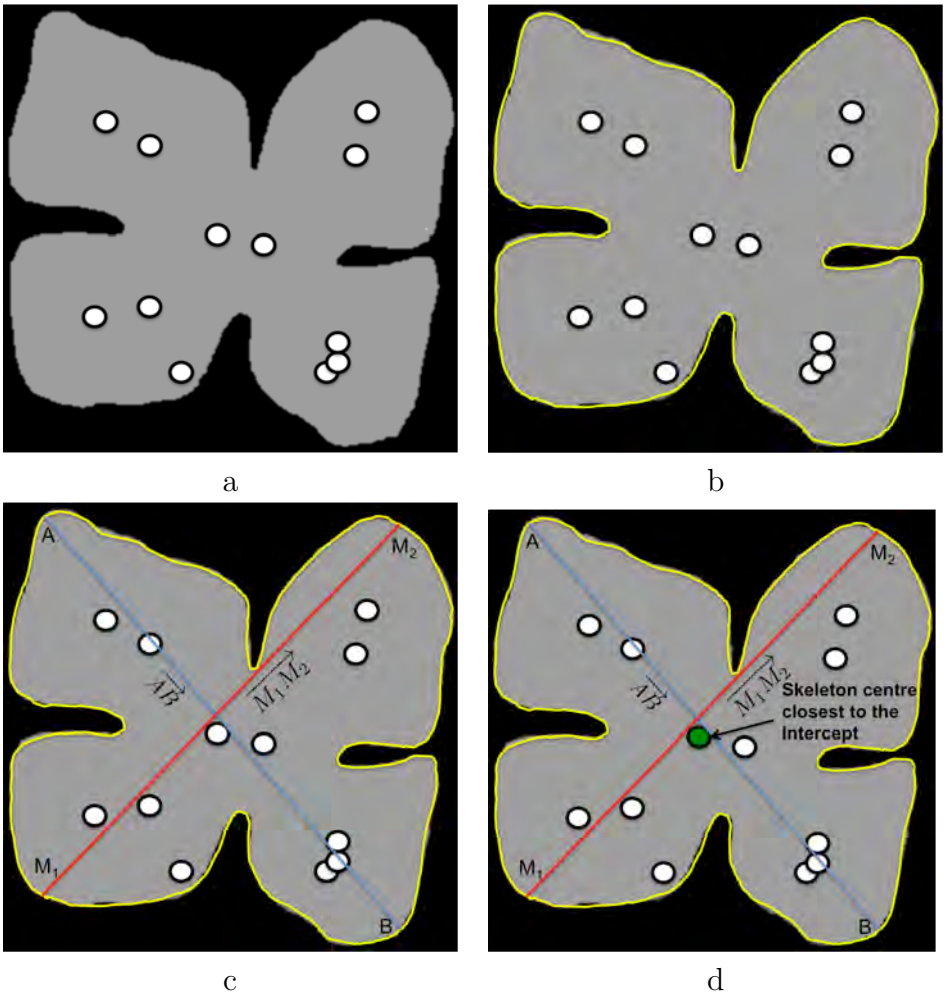


FIGURE 4.14: Extreme points centre assigning. a), branch points found from skeletonisation (Points have been artificially enlarged for ease of viewing). b), perimeter of the shape. c), find longest line in approximately perpendicular direction. d), assigning the centre closest to the intercept of the two lines as the centre of the dendrite.

the original binary shape are found and then the centre of geometry of these four points is found. This centre of geometry is the Gaussian Centre.

4.2.8 Symmetry-Based Feature Extraction

Put forward by Tschopp *et al* [34, 36, 152] the symmetry-based feature extraction technique takes advantage of the morphology of a dendrite similar to the skeletonisation based technique. In this case the morphology is the four-sided morphology present in many materials that solidify dendritically, for example Ni-superalloys [34, 36, 153] and aluminium copper. The technique will be briefly explained below however the reader is pointed towards the original papers [34, 36, 153] and the web-based example written by Tschopp [150] for a more rigorous and in-depth explanation of the process behind the technique.

This method as put forward in the literature unlike the others presented here does not rely upon a binarised input but rather an optical image. However the current method has been slightly altered from the previous work by Tschopp *et al* [34, 36, 150, 153]. In this thesis the authors chose to do some preprocessing of the optical micrographs prior to analysis. A top hat filter was applied to the image and subsequently the symmetry-based feature extraction took place. This was done to remove any non-uniform illumination across the surface of the sample. Moreover an active contours based segmentation method was employed to remove any interdendritic grains which can affect the method negatively [34, 36, 150, 153].

An individual pixel is chosen within the image, then the local neighbourhood of pixel intensities is obtained. The image is then rotated by 90 degrees and the next set of neighbourhood intensities are obtained. This step is repeated three times in total. Subsequently an average pixel intensity and four-fold symmetry of each pixel is calculated from the four images. Finally the dendrite cores can be found by standard image segmentation techniques such as thresholding.

4.2.9 Convolutional Neural Network Centre Finding

A neural network was created and used to try and find the centre of a dendrite by means of artificial intelligence. The output of the technique is a probability map indicating the liklihood of the dendrite centre at each pixel location across a microstructure.

To this end a convolutional neural network was created in *Pytorch* (an open-source Python library) with an architecture consisting of four convolutional layers, a maxpooling layer, then three linear layers. It was trained using patches of size 121x121 from the binarised Ni-superalloy where the input training data consisted of a 'True' and 'False' sets of pictures. The 'True' images were patches where the central pixel of the 121x121 square was the centre of the dendrite assigned chosen by the operator. The 'False' images were images of size 121x121 cropped randomly from the binarised microstructure.

The training dataset consisted of 4000 images of dendrites, 2000 of which were 'True' and the other 2000 the 'False' images. The network was trained using a minimum least squares loss optimiser.

After training the **CNN** was used to analyse each pixel in the microstructural images used for comparing the different dendrite centre finding techniques. The output for each (i, j) pixel is a probability between 0 and 1, where 0 is likely not a centre and 1 is most likely to be a centre. This as a result created a three dimensional probability surface across the input image. Thus, the centre of the dendrite/dendrites within the image is/are the peaks in this surface.

4.2.10 Dendrite centre finding comparison

The different dendrite centre finding techniques were trialled and tested on a number of dendrites traced and binarised from a series of nickel superalloy slices. In

total 750 dendrites of various sizes and shapes were used to test the different methods. An example of one of these traced micrographs is given in Figure 4.15. These dendrites consisted of both dendrites within the bulk of the microstructure and edge dendrites which are on the circumference of the casting. The methods were first trialled on this data set as it is much more simplistic than the **CT**'ed Al-10 wt% Cu micrographs. As such, if a technique could not adequately analyse one of these nickel dendrites then it would not in all likeliness work on the more complex shapes.

In order to make the data comparable for each dendrite the location of each centre was normalised in the same fashion. A bounding box was fitted around the dendrite and the width (w) and height (h) of the box are then used to give a normalised coordinate system. The bottom left corner of the bounding box is the new (0, 0) coordinate. The top right corner has a coordinate of (w, h). The dendrite centre is then the location of point in this bounding box coordinate system. This location is then normalised between 0 and 1 by means of a simple division (Equation (4.5)). This new normalised coordinate system (x_0, y_0) gives the location of the centre of the dendrite between 0 and 1, where points (0, 0) and (1, 1) are thus the extremities of the bounding box:

$$x_0 = \frac{x}{w} \tag{4.5a}$$

$$y_0 = \frac{y}{h} \tag{4.5b}$$

A number of common shape factors were used to describe the dendrite shapes and are as defined as follows:

Area: The number of pixels in the dendrite

Aspect ratio: A function of the largest diameter (d_{min}) across a shape to the largest perpendicular diameter (d_{min}) to it. The closer the value is to 1 the

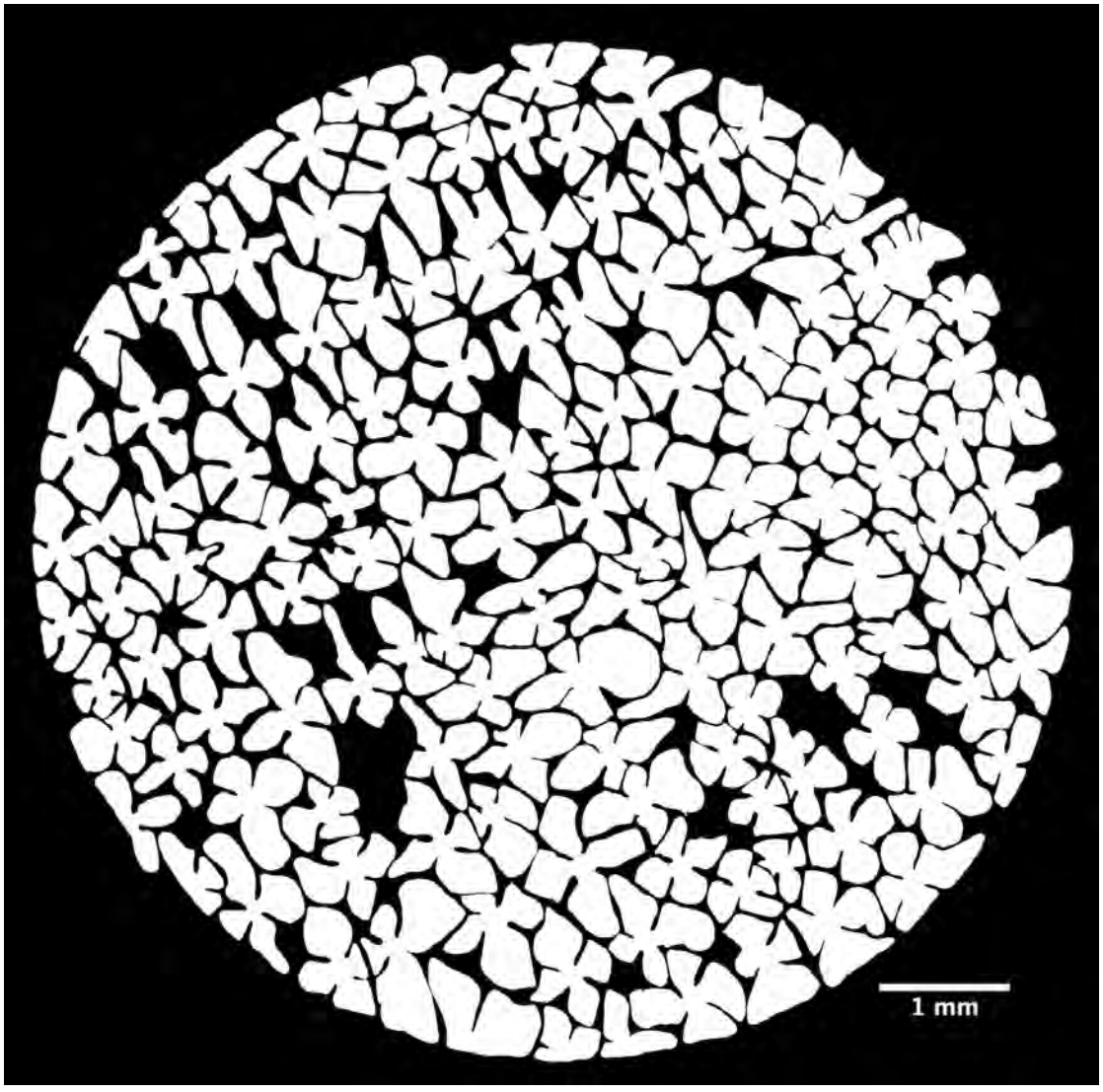


FIGURE 4.15: Example traced directionally solidified nickel superalloy micrograph used to test the various centre finding techniques.

more regular the shape.

$$A_R = \frac{d_{min}}{d_{max}} \tag{4.6}$$

Circularity: The degree to which a shape approaches a circle. Varying from 1, for a perfect circle, to infinity [154]. Where A is the area and P is the perimeter.

$$f_C = \frac{4\pi A}{P^2} \tag{4.7}$$

Compactness: A measure of how compact a shape is. Defined as a the area of the shape (A) divided by the area of the minimum bounding circle (A_{bound}). For a circle the value is 1 as the area and its minimum bounding circle are equivalent and identical. For more complex and irregular shapes the value approaches 0.

$$f_{comp} = \frac{A}{A_{bound}} \tag{4.8}$$

Convexity: A measure of surface roughness of a shape, defined as the convex hull perimeter (P_c) divided by the true perimeter (P). The rougher the shape the greater the real perimeter is and thus the lower the value of convexity. This shape factor is also referred to as the waviness factor. A more irregular dendrite which has a large number of tertiary arms is likely to have a smaller value for the convexity.

$$f_w = \frac{P_c}{P} \tag{4.9}$$

Elongation: The measure of how stretched a shape is, *i.e.* the more like a needle the higher the value of the elongation factor, which is calculated using the largest diameter (d_{min}) across a shape and the largest perpendicular diameter (d_{min}) to it.

$$f_E = \frac{d_{max} - d_{min}}{d_{max}} \tag{4.10}$$

Eccentricity: The value of the eccentricity of the ellipse with the same second moment of area of the binarised dendrite, f_{ecc}. Where the eccentricity is defined as the distance between the foci of the ellipse and the major axis length (d_{max}). It is a value between 0 and 1 where 0 is a circle and 1 is a straight line.

Roundness: Ratio of the area (A) to the length of the major axis (d_{max}) normalised between 0 and 1. The closer the value to 1 the rounder a shape is, *i.e.* the less stretched in one axis.[154]

$$f_R = \frac{4A}{\pi d_{max}} \tag{4.11}$$

Examples of all of these for regular, irregular and common dendritic shapes can be seen below in Table 4.1. The results of trialling the methods on all 750 dendrites are given in Figures 4.16 to 4.23. Values for the means, standard deviations and variances for the different scaled distances can be found in Table 4.3. The mean, standard deviation and variance for each of the shape factors for the nickel superalloy slice given in Table 4.2 as well as values for the an aluminium-copper slice.

It is clear from Figures 4.16 to 4.23 that there is a clear shape dependence on the methods for finding the centre of dendrite. In each case some of the methods perform much better than others, this can be visualised by comparing each of the plots in Figures 4.16 to 4.23 methods which are closer to the 'true' hand-assigned centre tend to have a denser spread of data concentrated towards the x-axis. Conversely techniques which have not worked well show much greater spread of data. It is clear from these plots that each technique does not work as well for dendrites which are on the edge of the microstructure. These dendrites are often less regular than inner-microstructure dendrites and can be more complex in shape (as seen by comparing the inner and outer dendrites columns in Table 4.3).

Shape	Area [pixels]	Aspect ratio	Circularity	Compactness	Convexity	Eccentricity	Elongation	Roundness
	2.91×10^6	1.00	1.00	1.00	1.06	0.00	0.00	1.00
	2.32×10^6	2.25	1.26	0.69	1.05	0.90	0.56	0.48
	8.81×10^3	72.8	22.8	0.132	1.02	1.00	0.986	0.0185
	2330	1.07	3.55	0.660	0.723	0.362	0.0680	0.435
	1580	1.15	3.78	0.801	0.605	0.496	0.132	0.655
	2530	1.07	3.48	0.701	0.719	0.366	0.0694	0.491

TABLE 4.1: Table of shape factors for different regular, irregular and dendritic shapes.

TABLE 4.2: Table showing the mean, standard deviation and variance values for the different dendrites obtained from the traced nickel superalloy sample and from the binarised aluminium-copper **CT** volume.

Shapefactor	**Ni-superalloy**			**Al 10wt% Cu**		
	$\bar{x}$	$\bar{\sigma}$	Var(x)	$\bar{x}$	$\bar{\sigma}$	Var(x)
Area	2.88×10^5	1.62×10^5	2.69×10^8	1330	1070	1.35×10^6
Aspect ratio	1.55	0.464	0.216	2.05	1.08	1.18
Circularity	3.47	1.38	1.91	6.92	5.29	27.9
Compactness	0.687	0.077	0.006	0.534	0.118	0.014
Convexity	0.756	0.078	0.006	0.776	0.186	0.035
Eccentricity	0.687	0.164	0.027	0.778	0.191	0.036
Elongation	0.310	0.160	0.026	0.435	0.199	0.040
Roundness	0.477	0.102	0.010	0.300	0.104	0.011

TABLE 4.3: Table showing the mean, standard deviation and variance values for the scaled distance between the hand assigned centres and the centres assigned by each of the different methods. Included are subsets of the data containing the values for only the inner or edge dendrites from the microstructures.

Method	**All Dendrites**			**Inner Dendrites**			**Outer Dendrites**		
	$\bar{x}$	$\bar{\sigma}$	Var(x)	$\bar{x}$	$\bar{\sigma}$	Var(x)	$\bar{x}$	$\bar{\sigma}$	Var(x)
Geo	0.207	0.157	0.0247	0.205	0.158	0.0249	0.227	0.153	0.0233
Skel	0.315	0.209	0.0435	0.310	0.207	0.0427	0.373	0.220	0.0484
Skel-Geo	0.224	0.1647	0.0271	0.220	0.162	0.0264	0.266	0.183	0.0334
Int	0.260	0.175	0.0307	0.2566	0.176	0.0308	0.297	0.169	0.0286
Sym	0.179	0.132	0.0174	0.756	0.131	0.0172	0.210	0.137	0.0187
Curv	0.255	0.168	0.0284	0.253	0.170	0.0287	0.270	0.160	0.0255
Gauss	0.238	0.158	0.0250	0.234	0.158	0.0248	0.247	0.163	0.0266
NN	0.323	0.215	0.0462	0.321	0.215	0.0461	0.349	0.217	0.0471

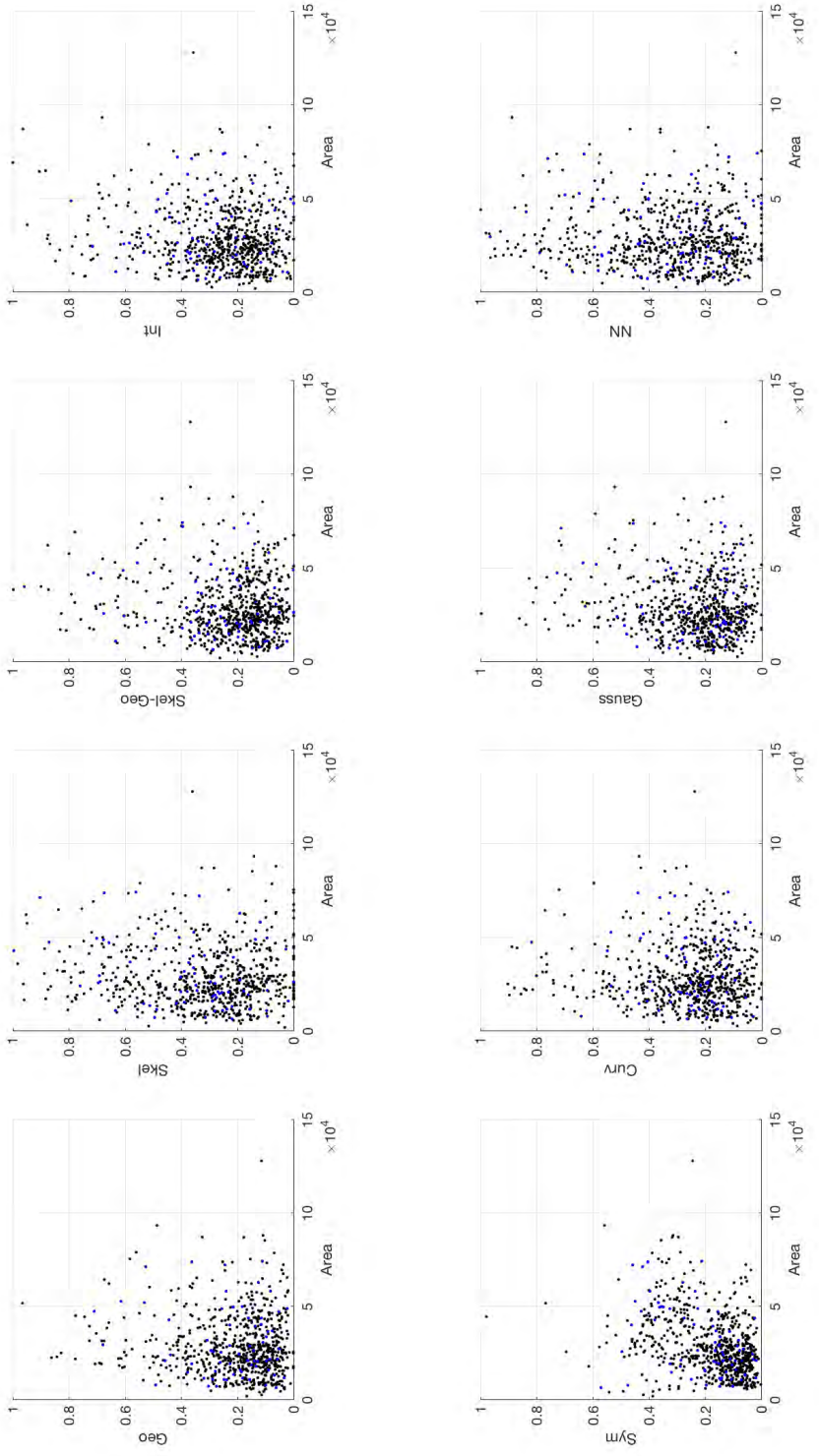


FIGURE 4.16: Distance between the hand assigned centre and the centres assigned using the different methods against the area in pixels of each dendrite. The black circles are the inner dendrites and the blue the edge ones.

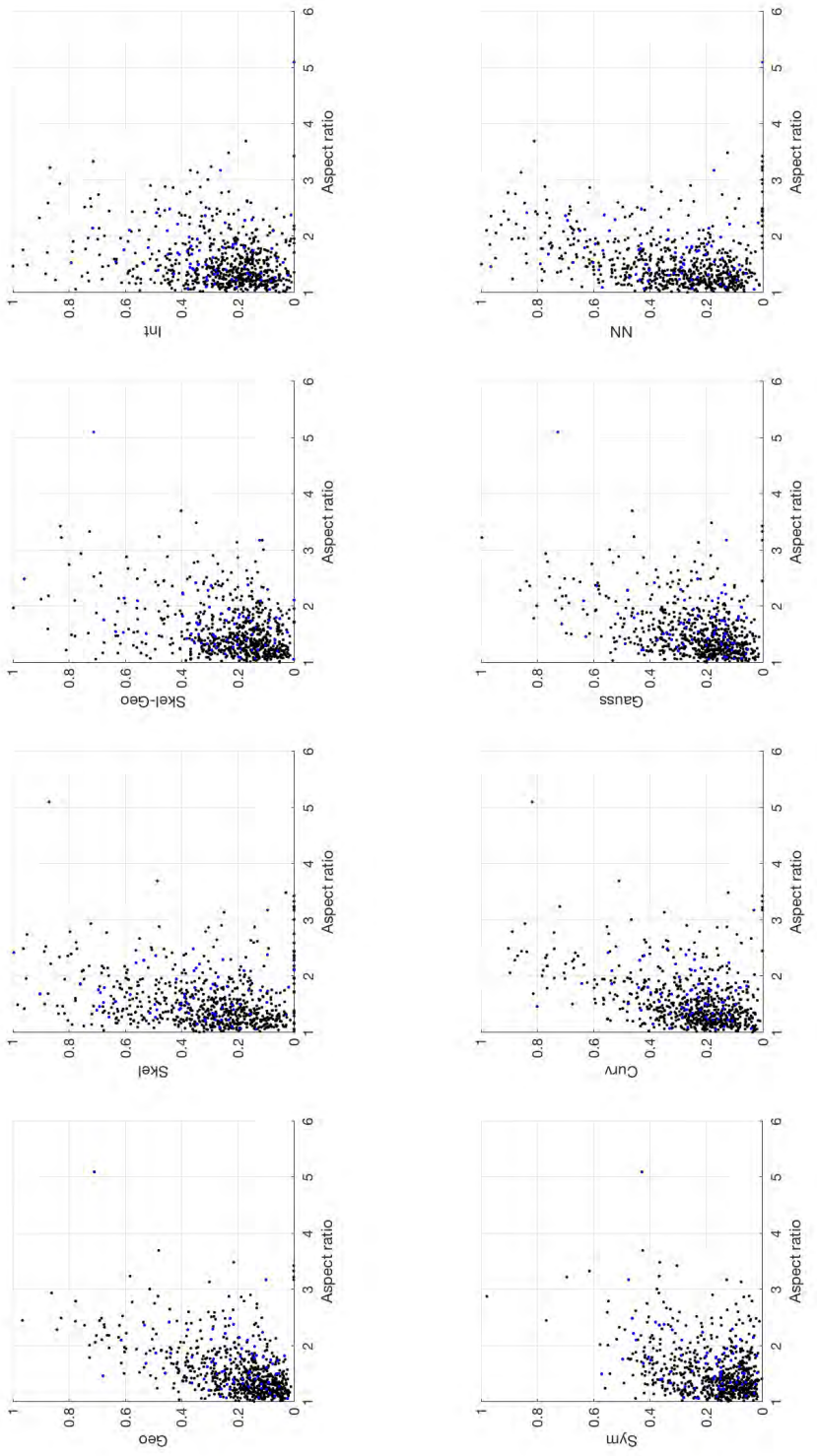


FIGURE 4.17: Distance between the hand assigned centre and the centres assigned using the different methods against the aspect ratio of each dendrite. The black circles are the inner dendrites and the blue the edge ones.

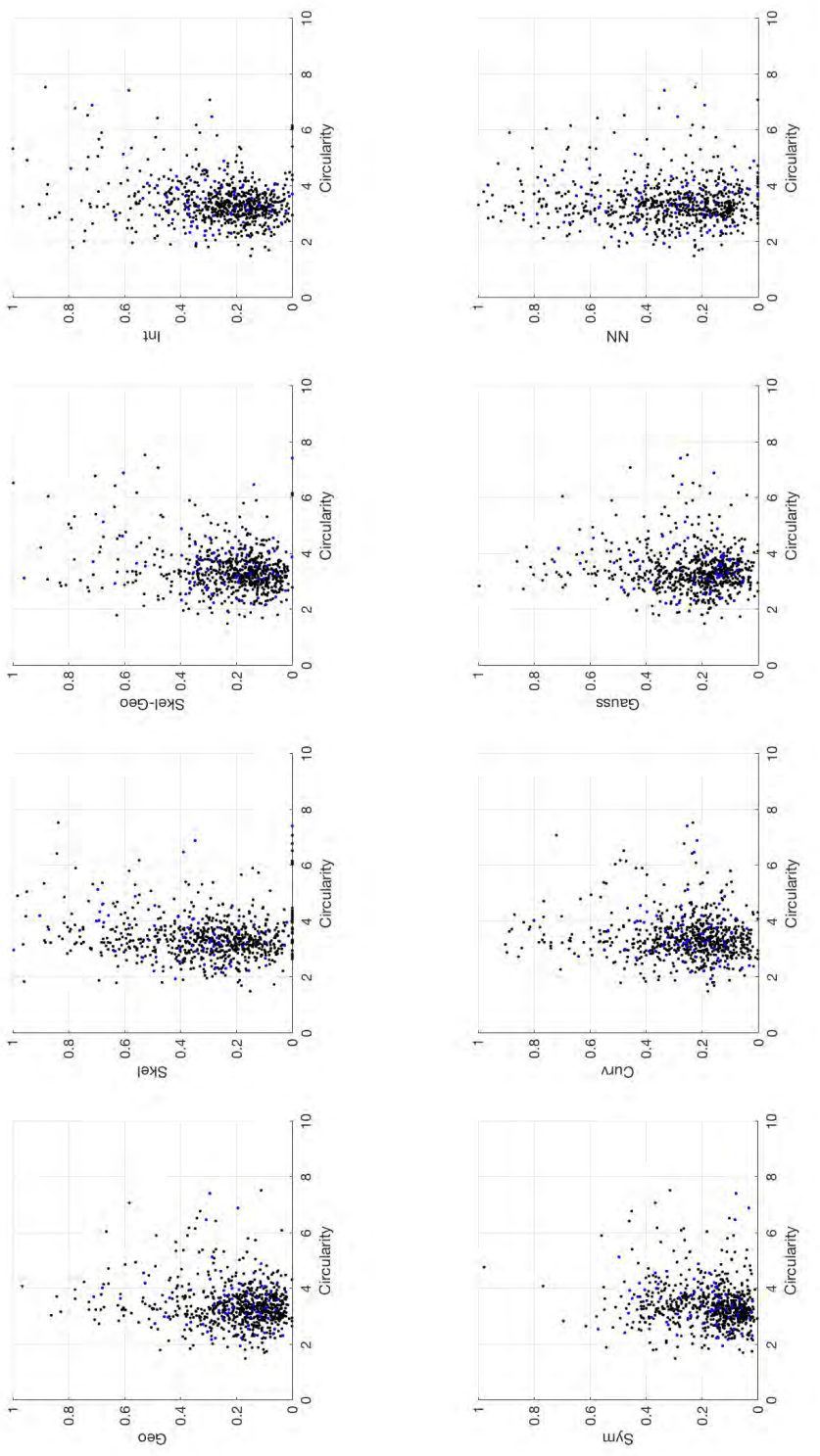


FIGURE 4.18: Distance between the hand assigned centre and the centres assigned using the different methods against the circularity of each dendrite. The black circles are the inner dendrites and the blue the edge ones.

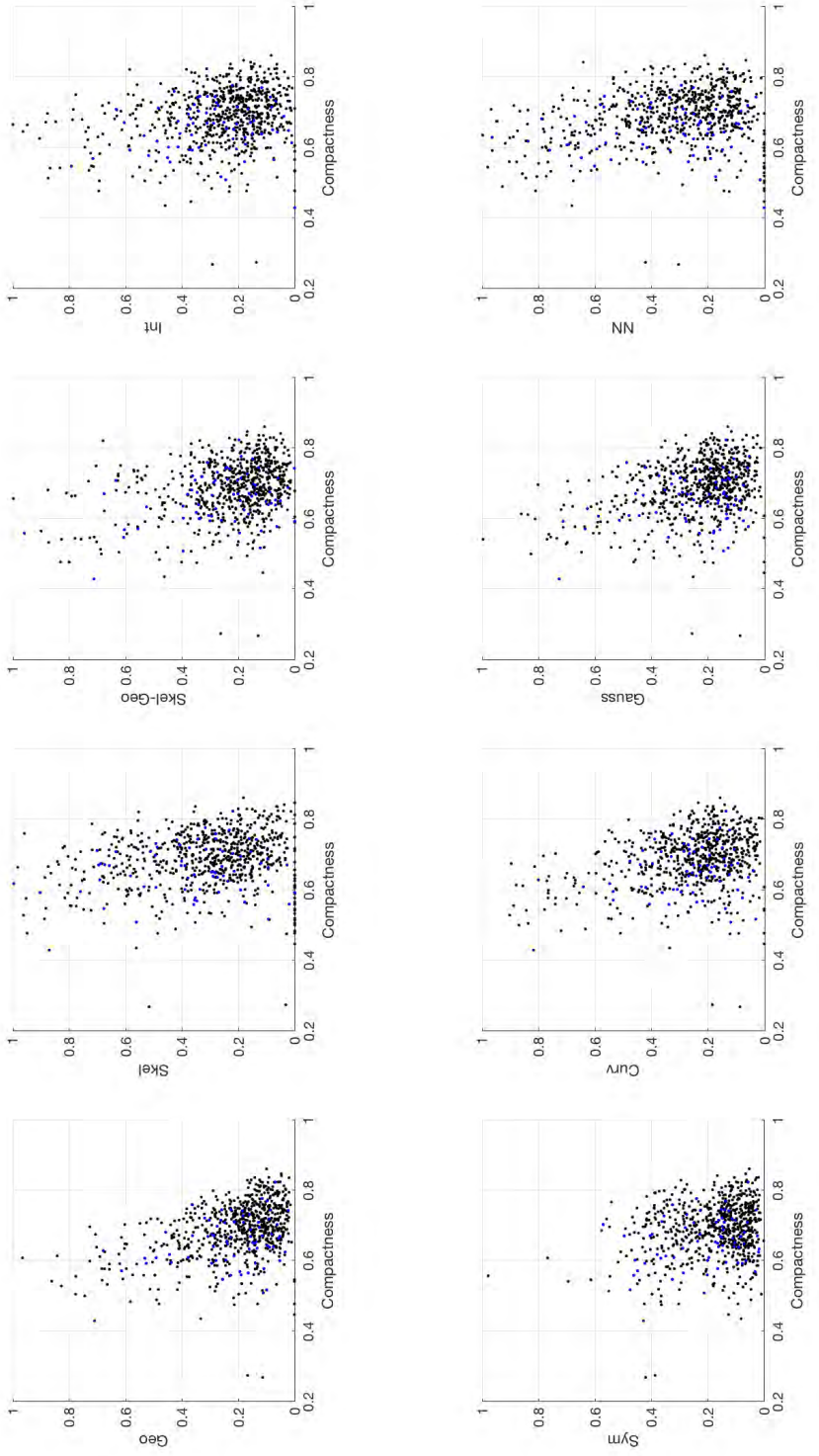


FIGURE 4.19: Distance between the hand assigned centre and the centres assigned using the different methods against the compactness of each dendrite. The black circles are the inner dendrites and the blue the edge ones.

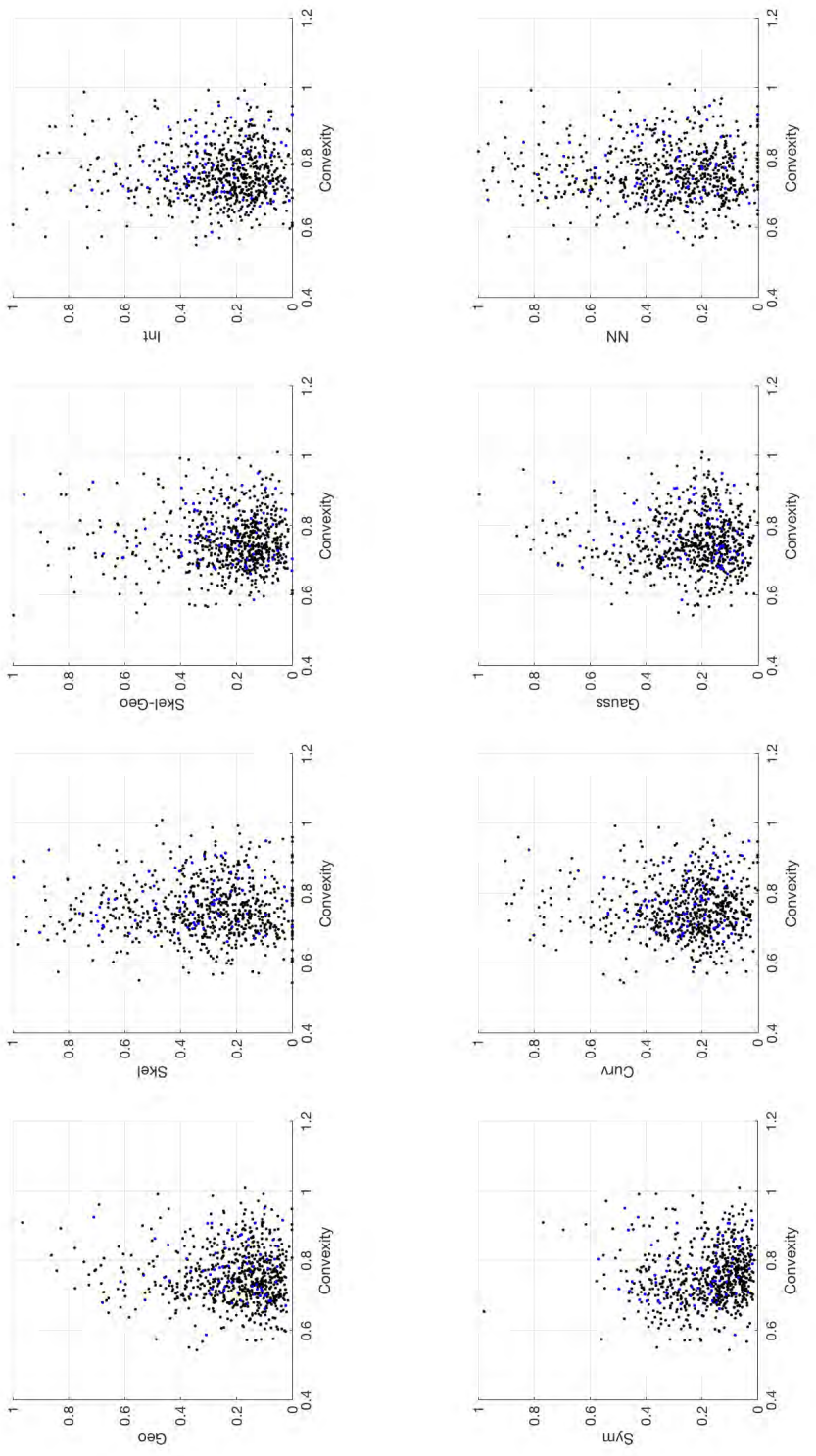


FIGURE 4.20: Distance between the hand assigned centre and the centres assigned using the different methods against the convexity of each dendrite. The black circles are the inner dendrites and the blue the edge ones.

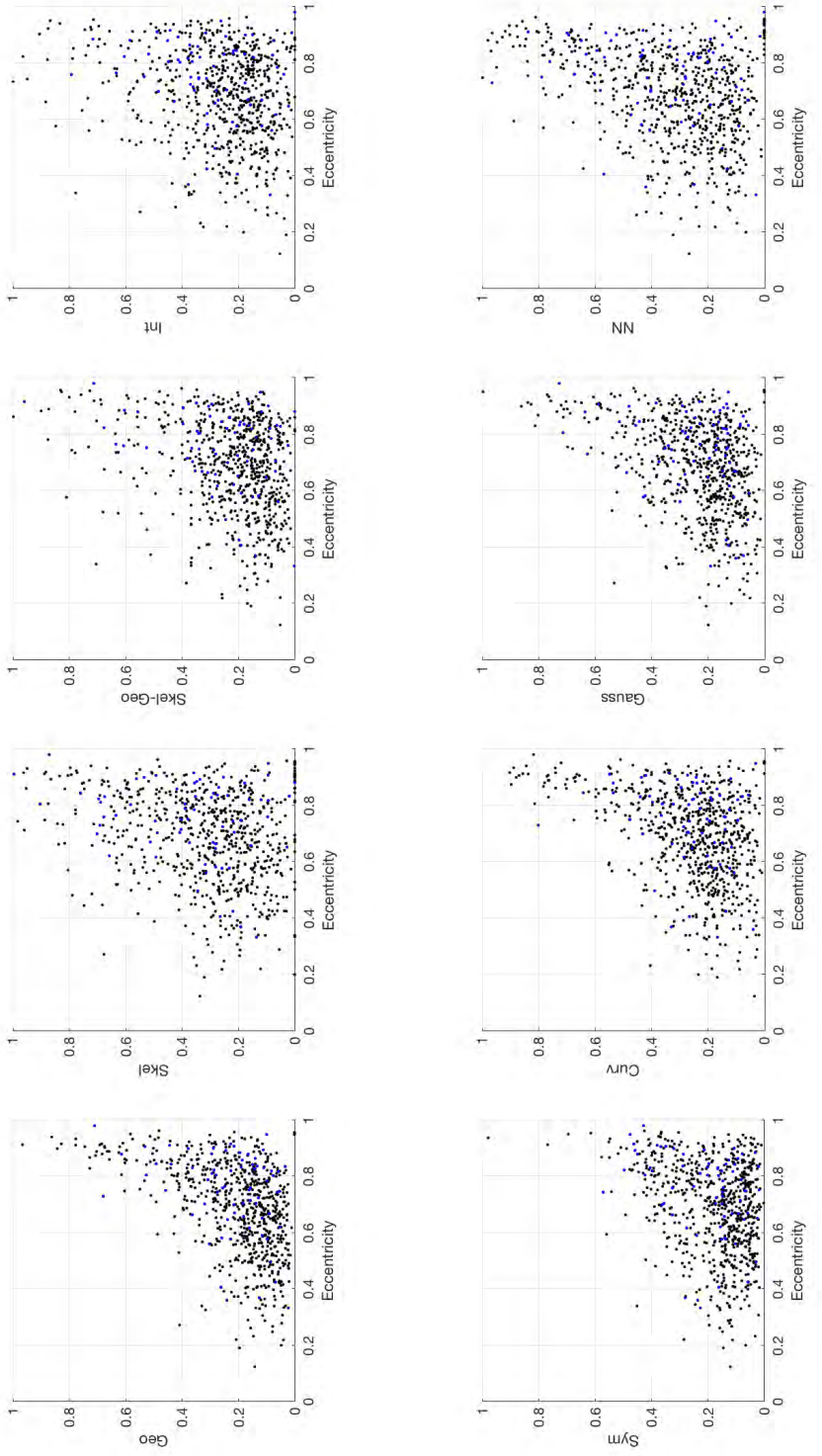


FIGURE 4.21: Distance between the hand assigned centre and the centres assigned using the different methods against the eccentricity of each dendrite. The black circles are the inner dendrites and the blue the edge ones.

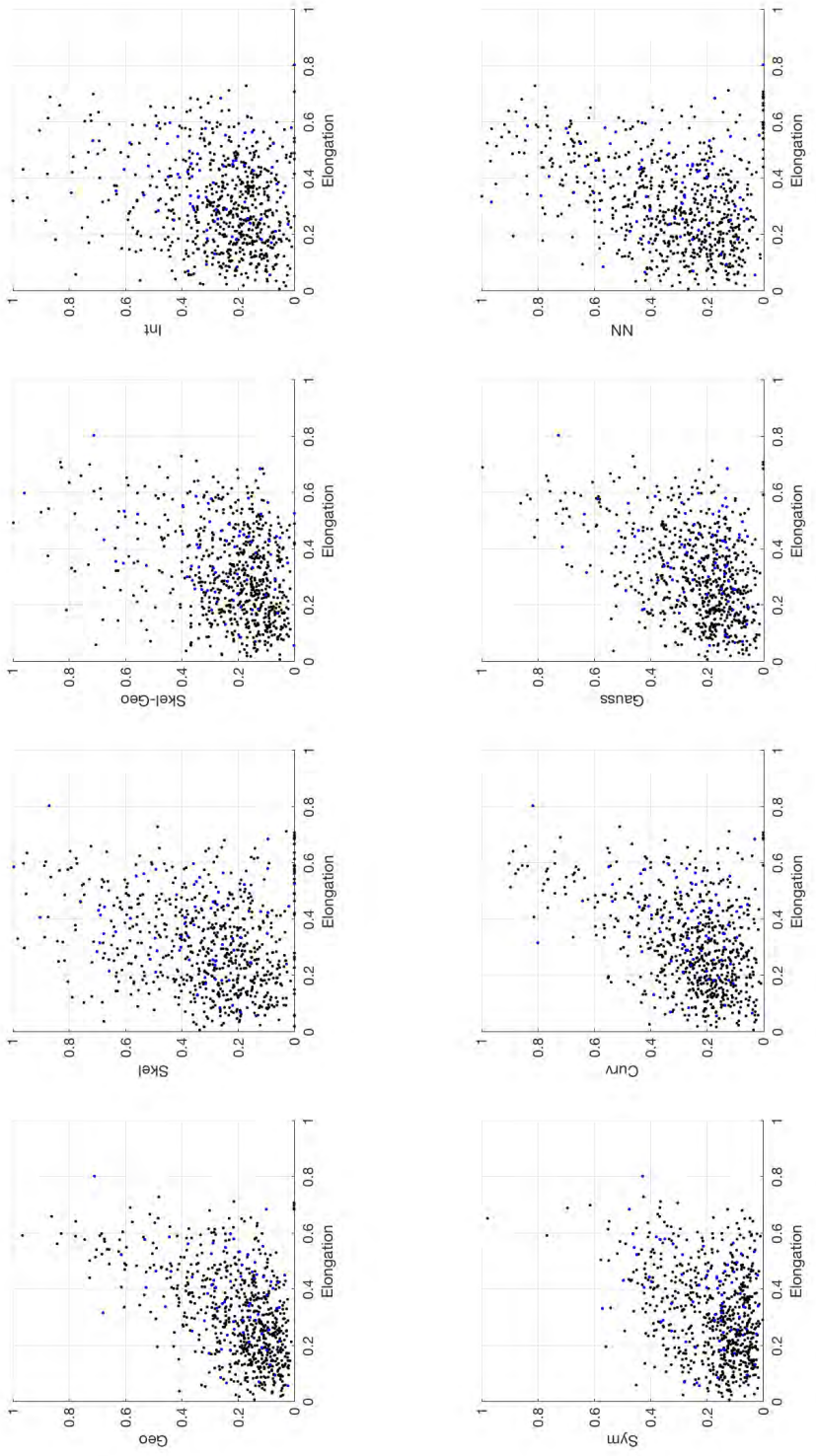


FIGURE 4.22: Distance between the hand assigned centre and the centres assigned using the different methods against the elongation of each dendrite. The black circles are the inner dendrites and the blue the edge ones.

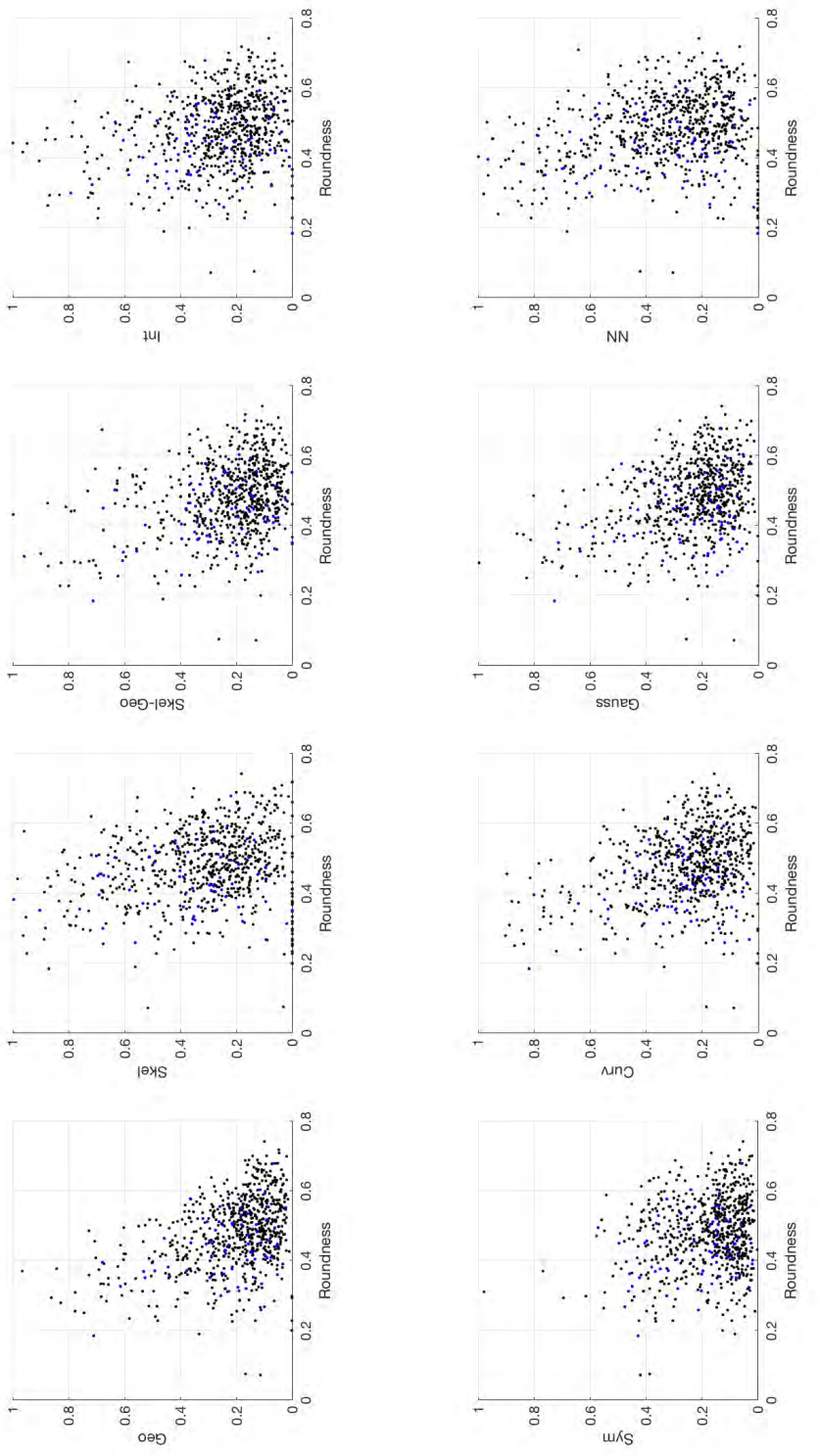


FIGURE 4.23: Distance between the hand assigned centre and the centres assigned using the different methods against the roundness of each dendrite. The black circles are the inner dendrites and the blue the edge ones.

Comparing the results given in Table 4.3 it is clear that the three methods that were the most accurate in finding the centre of the dendrites were–in order of precedence–the symmertry-based feature extraction, centre of geometry, and finally the skeleton-geometry methods. This can be seen quantitatively in Figures 4.16 to 4.23 as in each case these three methods are the methods which show the densest scattering of points for each shape factor. Therefore by extension being the best techniques for this analysis.

The neural network based method whilst novel and initially promising was the worst performing of the eight methods across each of the shape factors. Quantitatively the least dense of each of the plots (Figures 4.16 to 4.23). Further to this as seen in Table 4.3 the **NN** performed badly in each of the statistical measurements for the inner, outer and all the dendrites combined together. The method may have suffered from too small a number of training images or possibly over or under-training. More exploration is needed into how the technique could be used to find the centre of a dendrite.

The three methods identified as the best performing (symmetry-based feature extraction, centre of geometry, skeleton-geometry) will now be trialled on a binarised Al-10 wt% Cu slice created using the scheme set out in Section 4.1.1. This was done to analyse how the more complex geometries of aluminium-copper dendrites cope with the different techniques.

4.2.11 Trialling Methods on a Binarised Al-10 wt% Cu Slice

The three best performing dendrite centre assigning methods–symmetry-based feature extraction, centre of geometry, skeleton-geometry–are used to analyse a single slice of a binarised Al-10 wt% Cu **CT** slice (Figure 4.8). These three methods will be analysed in terms of their accuracy, precision, and the total time taken to

find the centre of each dendrite in the slice. The results of which are given in Table 4.4 and Figure 4.24. The results of the shape factor analysis with the three different methods is given in Figures 4.25 to 4.32. Finally the mean, standard deviation and variance of the shape factors for the aluminium-copper dendrites is given in Table 4.2.

As can be seen by comparing the results for different methods in Table 4.4 and Figure 4.24 the centre of geometry method is the closest to the hand assigned centres, followed by the skeleton-geometry centre and finally the symmetry-based feature extraction method. The centre of geometry being the best method may be as a result of the smaller area of the dendrites in comparison to the Ni-superalloy sample (Table 4.2). As with a smaller area in terms of pixels will mean a smaller number of points that the centre of geometry can be assigned to. Moreover the Al-Cu dendrites are more irregular in almost every measurable way as such the symmetry-based method is likely not to work as well.

As can be seen from Table 4.2 these dendrites are less: round, compact; less likely to be circular (greater value of f_C), and more convex. This can be seen quantitatively by comparing Figure 4.8 with Figure 4.15. In Figure 4.8 the dendrites are much less regular with a higher aspect ratio (Table 4.2), they also show tertiary arm growth. All of these features make a single dendrite less symmetrical, and thus less likely to work with a technique that requires symmetry in order to find the 'true' centre of a dendrite.

In terms of calculation time–using Matlab 2017b and a Windows machine with and intel i5 CPU–the centre of gravity method was also the fastest, taking approximately 20 seconds to calculate all the dendrites in the slice. The skeleton-geometry method finished in 3 minutes. Finally the symmetry-based feature extraction took 32 hours to complete the single slice. This length of time would not be acceptable for scaling up the technique to cover all the slices obtained from a **CT**'d volume

as in this thesis. As a single volume contains approximately 2300 slices this would simply not be acceptable to undertake in any reasonable length of time without serious increases in computational power or parallelisation. Moreover as the technique performed quite badly on the aluminium-copper dendrites as compared to the nickel superalloy ones there is no vast improvement in the dendrite finding technique to warrant such a drastic length of time for this centre finding method.

The skeleton-geometry method whilst performing worse than the centre of geometry method does provide the user with other useful information, such as the skeleton of the dendrite. This skeleton can be used to obtain other information on the dendrite such as orientation (see Section 4.8). As a result, whilst the method is not as precise as the centre of gravity technique it is the method which will be chosen for the analysis of the directionally solidified aluminium-copper rods. Moreover in order to compensate for this inaccuracy along the length of the sample a simple thresholding technique is used and implemented (summarised in Section 4.4) to remove any erroneous points from the data.

4.3 Primary Dendrite Arm Spacing Calculations

There are several different methods found within the literature for the calculation of the **PDAS** [32, 107, 132, 133]. The most common of which is the bulk or average **PDAS** method [31, 32, 107, 132, 133, 155]. This method is simple relying upon only knowing the number of points within a micrograph, N, and also the area, A the analysis has taken place across. c is a parameter dependent on the microstructural packing [107].

$$\lambda_1 = c\sqrt{\frac{A}{N}} \tag{4.12}$$

TABLE 4.4: Table showing the mean, standard deviation and variance values for the scaled distance between the hand assigned centres and the centres assigned by the centre of geometry, skeleton-geometry and symmetry-based methods tested on the Al-10 wt% Cu **CT** slice. Included are subsets of the data containing the values for only the inner or edge dendrites from the microstructures.

Method	**All Dendrites**			**Inner Dendrites**			**Outer Dendrites**		
	$\bar{x}$	$\bar{\sigma}$	Var(x)	$\bar{x}$	$\bar{\sigma}$	Var(x)	$\bar{x}$	$\bar{\sigma}$	Var(x)
Geo	0.2061	0.1400	0.0196	0.2060	0.1400	0.0196	0.2181	0.1497	0.0224
Skel-Geo	0.2917	0.2002	0.0401	0.2912	0.1997	0.0399	0.3382	0.2544	0.0647
Sym	0.3192	0.1783	0.0318	0.3196	0.1785	0.0319	0.2879	0.1707	0.0291

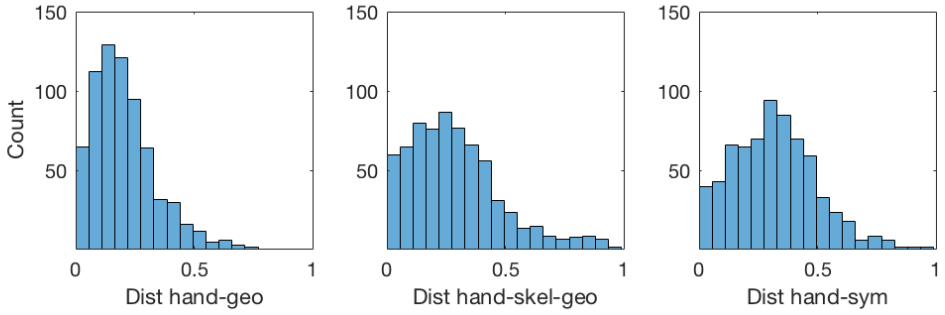


FIGURE 4.24: Histograms of the distances between the three chosen methods and the hand-assigned centre of gravities for the aluminium 10 wt% copper **CT**'d slice shown in Figure 4.8

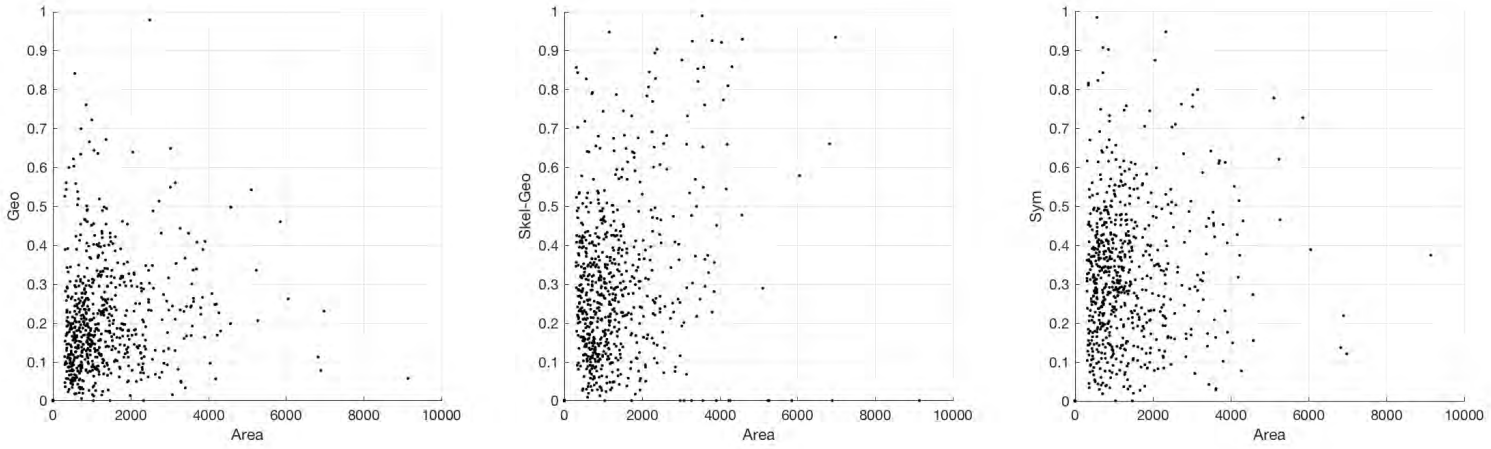


FIGURE 4.25: Distance between the hand assigned centre and the centres assigned using the different methods against the area in pixels of each dendrite for the aluminium-copper **CT**'d slice. The black circles are the inner dendrites and the blue the edge ones.

FIGURE 4.26: Distance between the hand assigned centre and the centres assigned using the different methods against the aspect ratio of each dendrite for the aluminium-copper **CT**'d slice. The black circles are the inner dendrites and the blue the edge ones.

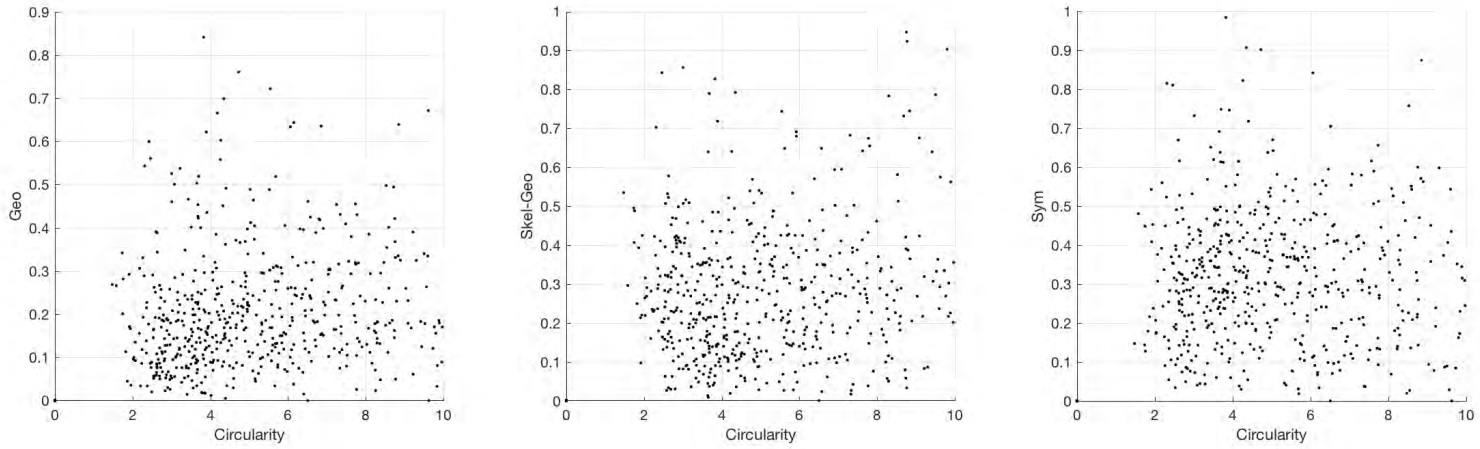


FIGURE 4.27: Distance between the hand assigned centre and the centres assigned using the different methods against the circularity of each dendrite for the aluminium-copper **CT**'d slice. The black circles are the inner dendrites and the blue the edge ones.

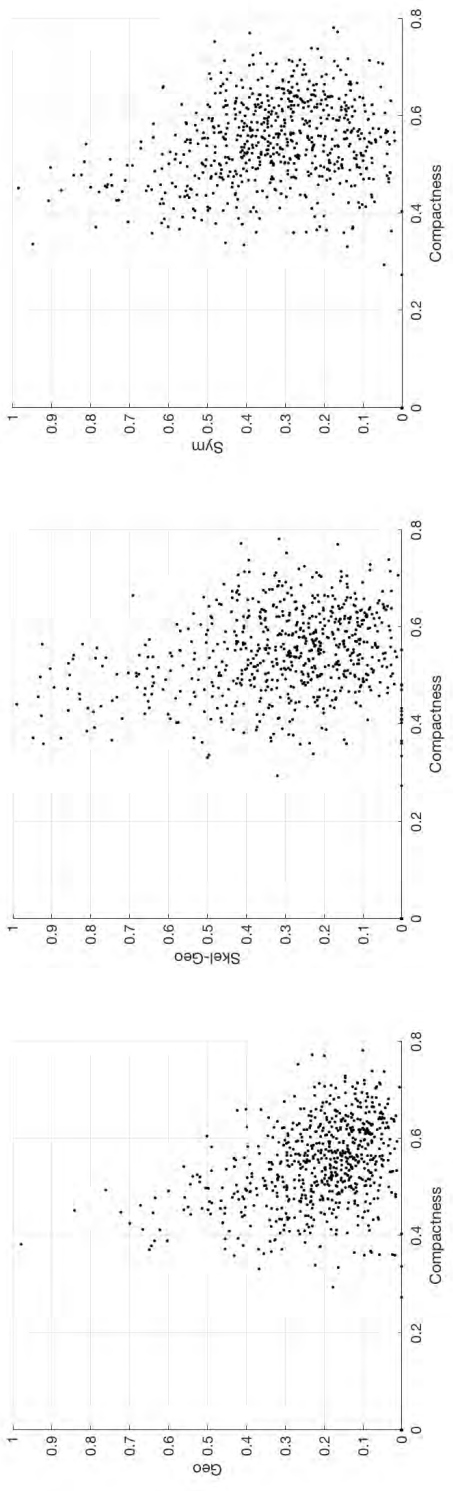


FIGURE 4.28: Distance between the hand assigned centre and the centres assigned using the different methods against the compactness of each dendrite for the aluminium-copper **CT**'d slice. The black circles are the inner dendrites and the blue the edge ones.

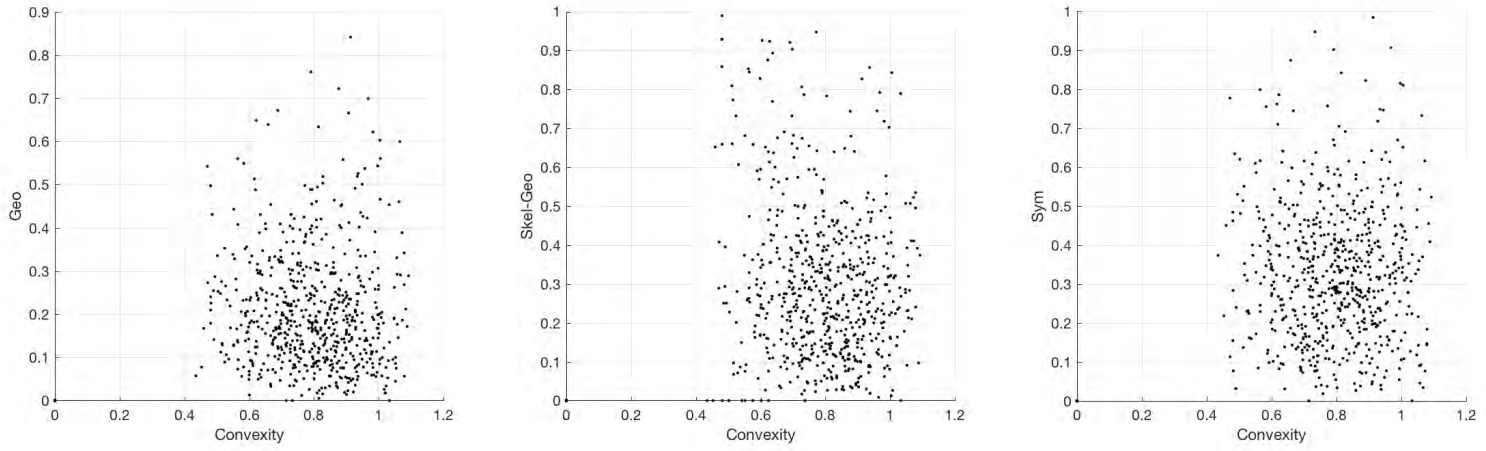


FIGURE 4.29: Distance between the hand assigned centre and the centres assigned using the different methods against the convexity of each dendrite for the aluminium-copper **CT**'d slice. The black circles are the inner dendrites and the blue the edge ones.

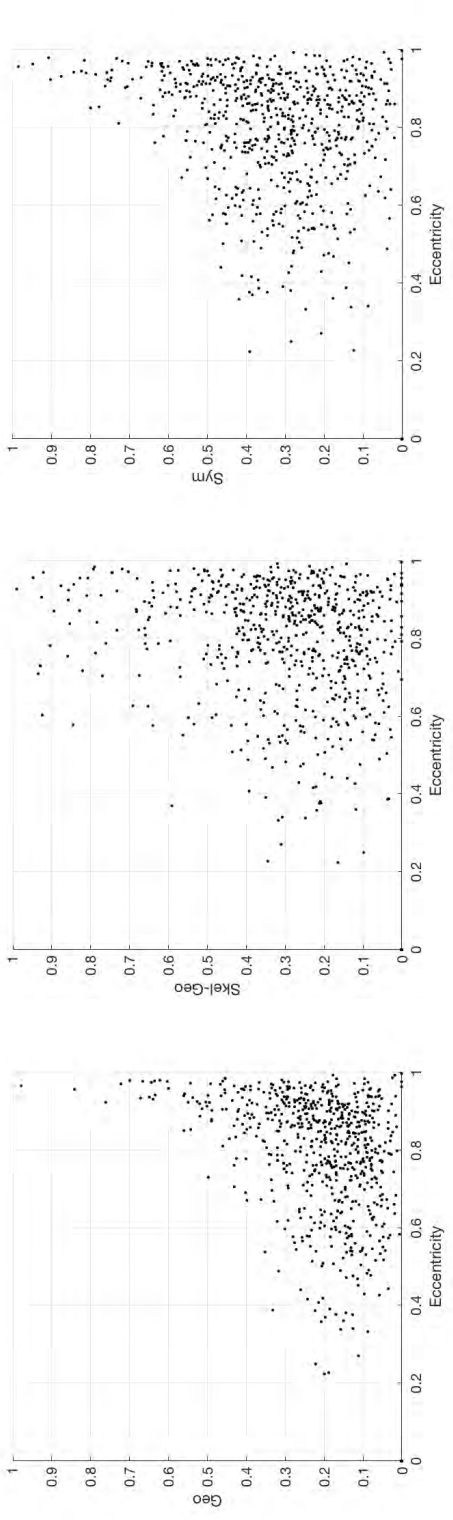


FIGURE 4.30: Distance between the hand assigned centre and the centres assigned using the different methods against the eccentricity of each dendrite for the aluminium-copper **CT**'d slice. The black circles are the inner dendrites and the blue the edge ones.

FIGURE 4.31: Distance between the hand assigned centre and the centres assigned using the different methods against the elongation of each dendrite for the aluminium-copper **CT**'d slice. The black circles are the inner dendrites and the blue the edge ones.

FIGURE 4.32: Distance between the hand assigned centre and the centres assigned using the different methods against the roundness of each dendrite for the aluminium-copper **CT**'d slice. The black circles are the inner dendrites and the blue the edge ones.

There are however some major drawbacks to this calculation. The most obvious of which being that this equation gives an average value rather than a range. This can be compensated by using the analytical expression to estimate the stable minimum and maximum λ_1 [12].

$$\lambda_{min} = \frac{2}{3}\lambda_1 \tag{4.13a}$$

$$\lambda_{max} = \frac{4}{3}\lambda_1 \tag{4.13b}$$

The three values of λ_1, λ_{min} and λ_{max} can be used to produce a standard distribution of all the estimated stable spacings within a microstructure with an average **PDAS** of λ_1. The standard distribution has λ_{min} and λ_{max} at the extremes and λ_1 as the point at the zenith of the distribution.

4.3.1 Minimum Spanning Tree

A minimum spanning tree (**MST**) can be used to calculate the local primary dendrite arm spacing of a point cloud obtained from a dendritic micrograph. This algorithm computes the minimum distance that will connect all the points within the cloud without creating a closed loop [132, 155, 156, 157].

Constructed using Prim's algorithm [157] the **MST** starts at an initial point within the point cloud and 'grows' outwards by connecting the first point to its nearest neighbour. This step is then repeated for the next point and all subsequent points until all of the dendrite centres are joined together in a tree which does not form a closed loop. The average length of all these connecting lines is the **PDAS**. As a result information on local distributions across the sample can be obtained.

One advantage of the **MST** method is that it provides information on the order or disorder of a point cloud and the likely cellular arrangement of the points as shown in Table 4.5 and fig. 4.33. By obtaining the normalised value for the distance between the points using the equation [158]:

$$m^* = \lambda_{MST} \frac{N-1}{\sqrt{NA}} \tag{4.14}$$

Where m^* is the normalised edge length of the minimum-spanning-tree **PDAS** λ_{MST}, N is the number of dendrites and A is the area. The normalised standard distribution σ^* of the set λ_{MST} is given by [158]:

$$\sigma^* = \sigma \frac{N-1}{\sqrt{NA}} \tag{4.15}$$

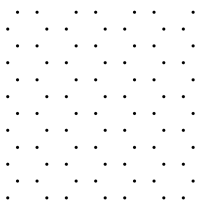
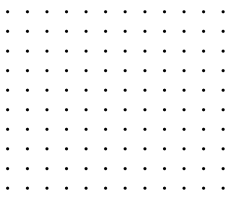
The σ is the standard distribution of λ_{MST}. In both instances the area, A is given by the estimated sample window put forward by Dussert *et al.* [156]:

$$A = \frac{H}{1-(f/N)} \tag{4.16}$$

This formula is best practice when the area of the sampling window is not known [132]. For the calculation of A the convex hull of the point cloud should be taken and its area, H, and number of edges, f, recorded.

One disadvantage of this method however is that it does not give information on the number of nearest neighbours for each of the dendrites analysed. The number of nearest neighbours must be estimated by comparing the m^* value to information taken from Table 4.5 and Figure 4.33 in order to obtain the most likely number of nearest neighbours for a specific distribution.

TABLE 4.5: Normalised average edge lengths, m^*, for select packing orientations.

Packing arrangement		m*
	Random	0.3
	Hexagonal close packed	1.075
	Hexagonal	0.877
	Square	1

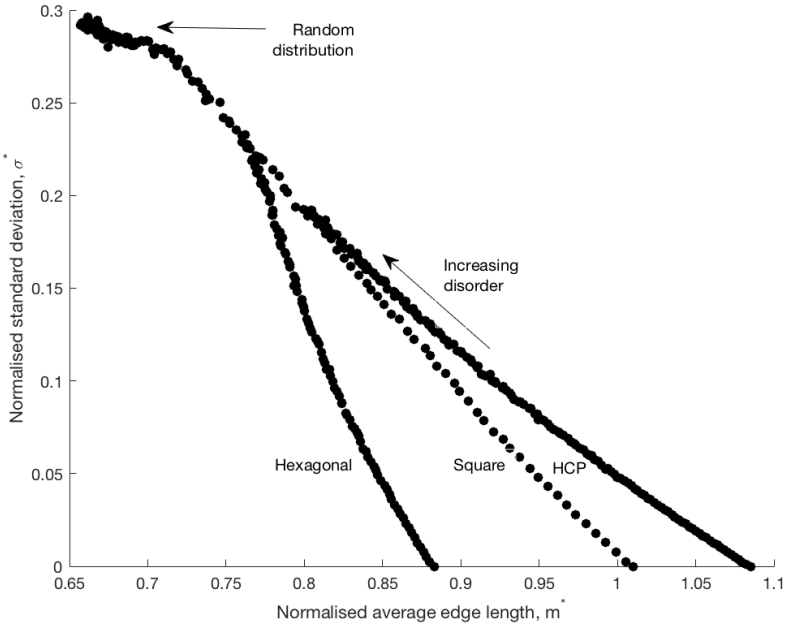


FIGURE 4.33: Comparison of different packing arrangements in Table 4.5 with varying levels of noise added.

4.3.2 Warnken-Reed Primary Dendrite Arm Spacing

The Warnken-Reed method is one that has been introduced within the last five years [107] and hopes to overcome the problems of the the classical method of *PDAS* calculating using equation Equation (4.12). This method has been outlined in much greater detail within the literature [32, 107, 133] and as a result will only briefly be introduced here.

This method takes the input centres and for each one finds the local *PDAS* by averaging the distance of the first three nearest neighbours ($\bar{x}$) and then obtaining the standard deviation of the three parameters (σ_x) and using the parameter α–the value of which is chosen arbitrarily–to create search radius (r) around the original central dendrite using the equation:

$$r = \bar{x} + \alpha\sigma_x \tag{4.17}$$

It is then checked if the fourth nearest dendrite centre is within this search radius. If it is not then the *PDAS* is the original $\bar{x}$ value calculated for the three centres and the number of nearest neighbours is 3. If it is within the search radius then a new average distance $\bar{x}$ is calculated incorporating all four of the distances. Subsequently a new standard deviation σ_x is calculated, after which the fifth nearest centre is checked to see if it falls within this threshold. If it does then the process is repeated until there are no more dendrites within this search radius. See figure Figure 4.34 for a step-by-step of the technique. For the current work α was set to 1.5 as in [32, 107, 133].

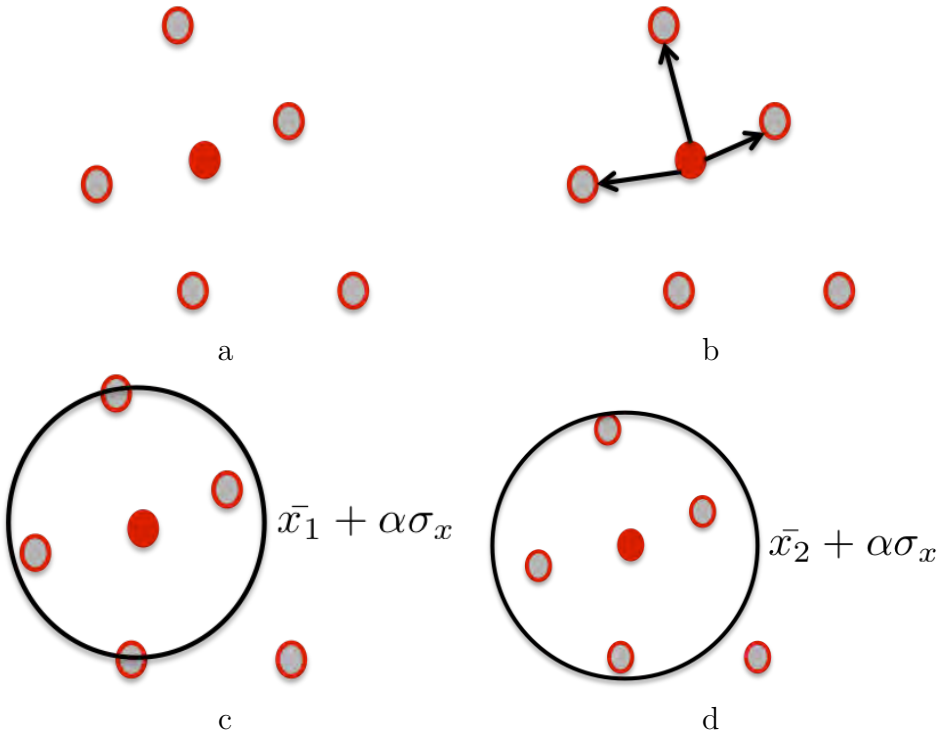


FIGURE 4.34: Step-by-step of the Warnken-Reed *PDAS* assigning technique. a) the dendrite centre to be examined. b) the calculation of the average distance $\bar{x}_1$ using the first three nearest neighbour centres. c) is the checking stage to see if the fourth furthest dendrite centre fits within the threshold distance $\bar{x}_1 + \alpha\sigma_x$. d) as it falls within the search radius a new search radius is created. However the fifth nearest centre does not fit within this search radius and as a result the technique stops here.

4.3.3 Voronoi Primary Dendrite Arm Spacing

The Voronoi method uses Voronoi tessellations–Figure 4.35b–to find the nearest neighbours which are the total number of regions with verticies touching the area containing the dendrite to be analysed. Once these nearest neighbours are found then the average distance between them and the dendrite centre which is being observed is calculated, see Figure 4.35c . This average distance is the local *PDAS* for that point. Each point within the microstructure has a value calculated for it. See Figure 4.35 for a step-by-step of the analysis.

4.3.4 Warnken-Reed-Voronoi Primary Dendrite Arm Spacing

The final method to be tested is the Warnken-Reed-Voronoi method. This technique combines both the Voronoi and Warnken-Reed methods in such a way that only the centres which share edges from the Voronoi tessellation can be used in the Warnken-Reed calculation of the local *PDAS*. This is described graphically in Figure 4.36.

4.3.5 Local PDAS Calculations on Hand-Assigned and Skeleton-Geometry Dendrite Centres

In Section 4.2.11 the skeleton-geometry method was chosen for finding dendrite centres of **CT** volumes. A comparison was needed between the 'perfect' hand-assigned centres and the skeleton-geometry centres to see if there is any change in the calculation of the local **PDAS** using any of the local **PDAS** finding methods in Section 4.3. In order to compare the two methods the local **PDAS** was calculated on the results of Section 4.2.11 taken from the Al-10wt %Cu slice of Figure 4.8.

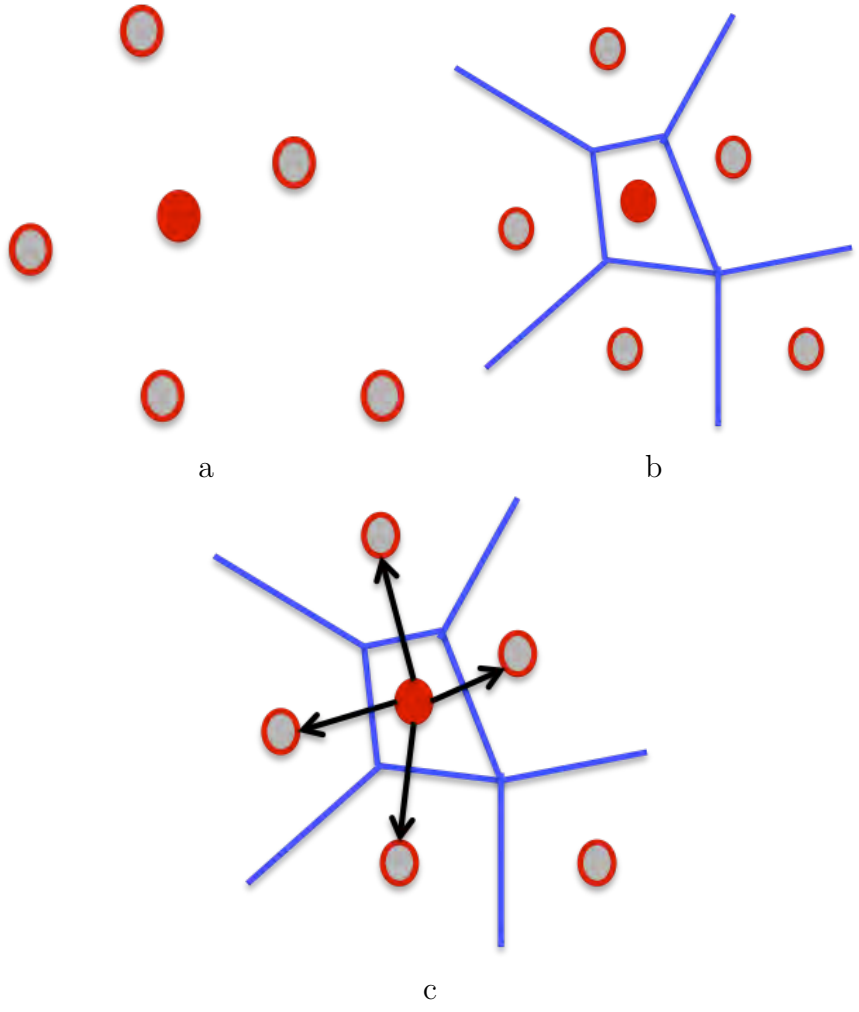


FIGURE 4.35: A step-by-step guide of the Voronoi technique to calculate local *PDAS*. a) is the dendrite centre to be examined and the surrounding microstructure. b) is the Voronoi tessellation. c) shows which other centres would be used to calculate the average distance for the local *PDAS*, i.e. only the ones with touching edges to the tessellation and not those that share vertices.

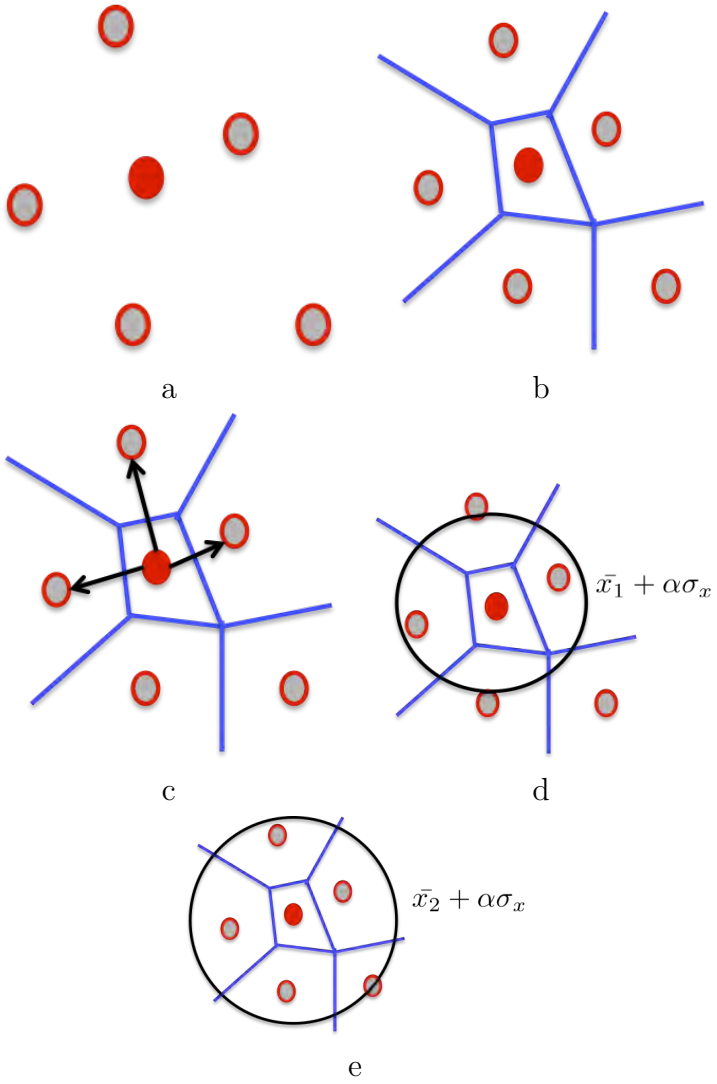


FIGURE 4.36: A step-by-step guide of the Warnken-Reed-Voronoi technique to calculate local *PDAS*. a) is the dendrite centre to be examined and the surrounding microstructure. b) is the Voronoi tessellation. c) is the calculation of the average distance $\bar{x}_1$ using the first three nearest neighbour centres. d) is the checking to see if the fourth furthest dendrite centre fits within the threshold distance $\bar{x}_1 + \alpha\sigma_x$. e) As the fourth value fits within the threshold then it is used to calculate the new search radius $\bar{x}_2 + \alpha\sigma_x$. However even though the fifth nearest point falls within the search radius as it does not share a tessellation edge with the central point being observed–only a vertex–the Warnken-Reed-Voronoi method does not count it. Therefore the *PDAS* is $\bar{x}_1$ and the central point has four nearest neighbours.

A series of histograms, shown in Figures 4.37 to 4.40, were created showing the spread of each of the **PDAS** calculation methods. For ease of comparison the bulk, or average, **PDAS** is superimposed onto these histograms. The average **PDAS** was calculated using Equation (4.12). The number of bins in each histogram of Figures 4.37 to 4.40 was calculated using the Freedman-Diaconis method [159]. The Freedman-Diaconis method calculates the optimal bin number using the inter-quartile range and number of data in the data set [159]. The average **PDAS** of each calculation and the standard deviation is reported in Table 4.6.

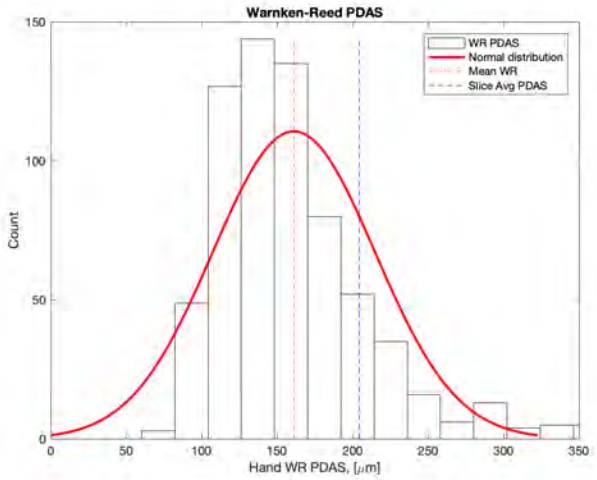
In subfigure c) of Figures 4.37 to 4.40 the percentage error between the calculated local **PDAS** using the different dendrite finding methods. The percentage error was calculated as the difference between the 'perfect' hand-assigned centres and the skeleton-geometry centres. The average percentage error, and the standard deviation is reported in Table 4.7.

As shown in Figures 4.37 to 4.40 and Tables 4.6 and 4.7 there is little difference between the final local **PDAS** calculated when either the hand-assigned or skeleton-geometry centres are used as a starting point. The average percentage error in each instance is less than 0.1 % the 'perfect' hand assigned result (Table 4.7). This equates to an error in each of the local **PDAS** calculation methods of approximately 0.1 - 0.2 μm. This low error was found when comparing all four of the local **PDAS** finding methods (Warnken-Reed, Voronoi, Warnken-Reed-Voronoi and minimum-spanning-tree). This error is below the resolution of the **CT** scanner used in this thesis. The highest available resolution was approximately 2 μm.

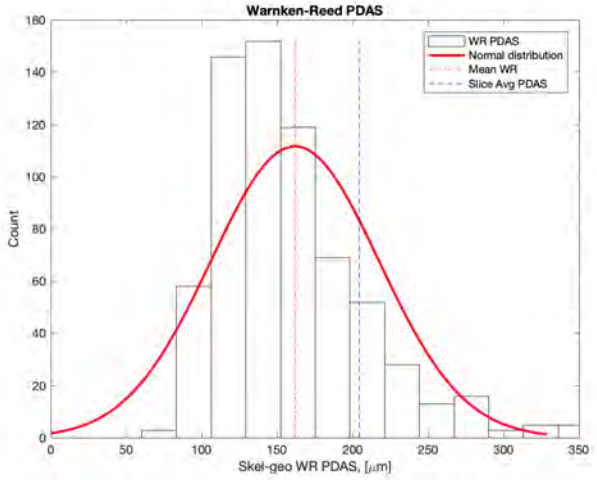
It is clear that whilst there may be a difference in the specific location of specific hand-assigned centres and the skeleton-geometry centres the minor differences in location do not affect the accuracy of the local **PDAS** calculations. Any erroneously assigned centres which could negatively affect the calculation of a local **PDAS** do not. The results in Figures 4.37 to 4.40 and in Tables 4.6 and 4.7 show

that for the calculation of an average local **PDAS** value there is essentially no difference between the 'perfect' hand-assigned centres and the skeleton-geometry centres. Moreover, Figures 4.37 to 4.40 show there is very little change in the spread of the data itself.

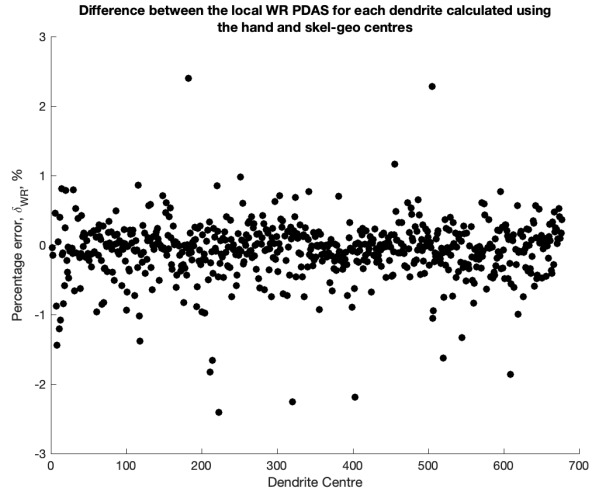
The results of the comparison show that there is little-to-no effect on the local **PDAS** calculated when using either hand-assigned centre or the skeleton-geometry assigned centre. There is only a small percentage error between the two different techniques. This percentage error, approximately 0-2 % (depending upon the method chosen), is well within acceptable experimental error. The calculation of **PDAS** using the skeleton-geometry method provides results which are essentially indistinguishable on a whole slice basis compared to calculating a **PDAS** using centres found by hand. As such, even though the skeleton-geometry method may be less accurate than assigning the centres of a dendrite by hand the time saving obtained by automating the dendrite centre finding process more than makes up for the errors.



a)

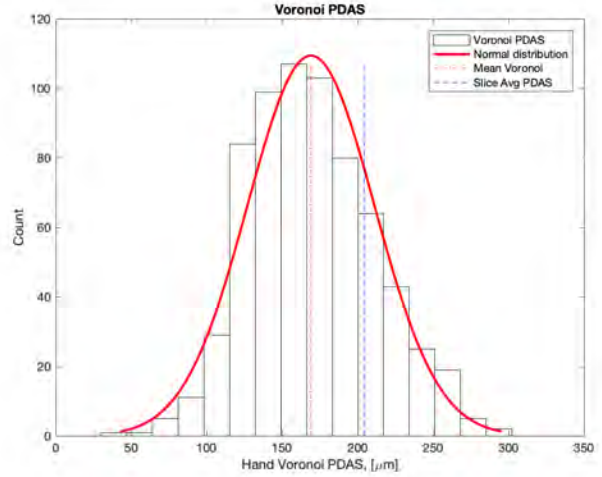


b)

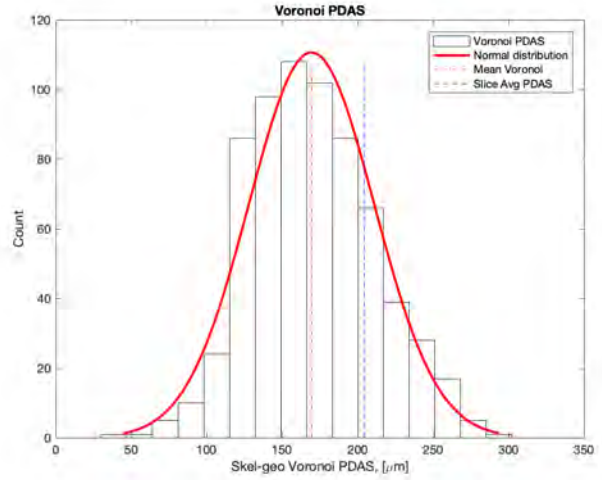


c)

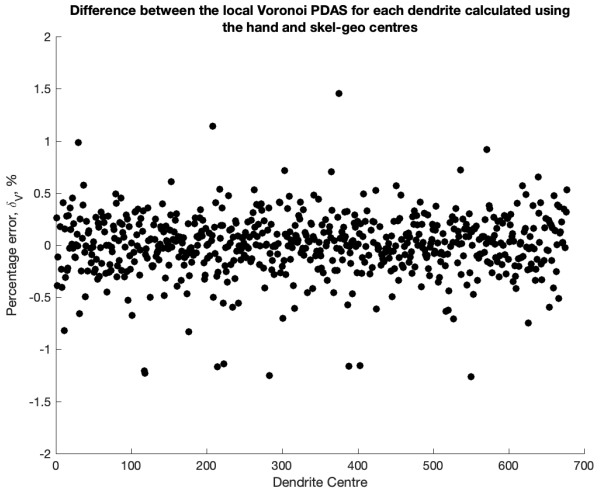
FIGURE 4.37: Histograms showing the a) Warnken-Reed **PDAS** of the hand assigned centres, b) the Warnken-Reed **PDAS** of the skeleton-geometry centres. Figure c) shows the percentage difference between the local PDAS calculated using the hand centres and the local PDAS calculated using the skeleton-geometry centres.



a)

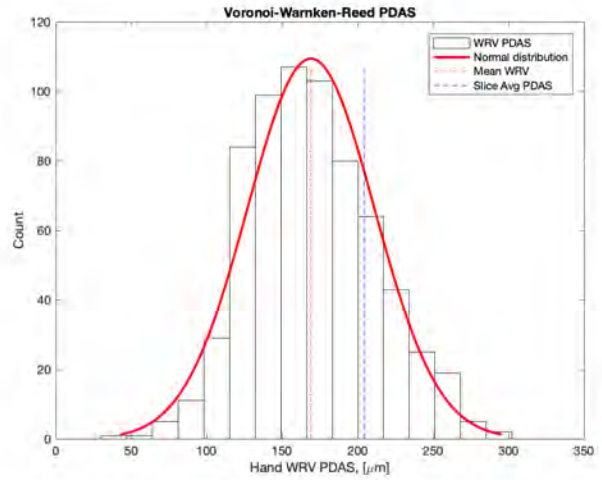


b)

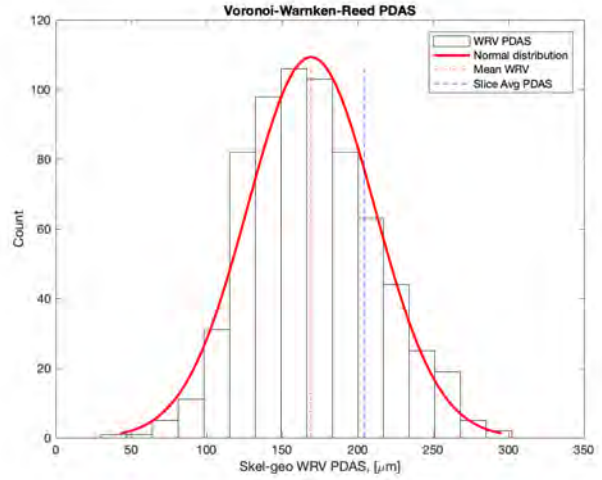


c)

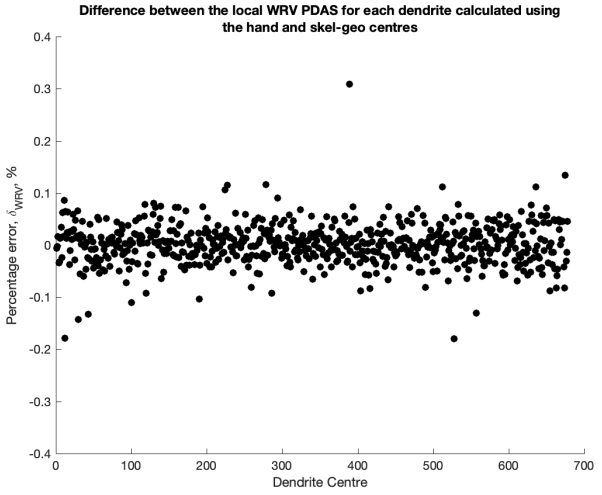
FIGURE 4.38: Histograms showing the a) Voronoi **PDAS** of the hand assigned centres, b) the Voronoi **PDAS** of the skeleton-geometry centres. Figure c) shows the percentage difference between the local PDAS calculated using the hand centres and the local PDAS calculated using the skeleton-geometry centres.



a)

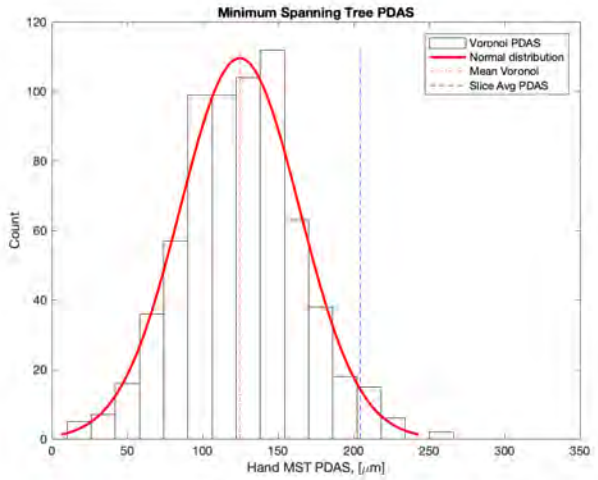


b)

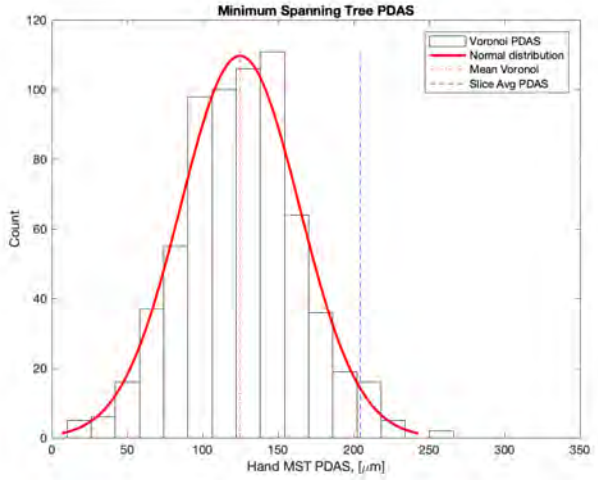


c)

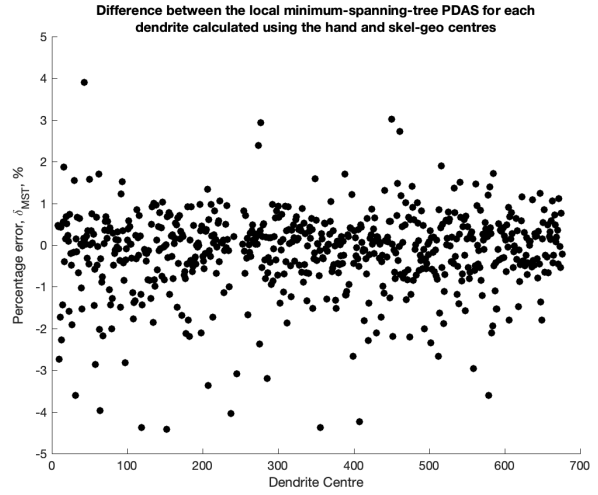
FIGURE 4.39: Histograms showing the a) Warnken-Reed-Voronoi **PDAS** of the hand assigned centres, b) the Warnken-Reed-Voronoi **PDAS** of the skeleton-geometry centres. Figure c) shows the percentage difference between the local PDAS calculated using the hand centres and the local PDAS calculated using the skeleton-geometry centres.



a)



b)



c)

FIGURE 4.40: Histograms showing the a) minimum-spanning-tree **PDAS** of the hand assigned centres, b) the minimum-spanning-tree **PDAS** of the skeleton-geometry centres. Figure c) shows the percentage difference between the local PDAS calculated using the hand centres and the local PDAS calculated using the skeleton-geometry centres.

4.4 Tracking Centres Along the Length of a Sample

After finding the centre of each of the dendrites the result is a three dimensional point cloud. This needs to be sorted to find a continuous line of centres that can be tracked and then subsequently analysed further.

This is achieved by a threshold based method on a layer by layer basis. By assigning a search radius ($0.1\lambda_1$ calculated using Equation (6.1)) around a single dendrite centre from slice 1 and then overlaying slice 2 on top it is easy to find which dendrite centres within the next slice fall into this threshold region using simple arithmetic. This process is then repeated for each newly assigned centre until there are no more slices to compare, or until there are no further points which fall into this threshold within a distance of approximately one secondary arm spacing in height. This is described graphically in Figure 4.41.

Repeating this for every point on the bottom slice leads to a 3-dimensional series of points that track the centres of the dendrites through the sample, and can be used to give information on changes in orientation or where they initiate or terminate.

As the initiation of new dendrites may occur during the solidification it is important to find where these occur and track them. This can be achieved by comparing an array containing all of the initial points in 3-dimensions with those that have been output from the centre tracking function. As a result these points can be compared themselves using the same method as outlined above and the new traces of the dendrite centres can be obtained.

TABLE 4.6: Comparison of the local **PDAS** calculation methods undertaken on the 'perfect' hand-assigned centres and the skeleton-geometry centres obtained from Figure 4.8. The statistics in this table are taken from Figures 4.37 to 4.40 a) and b).

	Warnken-Reed		**Voronoi**		**WRV**		**MST**	
	hand	skel-geo	hand	skel-geo	hand	skel-geo	hand	skel-geo
$\bar{\lambda}$, μm	161.03	161.72	169.01	169.41	169.72	169.12	124.56	124.67
σ,μm	53.80	55.66	42.01	41.48	42.01	42.05	39.45	39.33

TABLE 4.7: Statistics for percentage error, δ between the hand and skeleton-geometry local **PDAS** calculations. The local **PDAS** calculation methods undertaken on the 'perfect' hand-assigned centres and the skeleton-geometry centres obtained from Figure 4.8. The statistics in this table are taken from Figures 4.37 to 4.40 c).

	Warnken-Reed	**Voronoi**	**WRV**	**MST**
$\bar{\delta_\lambda}$, %	0.018	0.051	0.0050	0.046
σ, %	0.79	0.45	0.035	1.400

4.5 Finding Initiation and Termination of Dendrites

It is important to locate the positions of newly initiated dendrites, or locations in the array where dendrites have been outcompeted. This can be achieved via an extension of the methods disclosed in Section 4.4. As the entire length of a tracked dendrite can be traced along the length of the sample from the bottom of the **CT** volume to the top (or where it is outcompeted) it is fairly trivial to locate where new dendrites are stabilised or outcompeted. The location of outcompeted dendrites can be found by locating the ends of the joined dendrite centres which are below the top of the sample. This end point corresponds to the top of the dendrite itself and the point at which it was outcompeted.

Finding points where new dendrites are initiated can occur in one of two ways: either a new unjoined centre line appears within the array and is unconnected to anything else (this corresponding to the nucleation of a new unconnected dendrite); or points where two centre lines intersect are found. This intersection of two lines corresponds to points at which the 'parent' dendrite branches by means of a tertiary arm stabilisation as detailed in Section 2.5.3.

The location of these initiations and terminations is mapped in three dimensions so that the locations of these points can be obtained. Furthermore the cumulative number of them can be calculated along the length of the sample.

4.6 Finding Misorientation of Dendrites

The tracking of dendrite trunks (as described above in Sections 4.4 and 4.5) allows for the calculation of each dendrites misorientation to the Z-axis ([001]). The calculation of the misorientation can be obtained by trivial vector algebra.

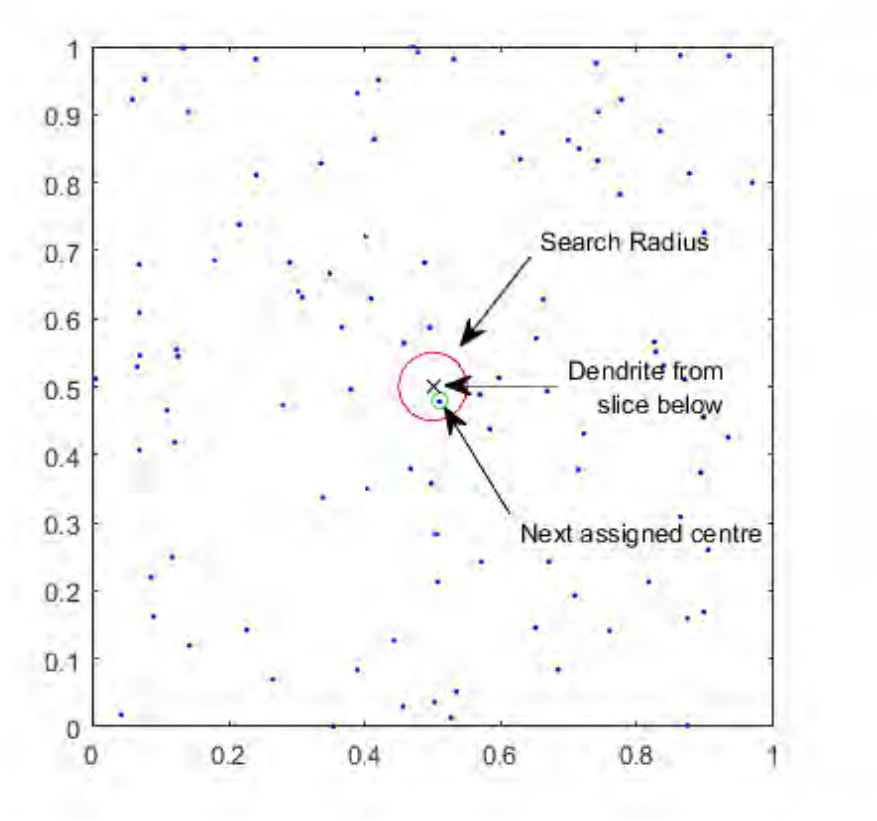


FIGURE 4.41: The distance search method of tracking the dendrite centres between slices. Method shown on a random data set of points.

As a 3D dendrite trunk trace is obtained this can be converted into a 3D vector. The dot product of the 3D vector and the Z-axis can then be used to find the orientation of the 3D dendrite vector. Further, the method can be used to calculate the misorientation of both the dendrites which are outcompeted and also new dendrites which are created. Comparisons of both the newly created dendrites and those outcompeted can then be produced. Such comparisons can be used to see what effect misorentation has on the outcompeted dendrites. It can also show if newly formed dendrites take on the orientation of their parent's.

4.7 3D Isosurface of Individual Dendrites

By binarising the stack of computerised tomography data as described in Figure 4.1 the individual dendrites can then be extracted and analysed individually. This is achieved by 're-stacking' the binary images into a 3-dimensional image stack. Next the binary stack is analysed to find all of the individual dendrites in the image stack. The dendrites can be easily found as they are the connected components within the data. An isosurface plot can thus be easily obtained by finding the surface of the individual dendrite.

An isosuface of the dendrite interface can be plotted for each of these unconnected dendrites. Subsequent smoothing of the voxels removes any errors from the original image analysis. Finally the centre lines obtained in Section 4.4 can be overlain on them to show the route the three dimensional tracking of the centres along the dendrite. A built up 3D image of a dendrite is thus produced.

4.8 Grain Orientation Finding From Optical Images

Electron Back Scattered or *EBSD* mapping is an extremely useful technique in a metallurgists arsenal to find the crystallographic orientation of a metal sample. By categorising the diffracted electron pattern when an electron beam interacts with the surface of a sample information on surface microstructure can be obtained. The pattern, which is characteristic of the crystal structure gives information on grain orientation; phases; grain boundaries; and the morphology of grains, which it does very successfully [137, 138, 139, 140, 141, 142].

However, the technique can be time consuming. Production of detailed mappings often takes hours, and can be very costly with the use of highly specialised apparatus required. There is also a limit to the size of the samples that can fit into the vacuum chamber of the machine which can be a limiting factor for analysis of very large samples. Unlike *EBSD* equipment however, optical microscopes are very common; simple to use; and can be found in almost every metallography lab. As a result a method that can analyse the texture of a metallographic sample using optical means would be very attractive, both in terms of cost savings and for ease of use.

Optical methods like this have become more prevalent within the literature such as directional reflectance microscopy (*DRM*) [139]. This technique should allow for large scale orientation mapping in less time (as compared to *EBSD*) by analysing the refraction of light across a polished sample at different angles. However this method and others like it are let down by the resolution that they can achieve. *EBSD* on the other hand can achieve much finer resolutions. In many instances high resolution is not required and the associated time cost brought about by it is not necessary. For example examining the surface of a sample with a course grain

structure there is no inherent advantage to finer resolution images if the grain structure is many orders of magnitude greater than the *EBSD* beam size.

Therefore the author would like to put forward two methods utilising optical microscopy and new image analysis methods to characterise surface orientation. The techniques outlined below are used to find the orientation of microstructural features such as a dendrite. Once the orientation of the dendrites within the image are obtained they are processed and subsequently assigned grains in a similar fashion to an *EBSD* measurement. The only difference between the two methods is the input. The first technique uses a binarised picture of a dendrite and the second finds the medial transform (or skeleton) first. Both techniques use a Gaussian filter to smooth the interface between the region of interest (the dendrite) and the background. By smoothing and calculating the divergence in the x and y for each pixel in the image dependent upon its intensity an angle between this vector and the horizontal can be obtained. Once these values are all sorted the orientation of the microstructural feature becomes prevalent.

4.8.1 Grain Orientation Finding Method

The sample was polished using standard metallography preparation techniques. Subsequently back-scatter electron microscopy was employed to reveal the dendritic structure. The microstructural images were then stitched and traced giving the input to the analysis. In order to obtain the orientation of an input shape a series of processes–outlined below in figure Figure 4.42–should be followed, each of these steps will be outlined subsequently in more detail.

Prior to any further image analysis taking place the input microstructure picture must be binarised with the region of interest being the foreground. This was achieved by tracing the dendrites obtained from the back-scattered images.

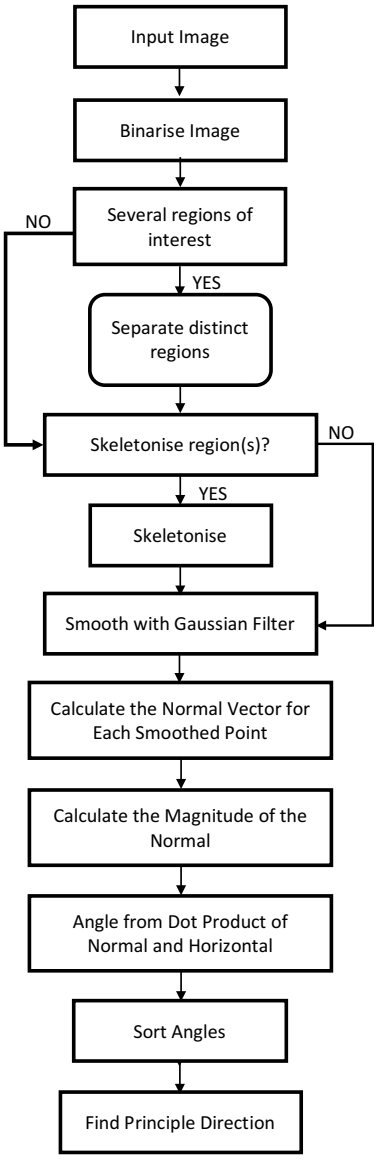


FIGURE 4.42: Process flow chart for finding the orientation of an input shape or dendrite.

Subsequently by using a two dimensional Gaussian distribution (equation Equation (4.18)) the transformation of each pixel with respect to its surroundings can be calculated. By smoothing out any local inhomogeneities along the perimeter of the dendrite to be analysed it reduces any associated errors that can be passed forward in the method.

$$G(x,y) = \frac{1}{2\pi\sigma^2} e^{\frac{x^2+y^2}{2\sigma^2}} \tag{4.18}$$

Where: G is the distribution as a function of the position. By smoothing the perimeter of the shape a normal vector can be calculated at each pixel across the interface. Without first smoothing the interface there is a tendency to assign the principle direction as 0, 90, 180, or 270. This incorrect result is due to the sharp interface between the background and foreground along the perimeter of the dendrite.

The divergence of each pixel must then be calculated in two dimensions in order to find the orientation of the dendrite. The u and v components of the normal vector $\begin{bmatrix} u \\ v \end{bmatrix}$ are found at every point within the image, *i.e.* for each pixel using Equation (4.19b) and the intensities of the surrounding pixels (ϕ).

$$u_{i,j} = \frac{d\phi_{i,j}}{dx} = \frac{\phi_{i+1,j} - \phi_{i-1,j}}{2a} \tag{4.19a}$$

$$v_{i,j} = \frac{d\phi_{i,j}}{dy} = \frac{\phi_{i,j+1} - \phi_{i,j-1}}{2a} \tag{4.19b}$$

Therefore the magnitude of the normal can be easily obtained using the formula:

$$r_{i,j} = \sqrt{u_{i,j}^2 + v_{i,j}^2} \tag{4.20}$$

Subsequently using the dot product between the normal vector and the horizontal, $\begin{bmatrix}1\\0\end{bmatrix}$:

$$\begin{bmatrix}u_{i,j}\\v_{i,j}\end{bmatrix} \cdot \begin{bmatrix}1\\0\end{bmatrix} = r * \begin{bmatrix}1\\0\end{bmatrix} \cos\theta \tag{4.21}$$

Which can be simplified to the following equation for θ giving the angle between the normal vector and horizontal:

$$\theta_{i,j} = \cos^{-1}\left(\frac{u_{i,j}}{r}\right) \tag{4.22}$$

All of the resulting angles calculated using equation Equation (4.22) are then sorted using a polar histogram. Thus the largest bin and therefore the principle angle can be obtained easily. The other three principle angles can be found simply by finding the other three peaks in the polar histogram. This algorithm uses the example of four-sided dendrites–common in aluminium or nickel alloys–however it could be easily altered to analyse dendritic microstructures with six-fold symmetry, for example in magnesium based alloys.

Once the four (or more) principle angles are obtained for each dendrite they are normalised into the range of 0 to 90° by subtracting 0, 90, 180, or 270° from them if the angle lies in the ranges 1-90°, 91-180°, 181-270°, 271-360° respectively.

Next a density-based spacial clustering (*DBSCAN*) is used to separate the different values into discrete clusters based upon each dendrites set of four angles. Points that are not within these clusters are assumed to be anomalies or noise [160]. The cluster number is then assigned to each dendrite separating them into one of distinct categories obtained from the *DBSCAN* algorithm, which are equivalent to grains.

4.8.2 Skeletonisation

A second method has been put forward involving skeletonising the image. The method reduces the input data down into a simpler and more manageable form. This skeleton is the thinest version of a shape described by a line whereby each point is equidistant to the boundary of the original shape. The skeleton serves as a representation of the original microstructural feature, which contains all the necessary information required to reconstruct it if dilated. As a regular dendrite has a rotational symmetry of approximately four, the skeleton will take the form of a cross with the intersection of the two lines near the 'centre' of the dendrite. This is then input into the the following parts of the algorithm described in Figure 4.42. This adapted method was developed to overcome errors that are sometimes present when using the whole shape of the dendrite itself. More detail of skeletonisation and other morphological techniques can be obtained in Gonzalez and Woods [126]. The algorithm used in this study was the native MATLAB 2016b function.

4.8.3 EBSD measurements

To compare the analysis method to *EBSD* maps of the polycrystalline nickel superalloy were made using Philips XL-30 (LaB6) fitted with a HKL *EBSD* system. The maps were stitched together using the Tango image manipulation software produced by Oxford Instruments.

4.8.4 Results of the Grain Orientation Technique

Both analysis techniques were trialled on a number of test cases Figures 4.43 to 4.47. These test cases compromise three different sets: the first a simple 2-d shape (Figure 4.43); the second a number of binary dendrites extracted from a Ni-superalloy microstructure (Figures 4.44 and 4.45); and finally two whole

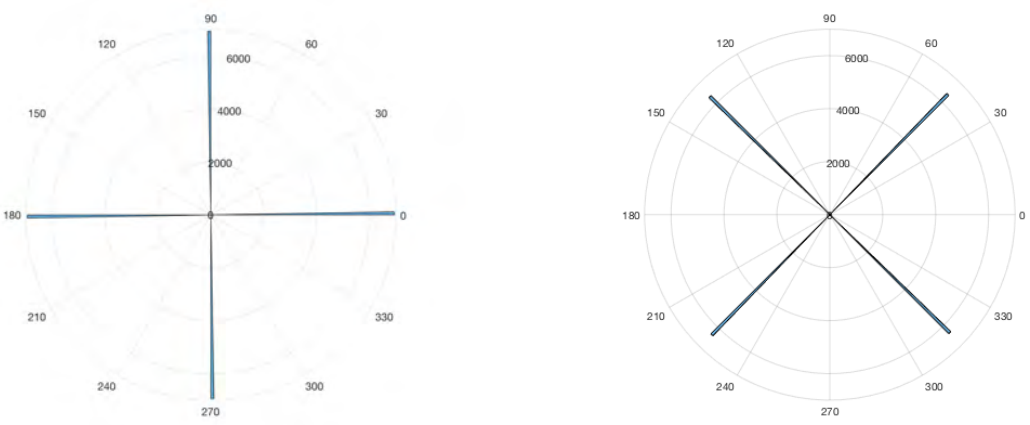
microstructural images, one which is a single crystal and the other polycrystalline (Figures 4.46 and 4.47 respectively).

The results for the idealised square are given in Figure 4.43 for both the skeletonised image and the non-skeletonised image. There is obvious symmetry to the polar histograms which stems from the nature of the input image. The square has four-folded symmetry and as a result the polar histogram reflects that. There is no primary orientation to the square due to it having four equal and possible principle orientationsFigure 4.43 and table 4.8. The shape is rotationally symmetrical with four angles output which are all 90° out of phase (Table 4.8).

The analysis for the two example dendrites are given in Figures 4.44 and 4.45. The orientations of each of these dendrites has been successfully found (Figure 4.44(b), Figure 4.45(b), and Table 4.8). In both cases there the angles are approximately 90° out of phase (Table 4.8).

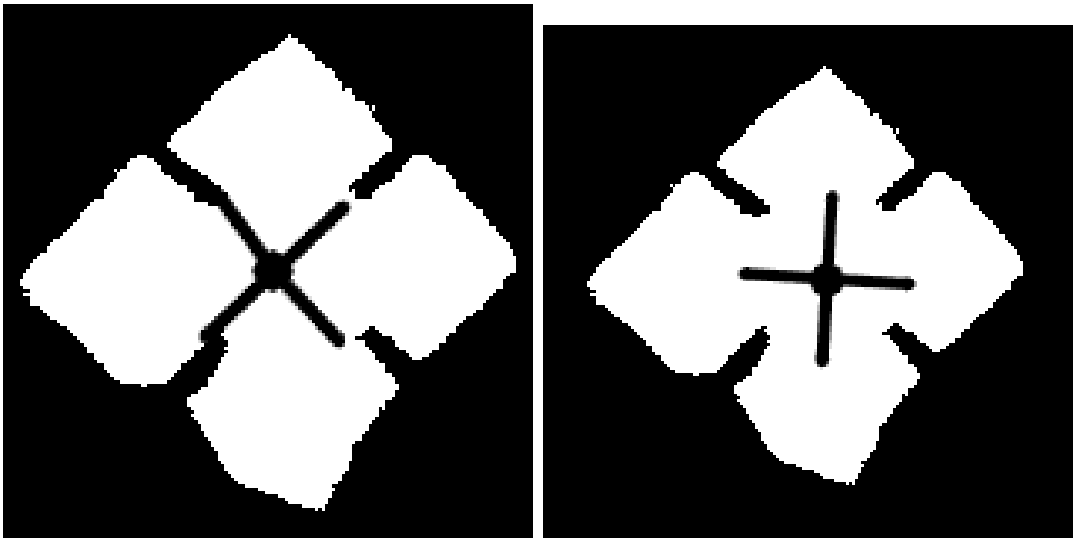


ai aii

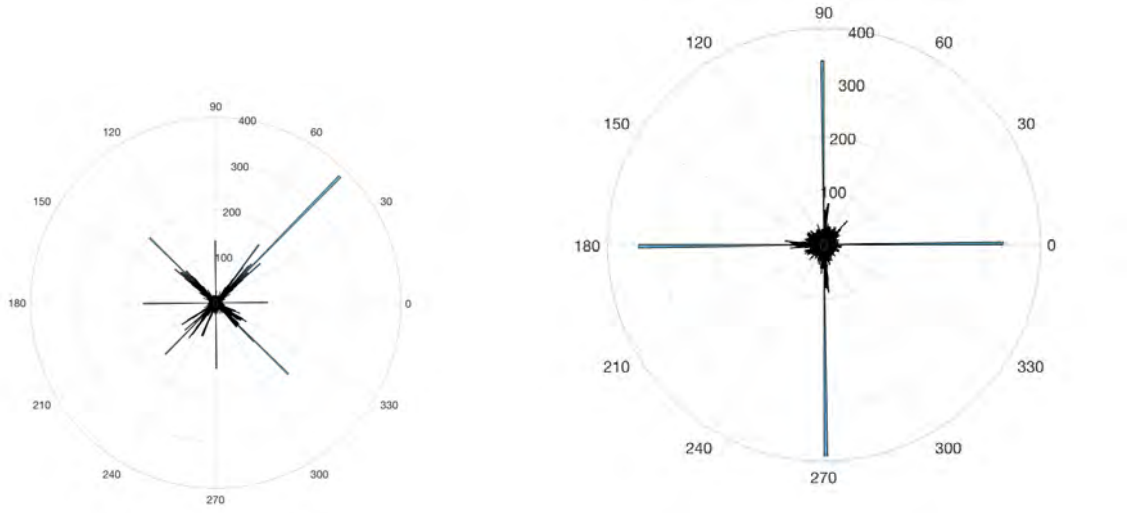


bi bii

FIGURE 4.43: ai) Square with its four principle directions overlain, with no skeletonisation. bi) The four principle angles of the square test shape which are shown in ai. aii) Square with its four principle directions overlain, with skeletonisation. bii) The four principle angles of the square test shape which are shown in aii.

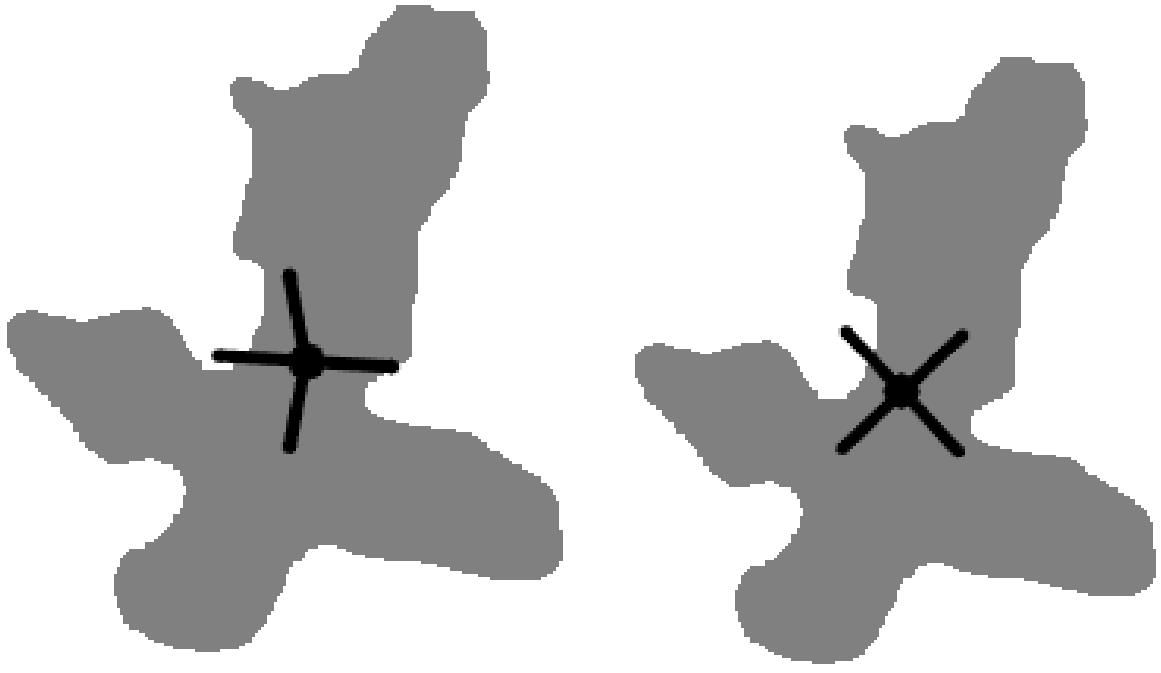


ai aii

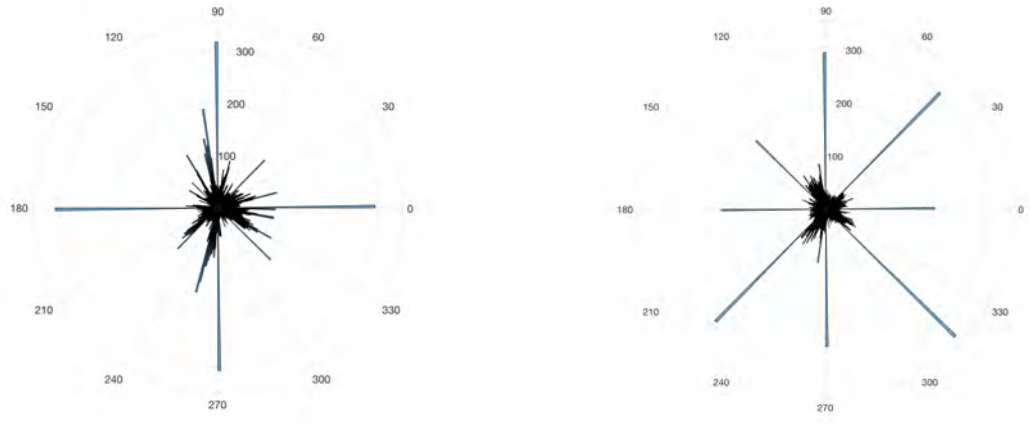


bi bii

FIGURE 4.44: ai) Dendrite 1 with its four principle directions overlain, with no skeletonisation. bi) The four principle angles of the dendrite test shape which are shown in ai. aii) Dendrite 1 with its four principle directions overlain, with skeletonisation. bii) The four principle angles of the square test shape which are shown in aii.



ai aii



bi bii

FIGURE 4.45: ai) Dendrite 2 with its four principle directions overlain, with no skeletonisation. bi) The four principle angles of the dendrite test shape which are shown in ai. aii) Dendrite 2 with its four principle directions overlain, with skeletonisation. bii) The four principle angles of the square test shape which are shown in aii.

Shape	Principle Angles [°]	Principle Angles, with Skeleton [°]
Square	0, 90, 180, 270	45, 135, 225, 315
Dendrite 1	90, 180, 265, 328	90, 182, 262, 327
Dendrite 2	0, 90, 179, 270	46, 138, 228, 316

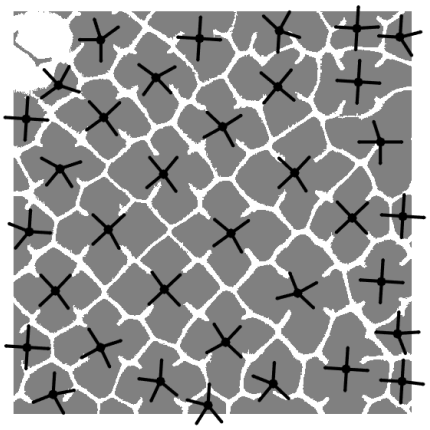
TABLE 4.8: Principle orientation of test shapes, without and with skeletonisation included

The whole microstructural images are presented in Figure 4.46 and Figure 4.47 for both single crystal sample (Figure 4.46) and polycrystalline samples (Figure 4.47). The images show the orientation of each of the dendrites with respect to the horizontal in degrees. Figure 4.46 show that the technique including the skeletonisation (Figure 4.46aii) step produces a much more uniform analysis of the sample when compared with the method not involving it (Figure 4.46ai). Moreover this can be seen in comparing the *DBSCAN* given in Figure 4.47b and c, and Figure 4.46b and c. The colour gives the assigned grain of each point, in Figure 4.46b and c there are only two grains either grain 1 or an anomaly, *i.e.* a point which has been incorrectly sorted. The polycrystalline sample was sorted into two separate grains with several instances of anomalies present on the edge of the image (Figure 4.47b and c).

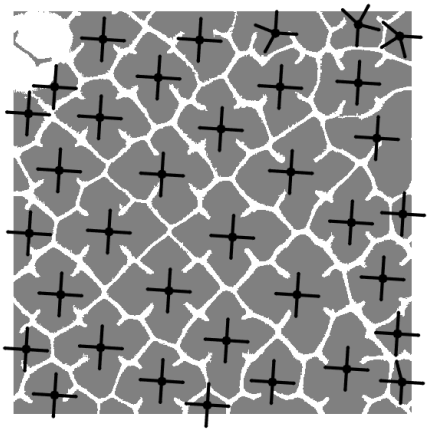
An **EBSD** map of the polycrystalline nickel superalloy shows that there were two different grains present within the microstructure (Figure 4.48). The **EBSD** map was overlain on the microstructural trace of the back scattered nickel superalloy sample (Figure 4.48b and Figure 4.47c) for ease of comparison of the two methods.

4.8.5 Analysis of the Grain Orientation Method

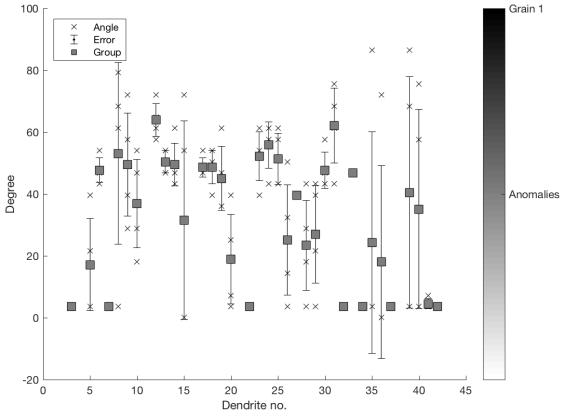
The four-fold symmetry of the square is reflected in the results of the analysis given in Figure 4.43 and Table 4.8. The angles obtained via the orientation method have 90° between them which is true for both techniques. The only difference is that the principle angles are rotated by approximately 45° using the skeletonisation



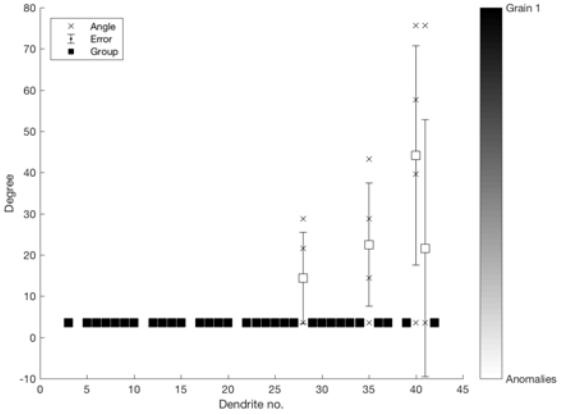
ai



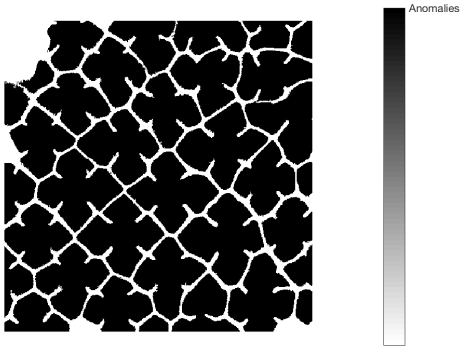
aii



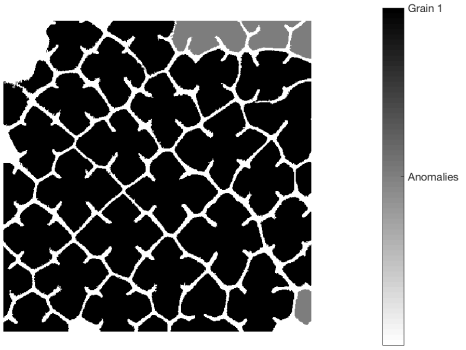
bi



bii

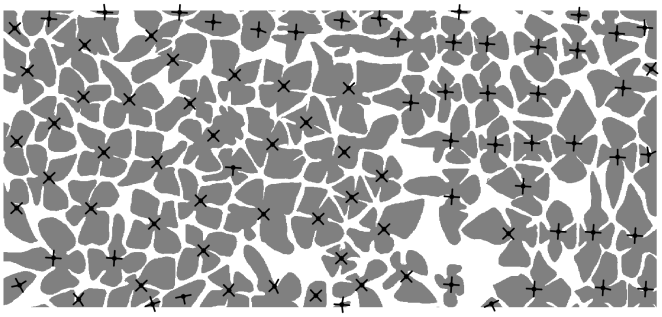


ci

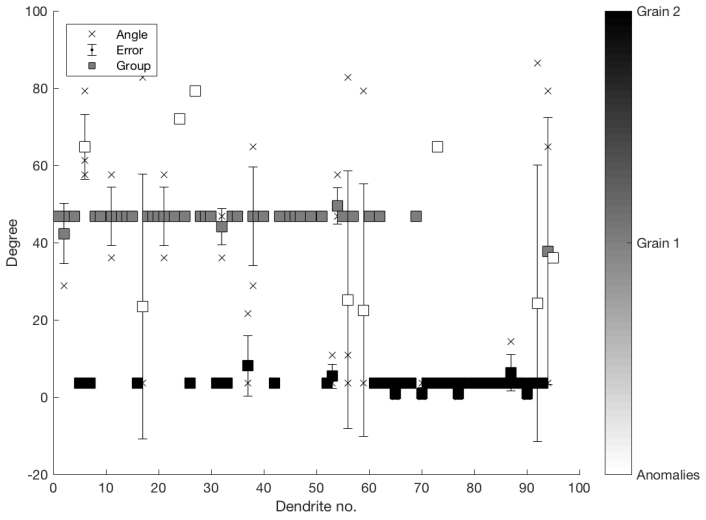


cii

FIGURE 4.46: ai and aii give the result of the technique without and with skeletonisation respectively on the microstructure. bi and bii show the DBSCAN sorting without and with the skeletonisatoin. ci and cii show the resulting sorted grain structure without and with the skeletonisation.



a

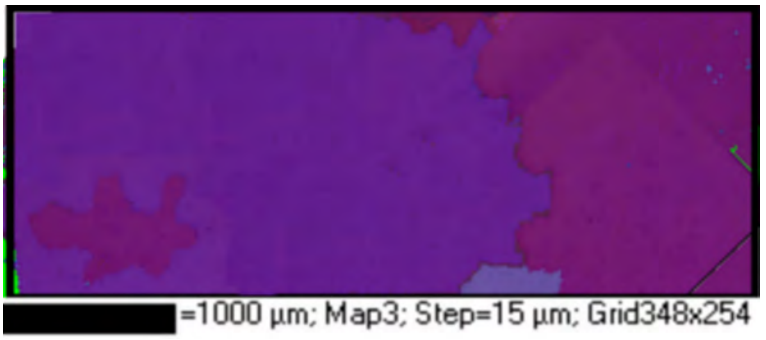


b

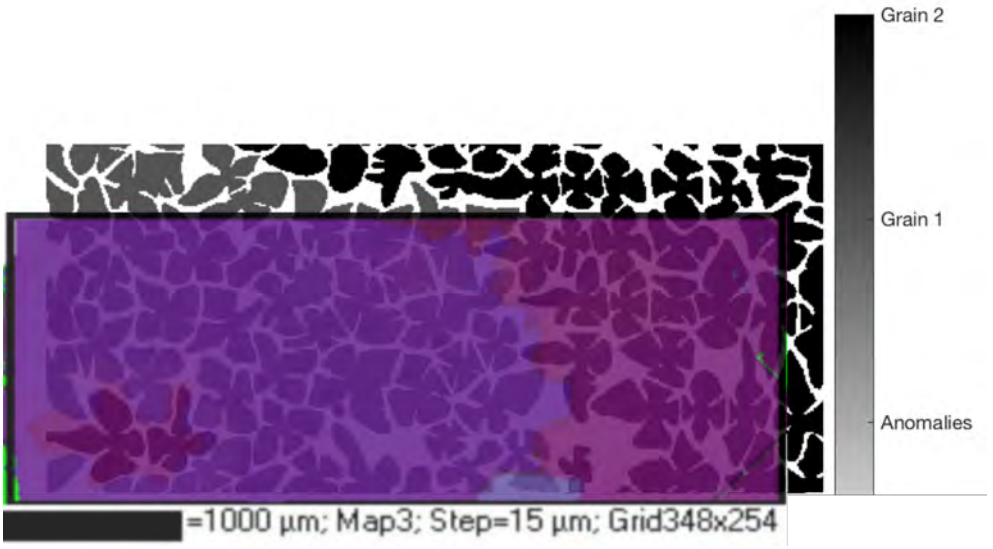


c

FIGURE 4.47: a) The four principle angles overlain on the dendrites. b) The result of the DBSCAN sorting. c) The dendrites sorted into grains.



a



b

FIGURE 4.48: a) *EBSD* map of the polycrystalline nickel superalloy sample. b) *EBSD* map overlain on the result of the dendrite sorting.

based technique (Figure 4.43bii). As the skeleton for a square is a one pixel thick cross with the tips of each of the lines close to the corner of the square itself this is to be expected. In either case the methods can find the orientation of simple shapes with four sided symmetry as is the case with Figure 4.43.

In both instances of the single dendrites (Figures 4.44 and 4.45) there is a clear four-fold symmetry shown on each of the polar histograms (Figure 4.44b and Figure 4.45b), which are given in Table 4.8. Moreover it is clear that like with the square (in Figure 4.43) the two methods give differing outputs for the dendrites (Figures 4.44 and 4.45 and table 4.8) again approximately 45° out of phase. In both cases the difference in the orientation is due to the input image, either the whole smoothed dendrite or the smoothed skeleton. As the objective is to obtain a technique which can be used to sort multiple dendrites into grains a consistency is needed in the technique, and this can only be tested by increasing the number of dendrites input. Therefore using a single crystal sample would be a good measure to test which of the two techniques is the most applicable and gave the most consistent results across a greater sample size.

Comparing the subfigures in Figure 4.46 it is clear to see that without the skeletonisation the technique does not work as well as with the skeletonisation step implemented. This is likely due to the the overload of information provided by the full shape of the dendrites. The skeleton reduces the input data resulting in a much more defined shape and thus output angles as compared to using the original binary shape of the dendrite. Without this step in place any perturbations along the perimeter of the dendrite being input can lead to the data being skewed as can be seen in Figure 4.46ai. In this example there is a much greater variation between all of the calculated angles for the different dendrites rather than a consistent set of results as seen in the method involving the skeletonisation (Figure 4.46aii, bii and cii). As the method without the skeletonisation step implemented did not

correctly sort a single crystal sample it was not trialled on the polycrystalline sample.

The skeletonisation method was trialled on a polycrystalline CMSX-4 sample (results shown in Figure 4.47). The method was successfully able to sort the dendrites into two distinct grains similar to those shown in the *EBSD* map (Figure 4.48). However there are several instances of anomalies as can be seen in Figure 4.47b Figure 4.47c. These anomalous dendrites are in all instances along the edge of the input image, and moreover are in each case cropped so only a small area of the dendrite is showing. As such the skeleton would not have accurately described the dendrite and would lead to an anomalous results shown in Figure 4.47b Figure 4.47c. In order to prevent these anomalies occurring dendrites on the edge should be excluded if they are only partially visible.

One further point of note is that the method was able to sort two dendrites within grain 1 which have a similar orientation to grain 2 which can be seen in Figure 4.48b. These dendrites could either be from an entirely new grain with the same orientation or connected to grain 2 casting. With a single two dimensional slice this however would not be possible to discern, as a result serial sectioning should be undertaken to see which is the case.

The comparison of the *EBSD* and this optical method show that whilst it will not give accurate crystallographic information it can be used to find separate grains quickly. One clear advantage of this method is that it can obtain the orientation of individual dendrites rather than only the entire grains like with an *EBSD* scan. Moreover when speed is of the essence (especially for large samples as is the case here) *EBSD* has an obvious disadvantage. Figure 4.48 itself took approximately 4 hours to produce whereas the equivalent optical image analysis took approximately 30 seconds of computational time and was able to characterise the sample to into grains with a similar level of accuracy.

4.8.6 Analysing the Grain Orientation Method for Use with Aluminium-Copper Dendrites

The orientation finding technique was shown to be able to sort binarised dendrites into a number of grains dependent on their orientation. The technique worked well with a traced single crystal and polycrystalline sample. It must also be trialled on binarised Al 10 wt% Cu images obtained as a result of the image binarisation regime put forward.

An investigation was made into how the ϵ and N values of the **DBSCAN** (minimum distance and minimum number of points respectively) affect the output grain morphology. A number of the results are given below in Figure 4.49.

As can be seen the results of the scan are not very promising for any of the ϵ, N pairings. The images shown in Figure 4.49 are just a small subset of the total number of ϵ, N pairings which were undertaken and analysed. However in all cases there were no adequate results which accurately separated the dendritic microstructure into grains. In specific areas correct separation did occur however there are many areas which were not accurately separated.

The failure of the technique may be due to several problems. One of the most likely is the difference in the morphology in the aluminium-copper dendrites than those of the nickel superalloy which are more regular. The aluminium-copper dendrites show much more tertiary arm growth which is simply not present within the analysed nickel superalloy samples.

One further issue may be due to the resolution of the image themselves. Whilst the input images are of the same size–approximately 2000x2000 pixels for the Al-Cu sample and 1000x2000 for the Ni-superalloy sample–the number of dendrites is much greater in the Al-Cu sample. Therefore the area of each dendrite in terms of number of pixels will be much smaller; and as the skeletonisation is dependent

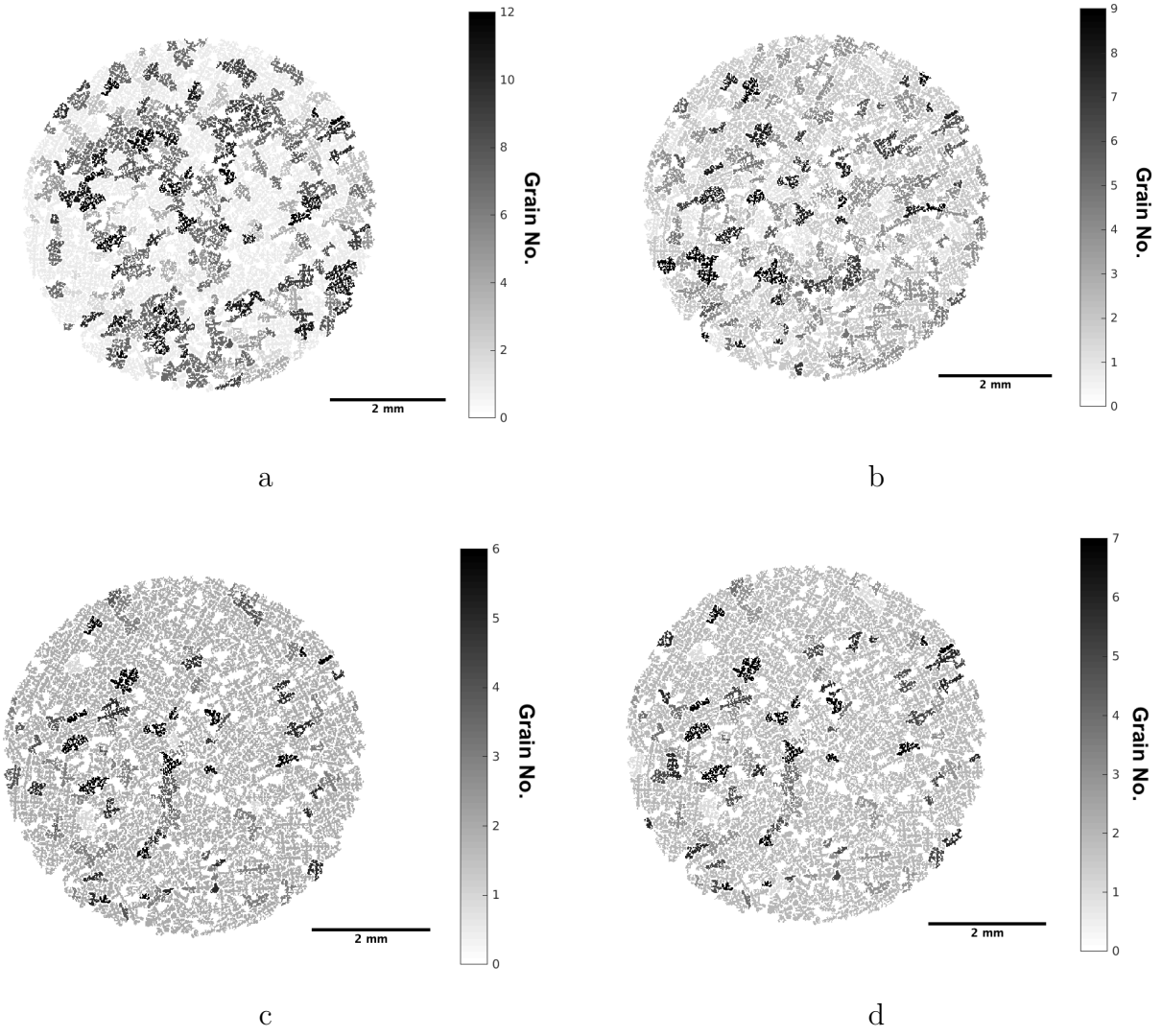


FIGURE 4.49: Results of the orientation based grain assigning resulting in erroneous results. a) N = 5, $\epsilon = 0.1$, b) N = 10, $\epsilon = 0.1$, c) N = 5, $\epsilon = 0.7$, d) N = 10, $\epsilon = 0.7$

upon the input area of the binarised dendrite it can have a large effect upon the results of the orientation finding algorithm. However it is most likely that the error in the dendrite orientation finding technique is a combination of both of these problems. This however is a limitation inherent currently in **CT** imaging as there is a minimum voxel size that can be reached when analysing volumes. Especially when analysing large diameter samples. Therefore in order for this technique to work correctly there needs to be better detectors available in **CT**s so smaller voxel sizes can be obtained. This will allow for better resolution images and image stacks.

Due to the failure of the grain finding technique put forward to find the dendritic orientation of the **CT**'d aluminium-copper data it will not be examined further within this thesis. Further work is needed to adapt this technique for use with other types of dendritic microstructures and not only Ni-superalloy samples.

Chapter 5

Experimental Analysis Results

All of the experimental samples detailed in Chapter 3 were successfully analysed using the schemes outlined in Chapter 4. As such, information on the **PDAS**, number of nearest neighbours and the location of dendrite initiations and deletions could be obtained. The three dimensional isosurfaces were computed showing the morphology of these dendrites in three dimensions.

In this chapter the results of each of the analysis methods will be outlined including the constant withdrawal rate samples: 40, 60, 80, 100 μms^{-1}. Then, subsequently, the varying withdrawal rate experiments which comprised of: 40 to 80 μms^{-1} (also detailed in the Appendix of Chapter 11), 40-60-80 μms^{-1}, and finally the 40-60-100 μms^{-1} sample.

A cross-section of the constant withdrawal rate 100 μms^{-1} sample is shown in Figures 5.1 and 5.2 which are indicative of the other samples.

Transverse sections of the 40-60-80 μms^{-1} sections taken in each region of the sample are given in Figures 5.3 to 5.5. Transverse sections of the 40-60-100 μms^{-1} sample are given in Figures 5.6 to 5.8

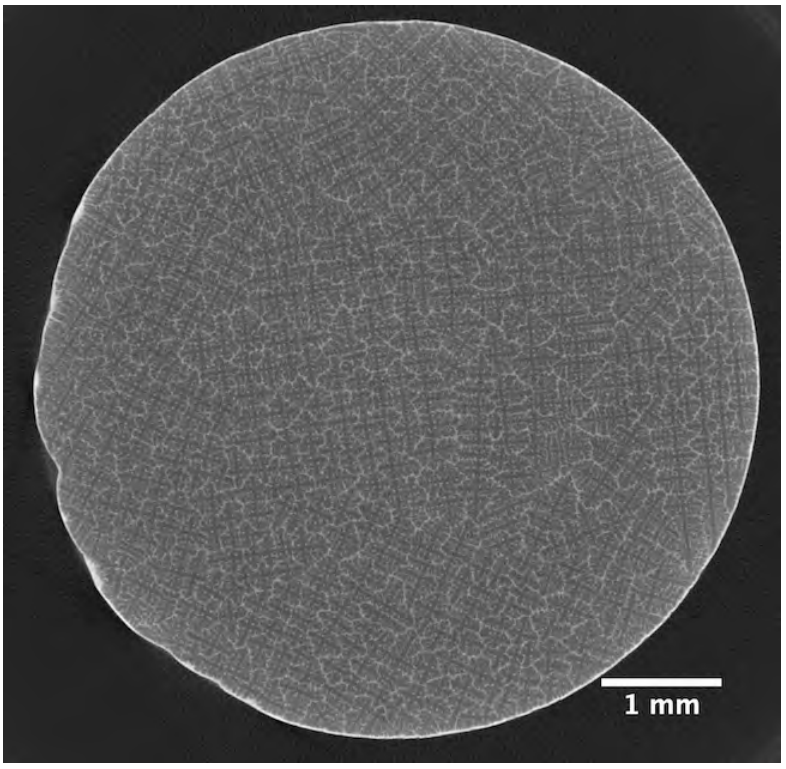


FIGURE 5.1: Transverse section of the constant withdrawal rate 100 μms^{-1} sample **CT** volume. $\lambda_{avg} = 260$ μm.

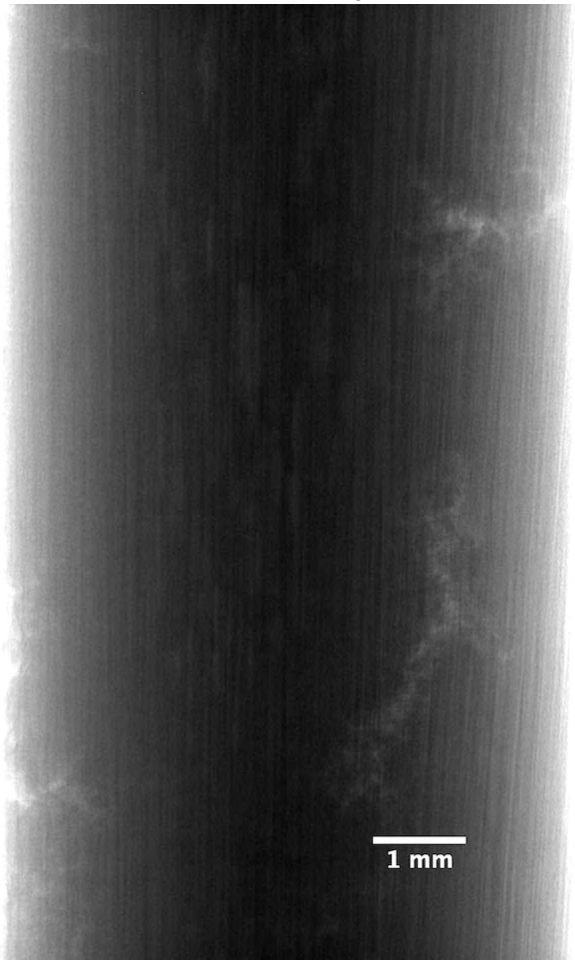


FIGURE 5.2: Side view section of the constant withdrawal rate 100 μms^{-1} sample **CT** volume.

5.1 Primary Dendrite Arm Spacing

The experiments detailed in Chapter 3 were analysed using the **CT** scanner and subjected to the image analysis methods detailed in Chapter 4. These techniques were successfully able to find the **PDAS** for each of the samples along the length of the scanned areas.

For the 40 μms^{-1} sample three volumes were evaluated. For the other samples with a constant withdrawal velocity only one **CT** volume was examined due to time constraints using the CT scanner.

For the samples where there is a change in the withdrawal rate the **CT** volumes were either taken so it encapsulated before, after and including the transition region (as is the case with the 40-80 μms^{-1} sample). Or, as is the case with both the 40-60-80, and 40-60-100 μms^{-1} samples a series of **CT** volumes were taken and analysed along the length of the sample encapsulating all the relevant length of the sample. For each sample the voxel size was approximately 2 μm^3.

For each of the samples the average **PDAS** for every five slices is given on the graphs (that is every 10 μm along the sample) in order to reduce noise in the results. This averaging of the slices was factored in when calculating the error bar for each of the samples. For the average **PDAS** results for the 60 and 100 μms^{-1} samples the error bar is too small to be seen clearly in each instance the error is approximately 1 μm (see Figures 5.15 and 5.25).

5.1.1 Constant Withdrawal Rate

Figures 5.10, 5.15, 5.20 and 5.25 show the primary dendrite arm spacing along the length of the **CT** volumes for the continuous withdrawal rate experiments. The graph showing the **PDAS** for the continuous withdrawal rate of 40 μms^{-1} (Figure 5.10) is taken across the largest length of the sample, which is approximately

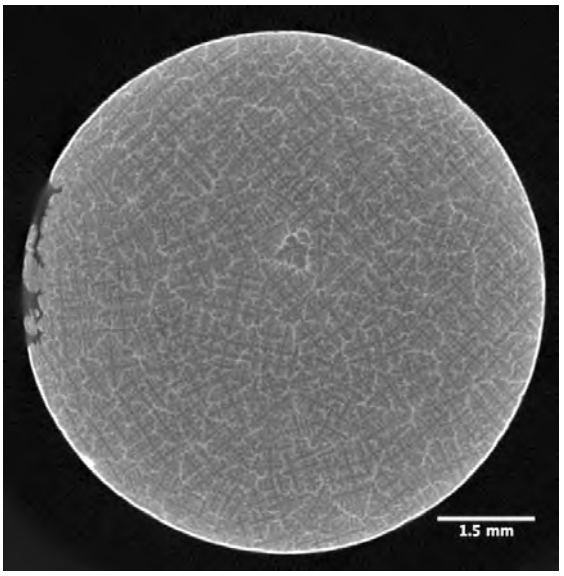


FIGURE 5.3: Transverse section of the 40-60-80 μms^{-1} sample in the 40 μms^{-1} region. $\lambda_{avg} = 300$ μm.

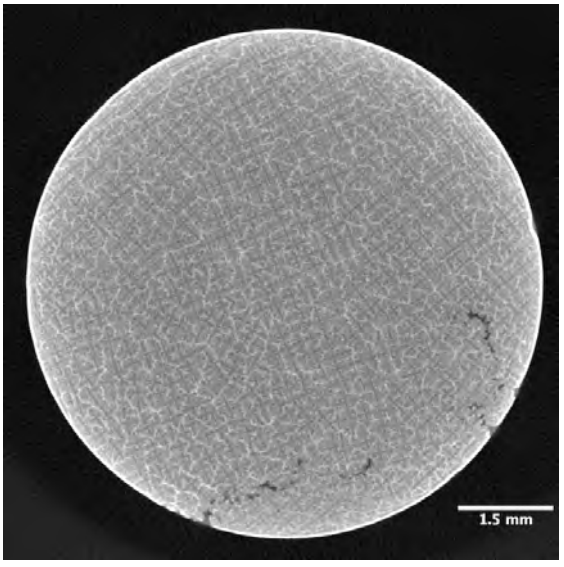


FIGURE 5.4: Transverse section of the 40-60-80 μms^{-1} sample in the 60 μms^{-1} region. $\lambda_{avg} = 250$ μm.

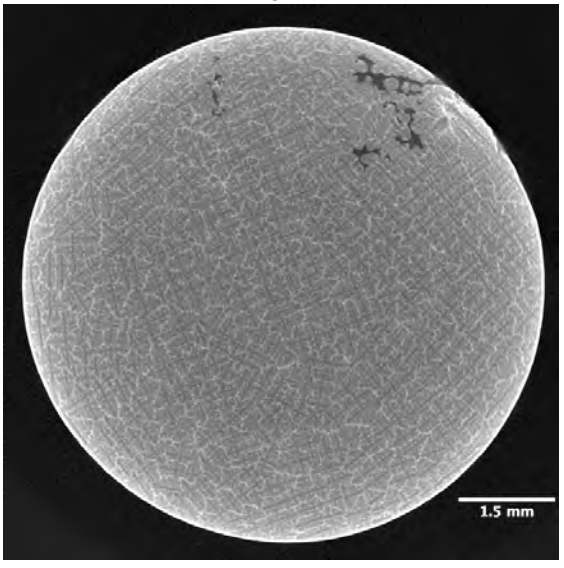


FIGURE 5.5: Transverse section of the 40-60-80 μms^{-1} sample in the 80 μms^{-1} region. $\lambda_{avg} = 230$ μm.

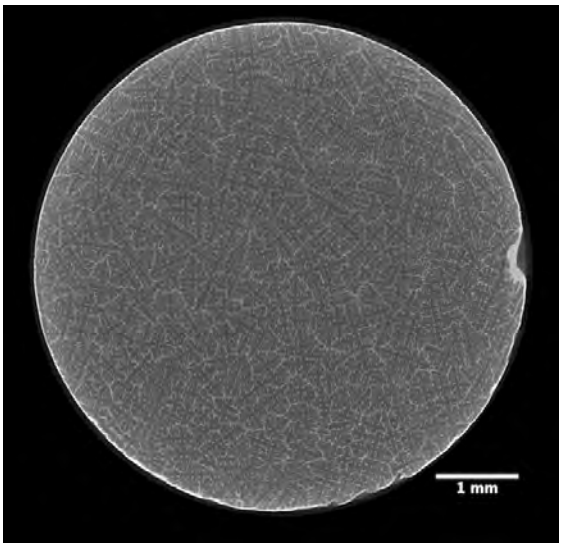


FIGURE 5.6: Transverse section of the 40-60-100 μms^{-1} sample in the 40 μms^{-1} region. $\lambda_{avg} = 295$ μm.

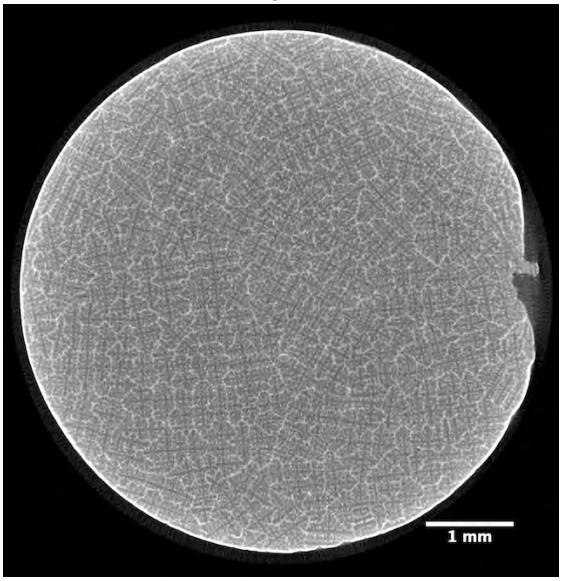


FIGURE 5.7: Transverse section of the 40-60-100 μms^{-1} sample in the 60 μms^{-1} region. $\lambda_{avg} = 270$ μm.

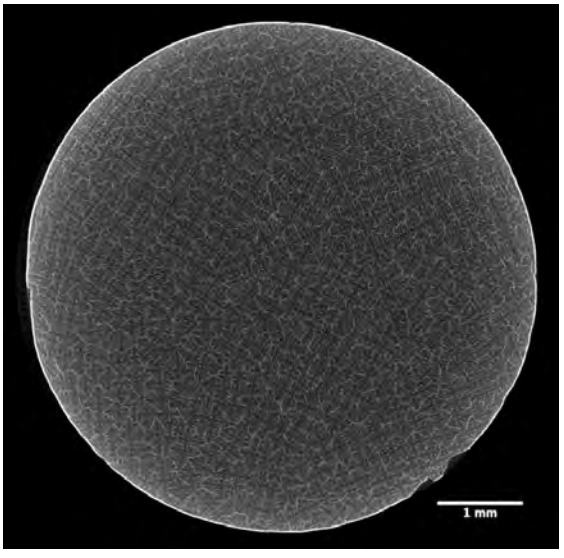


FIGURE 5.8: Transverse section of the 40-60-100 μms^{-1} sample in the 100 μms^{-1} region. $\lambda_{avg} = 240$ μm.

equal to 20 mm. This is a substantial length of the sample itself and coincided with a total of three continuous **CT** volumes along the length of the sample.

The slices started 30 mm from the point where the sample was held prior to withdrawal. The curves in the graph show the average or bulk spacing using Equation (6.1) and the maximum and minimum spacings defined as $4/3\lambda$ and $2/3\lambda$ respectively. The local spacing is calculated for each slice along the length of the sample using the methods outlined in Section 4.3 which include the Voronoi, Warnken-Reed, Warnken-Reed-Voronoi and minimum spanning tree techniques. The graph shows relatively constant **PDAS** along the entire length however there are two notable points where there are sudden increases in the value can be seen which are at 0.25 mm and 1.75 mm. In both cases these points coincide with the location of pores within the sample. Dendrites are outcompeted by the vacancy and then new dendrites are created around and above it which returns the system to a steady state. Thus the **PDAS** returns to approximately the same value it was before.

Similar to this are the other three constant withdrawal rate samples (Figures 5.15, 5.20 and 5.25) which all show relatively constant **PDAS** along the length of the sample. The one notable exception however is Figure 5.20 which shows an increase in the **PDAS** along the entire length of approximately 50 μm for the average spacing. This increase is much less pronounced in the calculations with the local spacing (Voronoi, Warnken-Reed, Warnken-Reed-Voronoi and minimum-spanning-tree). This would imply that there are number of dendrites being outcompeted and removed here thus reflected in the increase in bulk spacing.

As the local **PDAS** does not change whilst the overall number of dendrites changes the spacing distribution in the array does not alter very much. This is the result of a vacancy within the melt which disrupts the growth of the dendritic array along the length of the sample. This being similar to the 40 μms^{-1} sample.

One final difference between this graph (Figure 5.20) and the others is that it begins at approximately 0.9 mm from the bottom of the **CT** volume. This missing section of approximately 0.9 mm in length was due to an unfortunate side effect of the image acquisition. When recombining the images from the **CT** scan there was a large amount of noise resulting from the Fourier transform used to create these images. This as a result gave a large degree of error in the dendrite centre finding techniques. As such, it was deemed that this section of the scan volume could not be used and a 'buffer' at the top of the volume was removed.

5.1.2 Increasing Withdrawal Rate

The results for the varying withdrawal rate samples is given in Figures 5.30, 5.38 and 5.50. In each of the figures there is a restructuring in the dendritic array as indicated by the changing value of the **PDAS** which decreases after each change in the withdrawal rate.

In each of these changing withdrawal rate samples there is a a delay in the dendritic array adapting to the new velocity as can be seen in Figures 5.30, 5.38 and 5.50. In each case with an increasing withdrawal rate there is a decrease in the **PDAS** to compensate.

The 40-80 μms^{-1} analysis shows that there is a reduction in the **PDAS** from an initial level of 320 μm to a new level of 230 μm after the velocity change. This transition takes place over 2.5 - 3 mm until it stabilises at the lower value. The 40-80 μms^{-1} sample (Figure 5.30) is described in more detail in the Appendix in Chapter 11.

The 40-60-80 μms^{-1} sample is shown in Figure 5.38. There is a decrease in the average **PDAS** from the initial 300 μm to approximately 250 μm after the first

velocity change. Then finally the average **PDAS** reaches 230 μm after the second transition.

Figure 5.50 shows the primary dendrite arm spacing of the 40 to 60 to 100 μms^{-1} sample. Unfortunately this sample became bent upon removal of the sample from the alumina crucible. A full scan of the entire length of this sample was therefore not possible. Due to the bend in the sample it could not be mounted completely straight within the **CT** scanner itself, with sections in the 60 μms^{-1} and 100 μms^{-1} regions not fitting correctly within the observation window of the **CT** camera. The transition regions were therefore not able to be imaged using a **CT** scanner. No metallographic segmentation was attempted due to the wish to keep the samples whole and unadulterated for subsequent study in further work undertaken at the **DLR**.

Attempts were made at scanning these bent sections. However, the resolution upon final reconstruction of the volume was approximately 20 μm which was too large for obtaining accurate information on the location of the dendrite centres.

A longer multi-scan was possible of the 40 μms^{-1} section. This region showed near constant **PDAS** with very little change along the length of the scans (approximately 30 mm).

The shorter scans of the 60 μms^{-1} and 100 μms^{-1} regions were obtained at points of the rod which were approximately straight. In these regions resolutions of approximately 2 μm were obtained. The 60 μms^{-1} scan was obtained at the midpoint between the first and second velocity change beginning at 61 mm and finishing at 67 mm above the bottom of the sample.

The 100 μms^{-1} scan was obtained approximately 8 mm after transition from 60 to 100 μms^{-1}. This volume began at 82 mm and finished at 88 mm from the bottom of the sample.

5.1.3 Increasing Withdrawal PDAS Rates of Change

The rates of change in the **PDAS** for each of the varying withdrawal rate samples was calculated by fitting a line between the point where the decrease in **PDAS** first occurred to the point where the transition had stabilised. These fits are shown graphically in Figures 5.32, 5.40 and 5.43 and the curves are tabulated in Tables 5.1 to 5.3. The tables also give the R^2 values for each of the fits.

In each instance it is clear that a linear fit is adequate in explaining the variation in the data. The R^2 value for each fit was greater than 0.9. In most instances the value was greater than 0.95 indicating the fit describes the data well.

The 40 - 60 - 80 μms^{-1} sample rate of change graphs (Figures 5.32, 5.40 and 5.43) were not altered to re-zero the X-axis from the points of velocity change. As there were two velocity changes the original distances were left on the X-axis for ease of comparison with the graph showing the full extent of the **PDAS** in Figure 5.38.

As can be seen in the constant withdrawal rate figures (Figures 5.10, 5.15, 5.20 and 5.25) the **PDAS** remains constant along through the **CT**'d volume of the sample. This is in contrast to the changing withdrawal rate samples, Figures 5.30, 5.38 and 5.50, which upon a change in withdrawal rate show a decreasing **PDAS**. The **PDAS** in each instance restabilises after a certain length of the sample. This is categorised by the levelling out of the **PDAS** with no further changes.

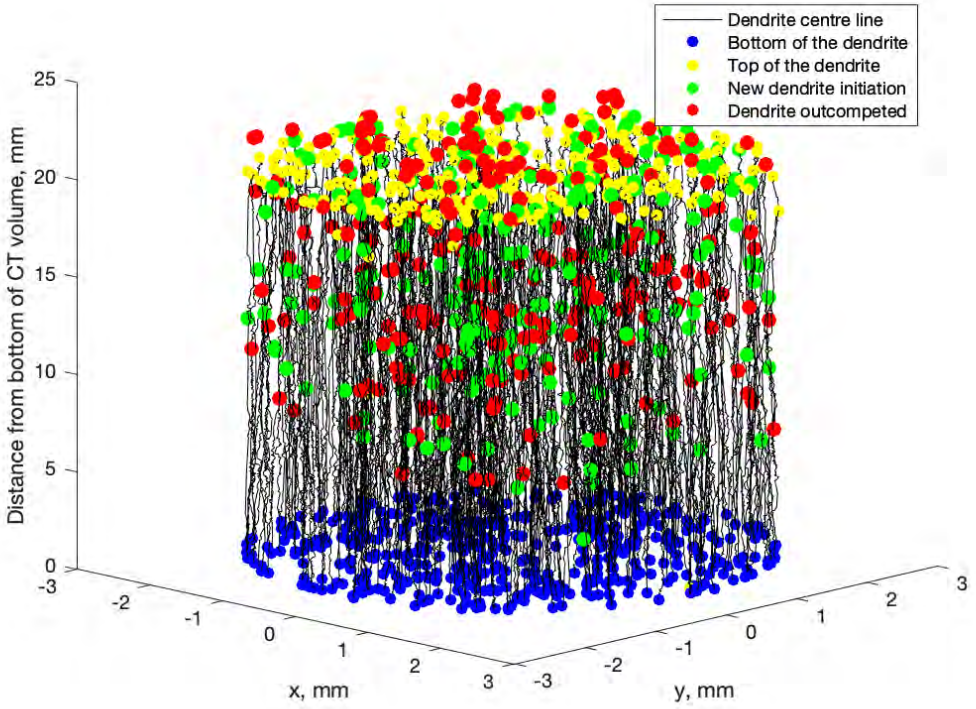


FIGURE 5.9: Dendrite forest of centres traced along the length of the 40 μms^{-1} sample.

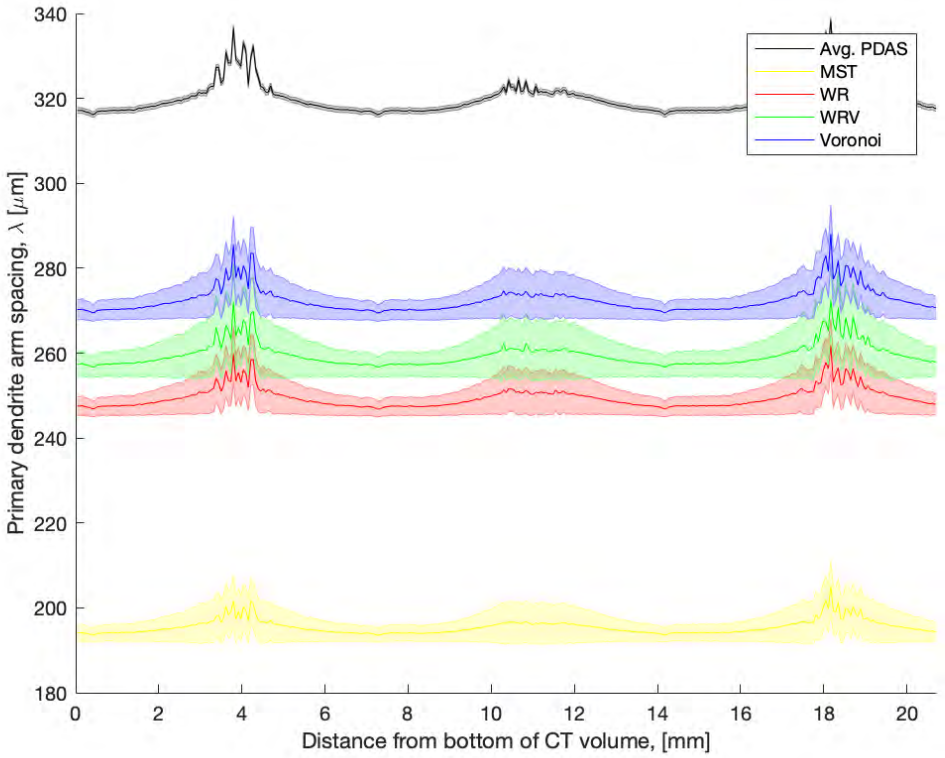


FIGURE 5.10: Primary dendrite arm spacing along the length of the 40 μms^{-1} continuously withdrawn sample.

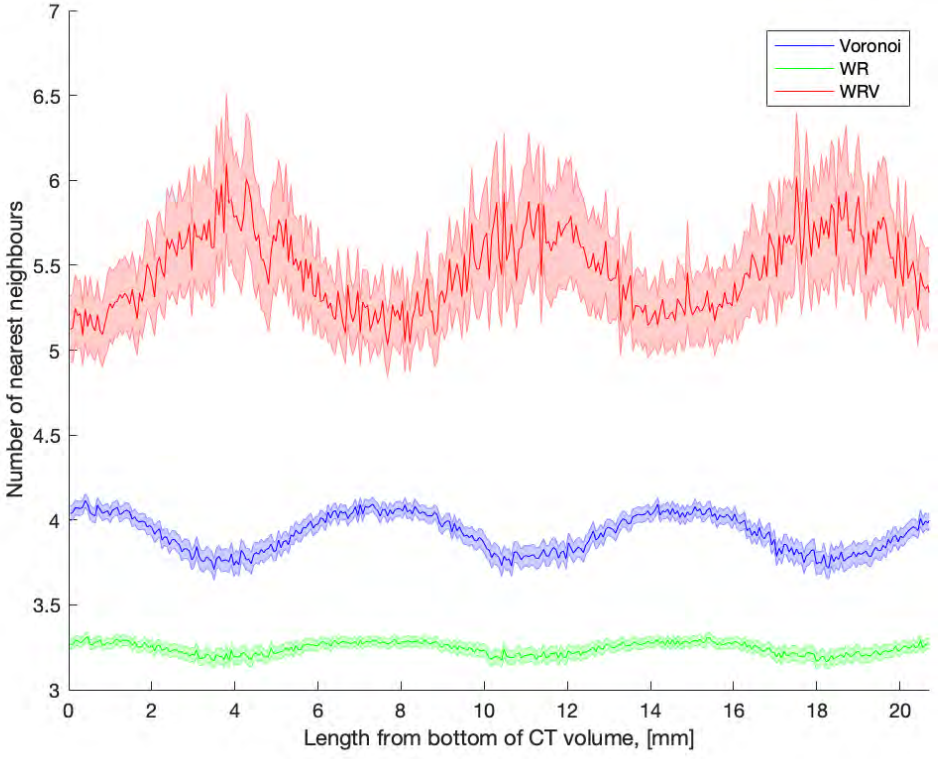


FIGURE 5.11: Number of nearest neighbours along the 40 μms^{-1} sample.

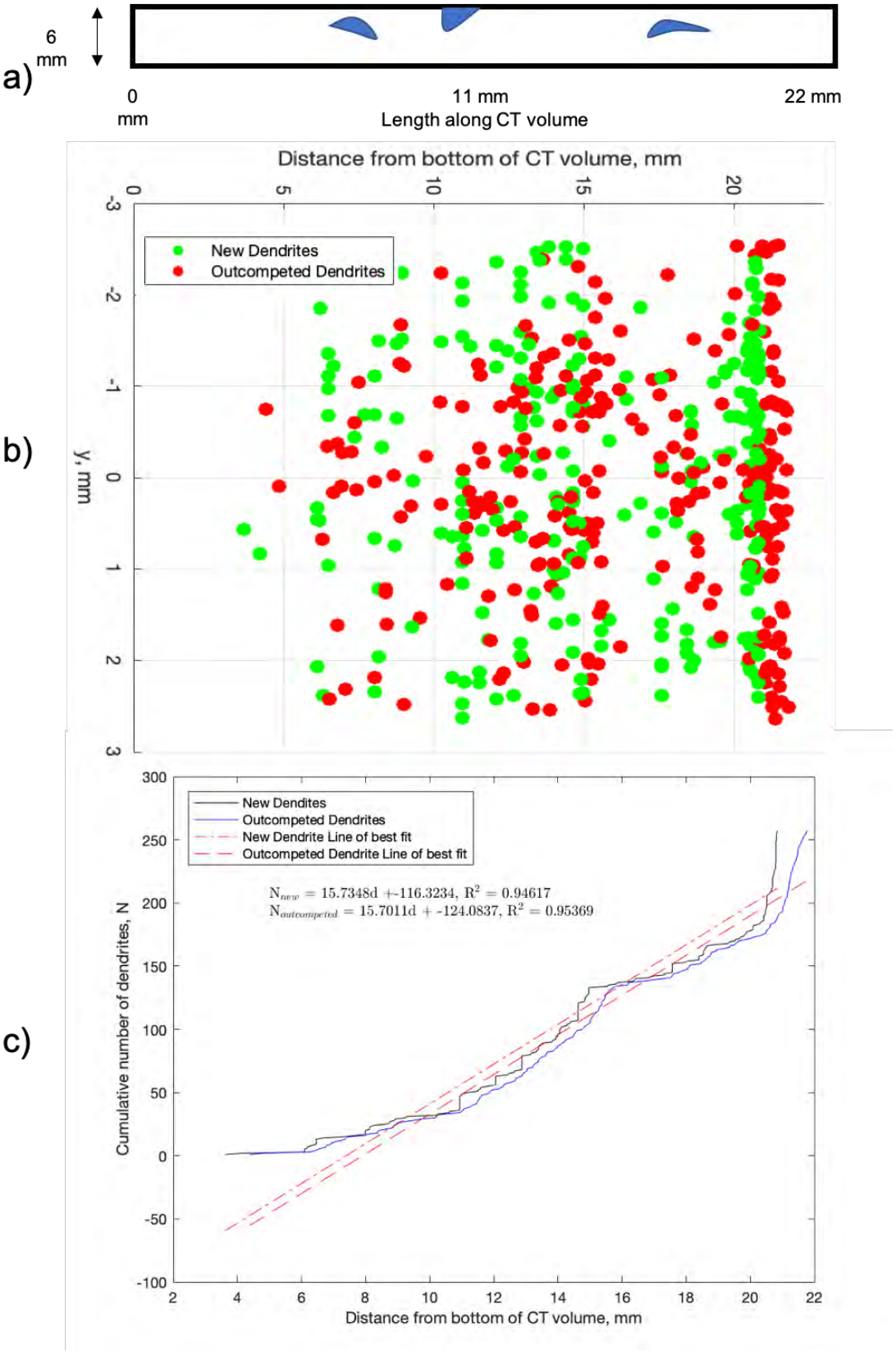


FIGURE 5.12: a) Schematic showing location of porosity within the 40 μms^{-1} continuously withdrawn sample. b) Location of new dendrites and outcompeted dendrites in the sample when viewed side on. c) Cumulative number of new and outcompeted dendrites with a linear fit.

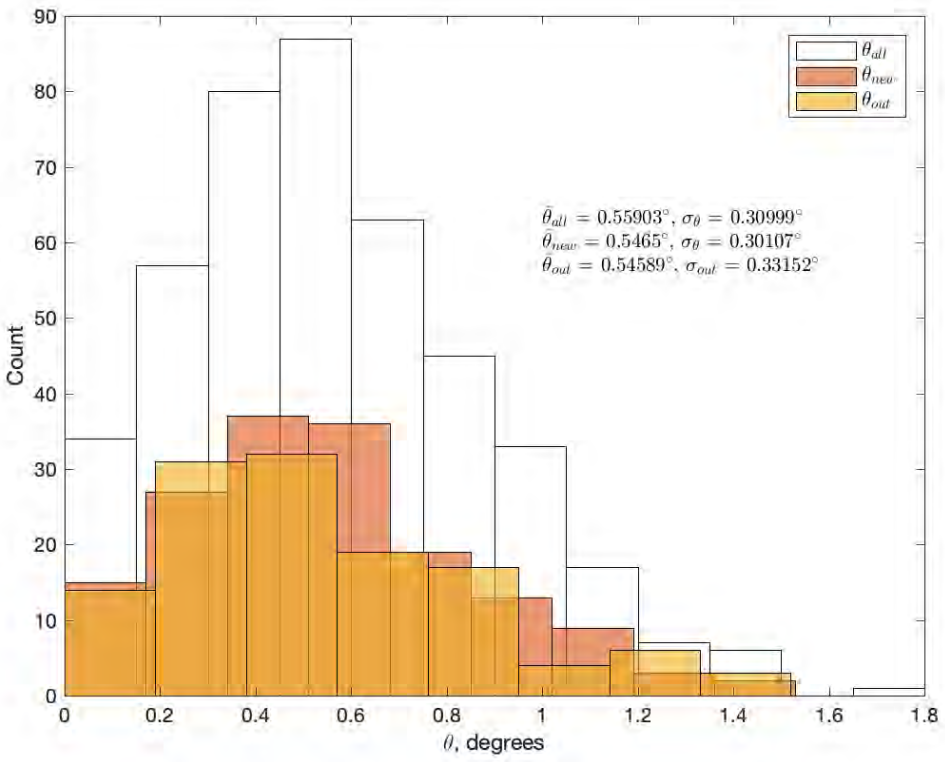


FIGURE 5.13: Orientation of the constant withdrawal rate 40 μms^{-1} sample for all dendrite primary trunks, outcompeted dendrites and newly created dendrites.

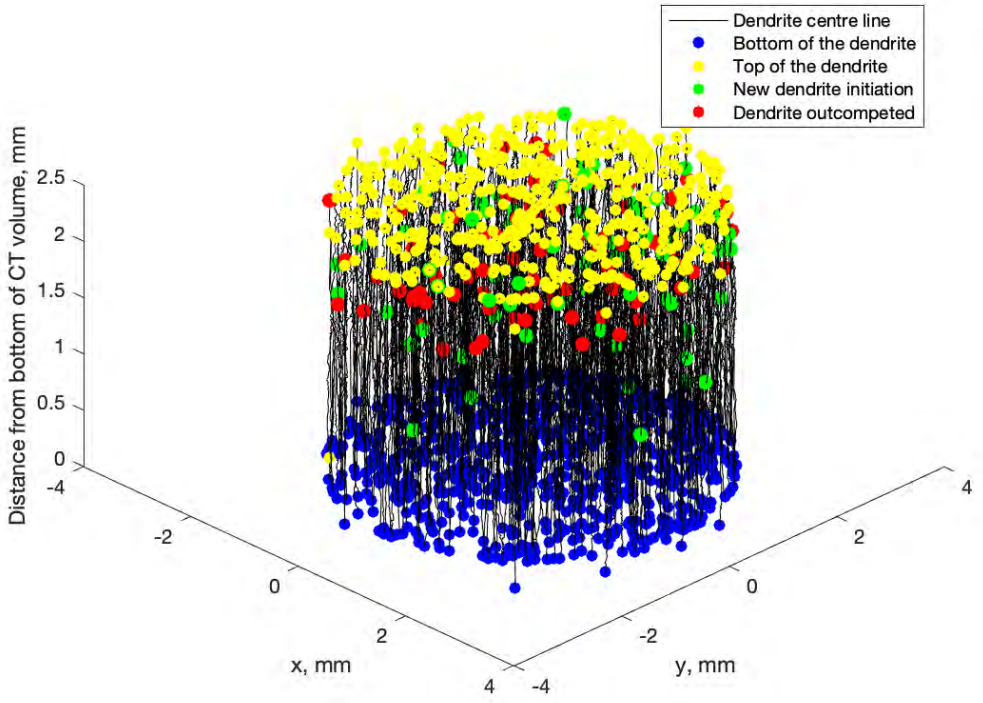


FIGURE 5.14: Dendrite forest of centres traced along the length of the 60 μms^{-1} sample.

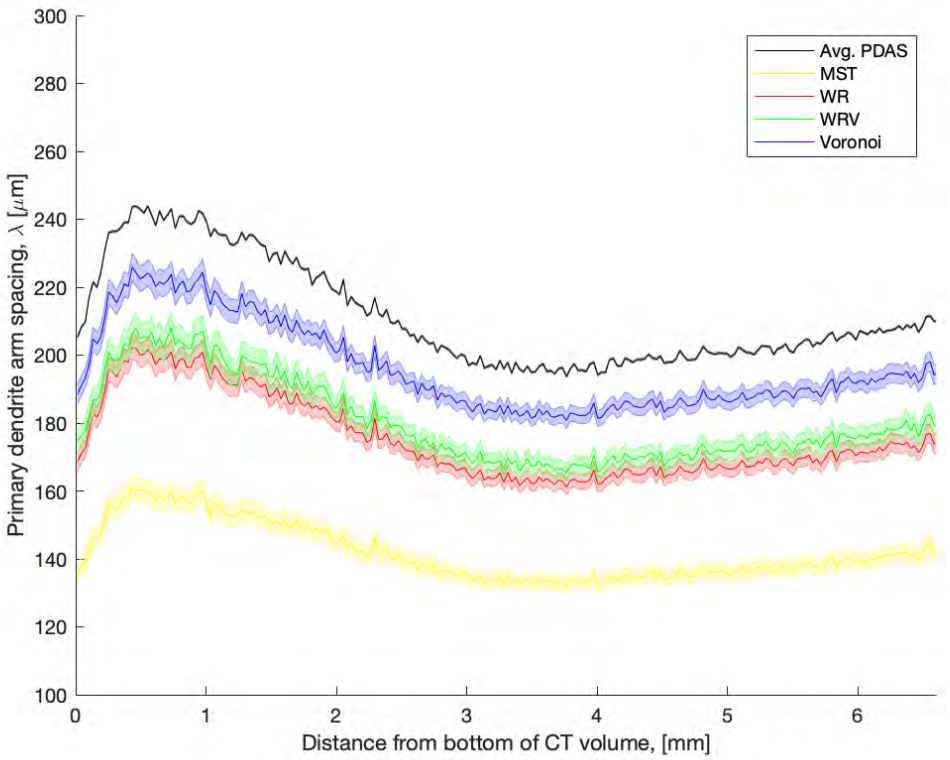


FIGURE 5.15: Primary dendrite arm spacing along the length of the 60 μms^{-1} continuously withdrawn sample. The average **PDAS** has an error of approximately 1 μm, whilst this is shown on the curve it is not clearly visible at this scale.

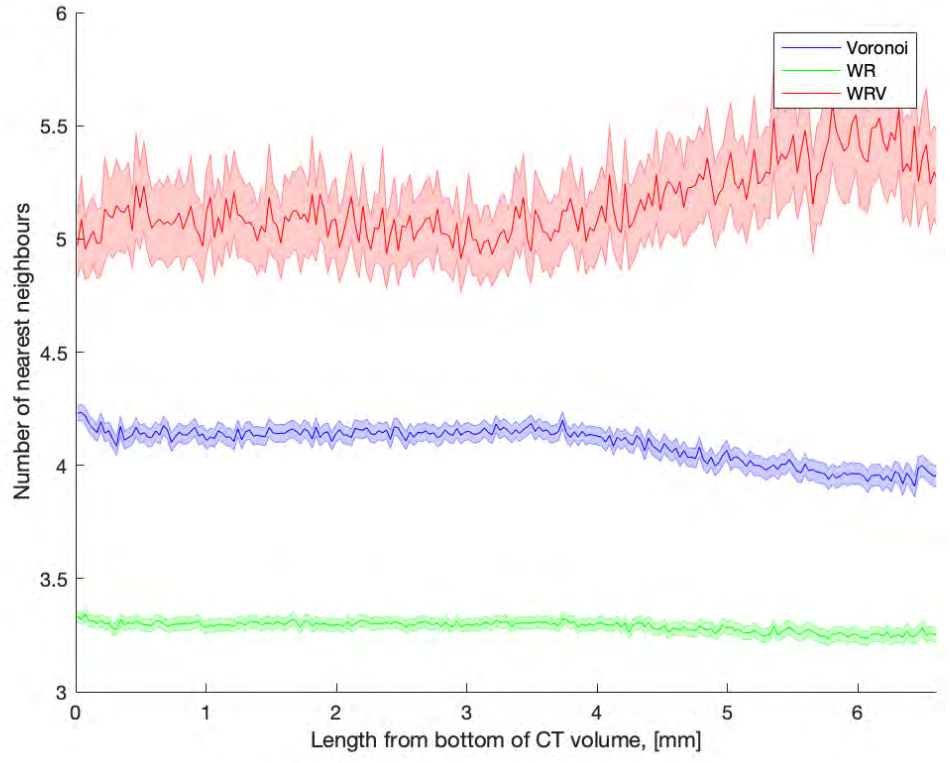


FIGURE 5.16: Number of nearest neighbours along the 60 μms^{-1} sample.

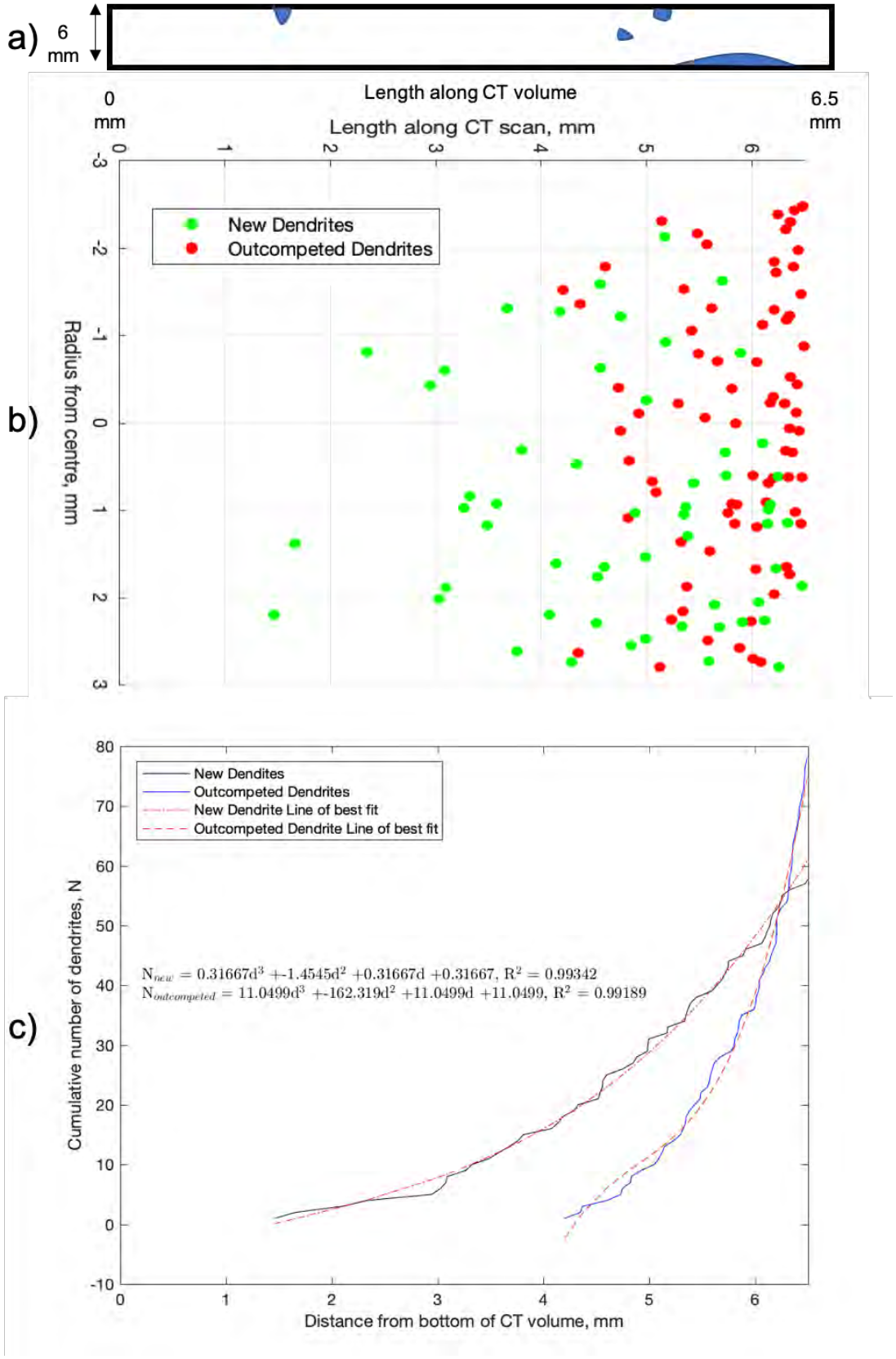


FIGURE 5.17: a) Schematic showing location of porosity within the 60 μms^{-1} continuously withdrawn sample. b) Location of new dendrites and outcompeted dendrites in the sample when viewed side on. c) Cumulative number of new and outcompeted dendrites with a third order polynomial fit.

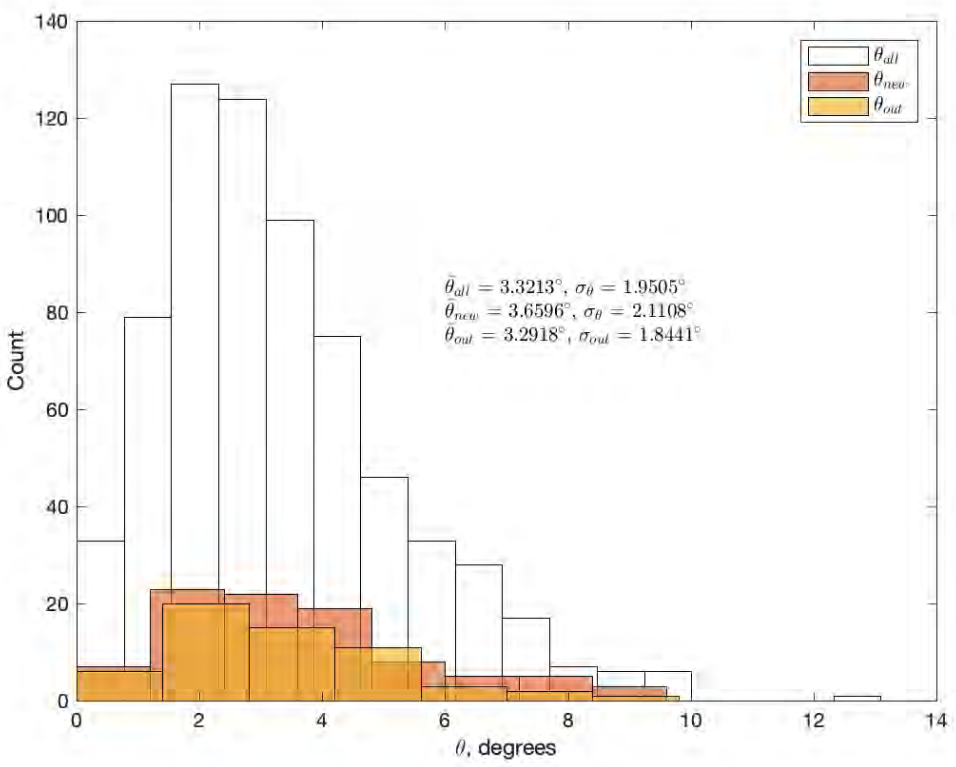


FIGURE 5.18: Orientation of the constant withdrawal rate 60 μms^{-1} sample for all dendrite primary trunks, outcompeted dendrites and newly created dendrites.

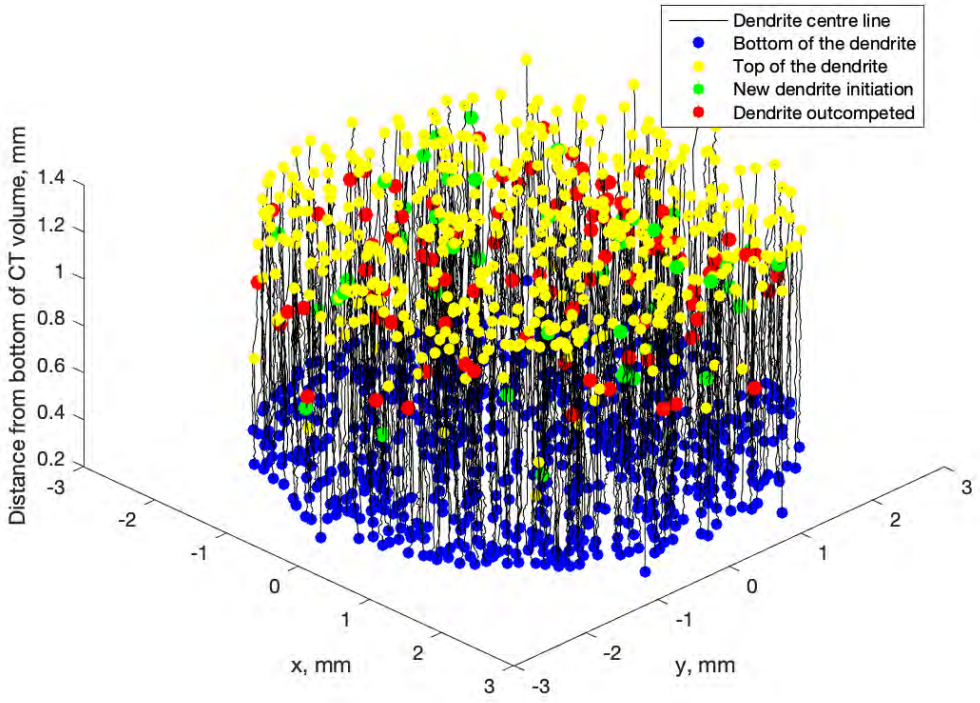


FIGURE 5.19: Dendrite forest of centres traced along the length of the 80 μms^{-1} sample.

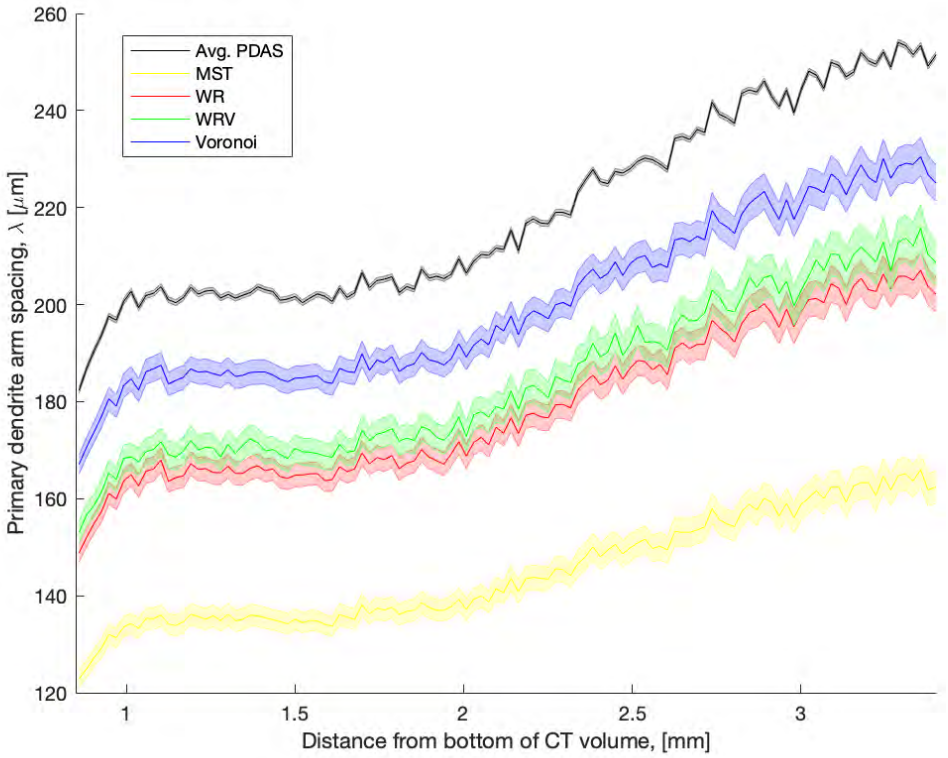


FIGURE 5.20: Primary dendrite arm spacing along the length of the 80 μms^{-1} continuously withdrawn sample.

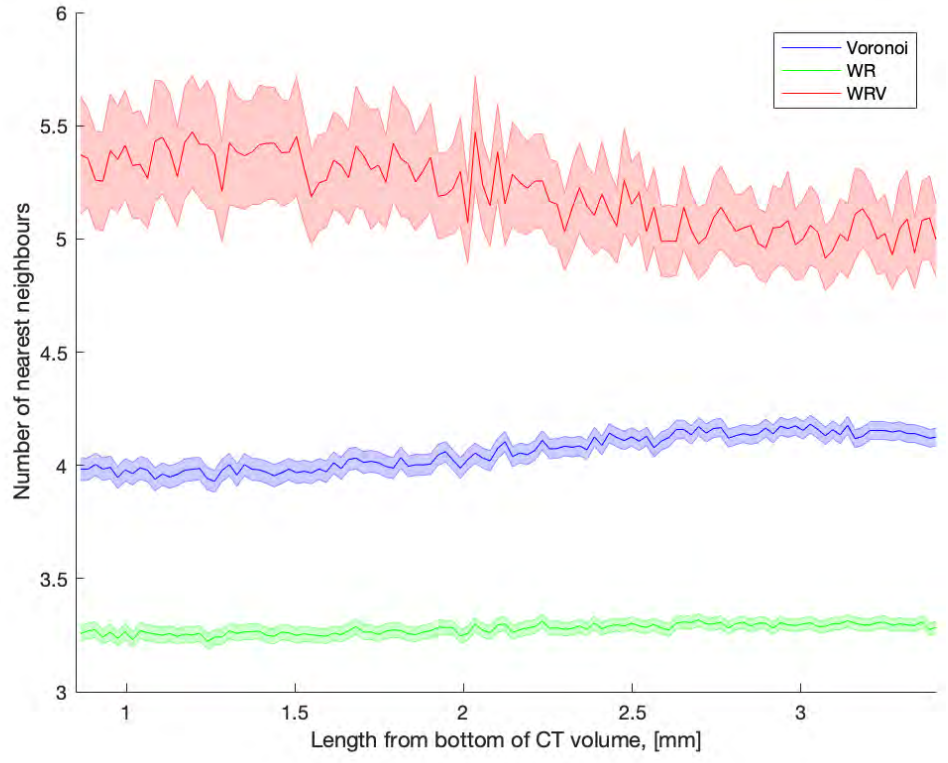


FIGURE 5.21: Number of nearest neighbours along the 80 μms^{-1} sample.

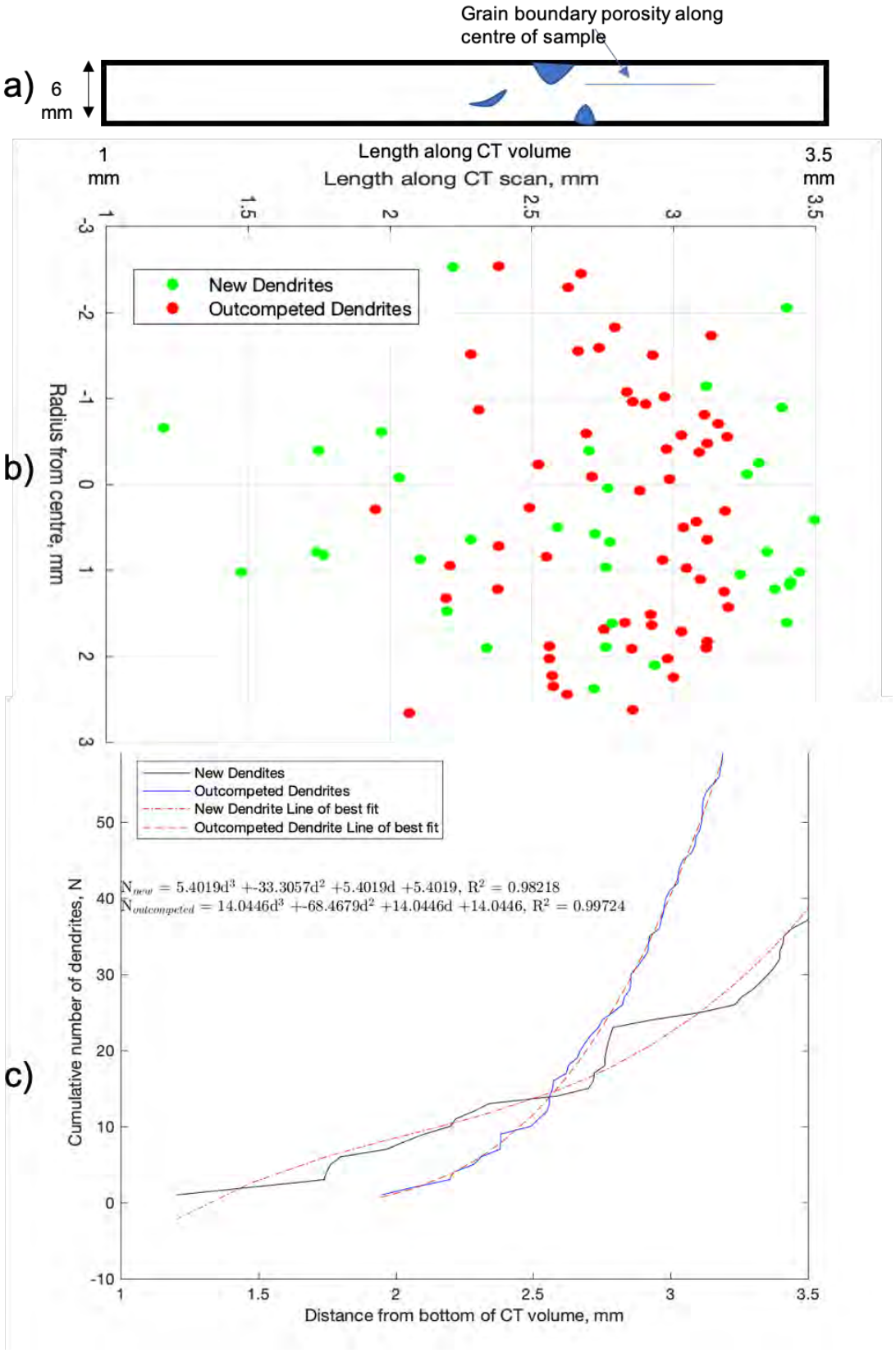


FIGURE 5.22: a) Schematic showing location of porosity within the 80 μms^{-1} continuously withdrawn sample. b) Location of new dendrites and outcompeted dendrites in the sample when viewed side on. c) Cumulative number of new and outcompeted dendrites with a third order polynomial fit.

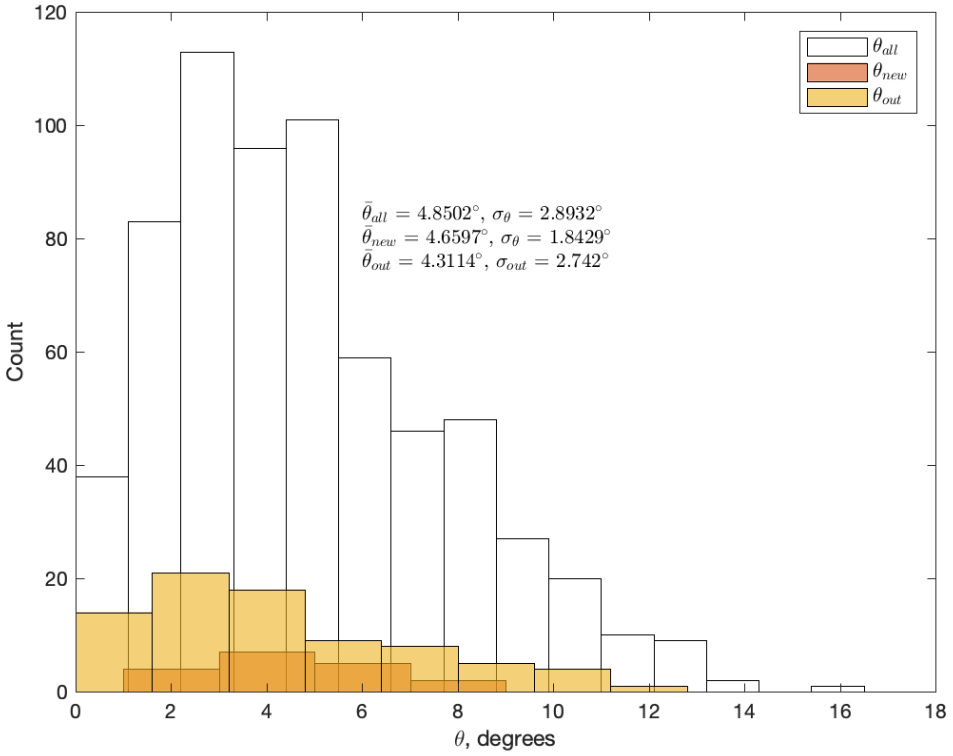


FIGURE 5.23: Orientation of the constant withdrawal rate 80 μms^{-1} sample for all dendrite primary trunks, outcompeted dendrites and newly created dendrites.

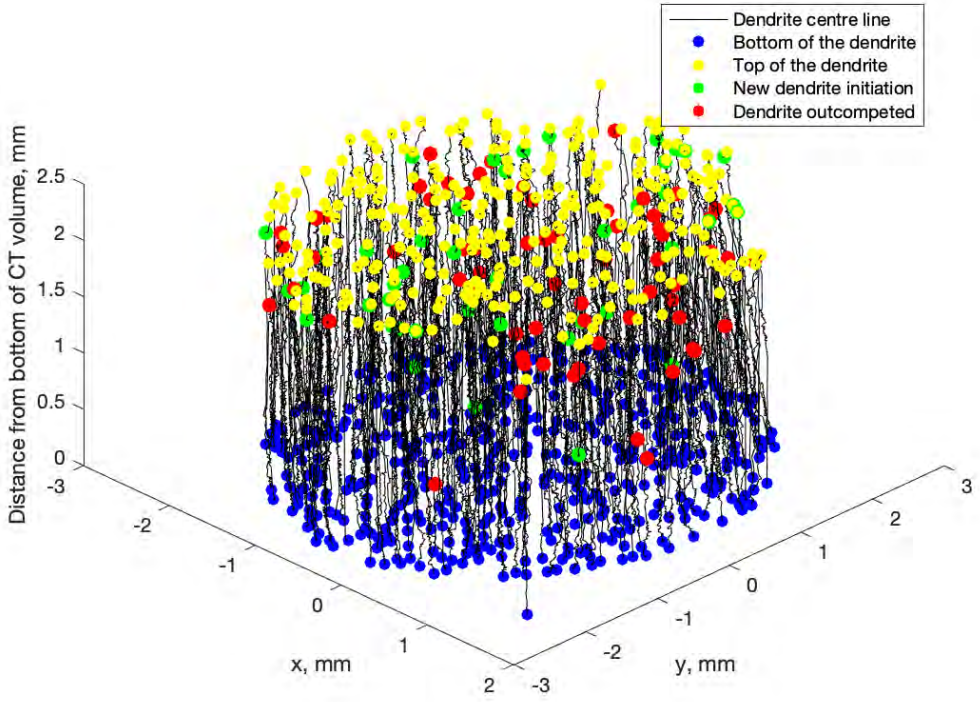


FIGURE 5.24: Dendrite forest of centres traced along the length of the 100 μms^{-1} sample.

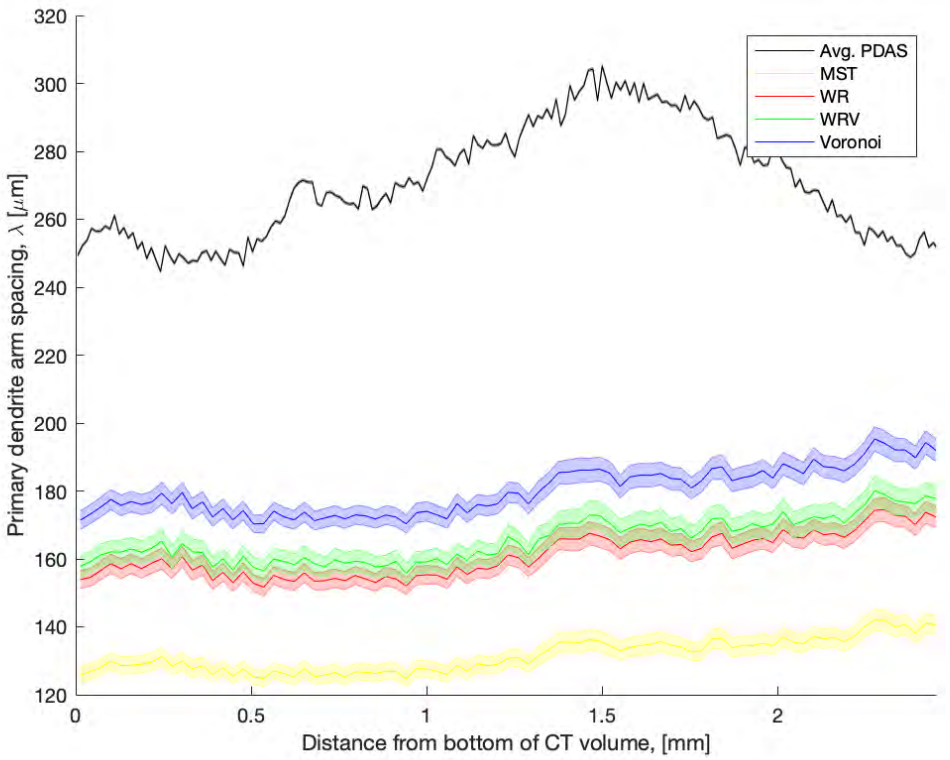


FIGURE 5.25: Primary dendrite arm spacing along the length of the 100 μms^{-1} continuously withdrawn sample. The average **PDAS** has an error of approximately 1 μm, whilst this is shown on the curve it is not clearly visible at this scale.

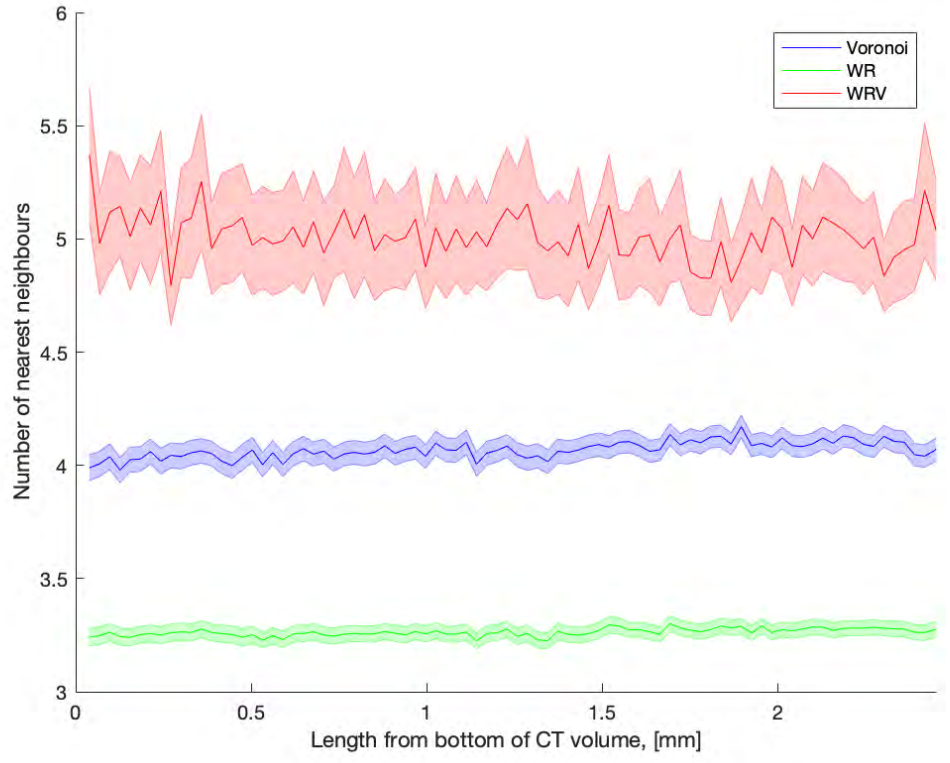


FIGURE 5.26: Number of nearest neighbours along the 100 μms^{-1} sample.

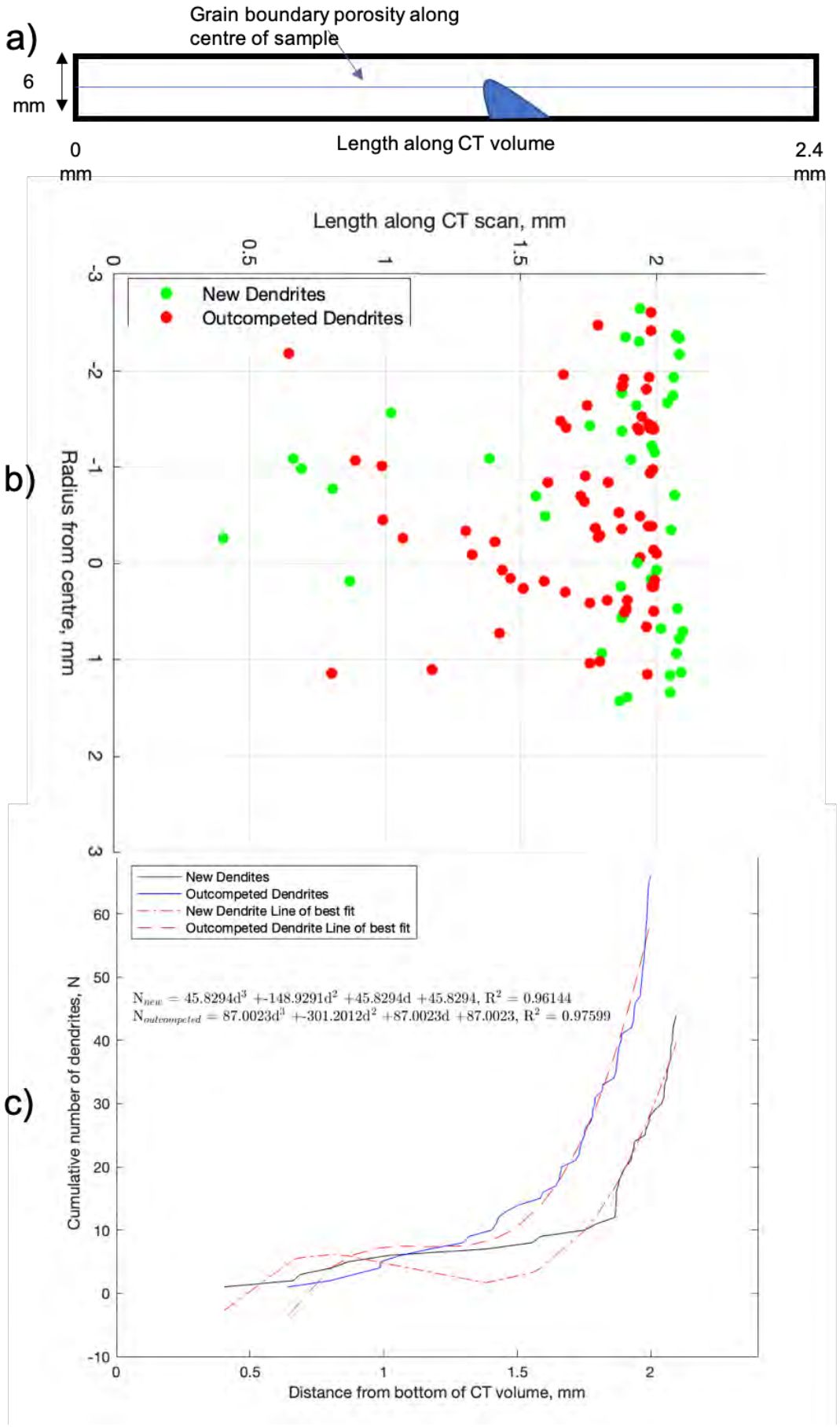


FIGURE 5.27: a) Schematic showing location of porosity within the 100 μms^{-1} continuously withdrawn sample. b) Location of new dendrites and outcompeted dendrites in the sample when viewed side on. c) Cumulative number of new and outcompeted dendrites with a third order polynomial fit.

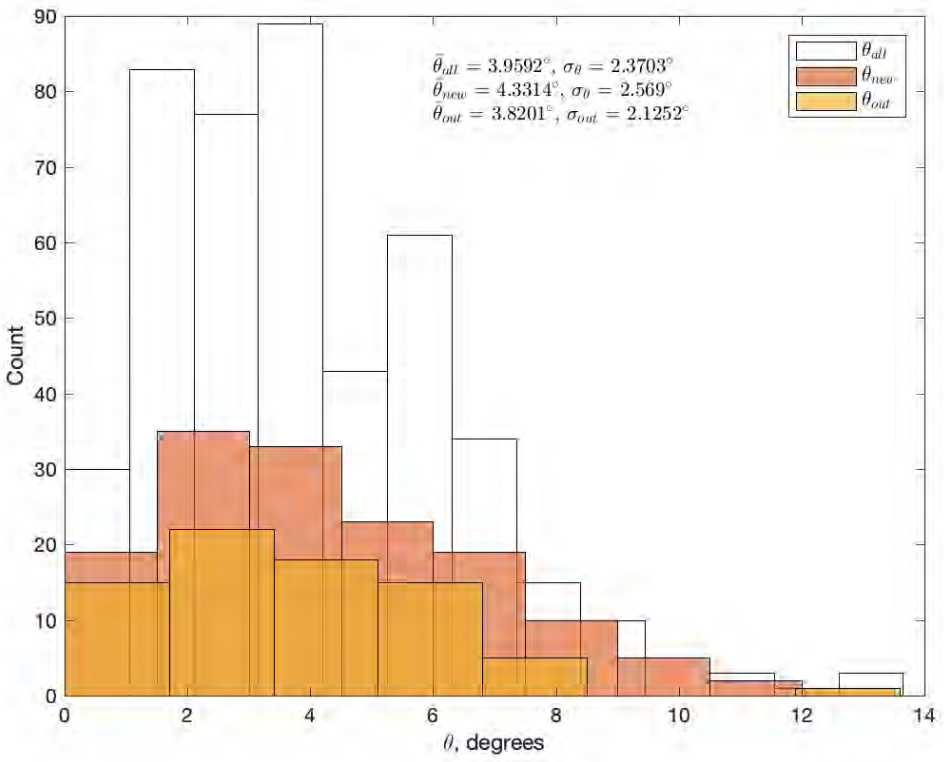


FIGURE 5.28: Orientation of the constant withdrawal rate 100 μms^{-1} sample for all dendrite primary trunks, outcompeted dendrites and newly created dendrites.

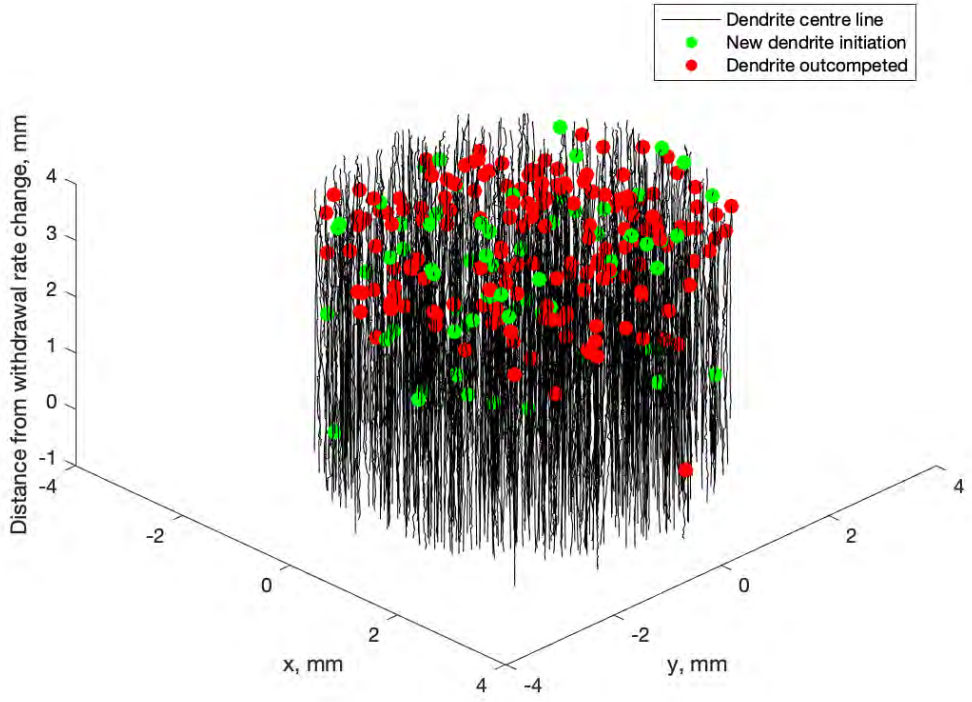


FIGURE 5.29: Dendrite forest of centres traced along the length of the 40-80 μms^{-1} changing withdrawal rate sample.

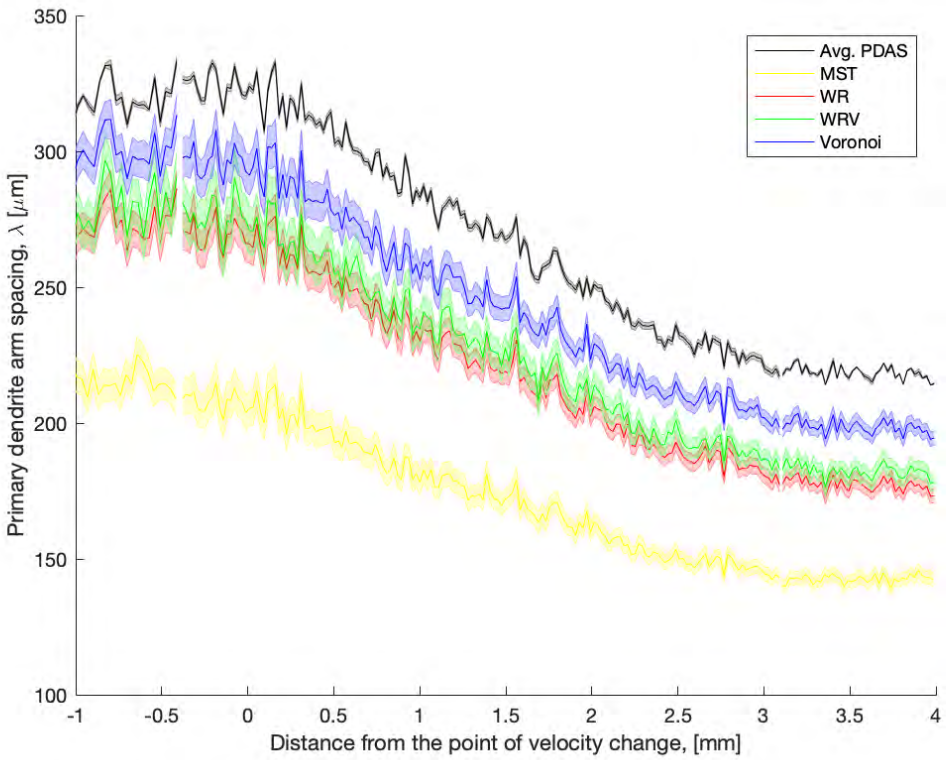


FIGURE 5.30: Primary dendrite arm spacing along the length of the changing withdrawal rate 40-80 μms^{-1} sample.

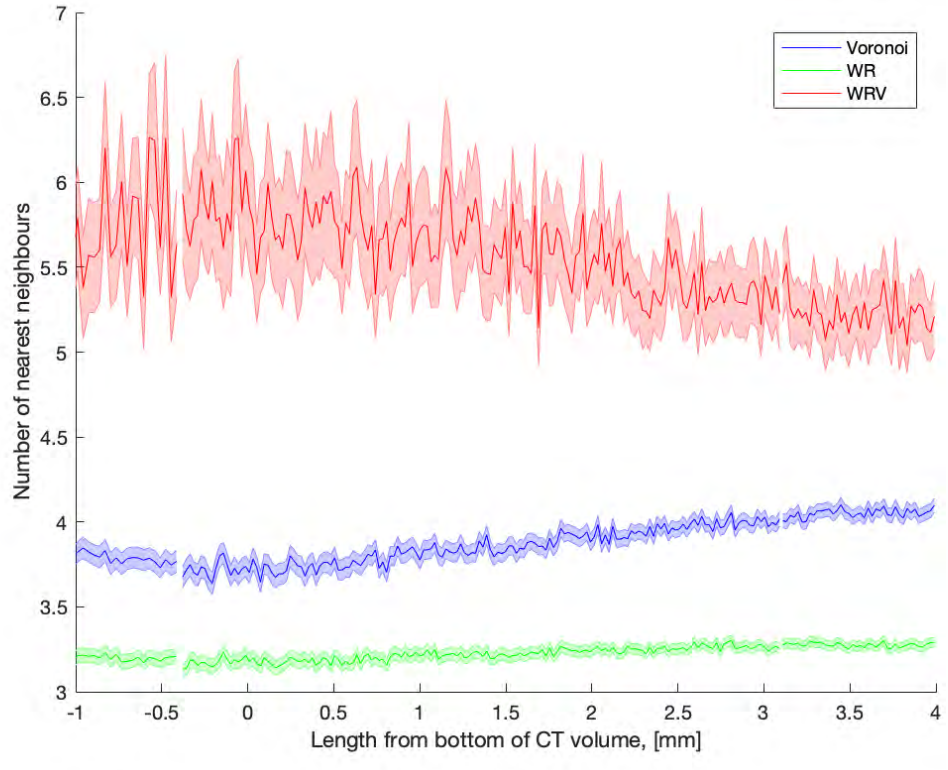


FIGURE 5.31: Number of nearest neighbours along the 40 to 80 μms^{-1} changing withdrawal rate sample.

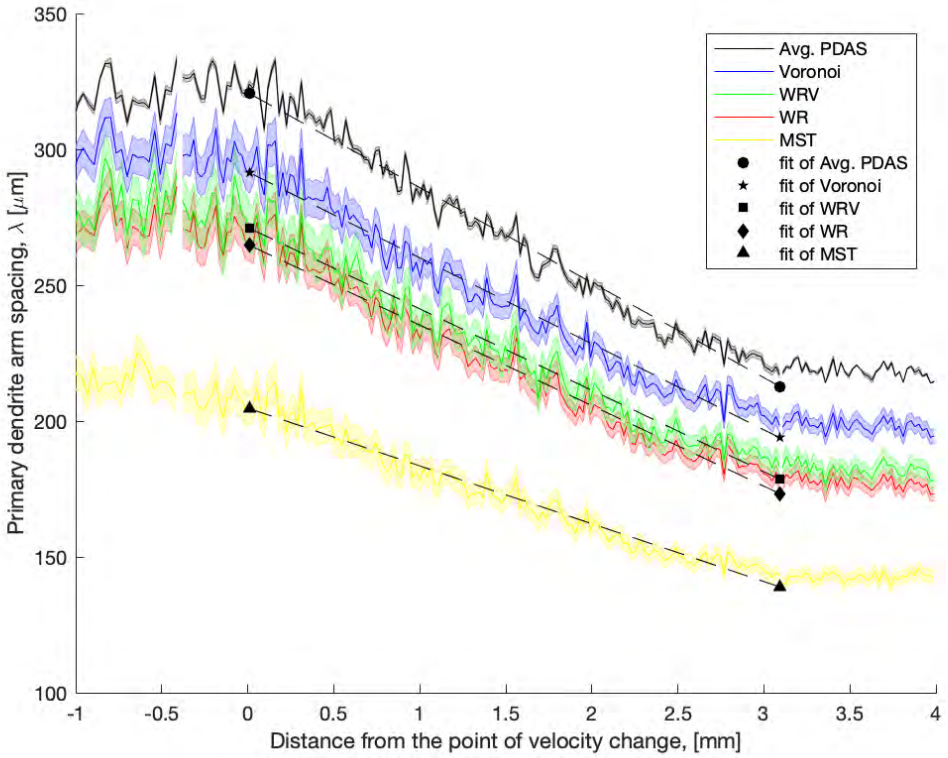


FIGURE 5.32: Primary dendrite arm spacing along the length of the changing withdrawal rate 40-80 μms^{-1} sample.

TABLE 5.1: Equations for each linear fit of each calculated **PDAS** as a function of distance from velocity change ($\lambda(d_{\Delta v})$) in Figure 5.32 and the goodness of each fit.

Symbol	**PDAS** Calculation Method	Equation, $\lambda(d_{\Delta v})$	R^2
●	Avg	-34.97$d_{\Delta v}$ + 320.87	0.9788
▲	MST	-31.63$d_{\Delta v}$ + 291.69	0.9700
♦	WR	-29.96$d_{\Delta v}$ + 271.24	0.9670
■	WRV	-29.64$d_{\Delta v}$ + 264.96	0.9713
★	Voronoi	-21.27$d_{\Delta v}$ + 204.75	0.9670

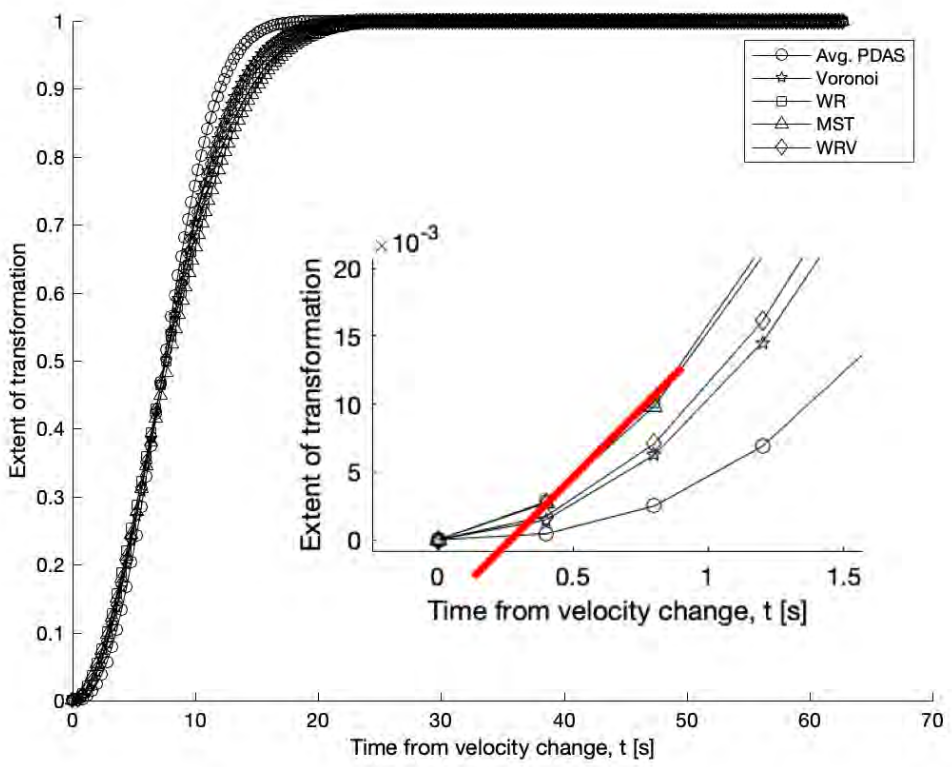


FIGURE 5.33: JMAK analysis of the change in **PDAS** after the withdrawal rate change from 40 μms^{-1} to 80 μms^{-1}. The inset shows a zoomed in portion of the graph showing an indication of the incubation time after the transition.

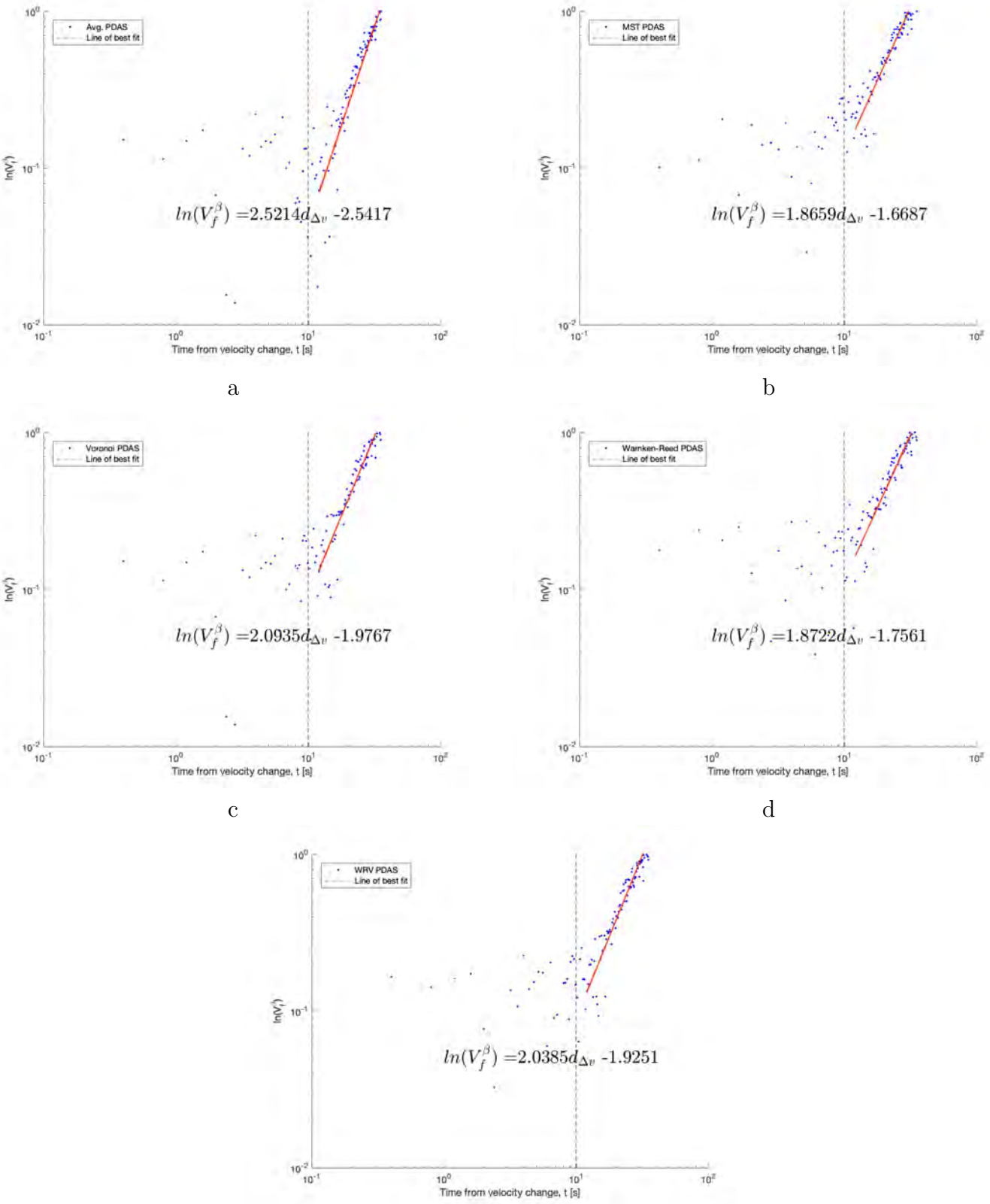


FIGURE 5.34: Results of Avrami analysis for the different **PDAS** calculation methods in the 40 - 80 μms^{-1} changing withdrawal rate sample after the withdrawal rate change from 40 μms^{-1} to 80 μms^{-1}. a) Average **PDAS**, b) MST **PDAS**, c) Voronoi **PDAS**, d) WR **PDAS**, e) WRV **PDAS**.

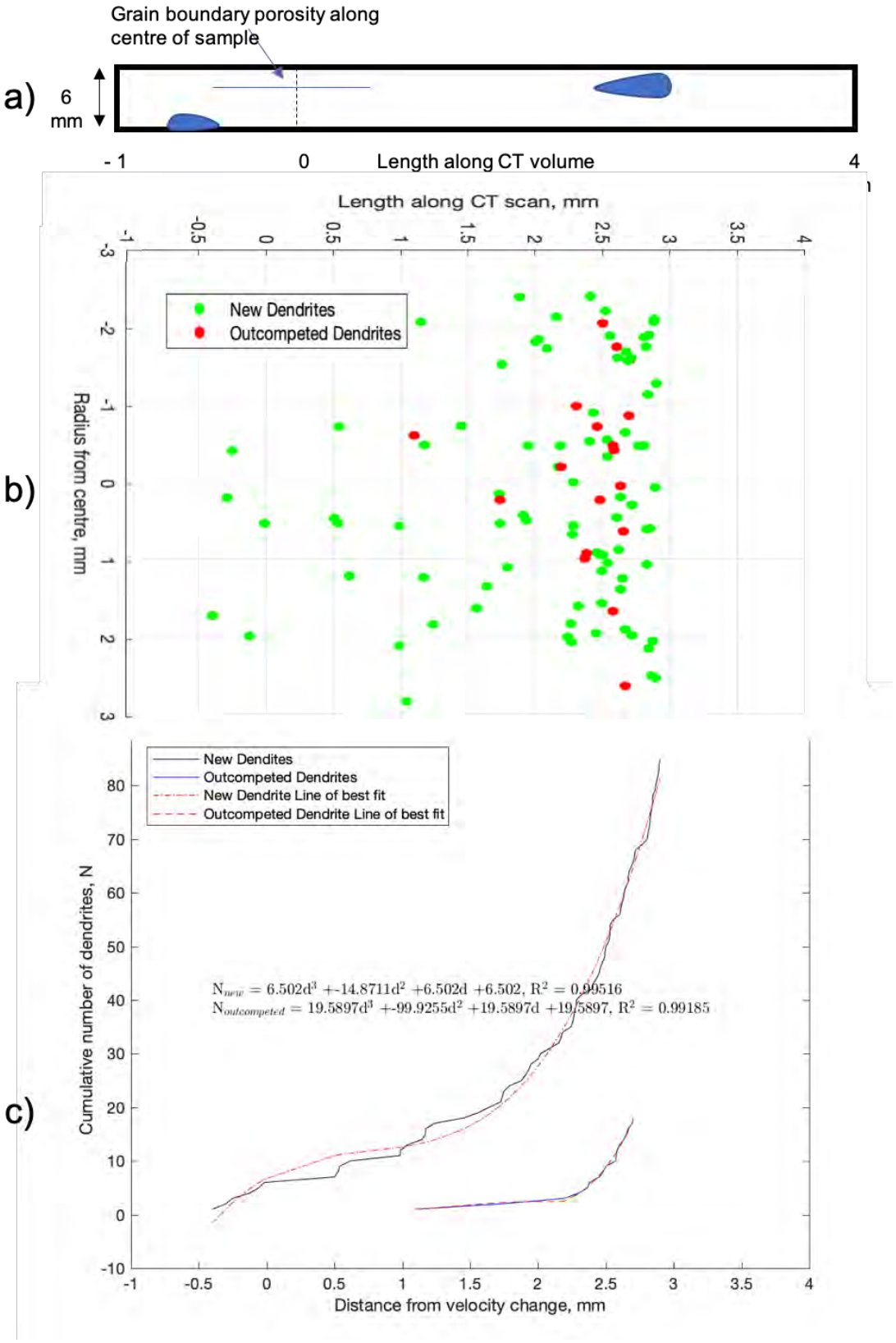


FIGURE 5.35: a) Schematic showing location of porosity within the 40-80 μms^{-1} changing withdrawal rate sample. b) Location of new dendrites and outcompeted dendrites in the sample when viewed side on. c) Cumulative number of new and outcompeted dendrites with a third order polynomial fit.

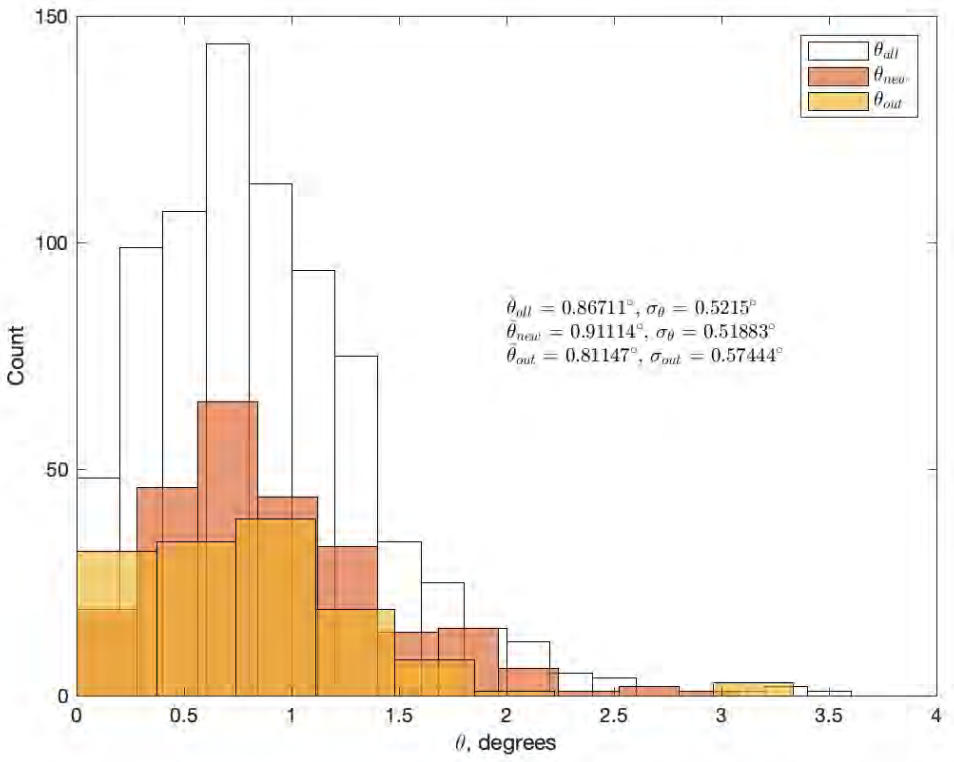


FIGURE 5.36: Orientation of the varying withdrawal rate 40-80 μms^{-1} sample for all dendrite primary trunks, outcompeted dendrites and newly created dendrites.

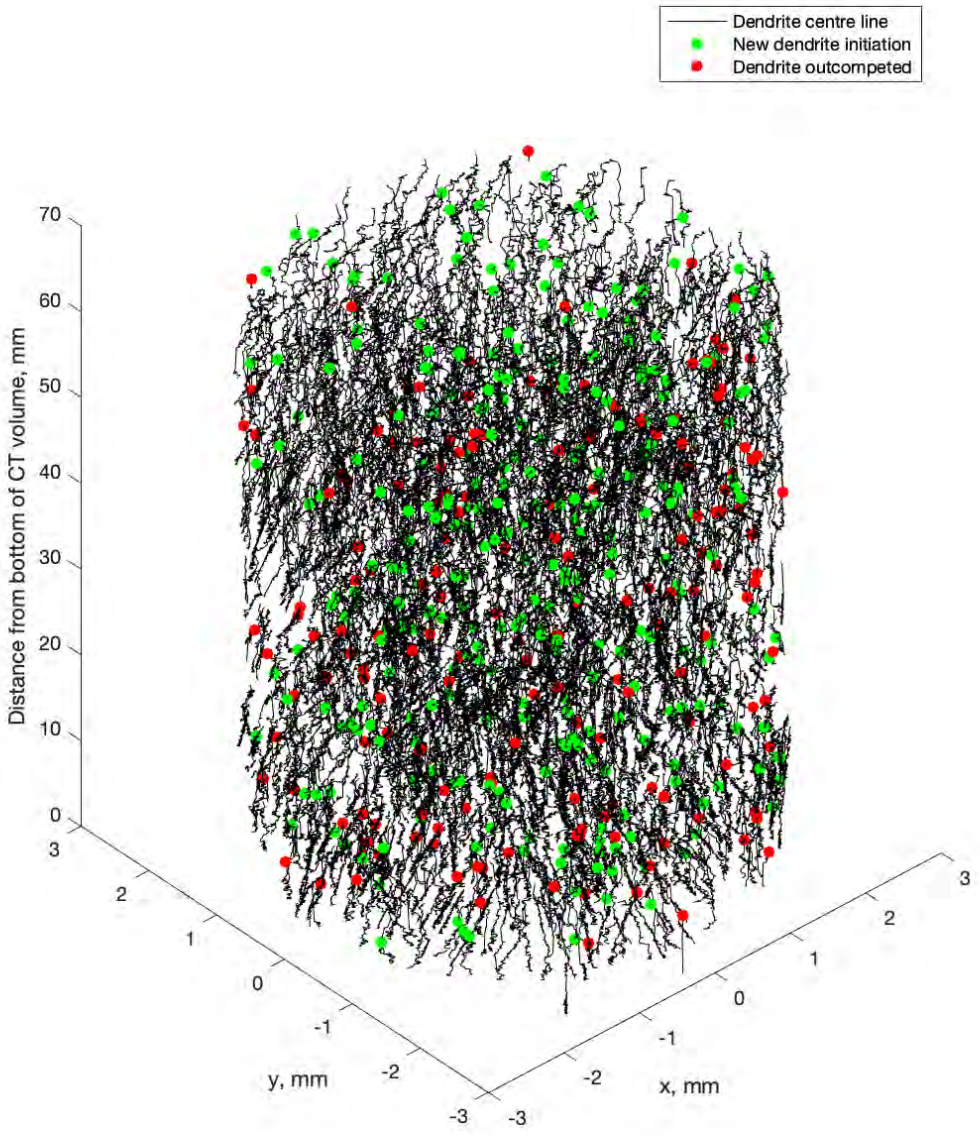


FIGURE 5.37: Dendrite forest of centres traced along the length of the 40-60-80 μms^{-1} changing withdrawal rate sample.

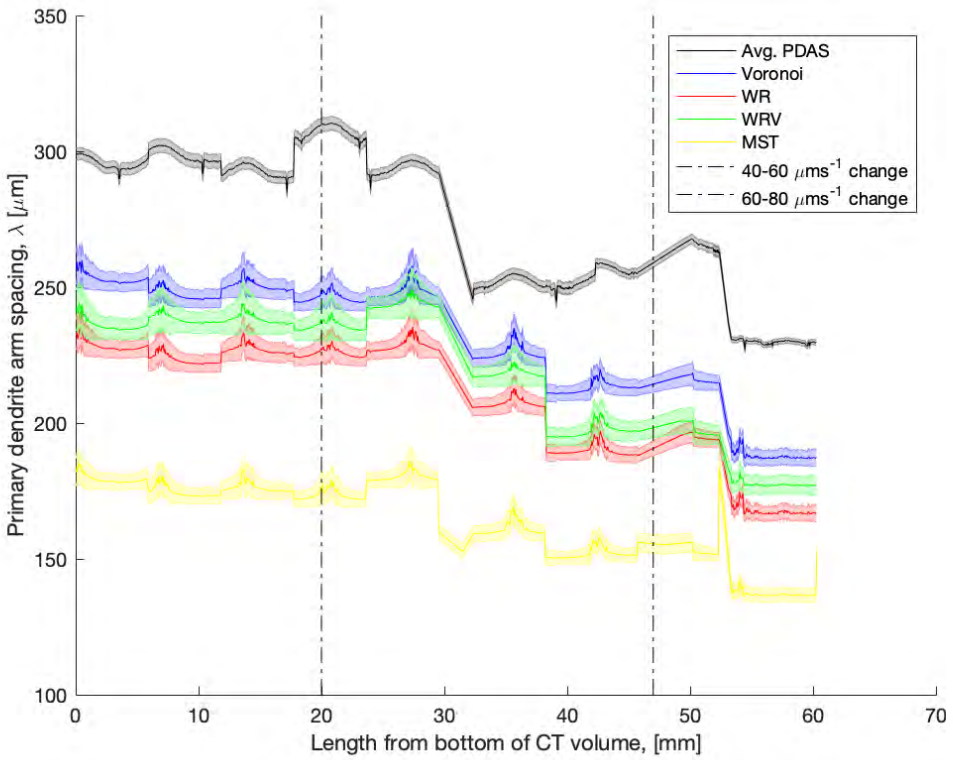


FIGURE 5.38: Primary dendrite arm spacing along the length of the changing withdrawal rate 40-60-80 μms^{-1} sample.

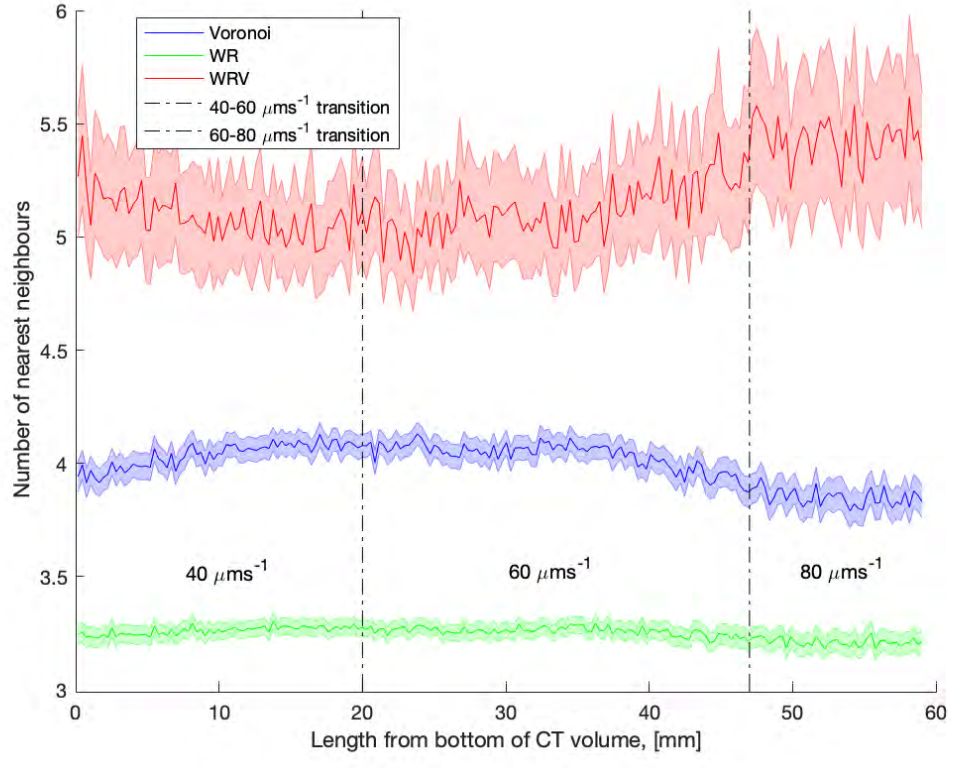


FIGURE 5.39: Number of nearest neighbours along the 40-60-80 μms^{-1} varying withdrawal rate sample.

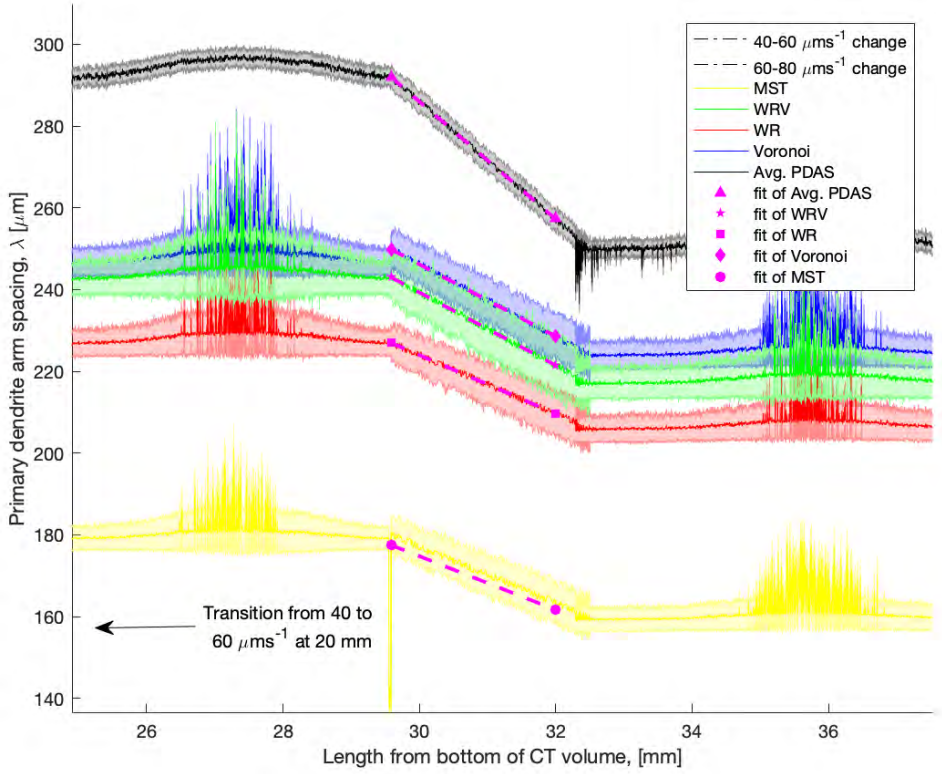


FIGURE 5.40: Primary dendrite arm spacing along the length of the changing withdrawal rate 40-60-80 μms^{-1} sample after the first withdrawal change from 40 μms^{-1} to 60 μms^{-1}

TABLE 5.2: Equations for each linear fit of **PDAS** as a function of distance from velocity change ($\lambda(d_{\Delta v})$) in Figure 5.40 and the goodness of each fit.

Symbol	**PDAS** Calculation Method	Equation, $\lambda(d_{\Delta v})$	R^2
▲	Avg	-14.38d$_{\Delta v}$ + 717.4	0.9992
●	MST	-6.562d$_{\Delta v}$ + 343.6	0.9984
■	WR	-7.178d$_{\Delta v}$ + 439.3	0.9975
★	WRV	-8.912d$_{\Delta v}$ + 506.7	0.9966
♦	Voronoi	-8.815d$_{\Delta v}$ + 510.6	0.9470

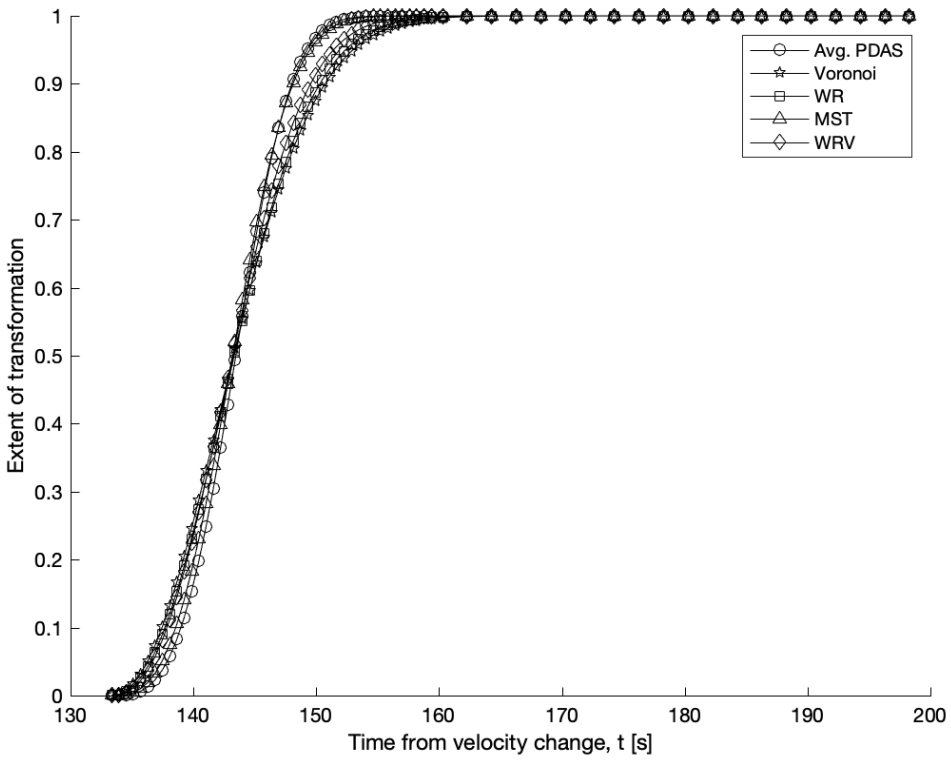


FIGURE 5.41: JMAK analysis of the change each of calculated **PDAS** after the withdrawal rate change from 40 μms^{-1} to 60 μms^{-1} in the 40-60-80 μms^{-1} sample.

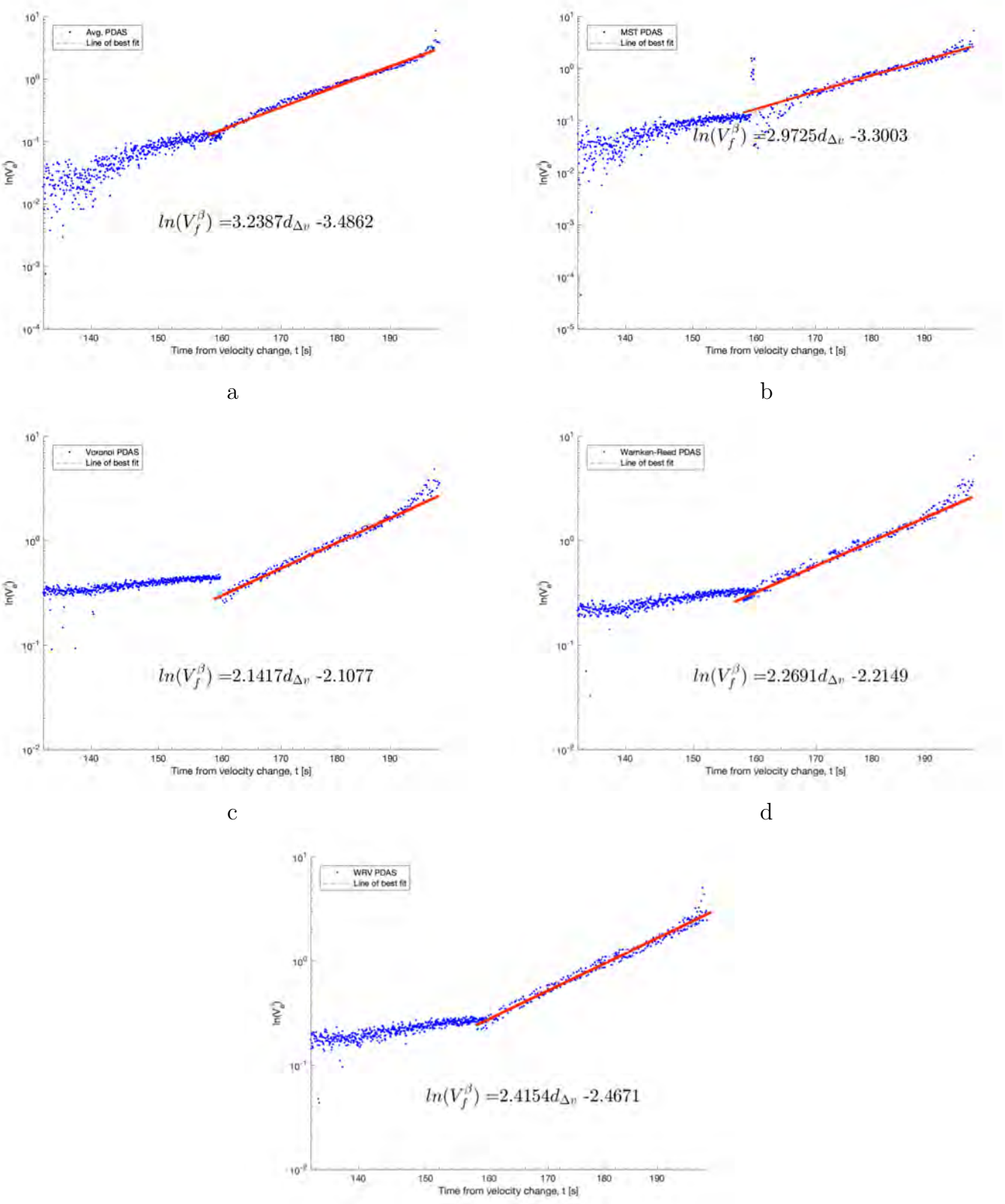


FIGURE 5.42: Results of Avrami analysis for the different **PDAS** calculation methods in the 40 - 60 - 80 μms^{-1} changing withdrawal rate sample after the withdrawal rate change from 40 μms^{-1} to 60 μms^{-1}. a) Average **PDAS**, b) MST **PDAS**, c) Voronoi **PDAS**, d) WR **PDAS**, e) WRV **PDAS**.

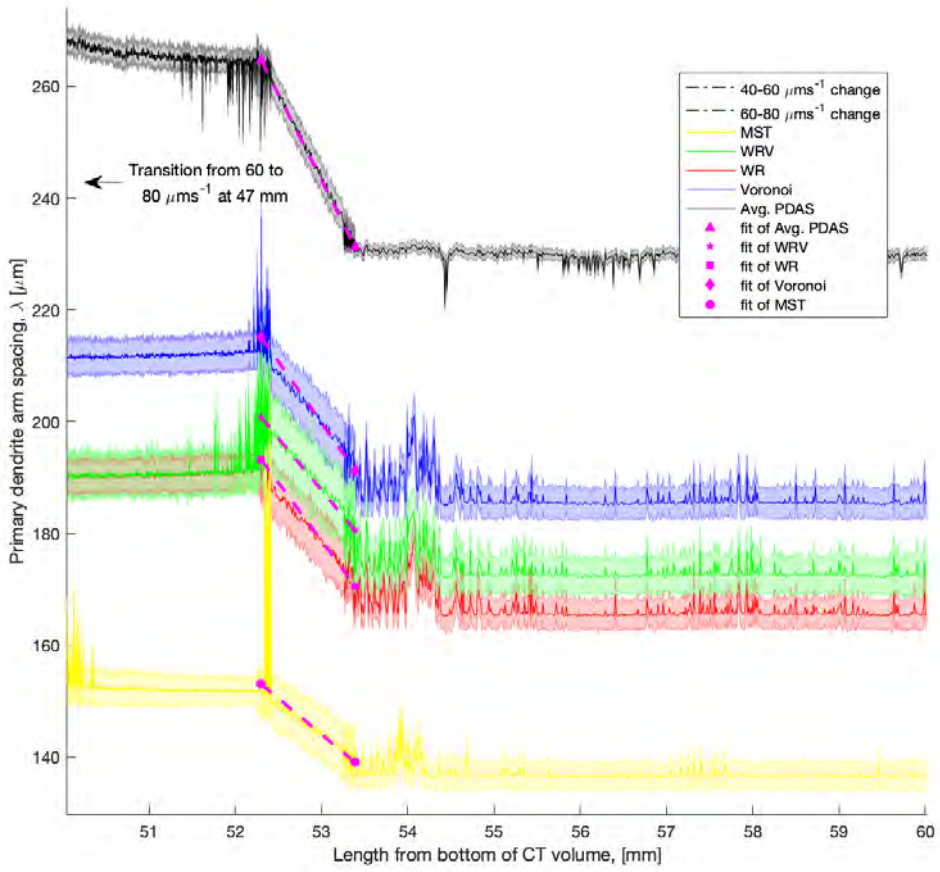


FIGURE 5.43: Primary dendrite arm spacing along the length of the changing withdrawal rate 40-60-80 μms^{-1} sample after the second withdrawal change from 60 μms^{-1} to 80 μms^{-1}

TABLE 5.3: Equations for each linear fit of **PDAS** as a function of distance from velocity change ($\lambda(d_{\Delta v})$) in Figure 5.43 and the goodness of each fit.

Symbol	**PDAS** Calculation Method	Equation, $\lambda(d_{\Delta v})$	R^2
▲	Avg	-30.74d$_{\Delta v}$ + 1872	0.9939
●	MST	-12.86d$_{\Delta v}$ + 825.4	0.9263
■	WR	-18.62d$_{\Delta v}$ + 1175	0.9232
★	WRV	-20.76d$_{\Delta v}$ + 1279	0.9327
♦	Voronoi	-21.91d$_{\Delta v}$ + 1361	0.9117

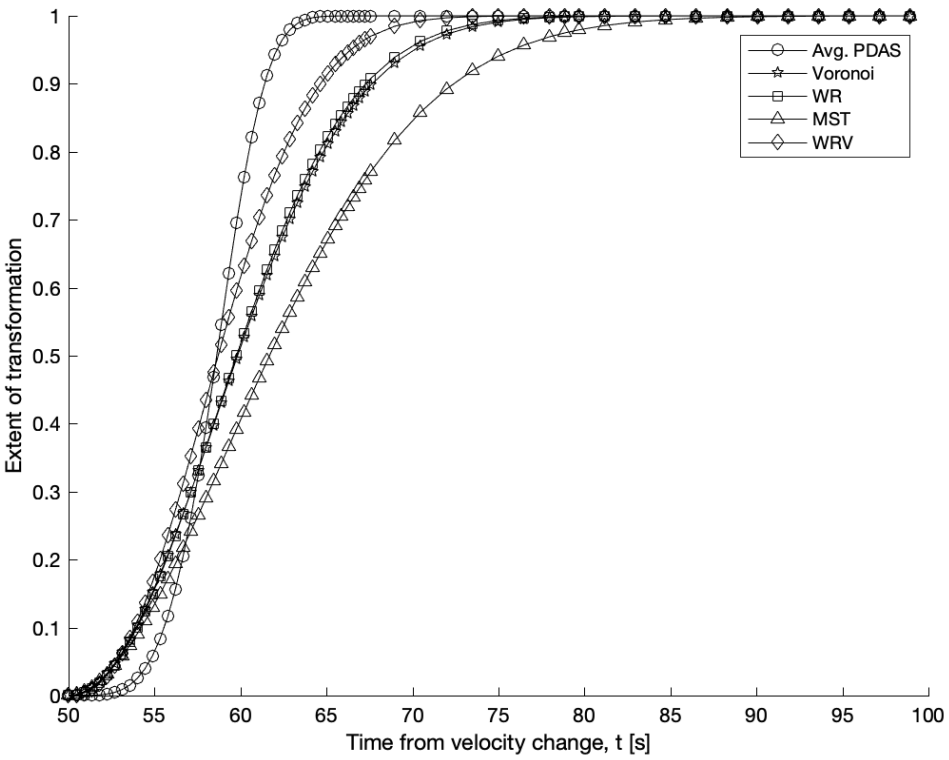
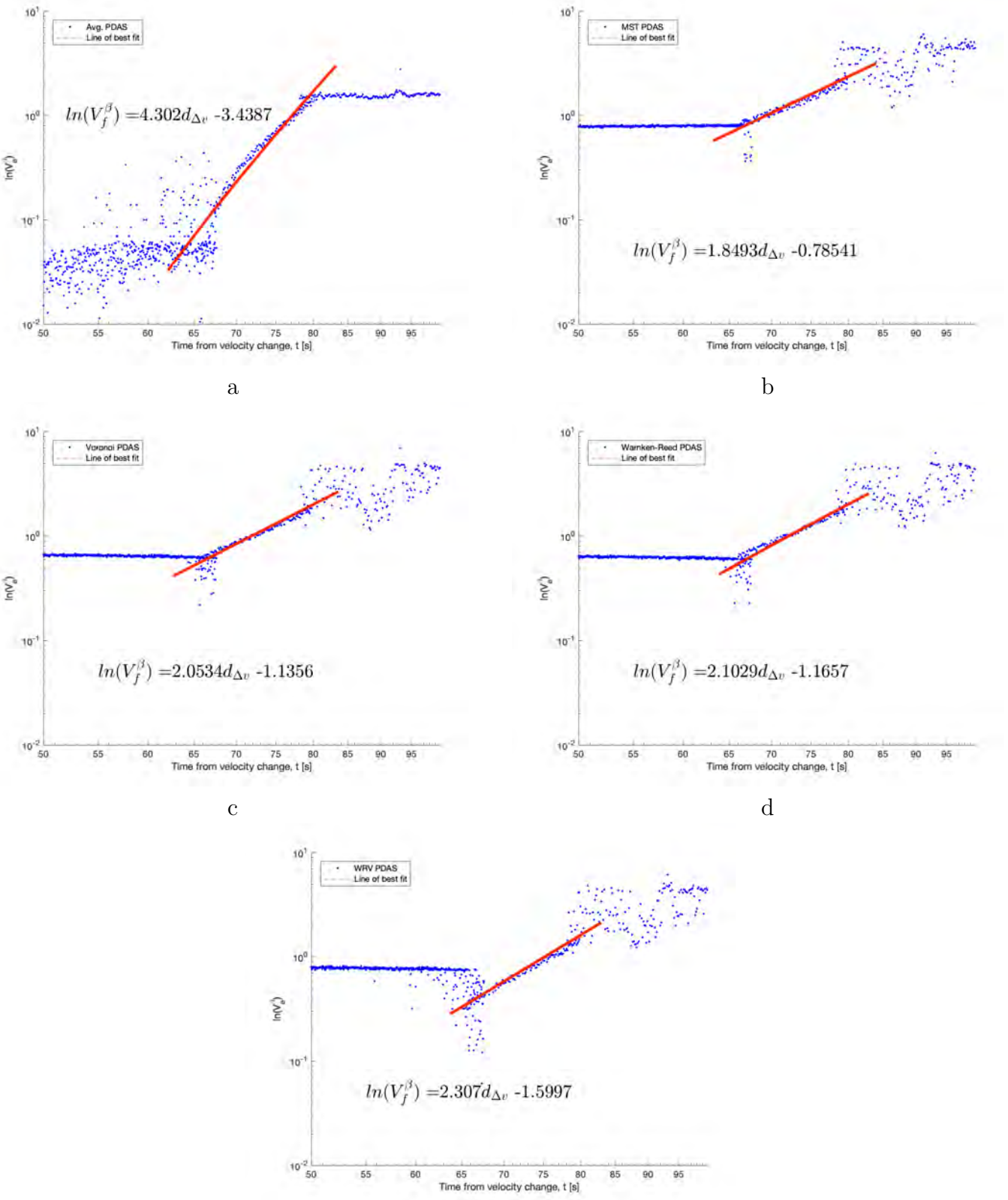


FIGURE 5.44: JMAK analysis of the change in each calculated **PDAS** after the withdrawal rate change from 60 μms^{-1} to 80 μms^{-1} in the 40-60-80 μms^{-1} sample.



a b c d e

FIGURE 5.45: Results of Avrami analysis for the different **PDAS** calculation methods in the 40 - 60 - 80 μms^{-1} changing withdrawal rate sample after the withdrawal rate change from 60 μms^{-1} to 80 μms^{-1}. a) Average **PDAS**, b) MST **PDAS**, c) Voronoi **PDAS**, d) WR **PDAS**, e) WRV **PDAS**.

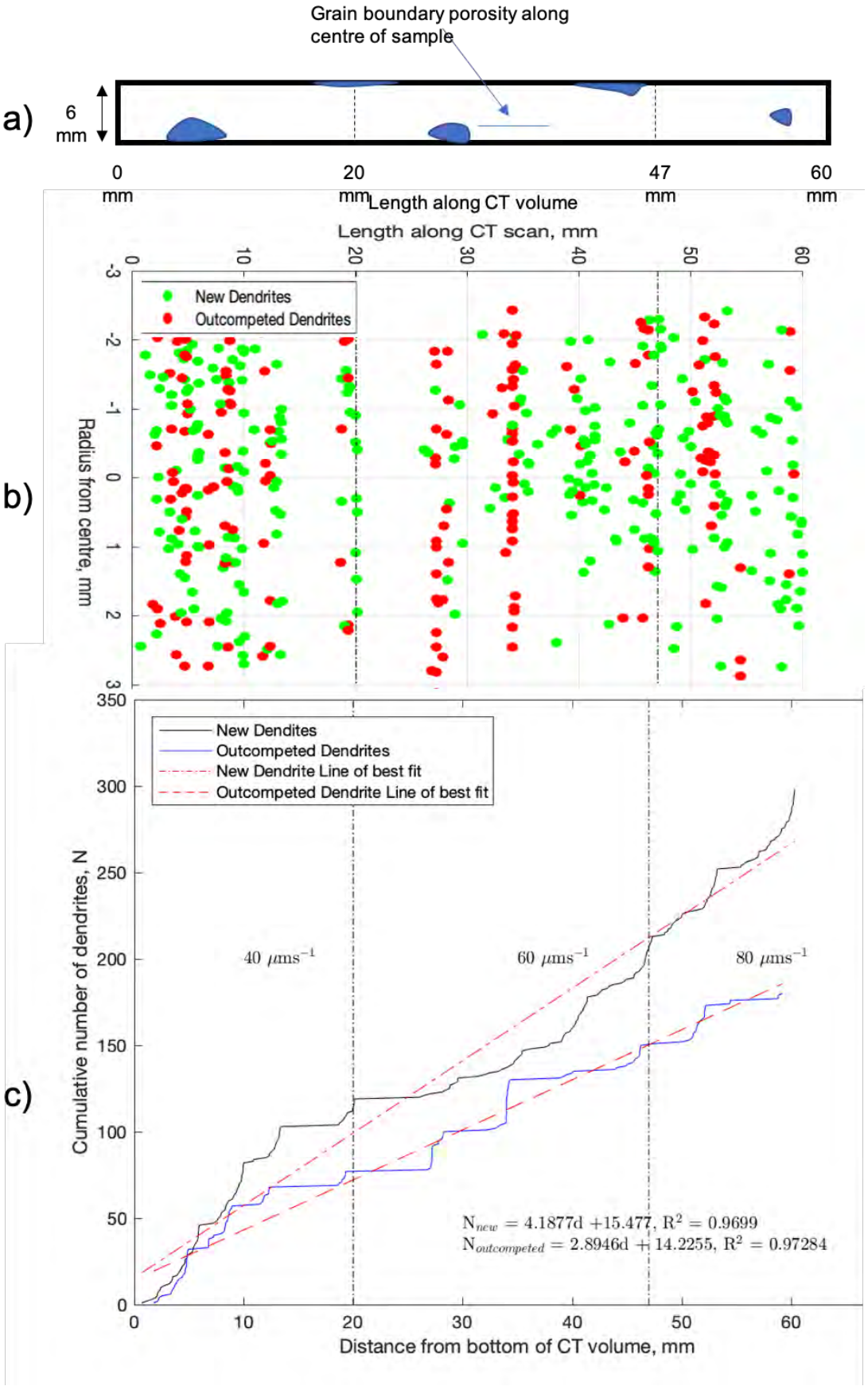


FIGURE 5.46: a) Schematic showing location of porosity within the 40-60-80 μms^{-1} changing withdrawal rate sample. b) Location of new dendrites and outcompeted dendrites in the sample when viewed side on. c) Cumulative number of and outcompeted dendrites with a linear fit for all the dendrites.

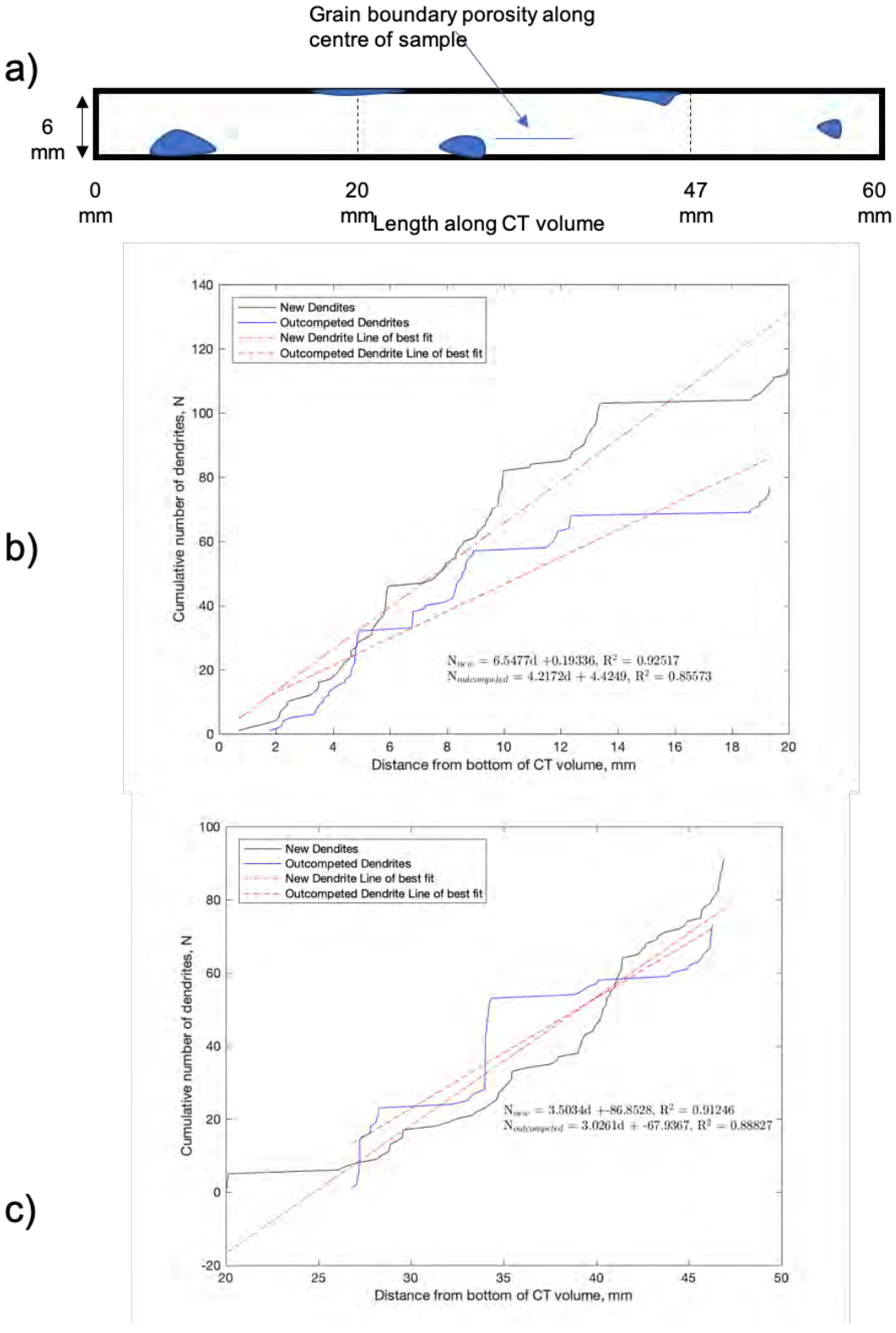


FIGURE 5.47: a) Schematic showing location of porosity within the 40-60-80 μms^{-1} changing withdrawal rate sample. b) Cumulative number of and outcompeted dendrites with a linear fit for the 40 μms^{-1} section. c) Cumulative number of and outcompeted dendrites with a linear fit for all the dendrites for the 60 μms^{-1} section.

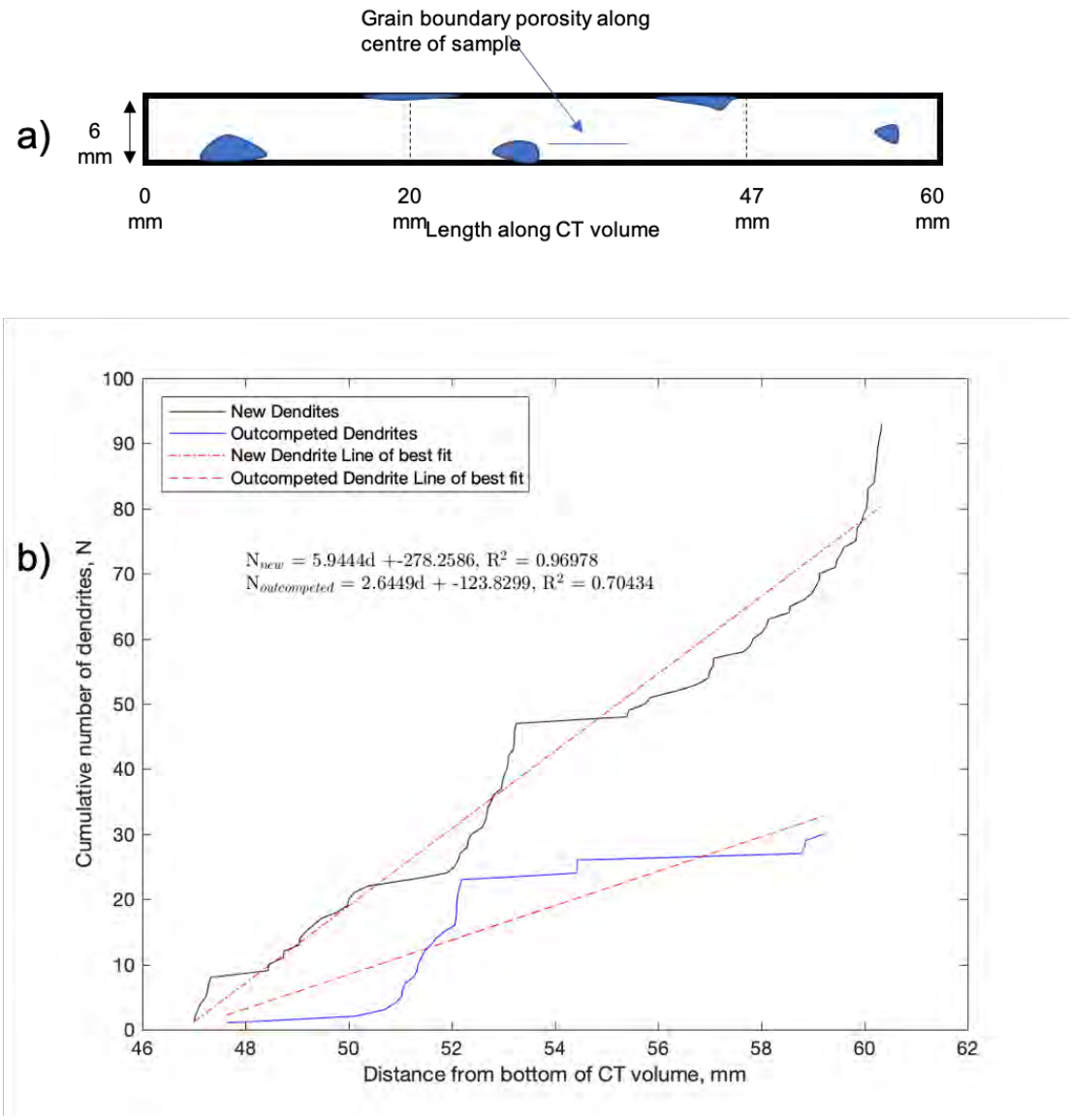


FIGURE 5.48: a) Schematic showing location of porosity within the 40-60-80 μms^{-1} changing withdrawal rate sample. b) Cumulative number of and outcompeted dendrites with a linear fit for all the dendrites for the 80 μms^{-1} section.

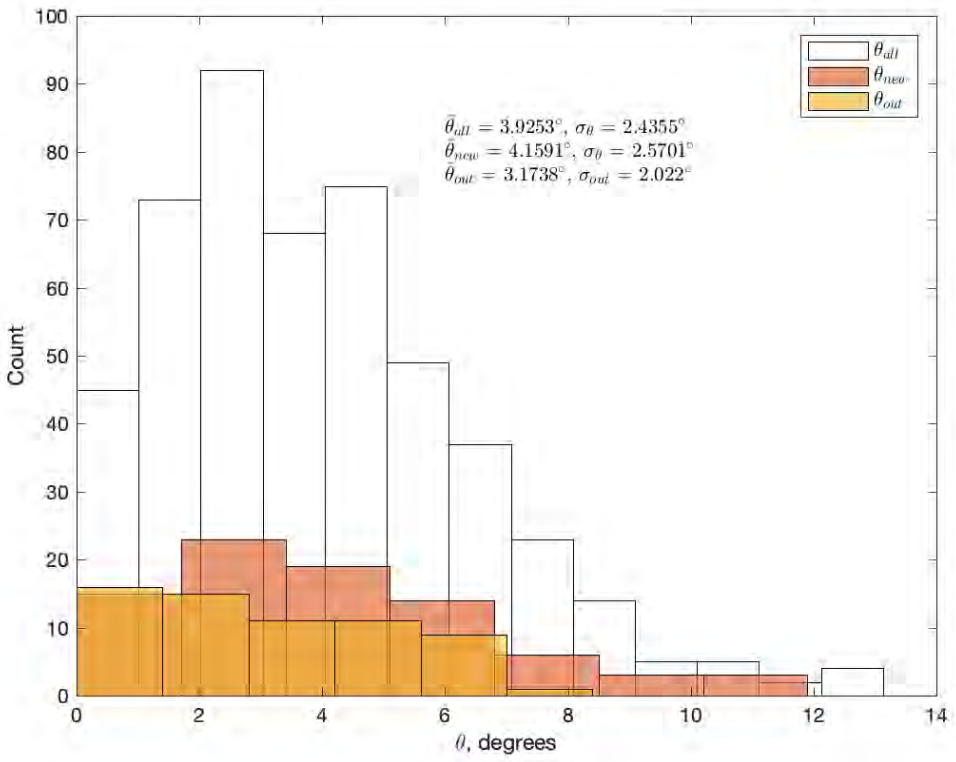


FIGURE 5.49: Orientation of the varying withdrawal rate 40-60-80 μms^{-1} sample for all dendrite primary trunks, outcompeted dendrites and newly created dendrites.

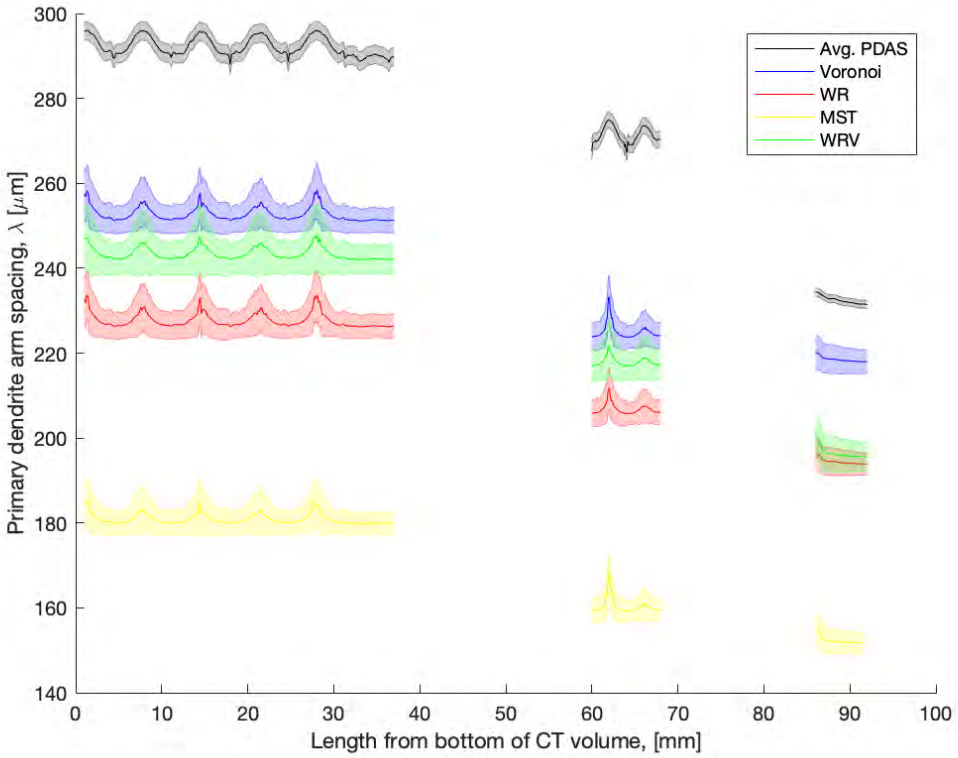


FIGURE 5.50: Primary dendrite arm spacing along the length of the changing withdrawal rate 40-60-100 μms^{-1} sample.

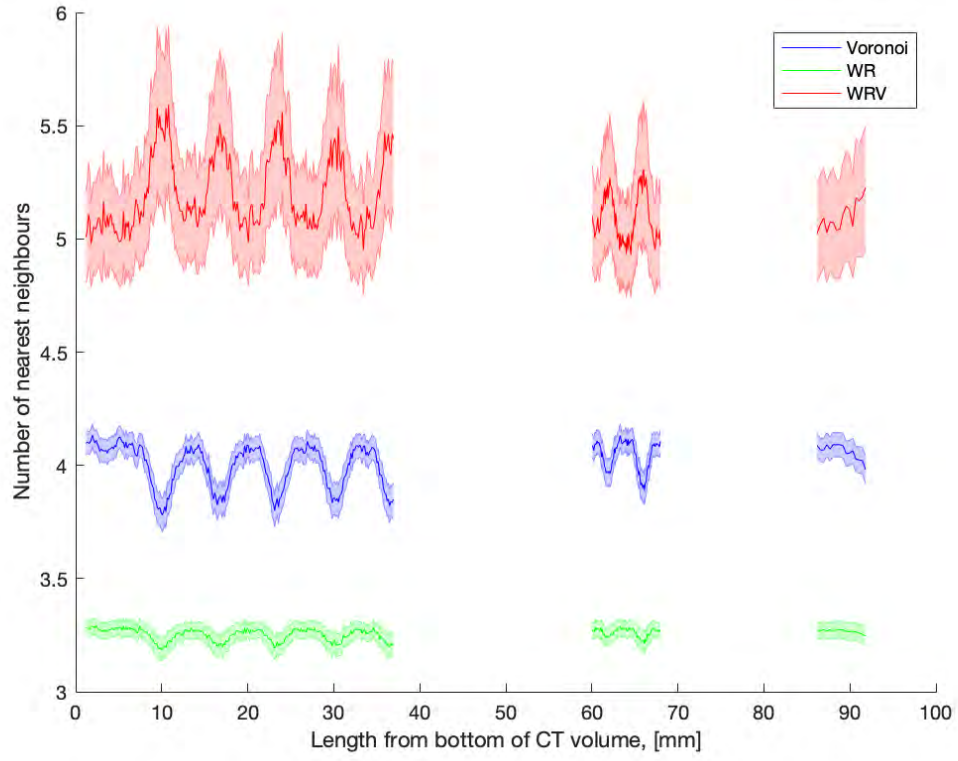


FIGURE 5.51: Number of nearest neighbours along the 40-60-100 μms^{-1} varying withdrawal rate sample.

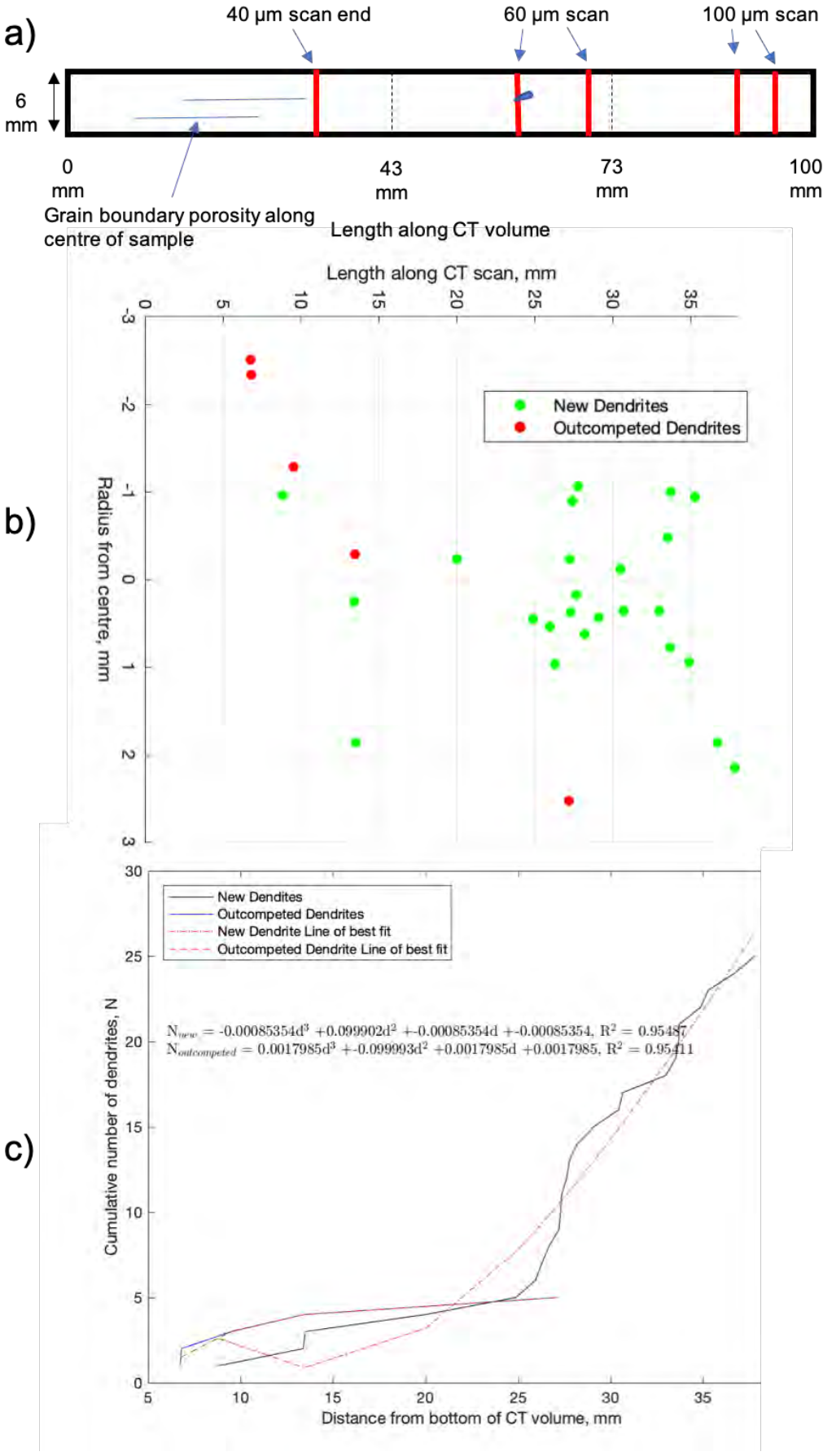


FIGURE 5.52: a) Schematic showing location of porosity within the 40 μms^{-1} section of the 40-60-100 μms^{-1} changing withdrawal rate sample. b) Location of new dendrites and outcompeted dendrites in the sample when viewed side on. c) Cumulative number of and outcompeted dendrites with a third order polynomial fit for the 40 μms^{-1} section.

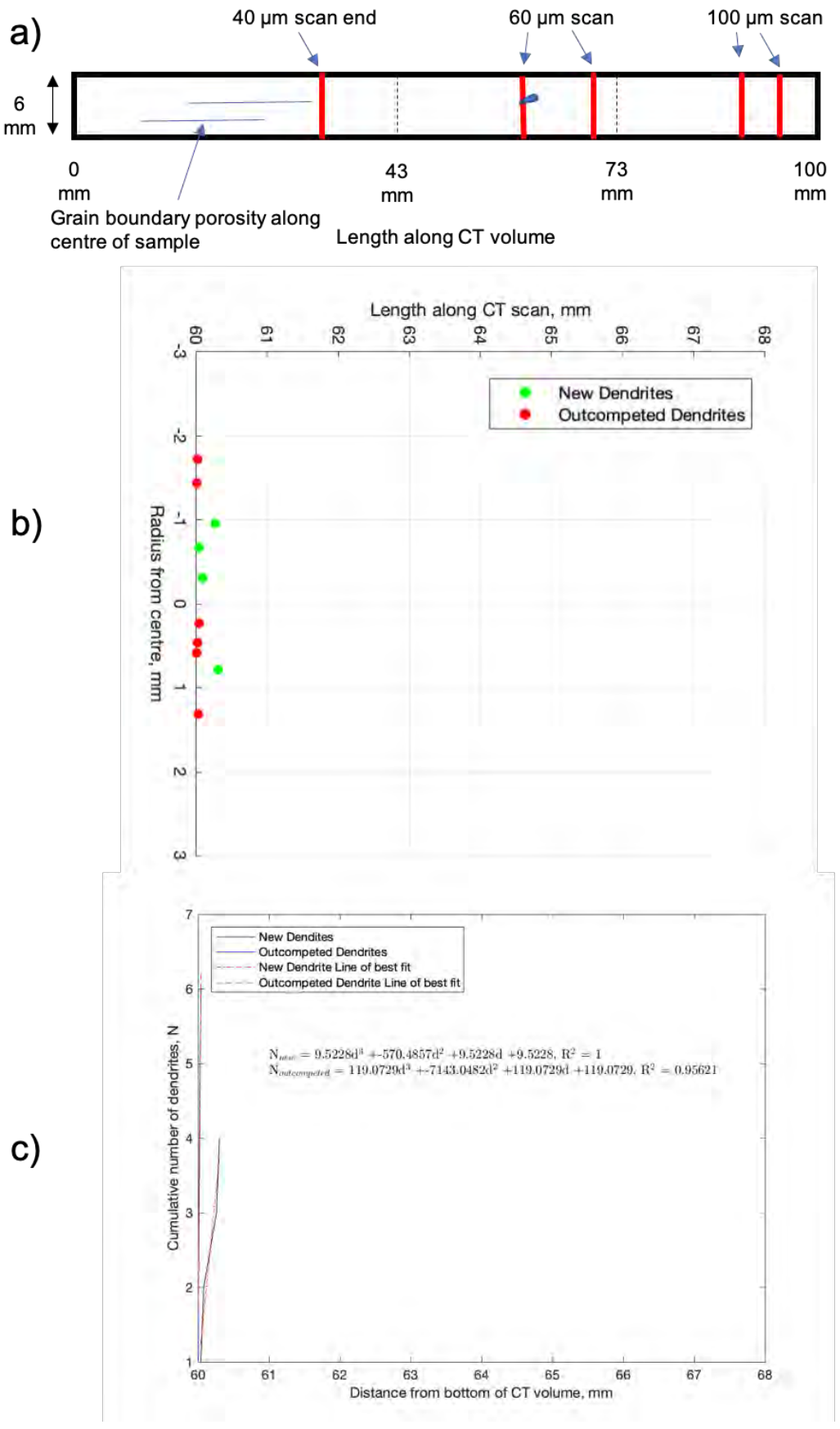


FIGURE 5.53: a) Schematic showing location of porosity within the 60 μms^{-1} section of the 40-60-100 μms^{-1} changing withdrawal rate sample. b) Location of new dendrites and outcompeted dendrites in the sample when viewed side on. c) Cumulative number of and outcompeted dendrites with a third order polynomial fit for the 60 μms^{-1} section.

5.2 Number of Nearest Neighbours Along the Length of the Samples

The number of nearest neighbours for each of the samples is given in Figures 5.11, 5.16, 5.21, 5.26, 5.31, 5.39 and 5.51. The number of nearest neighbours was calculated using the Voronoi, Warnken-Reed and Voronoi-Warnken-Reed methods. For the constant withdrawal rate samples Figures 5.11, 5.16, 5.21 and 5.26 the number of nearest neighbours remains constant along the length of the sample. However for the samples which undergo a change in the withdrawal rate–Figures 5.31, 5.39 and 5.51–it can be seen that there is a change in the number of nearest neighbours in each case which corresponds to the location of the withdrawal rate change.

5.3 JMAK and Avrami

The changing withdrawal rate experiments were analysed using **JMAK** and Avrami equation Equation (2.12) in Figures 5.33, 5.34, 5.41, 5.42, 5.44 and 5.45 and section 5.9. The equations calculated from fitting curves for each of the lines are shown on the figures themselves. The Avrami fits for the Warnken-Reed **PDAS** are collated in Table 5.4 and shown graphically in Section 5.9.

5.4 Porosity Within the Samples and Location of Newly Initiated and Outcompeted Dendrites

The schematic sub-figures a) in Figures 5.12, 5.17, 5.22, 5.27, 5.35, 5.46 to 5.48, 5.52 and 5.53 show the approximate locations of porosity within the sample. These schematic figures were created by reviewing the **CT** images of the samples slice by slice and noting the approximate location along the length of the sample and size of said porosity.

In sub-figures b) of Figures 5.12, 5.17, 5.22, 5.27, 5.35, 5.46 to 5.48, 5.52 and 5.53 the location of newly created dendrites and those outcompeted are shown along the length of the sample. The cumulative number of newly formed dendrites and outcompeted dendrites are then shown in sub-figures c) of Figures 5.12, 5.17, 5.22, 5.27, 5.35, 5.46 to 5.48, 5.52 and 5.53. As can be noted between the schematic figures and the location of dendrites being outcompeted there is a clustering of dendrites being outcompeted in parts of the sample with porosity present. Especially in locations where pores are within or toward the centre of the samples.

5.5 Misorientation of the Dendrites to the Z-Axis

The misorientation of the dendrites as calculated using the method described in Section 4.6 are given in Figures 5.13, 5.18, 5.23, 5.28, 5.36 and 5.49. In each case the newly created dendrites show a strong alignment to the parent dendrites. The dendrites which are outcompeted have a mean angle which is generally a number of degrees from the average for the whole dendrite array.

TABLE 5.4: Avrami equations fitted for the Warnken-Reed calculated **PDAS** for the changing withdrawal rate samples.

Transition	**Avrami Equation**	R^2
40 - 60 μms^{-1}	$2.25\mathrm{d}_{\Delta v} - 2.21$	0.911
60 - 80 μms^{-1}	$2.10\mathrm{d}_{\Delta v} - 1.17$	0.869
40 - 80 μms^{-1}	$1.87\mathrm{d}_{\Delta v} - 1.76$	0.967

5.6 Minimum-Spanning-Tree Packing Factor

The packing factor for each of the samples obtained from the **MST** method are shown in Figures 5.54 to 5.56. The value of σ^* and m^* was calculated for each slice along the length of each of the **CT** volumes. As the 40-60-100 μms^{-1} sample was damaged the results of the **MST** method are not shown for the three regions. There was little to no variation shown in this sample from the results seen in any of the other samples. The constant withdrawal rate samples 40, 60 and 100 μms^{-1} were indicative of the results of the 40-60-100 μms^{-1} sample.

5.7 PDAS for All samples

The local and bulk **PDAS** for each of the samples is collated from Figures 5.10, 5.15, 5.20, 5.25, 5.30, 5.38 and 5.50 into Figure 5.57 and Table 5.5 for the Warnken-Reed PDAS. The results of the other local **PDAS** calculation methods are given below in Figure 5.58. The tabulated results in Figure 5.57 are shown in comparison with curves calculated with the hunt, Trivedi, Kurz-Fisher and Bouchard-Kirkaldy given by Equations (2.23) to (2.26). The curves were calculated using the data taken from Table 1 of Chapter 11 and Table 9.3 of Chapter 9.

The rates of change for the changing withdrawal rate samples calculated using the Warnken-Reed PDAS are collated for ease of reference in Table 5.6. These results show that there is an increase in the rate of change in **PDAS**/mm as the final velocity increases, and also as the change in velocity increases. The rates of change in each of the **PDAS** calculation methods are shown graphically in Section 5.9, the rates of change in this graph are given in $\mu m/\mu m$.

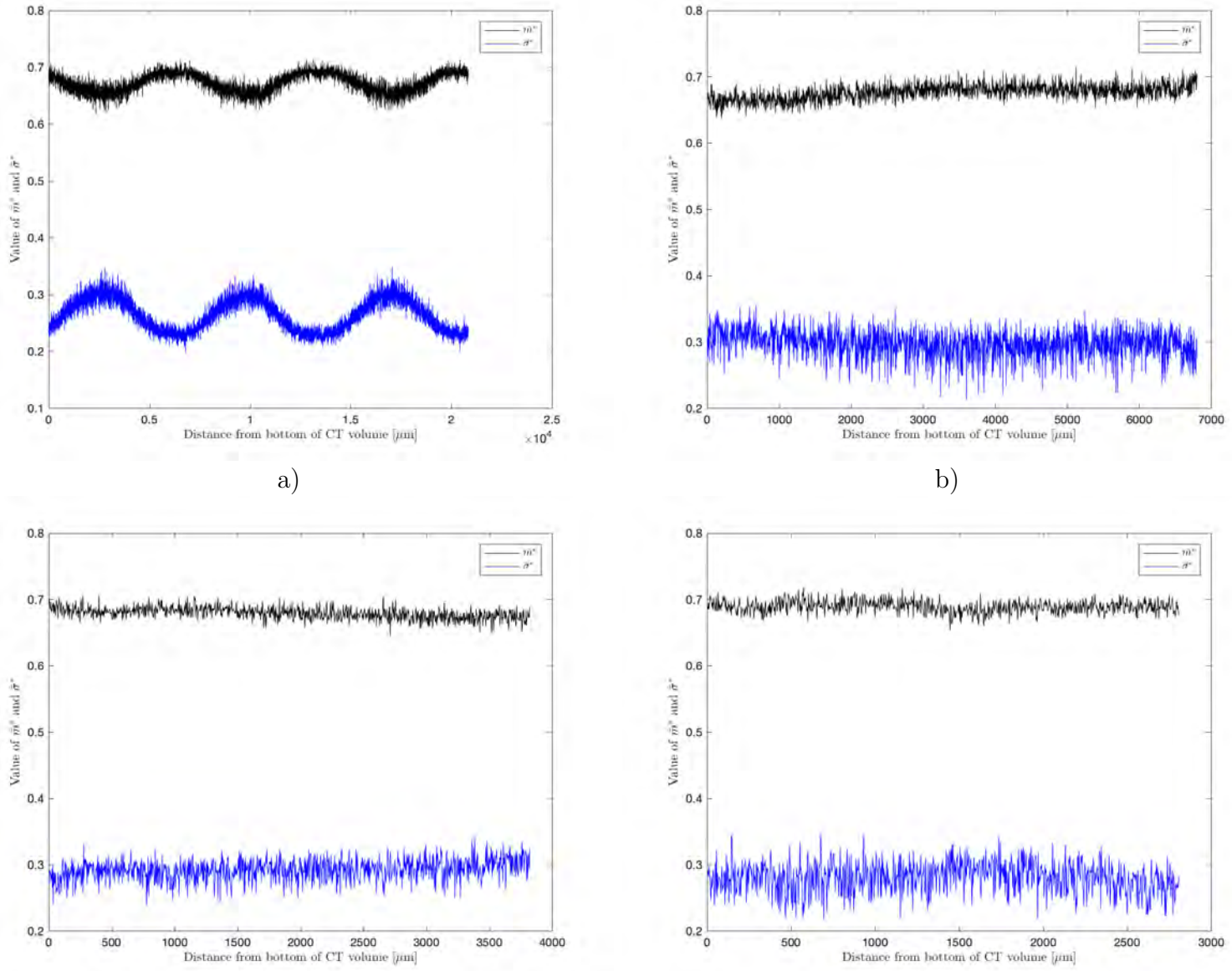


FIGURE 5.54: a) The $\bar{m}^*$, $sig\bar{m}a^*$ pairing for each slice along the length of the 40 μms^{-1} sample. b) The $\bar{m}^*$, $sig\bar{m}a^*$ pairing for each slice along the length of the 60 μms^{-1} sample. c) The $\bar{m}^*$, $sig\bar{m}a^*$ pairing for each slice along the length of the 80 μms^{-1} sample. d) The $\bar{m}^*$, $sig\bar{m}a^*$ pairing for each slice along the length of the 100 μms^{-1} sample.

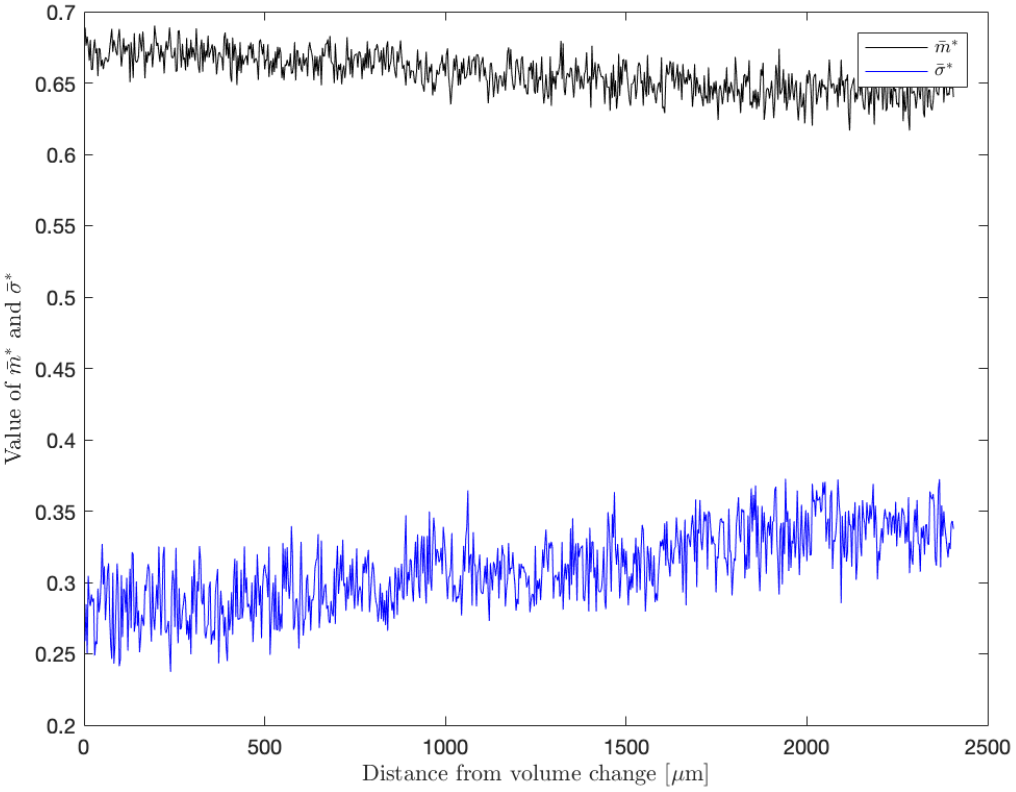


FIGURE 5.55: The $\bar{m}^*$ $\bar{sigma}^*$ pairing for each slice along the length of the 40-80 μms^{-1} changing withdrawal rate sample.

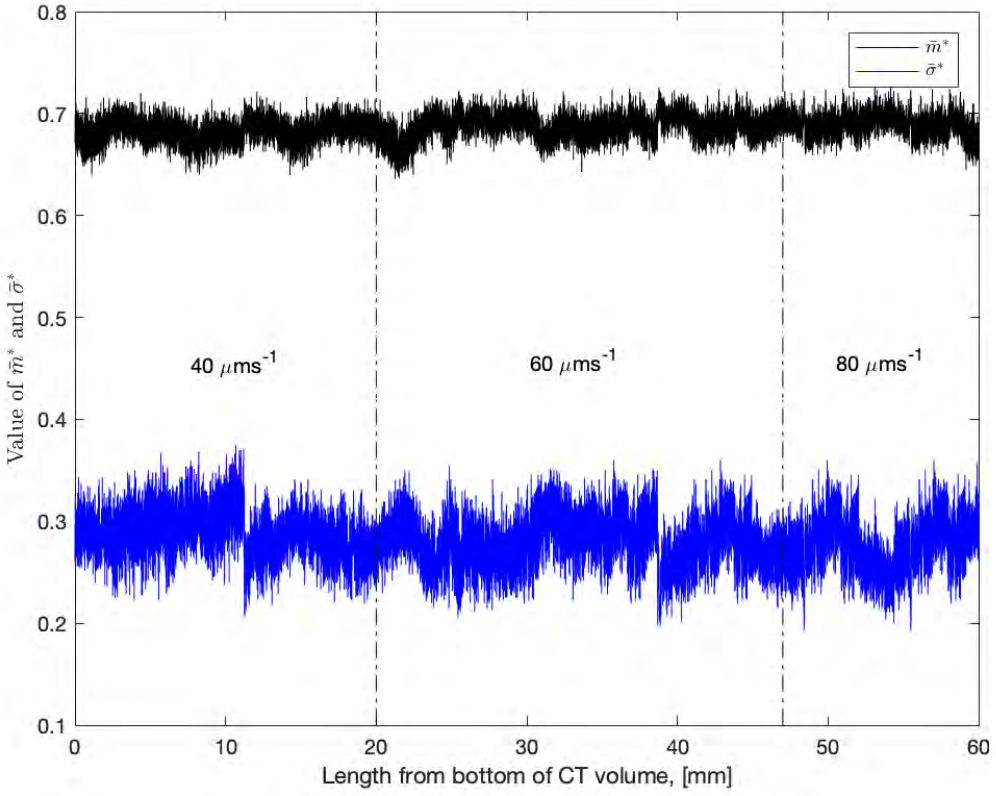


FIGURE 5.56: The $\bar{m}^*$ $sig\bar{m}a^*$ pairing for each slice along the length of the 40-60-80 μms^{-1} changing withdrawal rate sample.

The incubation and end of transition times for the changing withdrawal rate samples are given in Table 5.7. The values are taken from the JMAK analysis in Figures 5.33, 5.41 and 5.44.

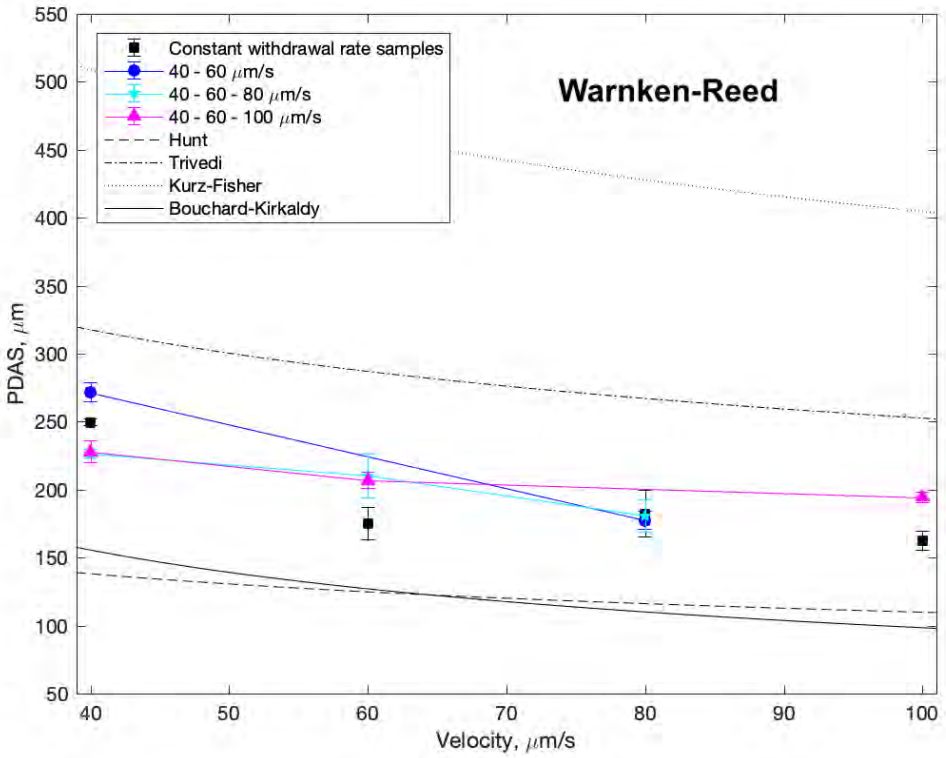


FIGURE 5.57: Collation of the average Warnken-Reed **PDAS** values for each of the samples. The calculated **PDAS** for the Hunt, Trivedi, Kurz-Fisher and Bouchard-Kirkaldy given in Equations (2.23) to (2.26)

TABLE 5.5: The mean Warnken-Reed **PDAS** for each of the constant withdrawal rate samples and the sections of the varying withdrawal rate samples.

Experiment	**PDAS for each withdrawal rate,** μm			
	40 μms^{-1}	60 μms^{-1}	80 μms^{-1}	100 μms^{-1}
Constant rate	249 ± 2.34	175 ± 12.2	182 ± 17.0	162 ± 7.04
Increasing rate experiments:				
40 - 80 μms^{-1}	271 ± 6.98	-	177 ± 6.78	-
40 - 60 - 80 μms^{-1}	226 ± 3.17	210 ± 16.2	181 ± 11.2	-
40 - 60 - 100 μms^{-1}	228 ± 8.22	207 ± 6.08	-	194 ± 3.78

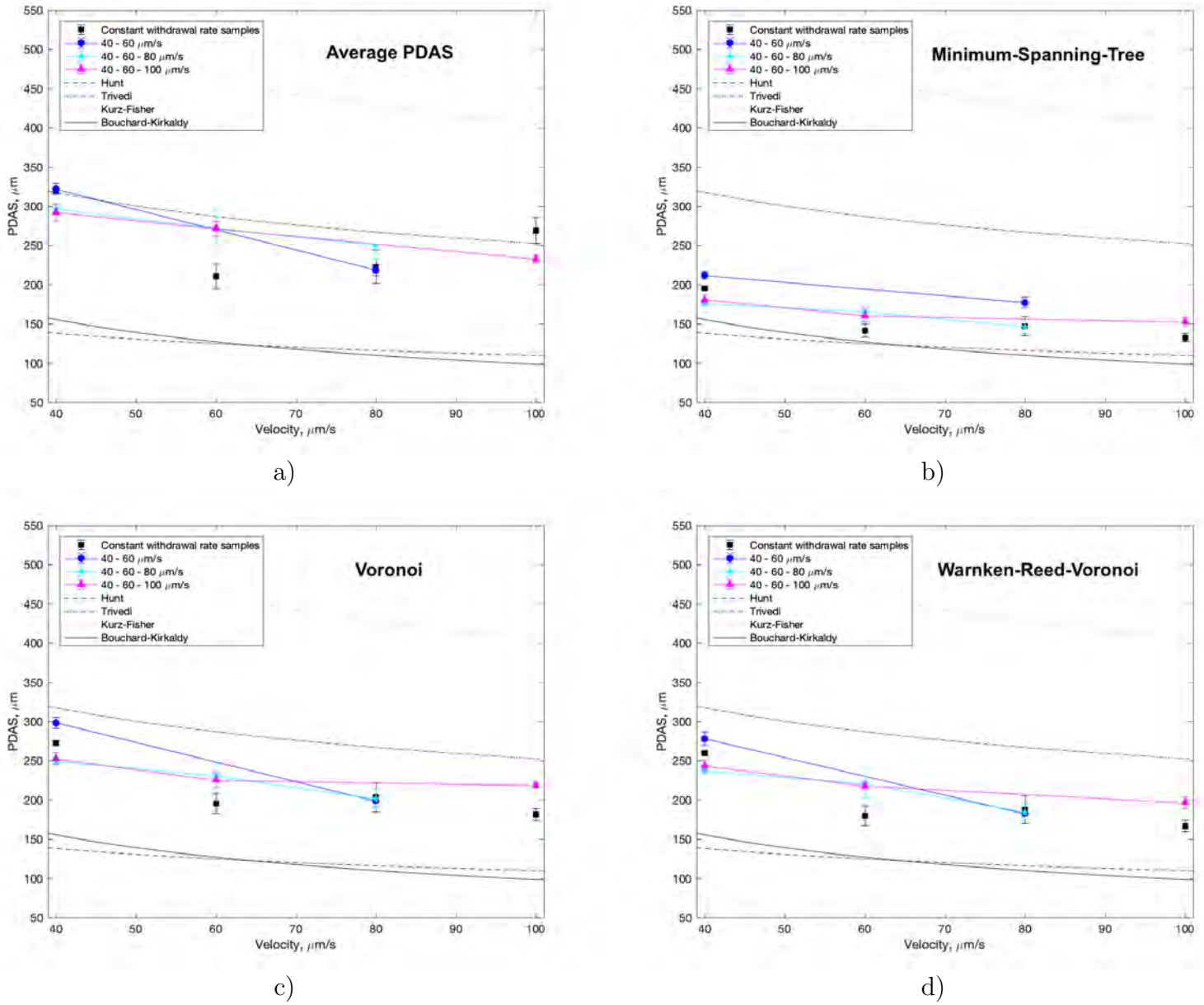


FIGURE 5.58: a) The mean average **PDAS** for each of the constant withdrawal rate samples and the sections of the varying withdrawal rate samples. b) The mean minimum-spanning-tree **PDAS** for each of the constant withdrawal rate samples and the sections of the varying withdrawal rate samples. c) The mean Voronoi **PDAS** for each of the constant withdrawal rate samples and the sections of the varying withdrawal rate samples. d) The mean Warnken-Reed-Voronoi **PDAS** for each of the constant withdrawal rate samples and the sections of the varying withdrawal rate samples.

5.8 Comparison of Warnken Reed PDAS Calculation Method with Theoretical Methods

The local **PDAS** Warnken-Reed results (taken from Table 5.5) were compared against the theoretical methods disclosed in Equations (2.23) to (2.26). Values of the theoretical **PDAS** was calculated with a thermal gradient of $\nabla T = 10\ 000$ Km^{-1} and the parameters in Table 9.3 and from reference [10] for each velocity. The scale of each Figure is 1:1. If a point lies along the x-y line it indicates that the Warnken-Reed method and theoretical calculation give the same value for the **PDAS**.

The Figures (shown in Figures 5.59 and 5.60) show good agreement for the local **WR PDAS** with the Trivedi equation (Equation (2.24)). This good agreement is shown for both the changing withdrawal rate samples and the changing withdrawal rate samples.

5.9 Experimental Results Against Relative Velocity Change

In order to understand which final microstructural or materials parameters are affected by the relative velocity change $\left(\frac{v_2-v_1}{v_1}\right)$ is plotted against a number of microstructural and materials parameters obtained during the experiment. These graphs are given below in Figure 5.61a-d, Figure 5.62a-d and Figure 5.63a-c.

Whilst fits have been given for the **WR** results in Figure 5.62b-d and Figure 5.63c due to the lack of points the accuracy of said fit cannot be given. Such fits are put forward to indicate possible trends which may be present in a more complete graph including further experimental results.

TABLE 5.6: The rate of change in **PDAS** for each of the changing withdrawal rate experiments for the Warnken-Reed calculations

Transition	**Rate of Change in PDAS,** λ/L**,** $\mu m/mm$
40 - 60 μms^{-1}	-7.178
60 - 80 μms^{-1}	-18.62
40 - 80 μms^{-1}	-29.64

TABLE 5.7: The incubation and the end of transition for the changing withdrawal rate samples after the changing withdrawal rates for the Warnken-Reed **PDAS** calculations obtained from the JMAK analysis. The error is associated with a possible measurement error when marking the location of the transition on the sample with a ruler.

Transition	**Length, mm**	**Incubation Time, s**	**Transition End, s**
40 - 60 μms^{-1}	2.34 ±0.5	133 ±8.0	172 ±8.0
60 - 80 μms^{-1}	3.44 ±0.5	50 ±6.3	93 ±6.3
40 - 80 μms^{-1}	2.13 ±0.5	0.3 ±6.3	27 ±6.3

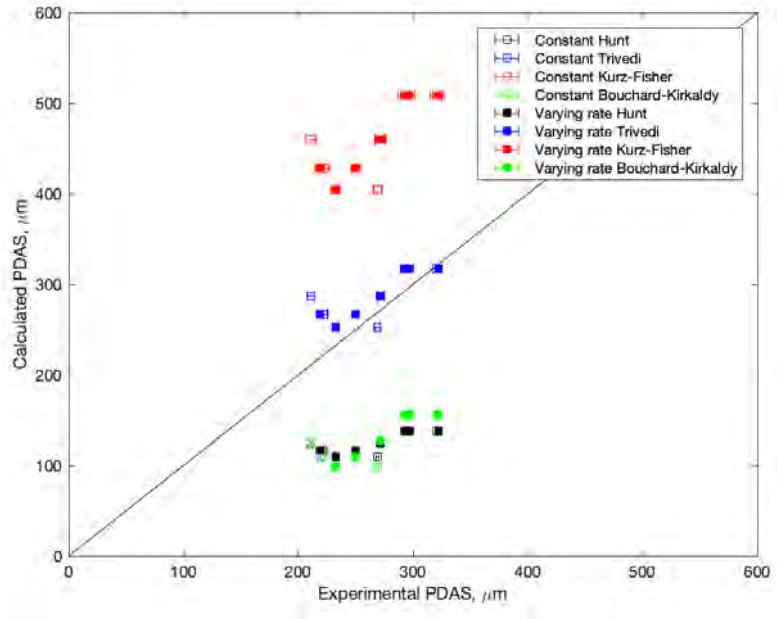


FIGURE 5.59: Results of theoretical **PDAS** models of Equations (2.23) to (2.26) compared to the average **WR PDAS**. Figure shows all samples.

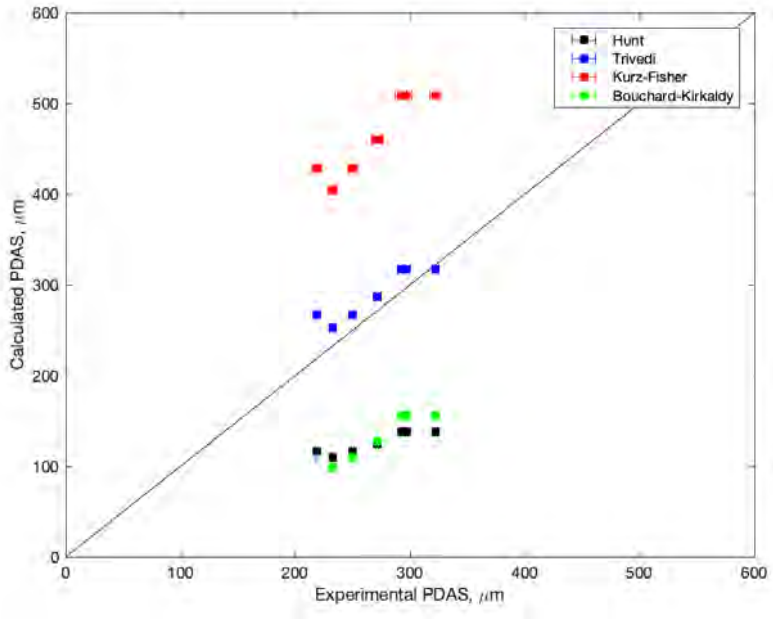


FIGURE 5.60: Results of theoretical **PDAS** models of Equations (2.23) to (2.26) compared to the average **WR PDAS**. Figure shows only changing withdrawal rate samples.

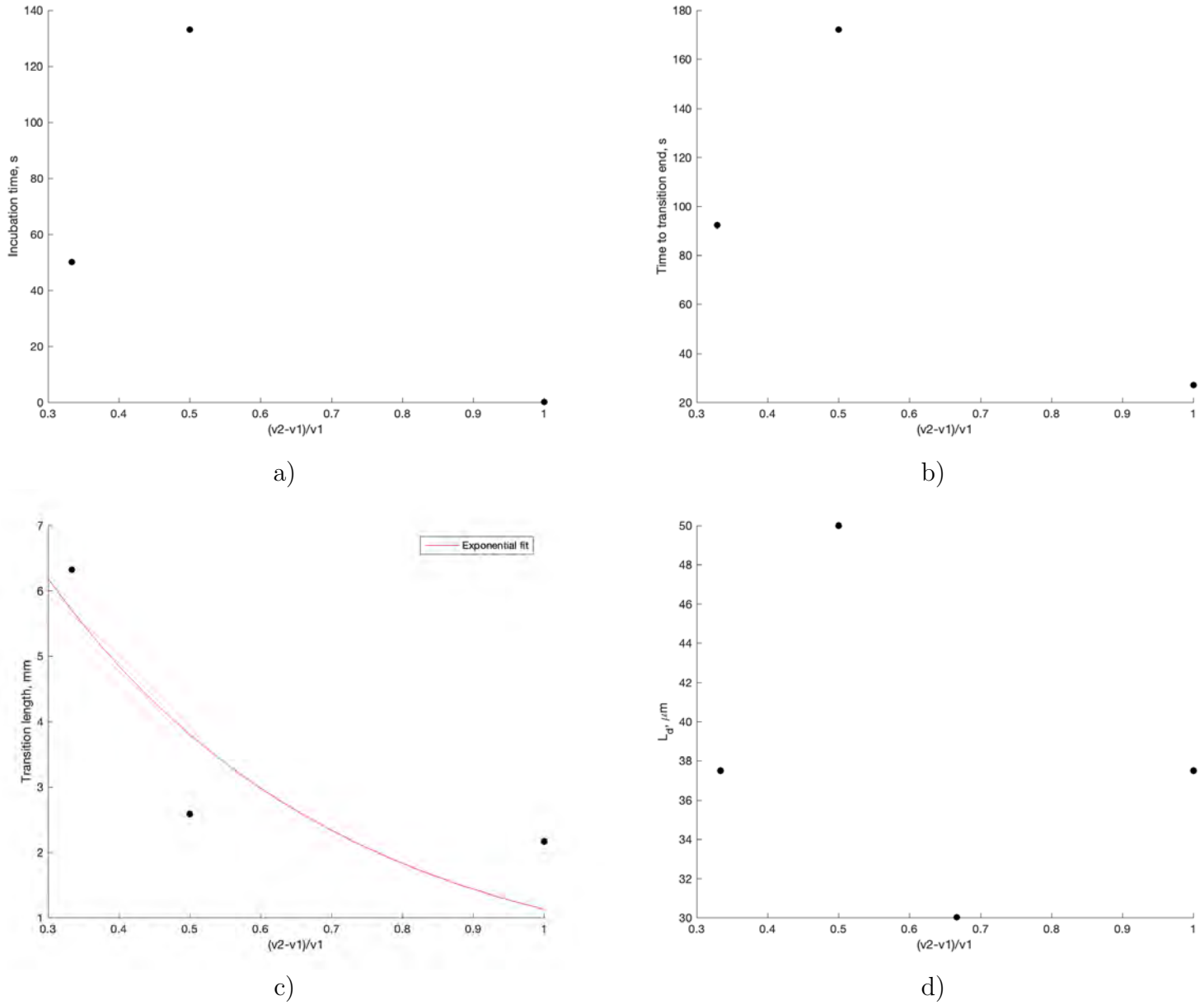


FIGURE 5.61: a) Incubation time against relative velocity change for the 40 - 80 and 40 - 60 - 80 μms^{-1} samples. b) Time until transition is completed against relative velocity change for the 40 - 80 and 40 - 60 - 80 μms^{-1} samples. c) Transition length against relative velocity change for the 40 - 80 and 40 - 60 - 80 μms^{-1} samples with an exponential fit. d) Diffusion length against relative velocity change for the 40 - 80 and 40 - 60 - 80 μms^{-1} samples.

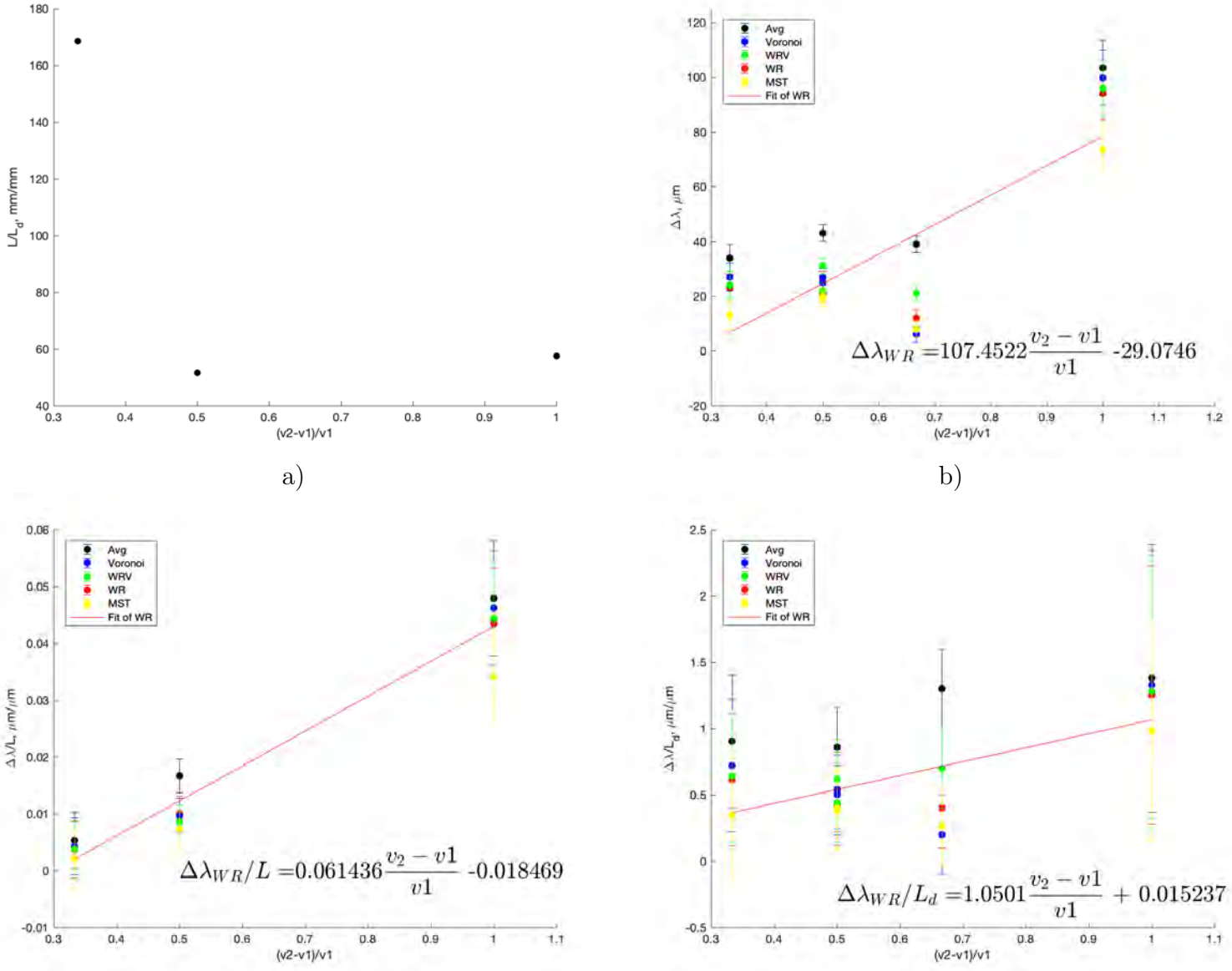
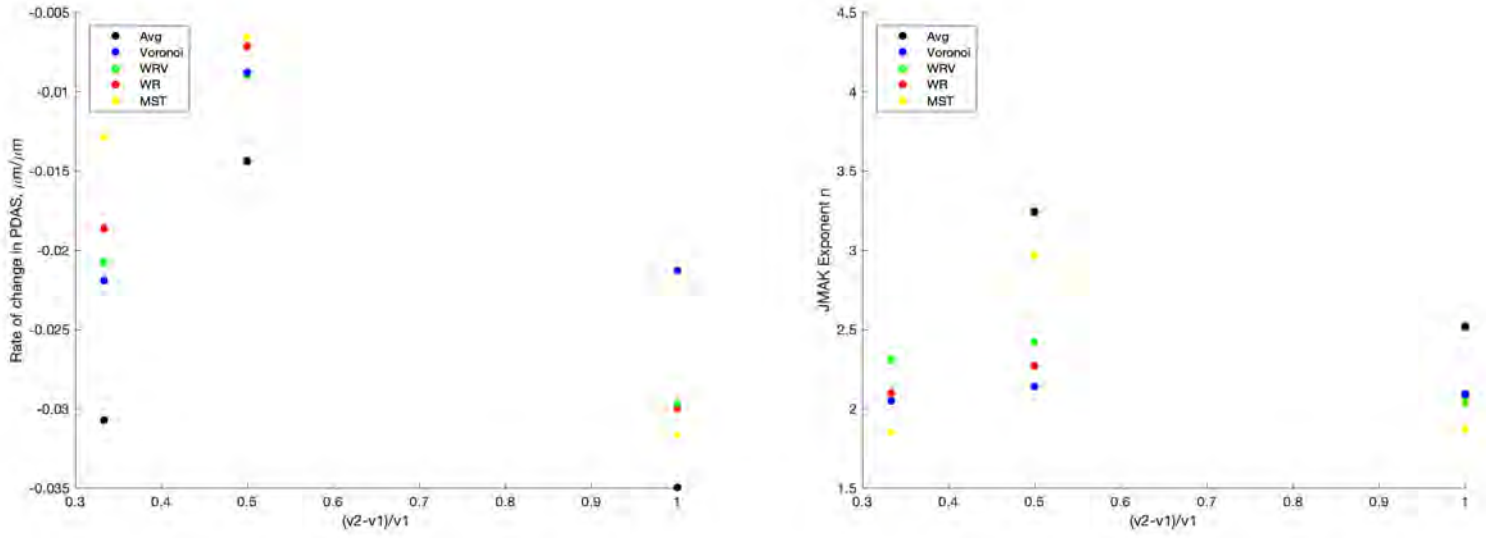
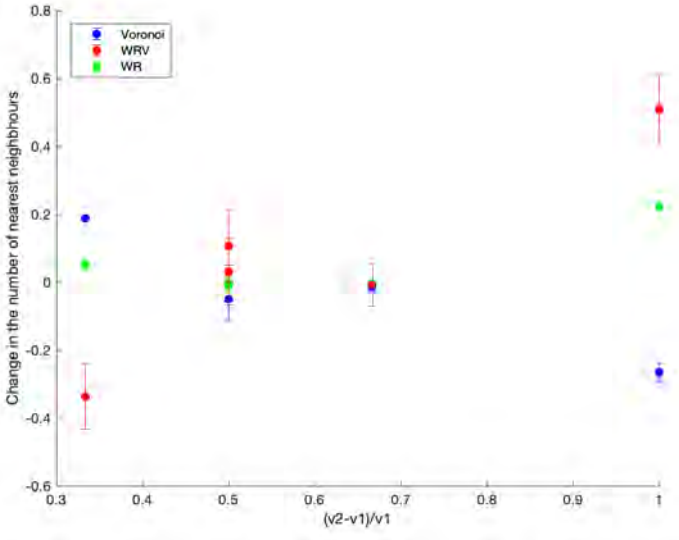


FIGURE 5.62: a) Transition length over diffusion length against relative velocity change for the 40 - 80 and 40 - 60 - 80 μms^{-1} samples. b) Change in **PDAS** before and after the transition against relative velocity change for each of the changing withdrawal rate samples. c) Change in **PDAS** over transition length before velocity change and after the array stabilises post transition against relative velocity change for each of the changing withdrawal rate samples. d) Change in **PDAS** over diffusion length before velocity change and after the array stabilises post transition against relative velocity change for each of the changing withdrawal rate samples.



a) b)



c)

FIGURE 5.63: a) Rate of change in **PDAS** for each relative velocity change. b) JMAK n exponent against relative velocity change. c) Change in the number of nearest neighbours for the Warnken-Reed, Voronoi and Warnken-Reed-Voronoi **PDAS** methods before and after the transition for each of the changing withdrawal rate samples.

5.10 Three Dimensional Dendrite Forests

By tracking the dendrite centres through each of the samples (both constant withdrawal rate and the varying withdrawal rate samples) using the method as described in Section 4.4 a series of three dimensional 'forest' plots can be created. These plots show the movement and growth of the dendrites along the entire length of the sample in three dimensions (Figures 5.9, 5.14, 5.19, 5.24, 5.29, 5.37, 5.64 and 5.65).

On these graphs are the locations of the various new dendrite initiations and terminations as described in Figures 5.9, 5.14, 5.19, 5.24, 5.29, 5.37, 5.64 and 5.65.

Shown in Figures 5.9, 5.14, 5.19, 5.24, 5.64 and 5.65 are the dendrite forest for the constant withdrawal rate samples. Figures 5.29 and 5.37 show those for the changing withdrawal rate samples. In these constant withdrawal rate samples there is little to no change in the forest's structure, with the tracked dendrite centres neither getting substantially closer together or further apart. There are however instances of dendrites being created and outcompeted as shown on the figures (Figures 5.29 and 5.37), but the location of these points are scattered throughout the sample.

For the changing withdrawal rate experiments (Figures 5.29 and 5.37) the locations of the initiations and termination of dendrites are in a much higher density after the location of the dendrite withdrawal change. This increase in the number of dendrite centres being tracked along the length of the sample coincides with the decreased **PDAS**.

A plot showing the centre line tracing of a single primary dendrite arm twice splitting by means of tertiary arm stabilisation to form three independent primary dendrite arms Figure 5.65. This figure was taken from the 60 μms^{-1} sample.

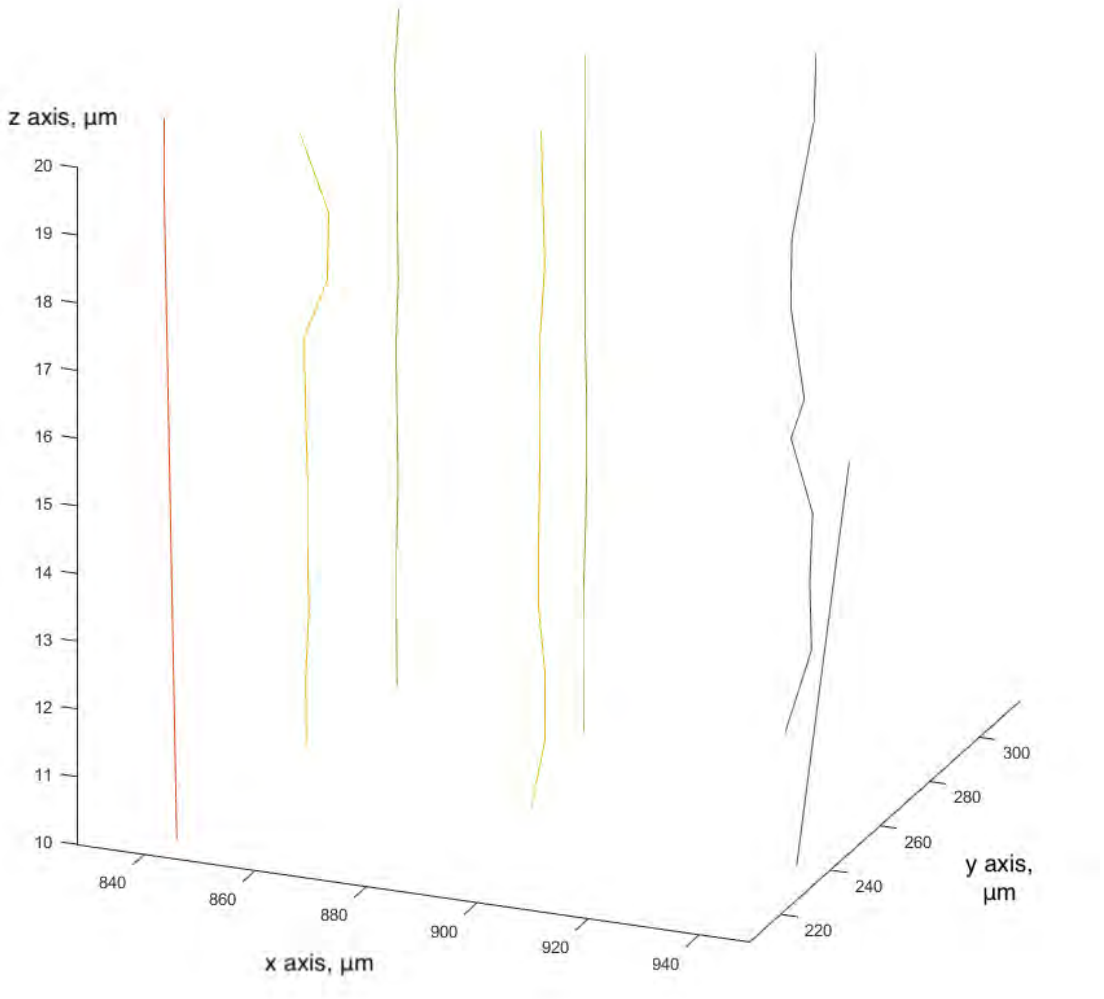


FIGURE 5.64: Zoomed in view of some dendrite centres traced from the 40 μms^{-1} sample.

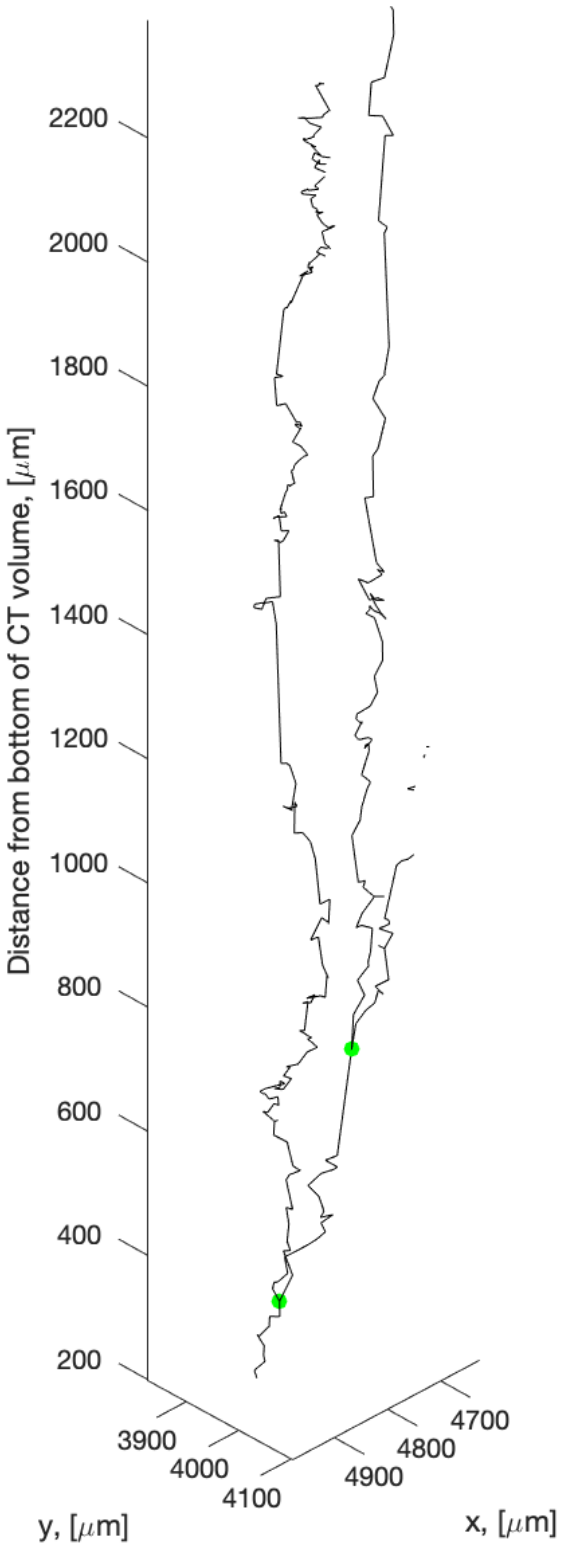


FIGURE 5.65: Zoomed in view of some dendrite centres traced from the 60 μms^{-1} sample. Two instances of dendritic branching can be seen. The single dendritic trunk at the bottom of the **CT** volume splits twice to form three primary dendrites. The two branching points are highlighted in green.

5.11 Tracking Dendrite Initiations and Terminations

Shown in Figure 5.12c, Figure 5.17c, Figure 5.22c, Figure 5.27c, Figure 5.35c, Figure 5.46c, Figure 5.47b, Figure 5.47c, Figure 5.48b, Figure 5.52c and Figure 5.53c are the locations of each newly created dendrite and the termination of a dendrite within the samples. For the constant withdrawal rate samples the number dendrites does not change substantially along the length of the sample, but there are a handful of new dendrites initiated and others which have been terminated. Seen in Figure 5.35c, Figure 5.46c are the total number of dendrites along the length of changing withdrawal rate the samples. There is a very small change in the total number of dendrites and as such only small changes in the **PDAS**.

For for the changing withdrawal rate samples (Figure 5.35c) there are an increased number of new dendrites formed that occur from the withdrawal rate change compared to the number of dendrites being outcompeted and terminated. As seen in Figure 5.35c the number of new dendrites created is not instantaneous but an ongoing process whereby new dendrites are continually created. This process is also seen in the samples under going two withdrawal rate changes as seen in the 40-60-80 μms^{-1} sample in Figure 5.46c, Figure 5.47b, Figure 5.47c, Figure 5.48b.

5.12 Isosurface Plots of Dendrites

In order to visualise the growing dendrites from the samples, individual dendrites were taken from the forests and rendered in three dimensions using Matlab. The dendrite centres were then overlain within the dendrites themselves. These renders are given in Figures 5.66 to 5.72 with each figure showing an alternative view of the same dendrite. Figure 5.72 show the skeleton-geometry centre assigning

method combined with the thresholding technique described in Section 4.4 with the erroneously assigned centre outside of the thresholding volume. In each of the figures (Figures 5.69 to 5.72) the skeleton-geometry method can be seen to correctly assign the centre of the dendrite in three dimensions apart from a single point of error.

To remove any errors the data was thresholded by finding the mean x and y coordinates of the all the data points irrespective of their z coordinate. Then a threshold cylinder was set up around this average points for each slice with a radius equal dependent upon 2σ, where σ is the standard deviation of the data set. These figures (Figure 5.72) show the skeletonisation method works along the length of the sample finding the centre as defined in Chapter 4.

A comparison of the skeletonisation and centre of geometry methods are visualised together in 3D in Figure 5.72c-e. The plan view Figure 5.72e shows that the centre of gravity method is offset towards the longest of the dendrite's four arms. The longest arm has the largest volume and as such any centre of gravity measurement would be offset in that direction.

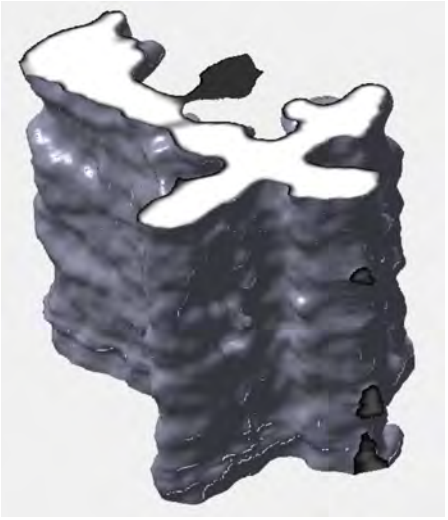


FIGURE 5.66: Isosurface of dendrite taken from 40 μms^{-1} constant withdrawal rate sample.

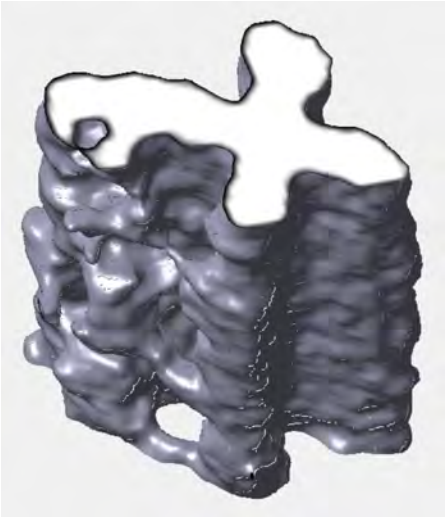


FIGURE 5.67: Isosurface of dendrite taken from 40 μms^{-1} constant withdrawal rate sample.



FIGURE 5.68: Isosurface of dendrite taken from 40 μms^{-1} constant withdrawal rate sample.

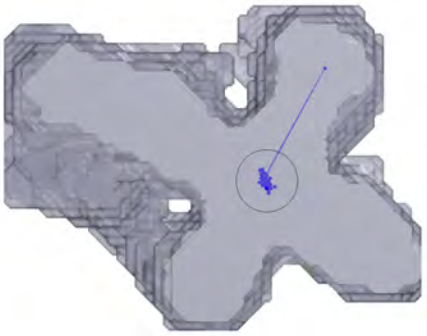


FIGURE 5.69: Isosurface with skeleton centres overlain

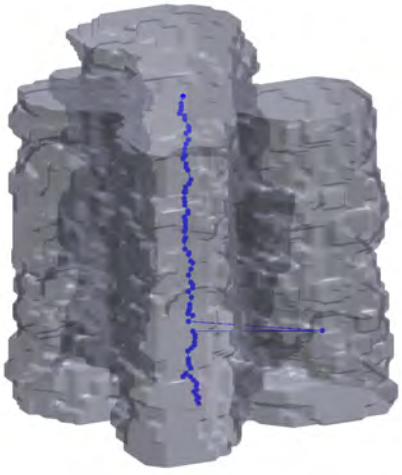


FIGURE 5.70: Isosurface with skeleton centres overlain.

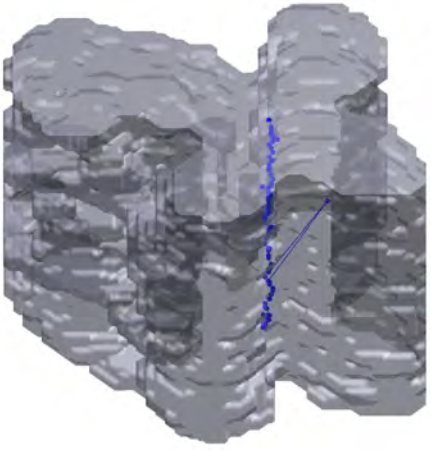


FIGURE 5.71: Isosurface with skeleton centres overlain.

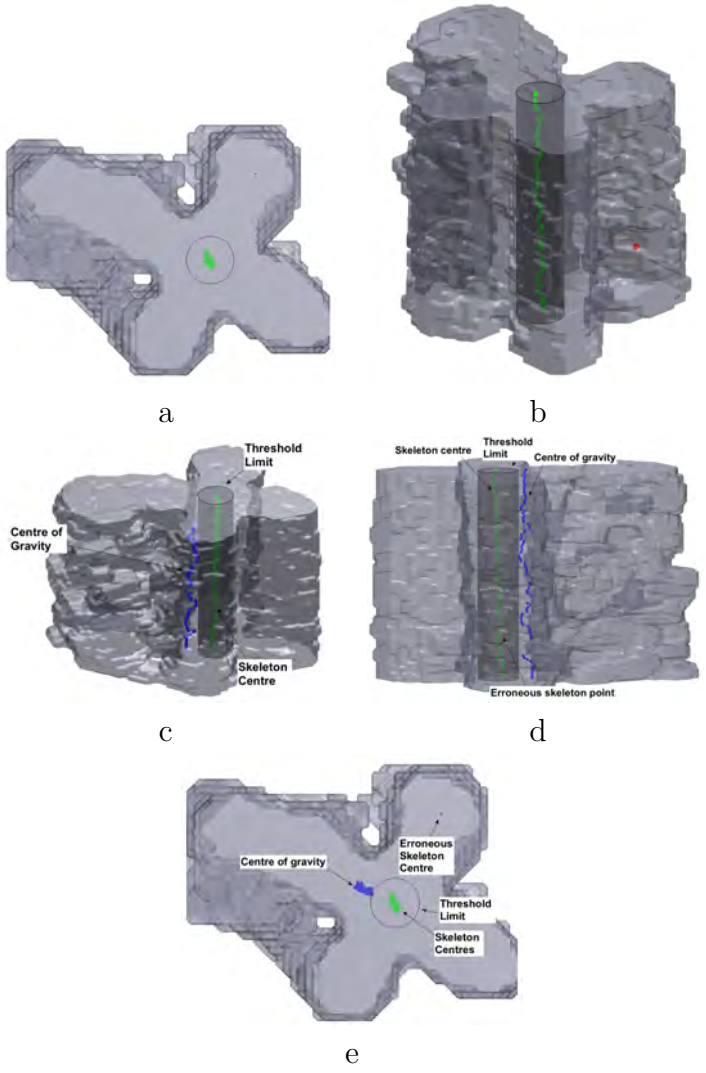


FIGURE 5.72: a) Isosurface with skeleton centres overlain and thresholded. b) Isosurface with skeleton centres overlain and thresholded. c)Side view of the isosurface with skeleton centres overlain and thresholded. Also shown is the centre of gravity for each slice along the length of the dendrite. d) Side view of the isosurface with skeleton centres overlain and thresholded. Also shown is the centre of gravity for each slice along the length of the dendrite. e) Plan view of the isosurface with skeleton centres overlain and thresholded. Also shown is the centre of gravity for each slice along the length of the dendrite.

Chapter 6

Discussion

The results given Chapter 5 show that for aluminium 10 wt% copper the primary dendrite arm spacing is dependent on the withdrawal velocity, which is commonly known from the following references: [10, 18, 22, 24, 25, 31, 50, 51, 52, 53, 54, 57, 58, 59, 60, 68, 69]. This effect can be seen in the restructuring of the dendrites in the primary dendrite arm spacing along the length of each of the samples (Figures 5.10, 5.15, 5.20, 5.25, 5.30, 5.38 and 5.50). Generally it is known that an increasing velocity results in a decreasing **PDAS** [10, 18, 22, 24, 25, 31, 50, 51, 52, 53, 54, 57, 58, 59, 60, 68, 69]. This is again reflected in the results of this thesis as shown in Figures 5.10, 5.15, 5.20, 5.25, 5.30, 5.38 and 5.50.

However what is not currently understood is how the **PDAS** changes with changing stimulus. Be that change in the withdrawal rate, v^*, or due to the thermal gradient across the sample, ∇T. Briefly, the Figures shown previously in Chapter 5 show that there is some lag between the change in the withdrawal velocity and the new stabilised **PDAS** forming. This distance is categorised by a gradual decrease from the higher **PDAS** at the lower velocity and the lower **PDAS** at the higher withdrawal velocity. As was also the case in work undertaken by Ma [12, 13] it is clear the new **PDAS** which stabilises after a change in withdrawal

rate is dependent upon the original **PDAS** and crystal structure prior to a withdrawal rate change. The samples do not show a complete reordering of the crystal structure which would likely occur if the **PDAS** change were independent of the original array structure. A complete reordering would likely have occurred if a **CET** was present in the sample.

In each case it is clear that an increase in the withdrawal velocity causes a decrease in the **PDAS**.

6.1 Accumulation of Error Through Analysis

There are a number of potential points in the analysis where error and uncertainties may have been introduced. The most notable being the voxel size of the initial **CT** scan. The voxel size obtained in this analysis was approximately 2 μm^3. Therefore any dendrite centre obtained could only ever be precise to within $\pm$ 1 μm^3 on the x, y or z axis. The 2 μm^3 used here was at the limit of what was achievable using the **CT** scanner available at the time of writing. However, in future lower resolution scanners will likely become available leading to higher fidelity scans of samples.

A potential issue with a voxel size which is too large is that it does not adequately show a dendrite. For example, a voxel size of 10 μm would be approximately the width across one of the aluminium-copper dendrites examined here. A voxel size of 10 μm^3 would not be useful when examining the dendrites in this thesis using the techniques described herein. As a general rule of thumb a cube voxel should have no side of length less than approximately $\lambda_{Avg}/10$ in order to give adequate information for any further image analysis. As the lowest average **PDAS** seen here was around 200 μm (see Figure 5.58a) and the voxel size was 2 μm^3 this was likely not a source of error in this analysis.

Whilst great care was taken, it is possible that the locations of the transitions were ± 0.5 mm out due to a measurement error when marking the sample prior to loading it in the **CT** scanner. As the transition location was marked using a ruler with 1 mm increments the incubation length (and thus incubation time) could be out by 0.5 mm.

Another possible reason for error in the samples is due to placing the dendrite centre in an incorrect location. This is an issue on an individual dendrite scale, but when analysing the whole array for a distribution in local **PDAS** there is less of a problem. When calculating a mean and standard distribution for the local **PDAS** any incorrectly assigned dendrite centres will be averaged out as shown in Chapter 4.

Incorrect illumination during the **CT** is a further reason errors may have been carried through the analysis. As shown in Figure 5.10 there is a cyclic increase and decrease in the **PDAS**. This is likely due to the centre of the sample being more illuminated than the ends during the **CT** scan with the knock on effect being an undersegmentation of the slices during the image analysis. Whilst the issue is only minor, causing an increase of approximately 5 - 10 μm in **PDAS** (approximately the standard deviation for each slice in each of the samples) in a cyclic fashion, it is likely present in all of the samples. In future more care is needed to ensure that the sample is uniformly illuminated by X-ray radiation, or further image correction is needed to correct the incorrect illumination along the length of the samples.

Finally, a further possible reason for error in the results and a high value of the average **PDAS** spacing was the presence of porosity in the samples. As porosity was not taken into account when calculating the average spacing it would have artificially inflated the bulk **PDAS** for slices where porosity is present. In future

Equation (6.1) should be adapted to take this into consideration using the following equation:

$$\lambda_1 = c\sqrt{\frac{A - A_p}{N}} \tag{6.1}$$

Where A is the total area, A_p is the area of porosity within the slice, N is the number of dendrites and c is a coefficient dependent on the array packing. Whilst porosity is present within the samples the area of porosity in each slice would have unlikely have affected the final **PDAS** substantially. However, as the area of porosity in each slice was not analysed in great detail only a subjective estimation on how the average **PDAS** changed can be put forward.

6.2 Constant Withdrawal rate

In each case the constant withdrawal rate samples show a relatively stable **PDAS** (Figures 5.10, 5.15, 5.20 and 5.25). There are instances in each sample where an increased **PDAS** can be seen, notably at approximately 11 mm in the 40 μms^{-1} sample (Figure 5.10). This sharp increase and decrease again corresponded to locations in the sample where porosity and air bubbles formed as shown in Figure 5.12a. These air bubbles disrupted the growth of the dendritic array during the solidification as the could not grow through this air pocket. This decrease in the number of actual dendrites growing caused an increase in the **PDAS** (less dendrites per unit area when calculated using Equation (6.1)).

Subsequently after the porosity ended, new dendrites could either nucleate on the surface of the inhomogeneity or more likely, be created by means of tertiary arm stabilisation. Above the porosity itself there is some restructuring of the grain

structure showing that grains that existed before the porosity grow into the new 'free' space above the porosity competing with other surrounding grains.

In each constant withdrawal rate experiment the steady state solidification is most similar to the Trivedi equation (Equation (2.24)) shown in Figure 5.59. This can be seen by comparing the results in Figures 5.10, 5.15, 5.20 and 5.25 and Equation (2.24). In the 40, 80 and 100 μms^{-1} cases the constant withdrawal rates are very similar to the output of the Trivedi equation of 310, 255 and 245 μm respectively.

In the case of the 60 μms^{-1} sample the analysed results of the experiment are lower than the calculated value of 280 μm. This is a 13% difference between the Trivedi calculated value and the experimental value.

One possible reason for this low value of the experimental **PDAS** in Figure 5.15 is that the initial crystal structure from bottom of the Al-10wt% Cu rod was at a **PDAS** large enough to be stable and therefore unchanged upon the beginning of the withdrawal of the sample. As the rod was melted back to this 'seed crystal' at the bottom of the sample solidification would have inherently started with the 'seed' crystal structure. If this original crystal structure is stable, upon the beginning of the withdrawal the dendritic crystal structure will not change as there is not enough energy in the system to alter the **PDAS** and reach a more stable and lower energy state. As such whilst there may be small changes in the overall structure in the dendritic array, such as new dendrites being created and other ones being outcompeted there is no overall change. This can be seen by the increase and then decrease in the **PDAS** in Figure 5.15 where between 0.1 and 1 mm from the bottom of the sample there is a slight change which then returns to the average **PDAS** again.

In order to compensate for this effect further experiments should be undertaken using a complete remelt of the metal; using a single crystal seed crystal to grow

the dendritic array; or alternatively allowing for a much longer length to allow for steady state growth to develop. That is, greater than 30 mm as described in Section 3.1. A complete remelt of the sample was not possible due to the sample and crucible holder design of the Bridgman furnace used in this work.

In each of the constant withdrawal rate samples there are small fluctuations in the number of new dendrites created by tertiary arm stabilisation and others out competed as shown in Figure 5.12c, Figure 5.17c, Figure 5.22c and Figure 5.27c. The curves for both the new and outcompeted dendrites showed either a square or cubic relationship as a function of the length of the sample. In each case the fits had and R^2 of greater than 0.95. Each of the Figures showed an initial curved section near to the bottom of the **CT** volumes which became more linear as time progressed. However, this curved section may just be due to a problem with the techniques used here. As this curved region was seen in all of the constant withdrawal rate samples it is likely that the image analysis methods are not sensitive enough to pick out the new or outcompeted dendrites formed in the bottom 10% of the samples. It is thus more likely that in regions where there is no porosity (here an excess of dendrites are outcompeted and new ones formed) that the restructuring is linear with a constant gradient. It stands to reason that an array is constantly fluctuating as new dendrites are formed and old ones are outcompeted, but as the constant withdrawal rate figures show the Figures 5.10, 5.15, 5.20 and 5.25 the overall **PDAS** remains constant. A refinement of the image analysis methods is required to ascertain if this is in fact the case.

By comparing the figures showing the cumulative change in new and outcompeted dendrites and the **PDAS** figures there is very little change in the **PDAS** (Figures 5.10, 5.15, 5.20 and 5.25). This indicates that whilst the **PDAS** may be stable and essentially unchanging on the macroscale on the microscale small fluctuations and changes cause the microstructure to constantly evolve. Some dendrites are outcompeted by other dendrites surrounding them, and other new ones

being formed by tertiary arm stabilisation when a gap in the dendritic structure emerges. This fluctuating microstructure is shown graphically on Figures 5.9, 5.14, 5.19 and 5.24. New dendrites are constantly being created whilst at the same time ones are being outcompeted. On the whole however the **PDAS** remains relatively constant throughout solidification of the sample. It is clear that in 3D polycrystalline arrays the dendritic structure is *metastable* and constantly readjusting to reach a more uniform and lower energy state. If the experiments were carried out for an infinite length of time, and along an infinite length of solidifying material, the systems would eventually reach a stable equilibrium.

This restructuring effect is also seen in work undertaken by Ma [12, 13] and more recently by Indrizzi *et al* [108]. These papers put forward dendritic tip tracking models that track the dendrite tips which can split forming new dendrites if certain criteria are reached. Such criteria are based on the distance between the dendrites dendrites. If they get too close together for a certain ∇T and v^* a dendrite is removed. Conversely if the dendrites get too far apart for a certain ∇T and v^* a new dendrite is created. The issue however with these models are that they do not take into account the off-axis growth of dendrites. In both models the dendrites grow anti-parallel to the ∇T. An advance on this technique validated on the results herein would be very advantageous. Not least due to the low processing power requirements of dendritic tip tracking simulations in comparison to cellular automata and phase field simulations.

The restructuring seen in the experiments is similar to the restructuring in two dimensions that has been modelled using cellular automata by Pineau *et al* [161] and in phase field and Tourret *et al* [162]. In both these papers the restructuring is due to the impingement of different orientation grain boundaries. Simulating this effect in three dimensions however is more computationally difficult.

Work undertaken by Takaki *et al* [163] on large scale dendritic microstructures

completed in approximately a week. It was however undertaken on a simulated single crystal sample without calculation of the fluid flow in the system. As the simulated structure was stable in Takaki [163] there was no impingement of the dendrites themselves and once a stable **PDAS** developed there were no dendrites being outcompeted or new primary arms forming. A more recent three dimensional phase field analysis undertaken by Guo *et al* [164] showed this microstructural restructuring caused in part by the misalignment between the grains.

Guo [164] shows–like in the present constant withdrawal rate experiments–that whilst a single dendrite may be out competed by impingement another will take its place. Thus in this manner the bulk **PDAS** can be conserved. Whilst Guo [164] however only analysed two impinging grains the present work has many more grains. In order to validate other three dimensional simulations with a greater number of grains it may be possible to use the data disclosed in this thesis in the future once computational analysis reaches the point that large microstructures containing hundreds of dendrites can be analysed.

6.3 Varying Withdrawal rate

Compared to the constant withdrawal rate samples in Section 6.2, the three samples produced under varying show changing **PDAS** along the length of the samples (Figures 5.30, 5.38 and 5.50). This is a widely know effect, increasing velocity results in a decreasing **PDAS** [10, 18, 22, 24, 25, 27, 31, 53, 58, 59, 60, 98]. A decreasing **PDAS** corresponds to an increase in the withdrawal velocity in each sample (Figures 5.30, 5.38 and 5.50). The change in the **PDAS** can be clearly seen when comparing Figure 2 in Chapter 11, Figures 5.3 to 5.5, Figures 5.6 to 5.8 for the 40-60, 40-60-80 and 40-60-100 μms^{-1} withdrawal rate sample. Each of these micrographs show that the microstructure has been restructured after the

velocity change. In each case this decrease in **PDAS** occurred over several mm rather than occurring instantaneously with a rate of change given in Table 5.6.

This gradual change in each sample (best seen in Figure 5.30) shows that there was no columnar to equiaxed transition taking place during the solidification, but rather a slower restructuring of the dendritic array along the length of the rod itself. The lack of a **CET** was to be expected. The dendritic array is rearranged by means of tertiary arm stabilisation and growth into a new primary arm (explained below in greater detail with reference to the 40-80 μms^{-1} sample in the Appendix in Chapter 11).

In each case where a there was a changing withdrawal rate the change in **PDAS** can be described by a linear equation. These linear equations are given in Tables 5.1 to 5.3 and 5.6. The gradients of these curves are also shown graphically in Section 5.9. In each case the R^2 value for each fit is greater than 0.9, and in most instances greater than 0.95. It is clear that the linear fits thus accurately explain the variation seen in the data. In these varying withdrawal rate cases here, the varying withdrawal rate is constant and steady state after an initial transient (when the **PDAS** begins changing) and before a final transient (when the **PDAS** is reaching a new stable level). The complete transition follows a sigmoidal curve as shown in Figures 5.33, 5.41 and 5.44. The author is unaware of any literature that shows a rate of change in the **PDAS** (as described here in this work) for a 3D array over a long transition period.

Whilst Ma [12, 13] shows changes in **PDAS** as a function of ∇T Ma did not show a rate of change over a length of the sample between a first value of ∇T and a second ∇T. The value of the **PDAS** was not tracked through each step. The **PDAS** in Ma's work was only recounted after each step and only once a stable **PDAS** was reached. Ma [12, 13] did not show the **PDAS** evolving and transitioning between these stable regions as is clearly shown in Figures 5.30 and 5.38

In the work of Ma there were simply too few dendrites to calculate a rate of change with respect to the length. In Ma's research the number of dendrites being tracked was around 5 - 20 [12, 13]. There were only small changes in the number of dendrites between each step. As there were so few dendrites if only a single new dendrite formed, or a single dendrite is outcompeted, then there was a relatively large change in the **PDAS**.

Similar to the work of Ma [12, 13] and Weidong *et al* [165] however, is that the samples showed that there was a distance between the step change and the beginning of the change in the PDAS. In the 40-60-80 μms^{-1} sample there was a distance of approximately 10 mm for the 40-60 μms^{-1} transition and approximately 5 mm for the 60 - 80 μms^{-1} transition before the **PDAS** began to decrease Figures 5.38, 5.40 and 5.43. Contrary to this was the the larger jump in the velocity of the 40 - 80 μms^{-1} transition sample Figure 5.32. This larger transition sample, unlike the samples of Ma [12, 13] and the 40-60-80 μms^{-1} sample, showed an almost instantaneous decrease in the **PDAS** from the point of the velocity change as shown in Figure 5.32

The gradients, or rates of change in the **PDAS**, of the changing withdrawal rate samples are all given in Table 5.6. As Table 5.6 shows the gradient for the Warnken-Reed calculated **PDAS** increases with a higher initial **PDAS** and with a greater velocity change.

Comparing the results with the relative velocity change, as described in Figure 5.63a, may not be the best way to compare the parameters obtained from this work. A relative velocity change calculation does not take into consideration the initial and final velocity, only the percentage difference between the two velocities. An alternative parameter maybe more useful for comparing rates of change such as one based on the change in the primary dendrite arm spacing before and after the transition.

A larger rate of change for a greater velocity change is to be expected. There is a greater impetus for the system to change more quickly and over a shorter length. This can be seen by comparing the 60 - 80 μms^{-1} of the 40 - 60 - 80 μms^{-1} sample with the 40 - 80 μms^{-1} sample and its single transition in Table 5.6. Whilst the final velocity is the same, and thus the diffusion length L_d (as seen in Table 3.3), the greater jump in the 40 - 80 μms^{-1} has a larger rate of change. It is put forward that greater changes in the velocity would result in a greater rate of change prior to a new stable **PDAS** being formed.

The results showing a greater Δv causing a greater $\Delta\lambda$ appears to agree with the results seen in Weidong *et al* [165]. Weidong *et al* [165] showed (in Table 2 of [165]) that samples solidified with a larger velocity jump stabilise in a shorter time. The experiments were undertaken on a succinonitrile model alloy [165]. A dendritic array subjected to a jump in velocity of $\Delta v = 44.8$ μms^{-1} stabilised after 40 s. Whereas, a dendritic array subjected to a jump in velocity of $\Delta v = 20.2$ μms^{-1} stabilised after 50 s.

Further the work of Weidong *et al* [165] and Ma [12, 13] showed that there was an incubation period from the initial velocity or thermal gradient change to the point where the first new dendrite appeared. This incubation time was also seen in the 40 - 60 - 80 μms^{-1} sample for both the 40 - 60 μms^{-1} transition (133 s incubation Table 5.7) and 60 - 80 μms^{-1} transition (50 s incubation, Table 5.7). Similar to the Weidong *et al* [165] there is a decrease in incubation time with increasing velocity. There is also a decrease in time until the transition ends and the dendritic array stabilises as was also seen in Weidong *et al* [165].

A much smaller incubation time occurred in the 40-80 μms^{-1} sample (as shown in Figure 5.33 and table 5.7). The shorter incubation time is likely due to the greater impetus from the higher velocity change driving an array restructuring. However, whilst great care was taken, it is also possible that the start of the transition may

be out by 0.5 mm due to a measurement error when marking the sample prior to loading it in the **CT** scanner. In this worse case scenario the start of the transition would have occurred 6.3 s later at 6.6 s. This is also a possibility in the location of the other transitions for the 40-60-80 μms^{-1}.

Further, in Ma [12, 13] there was shown to be a threshold change in the ∇T required before the dendrite array changed. The change resulting in an a new dendrite forming when the ∇T increased or a dendrite being outcompeted when the ∇T decreases. It is put forward that in this respect pseudo-2D solidification experiments (as seen in [12, 13, 44, 55, 60, 109, 115]) may have more of an effect on the latency. As the array is constrained, due to the decrease in the number of dimensions from 3 to 2.5, it will clearly take longer for a new dendrite to stabilise and decrease the **PDAS**. There is a lack of room for a new dendrite to grow into.

Ma also theorised that only when a change in the withdrawal velocity or thermal gradient resulted in a calculated **PDAS** outside of the range of $2/3\lambda$ - $4/3\lambda$ (where λ was the **PDAS** prior to the change) would cause the array to restructure. This hypothesis showed good agreement with the samples of Ma [12, 13] but did not agree with the results of the experiments seen here. Each of the varying withdrawal rate samples showed a change in **PDAS** (as shown in Table 5.5 and fig. 5.57) even though the withdrawal rate changes occurred within the $2/3\lambda$ - $4/3\lambda$ range.

It is put forward pseudo-2D experiments do not incorporate the whole complexity of 3D growth. In order to investigate latency in changing withdrawal rate experiments and to study whether there is a large enough velocity change to restructure the array experiments should be undertaken on 3D arrays. However, direct comparisons between a pseudo-2D array and a 3D sample solidified under the same conditions should be undertaken.

6.3.1 40-60-100 μms^{-1} Sample

As in both other varying withdrawal rate samples described above and in Chapter 11, the 40-60-100 μms^{-1} again demonstrates the decreasing **PDAS** as the withdrawal rate changes (Figure 5.50).

Unfortunately due to damage to the sample upon removal from its crucible a full scan of its entire length was not possible. Scans of three sections were successfully made in the 40, 60 and 100 μms^{-1} regions as shown in Figure 5.50.

The results shown in Figure 5.50 are different to the calculated values from Table 3.3 obtained using Equation (2.26). For the 40 μms^{-1} region the **PDAS** is approximately 300 μm when calculating the bulk **PDAS** using Equation (4.12). This **PDAS** is similar to the value obtained along the 40 μms^{-1} sample (Figure 5.10) and both the 40 μms^{-1} sections of the the two other varying withdrawal rate samples (Figure 4 in Chapter 11). The same was also true for the 60 μms^{-1} and 100 μms^{-1} sections of the samples. In both instances these sections were closest to the values of the constant withdrawal rate samples than the calculated values in Table 3.3.

A repeat of the this experiment would need to be undertaken. Unfortunately there was no time for further experiments in this current work. The future works would be used to ascertain the length of **PDAS** transition from one stable **PDAS** to the next stable value at a higher withdrawal velocity.

6.4 Stabilisation Length in Terms of Diffusion Lengths

The length of the sample taken to reach a new stable **PDAS** was examined for the 40-80 μms^{-1} and 40-60-80 μms^{-1} samples (Figures 5.30 and 5.38) in terms of

the number of diffusion lengths, L_d it took. Unfortunately as the 40-60-100 μms^{-1} sample (Figure 5.50) was bent a complete **CT** volume of the entire length was not available and such this analysis could not be undertaken.

The stabilisation of the new primary dendrite arm spacing took place over a number of diffusion lengths dependent upon reaching the new withdrawal rate. The 40-80 μms^{-1} sample stabilised after 56.8 times the diffusion length L_d from the initial velocity change. For this alloy and speed was 37.5 μm (Table 3.2). This value of $56.8L_d$ corresponded to a length of 2.13 mm obtained from the JMAK analysis in Figure 5.33.

The 40-60-80 μms^{-1} sample showed a much longer dependence on the diffusion length for this sample. In this instance for the transition from 40-60 μms^{-1} the transition took place over $240L_d$ from the initial velocity change. Where $L_d = 50$ μm in the 60 μms^{-1} region. This corresponded to a length of 12 mm from the initial velocity change.

Subsequently on the change from 60 to 80 μms^{-1} the transition took place over $186L_d$, where $L_d = 37.5$ μm in the 80 μms^{-1} region. This corresponded to a length of 6.5 mm. These lengths are longer than the reported ones from the 40 to 80 μms^{-1} sample.

One possible reason that this transition took much longer for the second sample is that the difference between the first and second velocities was much smaller, 40 μms^{-1} for the 40-80 μms^{-1} transition. Rather than 20 μms^{-1} in both the 40-60 μms^{-1} and 60-80 μms^{-1} transitions.

As the difference is smaller in the 20 μms^{-1} transitions there could be less of an impetus in the system to reorder the dendritic array to a more stable and lower **PDAS** value. Therefore the creation of new primary dendrite arms by tertiary arm stabilisation will take place over a longer period. This small incremental change results in far fewer number of new dendrites (as shown in Figure 5.46c,

Figure 5.47, Figure 5.48c for the first and second velocity changes) as compared to Figure 4 of Chapter 11 where there is a much greater number of new dendrites formed. Figure 4 of the Appendix in Chapter 11 shows there is a near constant number of new primary dendrite arms being created with the new dendrites being created at a faster rate than in the 40-60-80 μms^{-1} samples.

This preliminary study indicates that the length that a new **PDAS** becomes stable depends not only upon the diffusion length L_d but also the magnitude of the withdrawal rate change. It is clear however that more research into this effect is needed.

6.5 PDAS Calculation Comparison

All of the samples (Figures 5.10, 5.15, 5.20, 5.25, 5.38 and 5.50 and Figure 4 Chapter 11) for the differing **PDAS** calculation techniques show the same spread across the data. The average **PDAS** calculation of Equation (6.1) is for each sample the highest value of all the differing methods. Next followed by the: Voronoi, Warnken-Reed-Voronoi, Warnken-Reed, and finally the minimum-spanning-tree. As reported in Chapter 4 the centre finding method has little to no effect on the resultant spread of local **PDAS** as shown when comparing the hand assigned and skeleton-geometry assigned centres in Tables 4.6 and 4.7.

The spread between all the different methods was consistent between all the samples studied. This shows that the differing methods for calculating the local primary dendrite arm spacing affect how the final average value for the slice is obtained.

At the two extremes are the average **PDAS** and the minimum-spanning-tree. The average **PDAS** calculates the average spacing of the dendrites across the sample

will always give the largest value for the **PDAS**. Whereas with the minimum-spanning-tree the **PDAS** as it finds the optimal and shortest route between all the dendrites has a much lower value comparatively. This can be seen qualitatively in graphs collating the calculated **PDAS** for each method Figure 5.58a and b, and in the graphs for each sample Figures 5.10, 5.15, 5.20, 5.25, 5.38 and 5.50. The average spacing is higher in every instance than the minimum spanning tree spacing.

The values for the other three techniques lie between these two extremes. The largest being the Voronoi technique, the smallest being the Warnken-Reed, with the Warnken-Reed-Voronoi lying between the two of them. Which, as the **WRV** technique is a combination of both the **WR** and Voronoi methods it is to be expected. Again, this can be seen qualitatively in graphs collating the calculated **PDAS** for each method Figure 5.57, Figure 5.58c, d, and in the graphs for each sample Figures 5.10, 5.15, 5.20, 5.25, 5.38 and 5.50

The Warnken-Reed method is the best technique for ascertaining the local **PDAS** distribution. The **WR** method only includes dendrites within a very small local area surrounding each dendrite analysed [32, 107, 133]. This reduction in the number of dendrites analysed means the method can more accurately analyse the dendrites with an over lapping solute and diffusional field which would have affected the growth of the dendrite through the sample. Only the closest dendrites, and therefore the ones most likely to affect the dendrites are thus used in the calculation. This is similar to the minimum-spanning-tree. However, the minimum-spanning-tree only searches for the very nearest neighbour. So in instances where a dendrite is impinged by two or more solute fields overlapping its own the **MST** method would not be able to detect this, but the **WR** method would.

As shown in Figure 5.57, Figures 5.59 and 5.60 the results of the Warnken-Reed

method lie between the Trivedi, Hunt and Bouchard-Kirkaldy lines. The Kurz-Fisher calculation is several hundred μm greater than the results of the Warnken-Reed results and overestimates the **PDAS**.

The best candidate for the estimation of the **PDAS** is therefore the Trivedi method. This can be seen qualitatively from Figures 5.59 and 5.60. The Trivedi method is the best of the four methods for calculating the **PDAS** for this aluminium 10 wt% copper solidified under varying withdrawal rates. This result was also found by Grunduz and Cadrili in their work on directional solidification of aluminium-copper alloys [31]. They found that low copper aluminium-copper alloys were best described by the Trivedi equation as compared to the other PDAS calculation methods of Hunt and Kurz-Fisher [31].

The Trivedi method provides the best fit for the Warnken-Reed calculation. All of the four calculation methods (in Equations (2.23) to (2.26)) predict a **PDAS** for a number of dendrites in a uniform distribution any deviation from the 'perfect' uniform array as predicted in these equations results in a lower **PDAS**. This is both shown here in the results of the experiments (Figures 5.57, 5.59 and 5.60) and known from the literature. By introducing randomness into the array it is well known that the local **PDAS** decreases [32, 107, 133]. The polycrystaline samples examined here had a high degree of randomness along the entire length of the samples (as shown by comparing Figures 5.54 to 5.56 with Figure 4.33) so any resulting local **PDAS** would be lower than the 'ideal' uniform value of Equations (2.23) to (2.26). Therefore, the Trivedi equation of Equation (2.24) is the equation which most accurately conveys the local **PDAS** of the Warnen-Reed method. Whilst there is a difference between the value obtained experimentally and the results of the Trivedi equation this difference can be explained simply due to the non-uniform array distribution of the samples.

The **WR** method however does fall down due to its reliance on a fitting factor α

which is not tied to any microstructural parameter [32, 107, 133]. The value of α, which was set to 1.5 in this study, could theoretically be set to any value. As such setting a value of α too high could possibly cover the entire sample and causing every dendrite to be assigned as a nearest neighbour. A value of α too small would mean that no surrounding dendrites are analysed at all resulting in a number of nearest neighbours of zero.

6.6 JMAK Analysis of Samples

The results of the JMAK analysis given in Table 5.4 for the Warnken-Reed analysis give a value for n between 1.8 and 2.25. As indicated by Table 2.1 and references [16, 17, 18, 19] this indicates that the phase transformation is 2D parabolic with a constant nucleation rate.

The nucleation rate for the experiments are believed to have been constant, this is reflected by the value of n calculated. The curves for rate of change of **PDAS** from start of transition till the end of the transition can be described by linear curves with an R^2 value in each case greater than 0.9 (Tables 5.1 to 5.3). New dendrites in the samples nucleated via stabilisation of tertiary arms from a parent dendrite forming a new stable dendrite. This process was continually occurring as the array microstructure progressed until at the end of the transition there were no 'available spaces' for tertiary arms to stabilise and grow into. The 'nucleation' of new primary trunks from tertiary arms stabilisation is not something that has been examined previously and cannot be directly compared to equiaxed crystal growth or spherulite growth. Both of these crystal structures have been examined substantially in the literature [16, 17, 18, 19, 20].

Furthermore, whilst the growth of dendrites here is diffusion controlled it is unlikely to be 2D. Directional solidification is a 3D process with the dendrites growing

in three dimensions. It is likely that that the value of n should be 2.5 for the experiments undertaken here [16, 17, 18, 19, 20]. However, one difficulty in comparing the values of n in Table 2.1 is that they generally relate to unconstrained spherulitic growth of polymers or equiaxed crystal growth [20]. The author is unaware of any literature concerning change in **PDAS** examined using JMAK. Therefore more analysis of similar experiments would be needed to understand what the value of n means for directional solidification of dendritic materials. More work is needed to understand how n relates to 3D directional growth of dendrites.

6.7 Number of Nearest Neighbours

The graphs showing the number of nearest neighbours along the length of all the samples are given in Figures 5.11, 5.16, 5.21, 5.26, 5.31, 5.39 and 5.51. The values were calculated using the Voronoi, Warnken-Reed and Warnken-Reed-Voronoi methods. Consistently for each sample the Warnken-Reed-Voronoi method had the largest number of nearest neighbours for each sample, compared to the Voronoi (2nd highest) and the Warnken-Reed method which contained the lowest number. It is clear that the combination of the two methods allowed the **WRV** technique to calculate the spacing involving more dendrites than is the case for only the **WR** or Voronoi methods individually. The number of nearest neighbours captured by each technique gives a clear indication of the search radius of each of the techniques. Implicitly the Warnken-Reed method has the smallest radius and the Warnken-Reed-Voronoi method has the largest.

A number of nearest neighbours for the minimum-spanning-tree could not be calculated. As this method works by joining all the points in one continuous line each point only has 'one' neighbour assigned by the method.

In each case the number of nearest neighbours in all samples remained relatively constant Figures 5.11, 5.16, 5.21, 5.26, 5.31, 5.39 and 5.51. The **WRV** method showed that there was an average five nearest neighbours for each dendrite in each slice. Four nearest neighbours for the Voronoi method and around 3.25 for **WR** technique. There is a lack of change in the number of nearest neighbours along the length of the samples, even when there is a change in the **PDAS** as in the changing withdrawal rate samples. A perfect hexagonal close packed structure would have six nearest neighbours. With each of the three different methods giving a value less than six it is clear there is a degree of randomness in the crystal array that each of the methods have picked up.

This implies that that whilst the dendritic array is changing continuously–with new dendrites being created or outcompeted–the array structure as a whole is not changing. The **WRV** method is closest to the hexagonal close packed structure that is the dendritic array would achieve if it were a perfect crystal. Hexagonal close packed dendrites would have six nearest neighbours. All of the examined **CT** volumes are polycrystalline however, therefore are unlikely to achieve this perfect six nearest neighbours. This is due, in part, to the degree of randomness that results from growth under convective conditions.

Moreover the dendrites themselves are not perfectly aligned with the horizontal but slightly misaligned, with the [001] axis of each individual dendrite misaligned as compared to the horizontal (as seen in Figures 5.13, 5.18, 5.23, 5.28, 5.36 and 5.49). This misalignment means that the number of nearest neighbours would not be accurately calculated, schematically shown in Figure 6.1.

One final possible cause for the lower number of nearest neighbours is that edge dendrites were included in the calculations. These edge dendrites have a lower number of nearest neighbours than ones in the bulk of the dendritic array. By including these perimeter dendrites in the averaging calculation there will be an

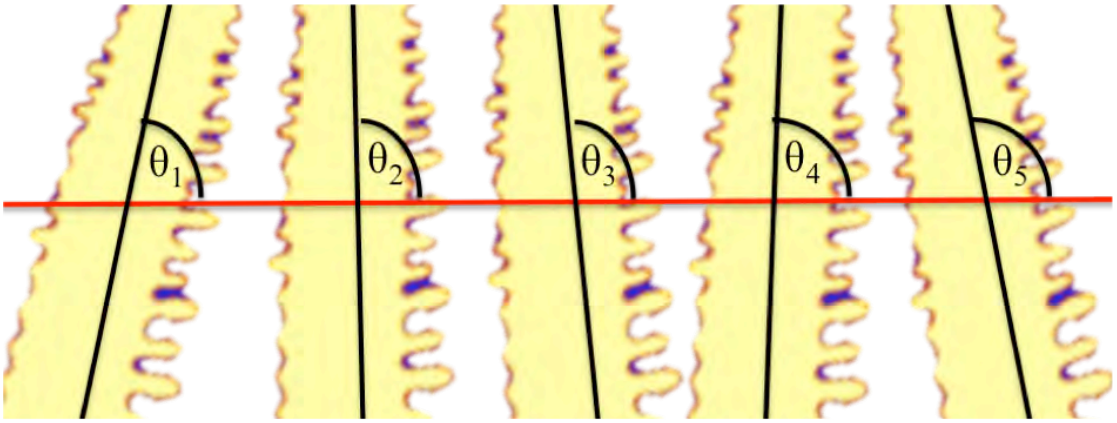


FIGURE 6.1: Schematic view of dendrites at an angle to the [001] direction (upwards to top of the page). The red line indicates a plane taken across the **CT** volume corresponding to an individual slice of the sample.

overall decrease in the number of nearest neighbours for each dendrites. The use of a convex hull operation could be used to remove these edge dendrites and give a more accurate analysis of the nearest neighbours. This has previously been done in the work by Tschopp *et al* on a 2D single-crystal array, rather than a polycrystalline array [32, 133].

6.8 Minimum-Spanning-Tree Packing Factor

Each of the samples show that the packing arrangement of the samples tended to be at the random distribution end (Figures 5.54 to 5.56) when compared with Figure 4.33. This is different to the results of the **WRV** technique which gave an average value of five nearest neighbours along the length of each sample which is close to the hexagonal packing arrangement which is seen in single crystal dendritic aluminium alloys.

However it is important to draw a distinction between the **WRV** and **MST** methods. The **WRV** technique merely finds the number of points within a threshold distance from the dendrite being examined [32, 107, 133]. The **MST** method on the other hand measures the uniformity of the packing [132, 155, 156, 157]. If–as is the case here–the microstructure is polycrystalline there will be a number of crystals all at different angles to each other (as in Figure 5.2 and shown schematically in Figure 6.1) there will be an inherent randomness seen in the results of the **MST** packing factor. This is reflected in the results of all the samples in Figures 5.54 to 5.56. The **MST** function would be much more useful if applied to a single crystal sample rather than, as here, to a polycrystalline sample.

MST analysis could be used to check which is the dominant force in spacing adjustment. Hexagonal close packed structures with the shorter distance between dendrites indicates that diffusion is the dominant force [18, 22, 132]. Square arrays

indicate that crystallography is dominant [18, 22, 132]. Analysing a single crystal sample would give a good indication of how the changing withdrawal rate affects the sample and if crystallography or diffusion is dominant. Due to the polycrystalline nature of the samples examined here such an analysis could not have been performed.

6.9 Experimental Results Against Relative Velocity Change

The graphs given in Figure 5.61a-d and Figure 5.62a indicate that there is little to no dependence on the transition length, incubation time, transition time, diffusion length, or L/L_d. This lack of dependence on these materials parameters may be due to the extremely small set of data used here. The small data set may give the appearance of randomness which may not in fact be present when more points are added to the data. However as shown by the fit in Figure 5.61c it is possible that there is an exponential relationship between the transition length, L and the relative velocity change.

Conversely the Figure 5.62b-d show there is a correlation with change in **PDAS**, $\Delta\lambda/L$, and $\Delta\lambda/L_d$. In each case the results giving a relatively positive trend. The graphs show an increasing relative velocity change increasing the value of the change in **PDAS**, $\Delta\lambda/L$, and $\Delta\lambda/L_d$. Whilst there is only a small number of points to draw a conclusion from it stands to reason that a larger jump between v_1 and v_2 would result in a greater change in the final **PDAS**. Similar results were seen by Ma [12, 13] for changing ∇T experiments in a transparent model alloy in 2.5D. A greater jump in the ∇T tended to result in a greater change in the **PDAS** after the jump.

Contrary to the change in **PDAS** there appears to be little affect on the change in the number of nearest neighbours for the each of the methods with respect to the relative velocity change. As shown in Figure 5.63c the points appeared to be scattered with no coherent trend being obvious. This random scattering of points may be due to the low number of results obtained here. Or, it may be that the relative change in withdrawal rate has no effect on the change in nearest numbers. In order to test how a dendritic array reacts to changes in relative velocity it may be better to undertake future experiments on single crystal alloys. The lack of a poly crystalline structure would lend greater understanding to how the array restructures after a change in withdrawal rate without the complexity of grain boundaries. For example, moving from a hexagonal close packed structure to a more square structure. This change is implicitly much harder to discern in polycrystalline samples due to the more random dendritic structure.

6.10 Misorientation of Dendrites in the Samples

The methods used here have been able to capture the misorientation of entire dendritic arrays in 3D (as shown in Figures 5.13, 5.18, 5.23, 5.28, 5.36 and 5.49), this has not previously been achieved. Whilst the technique for finding the misorientation is fairly trivial, being only simple vector arithmetic, it allows for much greater analysis of samples as compared to visual inspection of samples. For example in the work undertaken on transparent model alloys as examined by Ma [12, 13]. In Ma's pseudo-2D experiments and other similar pseudo-2D experiments (such as [44, 55]) misorientation could have only been calculated for a limited number of dendrites over a limited length of sample. In contrast here the author was able to analyse greater lengths of samples (up to 20 mm in length for the 40 μms^{-1} sample Figure 5.13). Compared to pseudo-2D experiments or longitudinal sections of 3D samples whole sample analysis in 3D shows clear advantages.

This analysis method would also allow for easy comparison with techniques such as **EBSD**. **EBSD** gives an idea of a grain's texture. So too, could a cluster of dendrite orientations be analysed to separate out grains and show texture in 3D, rather than only 2D from **EBSD**. By clustering dendrites into similar orientations, in a similar fashion as to the clustering of orientation in Section 4.8, individual dendrites could be sorted into grains. In each case the similar grains would have dendrites with largely similar or identical misorientations. The result would be a method by which 3D arrays of dendrites could be sorted into different grains, textures and orientations without the need for extensive serial sectioning and **EBSD**.

Comparing the location of the dendrites which are outcompeted and location of pores within the sample with the misorientation angles it is clear that rather than dendrites being outcompeted due to a large misorientation it is infact porosity which is the driving force for dendrites being outcompeted. For example comparing Figure 5.17 and Figure 5.18 the dendrites being outcompeted show good alignment with the rest of the dendrites within the sample. The same is true for all of the other samples in Figures 5.13, 5.22, 5.23, 5.27, 5.28, 5.35, 5.36, 5.46, 5.49, 5.52 and 5.53.

It is therefore clear that when either the velocity of the samples remains constant, or increases due to a step change, the main reason that dendrites become outcompeted in these samples is due to the presence of porosity in the sample. The pores block the continued growth of the dendrite trunk. In each instance of a pore being present in the sample there is an immediate increase in the number of new dendrites created by tertiary arm stabilisation after the pore (Figures 5.17, 5.22, 5.27, 5.35, 5.46, 5.52 and 5.53). The primary trunks once growing past the top of the pore implicitly cover the surface with secondary arms. Tertiary arms then grow from the secondary arms, stabilise, and then grow forming new primary trunks. Or, new dendrites initiate on the surface of the pore. The dendritic array adapts to return to the same pre-porosity **PDAS**, or as close as possible to it.

This reconstruction is clearly seen when comparing Figure 5.25 and Figure 5.27a. The average **PDAS** increases at the point coinciding with the pore. After the pore the average **PDAS** then returns to its 'optimal' level.

This outcome is different to the results of the pseudo-2D experiments of Ma [12, 13]. Ma showed that it was dendrites coming too close together that was the main cause for them to become outcompeted. Whilst some of the dendrites in the current samples surely were outcompeted due to overlapping solute fields and impingement (notably in areas with no porosity present) the overwhelming cause of dendrites being outcompeted was due to porosity. It is suggested that in samples without porosity present the main cause for outcompetion of dendrites would be the overlapping of solute fields and impingement as seen by Ma [12, 13].

However, rather than repeating the experiments in 3D repeating the pseudo-2D experiments of Ma would reasonably capture the effect of porosity within the sample. It is suggested that similar restructuring would be seen in a pseudo-2D sample such as Ma's [12, 13] and others [44, 55, 60, 109, 115] if porosity were present or introduced into those experiments. In this instance the author suggests that pseudo-2D samples would sufficiently capture the dendritic restructuring.

Regarding the microporosity along the majority of the samples (Figures 5.17, 5.22, 5.27, 5.35, 5.46, 5.52 and 5.53) there did not appear to be any effect on the misorientation as expected. The micropores became embedded between secondary arms (as was the case in the recently reported results of Zhang *et al* [49]) and did not impinge or prevent the growth of the tertiary arms. Nor conversely, did it promote the creation of new dendrites. The results of this experimental work show good agreement with the cellula-automata simulations undertaken by Zhang *et al* [49] on pseudo-2D simulation volumes.

In cases where new dendrites were created by tertiary arm stabilisation the newly formed dendrites have good alignment with their parent dendrites as shown in

Figures 5.17, 5.22, 5.27, 5.35, 5.46, 5.52 and 5.53. The average misorientation of the newly formed dendrites is very similar to the parent dendrites they form from. This is to be expected. It is well known that branching dendrites are orientated in the same manner as their parents. This has been shown over many years in model transparent alloy experiments [12, 13, 46, 60, 134] and in also metal alloy solidification [44, 55, 115]. The result of this again confirms the results as shown in Ma's work [12, 13]. Further, there appears to be no change between the results of the Ma's work in pseudo-2D and those in 3D as analysed here. Again it appears that pseudo-2D experiments can accurately portray 3D solidification without the need or complexity of 3D solidification itself.

In each case of analysing the misorientation of the new and outcompeted dendrites it is suggested here by comparing the results to the previous work of Ma [12, 13] and others [44, 55, 60, 109, 115] that pseudo-2D experiments can capture all the complexity of 3D growth in a more simplistic fashion. Pseudo-2D analysis is much easier to undertake than 3D experimental work. It is also much easier to image using optical or X-ray **CT** imaging. The downside of pseudo-2D analysis is that it is generally purely for use in research. There are very few applications in industry which require single dendrite thick directionally solidified samples.

6.11 3D Dendrite Forests

Three dimensional plots were created showing the tracked dendrite centres along the lengths of the experiments (Figures 5.9, 5.14, 5.19, 5.24, 5.29, 5.37, 5.64 and 5.65). These figures show that the dendritic growth is fairly constrained along the z-axis, that is parallel to the withdrawal direction, more clearly seen in Figure 5.64. A number of new dendrites were observed to have formed by tertiary arm stabilisation. This is more clearly shown in the zoomed in plot of the 60

μms^{-1} in Figure 5.65. This figure gives credence to the idea that the dendritic array will restructure by tertiary arm stabilisation.

However as the algorithm used to undertake this analysis as described in Section 4.5 finds the new primary arms which are merely connected to a previous dendrite trunk that it formed this cannot be said for certain. One possible other branching mechanism is by means of dendrite tip splitting forming two new dendrites. This would give a 'seaweed' type morphology [31]. This dendrite restructuring method was not seen when observing the slices of the **CT** volume. As such, tertiary arm stabilisation is the most likely candidate for the method of new stabilised primary arms forming.

The method by which dendrites were removed from the dendritic array was by out competition with dendrites continuing to grow in front of the dendrite which is outcompeted. Dendrites along the entire length of the samples were shown to be outcompeted. Small fluctuations on the microscale caused dendrites to be constantly created or outcompeted, even in steady state growth. This showed that at least for the samples analysed the dendritic array was not perfectly stable but metastable.

6.12 3D Dendritic Isosurface Comparison

3D plots of the dendrites taken from the the constant 40 μms^{-1} withdrawal rate sample (Figures 5.66 to 5.68) show dendrites with fairly straight primary trunks. The render (Figure 5.68) shows that the secondary arms are not continuous up the length of the sample but rather they undulate in and out as can be seen by the gap between the secondary arms on the left hand side of the dendrite.

The 3D isosurface plots shown in Figures 5.69 to 5.71 show the 3D nature of the dendrites themselves over several hundred slices. The centre of the dendrites is

shown using two different methods, the centre of gravity and the skeleton centre. The method closest to the 'true' centre of the dendrite as defined in Chapter 3 is the skeleton centre method. As can be seen in Figures 5.69 to 5.71 the skeleton centre line is at the intersection of the dendritic arms in the centre of the cross. It is clear that the skeleton centre method is the better of the two different techniques. Further adding to the reasons given in Chapter 4 that the skeletonisation method is the best of the methods trialled.

The skeletonisation method remains fairly consistent and straight along the length of the sample as seen in Figure 5.72. Along the length of the sample there is only a single instance of an erroneous centre being assigned (shown in red in Figure 5.72).

The isosurfaces themselves are fairly straight with minimal change or movement in the main dendritic trunk. No branching can be seen on this volume implying that this dendrite was stable whilst growing along the length of the volume. Whilst the isosurfaces have not been used to obtain a **SDAS** in this work it is clear values for the **SDAS** could be easily obtained in further work, and importantly without the need for destructive analysis of a sample.

Chapter 7

Conclusions

The aim of this thesis is to provide new methods for the analysis of dendritic structures in 3D which has successfully been carried out. Specifically for the analysis of aluminium 10 wt% copper alloys using computerised tomography. The body of work presented here acts as the basis for further work as part of the **MICAST** project with **ESA**, **DLR** and the University of Birmingham in order to investigate the effect of gravity on the solidification of directionally solidified dendritic materials. This thesis acts as an exploratory work prior to further research being undertaken. A series of recommendations for further work following this thesis can be found in Chapter 8.

7.1 Image Analysis Techniques and Centre Finding Methods

A series of image analysis techniques have been analysed in detail specifically for analysing large scale **CT** volumes. The method chosen to analyse the **CT** volumes was one based on an active contours method. This segmentation technique when combined with a top-hat pre processing step showed the greatest promise for

correctly segmenting images. Active contours based segmentation had been used previously to great success in life sciences and shows great promise in materials science for separating dendrites from the background.

The active contours method combined with the watershed segmentation successfully allowed for the segmentation and further analysis of the sample. By combining the two methods the **CT** volume was successfully segmented, with conjoined dendrites separated into two distinct and unjoined dendrites.

The image analysis method was parallelised for each slice. Parallelisation allowed for large reductions in the computation time needed to analyse the whole **CT** volumes. Each slice could be individually analysed irrespective of the others parallel computing techniques were employed, such as the use of multiple CPUs and GPUs. The time taken to undertake analysis was reduced by a factor of n where n is the number of CPUs.

After segmentation the **CT** volumes were analysed using the skeletonisation based centre finding technique. This skeletonisation based method was the best centre finding technique of the eight testes. It also provided the skeleton which can be used in the skeleton based grain orientation method in Section 4.8. This method whilst shown to work on larger Ni-superalloys dendrites could not work on the aluminium-copper. A possible reason for this is that the resolution of the images was too low as such not allowing the technique to work as well. One further reason the technique may not have worked is that the aluminium-copper dendrites show much greater tertiary arm growth than Ni dendrites. This may have also affected the technique.

7.2 Dendritic Centre Finding Methods

A number of dendrite centre finding methods were trialled in this thesis. Some taken from the literature and the others put forward here. A number of criteria based on shapefactors were put forward which can be used to find the best technique for each shape of dendrite. The best method was the skeletonisation combined with a centre of gravity based method.

This technique was successfully used to find both the skeleton of the dendrite and also the centre of the dendrite to a high degree of accuracy. It was shown that there is little error between the skeleton-geometry and hand assigned method when the whole of the array in a slice was taken into consideration. Even if several points in the array were not assigned correctly the average local spacing averaged out.

7.3 Local and Bulk PDAS Calculation Methods

The **PDAS** was successfully calculated for all of the samples using a variety of techniques: bulk, Warnken-Reed, Voronoi, Warnken-Reed-Voronoi and minimum-spanning-tree. It is tentatively put forward that the Warnken-Reed method provides the most incite into the local structure of a dendritic array. As the **WR** method only takes into account the very closest neighbours it is more likely to only give information on the neighbouring dendrites which effect the growth of the observed dendrite due to overlapping solute fields. The other **PDAS** methods only take into account the very closest dendrite (in the case of the **MST** method) or, they take into account too many neighbouring dendrites (in the case of **WRV** and Voronoi).

The theoretical method which most closely resembled the obtained local **WR PDAS** was the Trivedi method (as shown in Figure 5.57). The **WR PDAS**

was slightly below the calculated Trivedi value which was expected as the Trivedi method calculates **PDAS** based on a uniform distribution rather than a more random distribution as in the samples here. The Trivedi method did however give good agreement with the results of the bulk **PDAS** calculation, which, like the Trivedi method assumes a uniform distribution of dendrites (see Figure 5.58a).

7.4 Effect on PDAS with Changing Withdrawal Rate

It is clear that the PDAS is dependent upon the withdrawal rate. Further it is clear that by changing the withdrawal rate an alloy system will adapt the dendritic array to form a new more stable **PDAS**. The dendritic microstructure adapts by means of tertiary arm stabilisation producing new primary dendrite arms.

This tertiary arm stabilisation occurs when there is an increase in the withdrawal rate. A larger magnitude of the increase–for example–from 40 to 80 μms^{-1} gives a much faster rate of change to the new stable **PDAS**. This new stable **PDAS** occurs over a certain number of diffusion lengths, L_d. Tentatively it is put forward that the number of L_d depends not only on the new velocity achieved but also on the magnitude of the velocity change.

A brief study was undertaken on changing withdrawal rates and their effects on materials parameters. It was clear that the change in **PDAS**, $\Delta\lambda$ is correlated to the magnitude of the velocity change.

Further the analysis of the samples show that whilst the **PDAS** may change the number of nearest neighbours does not change substantially along the length of all the samples analysed. Packing of the dendritic array remains fairly constant along the length of the sample at approximately five nearest neighbours for the

Warnken-Reed-Voronoi method. This implies that the structure of the dendritic array is near hexagonal close packed.

In each experiment there was no columnar to equiaxed transition seen as such the assumptions that the withdrawal rate changes would not cause a **CET** are valid. These four different velocities were shown on the solidification map in Figure 3.6. In each of the scanned samples there was only columnar dendritic growth with no equiaxed crystals formed within the melt. For an aluminium 10 wt% copper the assumptions used given to create the map can be said to be validated.

7.5 Visualisation of Individual Dendrites and Dendritic forest

The dendrites themselves were able to be tracked along the length of the different withdrawal rate samples. This showed a clear advantage over the results of Ma [12, 13] which were only obtained in pseudo-2D. The images showing the dendritic forests and the individual dendrites themselves. Instances in the dendritic forests of tertiary arm stabilisation were found and shown. This tertiary arm stabilisation was shown to be the method that the microstructure changes the **PDAS**. In each of the changing withdrawal rate samples it is this mechanism rather than a **CET** that occurs as shown on the dendrite forest plots.

7.6 Whole Sample Analysis

The methods presented here can be used to perform whole sample analysis of dendritic microstructures. Whilst an aluminium copper alloy was analysed here any columnar dendritic material could be analysed. So long, that is, that the sample can be imaged in a **CT** scanner.

The methods outlined here could be used to create an automated technique for analysing large samples for non-destructive testing. The method could automatically find changes in the **PDAS** and also in future could be used to find the locations of a columnar to equiaxed transition. The location of this transition can coincide with the end of the tracked columnar dendrites.

One downside of the techniques outlined here however is that they would only work for samples which have already been solidified. Only post-solidification analysis can be undertaken rather than *in situ* imaging. The issue here being that current tomography devices require a sample to rotate and capture many individual 2D images to be stitched together. If however, a tomography machine could be produced being able to capture a sample in 360 instantaneously without a turntable the techniques to track the dendrites used here could capture the growth in almost real time. By tracking the moving interface only the dendrite slices near to the interface would need to be evaluated within the mushy zone. Rather than the whole sample each time step.

Chapter 8

Future Works

A number of possible future works are thus outlined for work continuing from this project. As the thesis compromised a very novel technique for the analysis of dendritic microstructures in three-dimensions there is a large scope for applying the technique(s) to many further scenarios and topics. As such the author provides this list as a succinct list of topics but however are not all encompassing the possible uses for the techniques outlined within this thesis.

1. Adapt the dendrite orientation technique for use with other microstructures;
2. Research more into the use of neural networks to find the centre of a dendrite;
3. More analysis needed into the affect of changing withdrawal rates and the length of sample needed for the restabilisation of **PDAS**:
   (a) Increasing withdrawal rates;
   (b) Decreasing withdrawal rates;
   (c) Increasing then decreasing the withdrawal rate;
   (d) Decreasing then increasing the withdrawal rate.

4. Research into how three dimensional dendritic arrays adapt around features within the sample, examples being:
   (a) Porosity;
   (b) Changes in core shape;
   (c) Changes in mould shape, e.g. increasing or decreasing diameter;
   (d) insoluble particles;
   (e) Secondary or tertiary phases;
   (f) Equiaxed crystals.
5. Analysis on higher resolution images allowing for more precise measurements of the dendrite centres;
6. Analysis of samples cast under extreme conditions:
   (a) Higher gravity levels;
   (b) Microgravity levels;
   (c) Magnetic stirring;
   (d) High pressures;
   (e) Low pressures;
   (f) Against gravity.
7. Tracking the dendritic crystal drift along the length of the samples in 3D
8. Effect of fragmentation at higher gravity levels:
   (a) With gravity;
   (b) Against gravity.
9. Changing copper concentration;

10. Investigate the change in dendrite shape factors along the length of the sample;

11. Investigate the change in dendrite shape factors before and after a velocity change;

12. Repeated on more technically relevant alloys;

13. Understanding the effect that diffusion length, L_d, and magnitude of velocity change has upon the length required for a new stabilised dendritic array to emerge;

14. Study the effect of grain boundary impingement in polycrystaline samples and compare with three dimensional cellular automata or phase field analysis.

Chapter 9

Appendix A: Aerogel Furnace Modelling

9.1 Introduction

Aerogel furnaces are extremely lightweight and compact so they can be used in situations where conventional furnaces cannot be used, for example in sounding rocket experiments [166]. They also allow optical temperature measurements due to the transparent nature of aerogel [37]. A typical design for one is shown in fig. 9.1. One drawback, however, is the lack of control of the metal solidification occurring within the furnace. Unlike with a Bridgman furnace where the pulling rate and thermal gradient can be easily controlled by withdrawing the sample, an aerogel furnace has one or two heaters fitted to the top or bottom of the crucible. The obvious advantage of a power down furnace of which the aerogel furnace is one variant is that they do not have any moving parts. As such they are very good for microgravity experiments as they take away some of the operational complexity and associated risks of moving parts which would be present in a small rocket based Bridgman furnace. The disadvantage however is only control of the solidification

front velocity and thermal gradient (v^* and ∇T respectively) is by manipulating the cooling rate of the top and bottom heaters. The complexity in producing a cooling regime with constant v^* and ∇T is exacerbated by the influence of latent heat and the changing values of the temperature-dependent c_p, ρ, and κ during solidification.

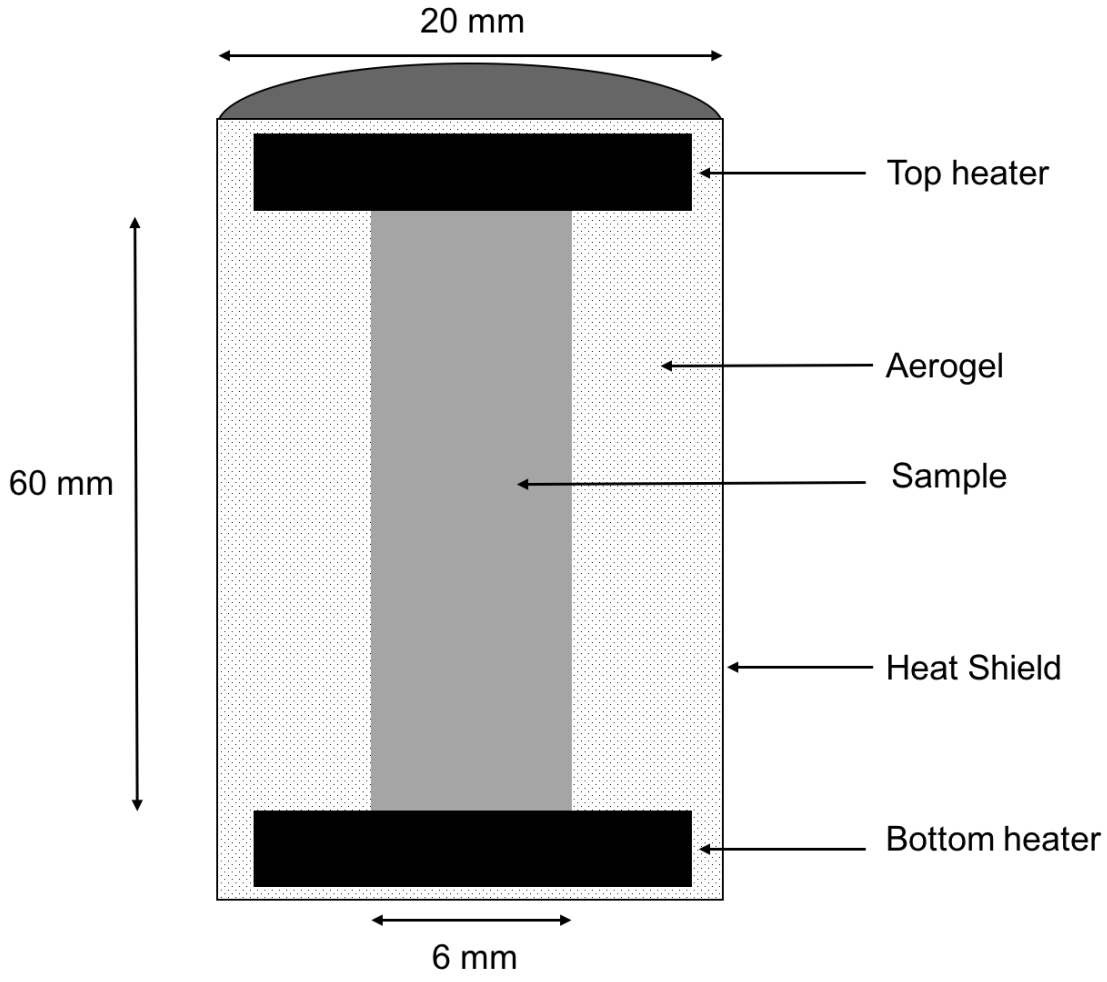


FIGURE 9.1: Schematic design of the aerogel furnace manufactured by the German Space Agency[14] (not to scale).

Previous work within the literature has shown that it is fairly trivial to control the front velocity[37]. However control of the thermal gradient ahead of the solidification front and not across the mushy zone was achieved[37]. In controlling the growth of dendritic crystals it is important to have a constant thermal gradient across the mushy zone, ∇T_{mushy} with a depth of d:

$$\nabla T_{mushy} = \frac{\Delta T_0}{d_{mushy}} = \frac{T_m - T_e}{d_{mushy}} \tag{9.1}$$

This is due to the thermal gradients–and front velocities, v^*–effect upon the primary dendrite arm spacing ($PDAS$)[10]:

$$\lambda_{1g} = a\left(\frac{16X_{Cu}^{\frac{1}{2}}\gamma_{sl}T_{Al}D_l}{(1-k)mL\rho_s\nabla T_{mushy}v^*}\right)^{\frac{1}{2}} \tag{9.2}$$

So obtaining a constant value for both ∇T_{mushy} and v^* would be ideal, but in real life small variations in these values can cause a change in the actual λ. However evolving microstructures are very dependent upon previously formed microstructure[167] and as a result an evolving dendrite array must overcome an energy barrier before destabilising and changing the λ[12, 144, 168]. As a result small variations in either parameter can have little effect on the final microstructure allowing for a range of stable values for ∇T and v^*[12, 169].

However one problem is that eq. (9.2) ignores the effect of fluid flow during solidification. This means that the λ calculated here is under purely diffusive conditions. A simple analytical scaling proposed by Diepers and Steinbach [62] based upon earlier work undertaken on binary alloys by Batallie *et al.* [33] and Lehmann *et al.* [170] leads to the following scaling law:

$$\lambda_{flow} = \lambda_{1g}\frac{g}{g_E}^{-\frac{1}{8}} \tag{9.3}$$

The applicability of which to reality has not been validated within the literature. As the function was derived from two experiments undertaken by Batallie *et al.*

[33] and Lehmann *et al.* [170] more experiments are needed to ascertain the validity of this equation.

In order to achieve the accelerations required there are various methods which can be employed. For microgravity ($g < g_E$) experiments can be undertaken for increasing lengths of time using drop tests, parabolic flights, sounding rockets, through to long term study on the International Space Station *ISS* [15, 29, 46, 97, 166]. However as the length of time for the experiments increases so too does the operational complexity, especially with producing samples and equipment for study aboard the *ISS*[29].

For unit gravity ($g = g_E$) experiments are relatively straight forward. This is in part due to the fact they can be undertaken on terrestrial equipment, such as Bridgman or other commonly available furnaces.

Finally for gravity levels greater than unit gravity ($g > g_E$) the use of a centrifuge is necessary. This is in order to produce centripetal forces necessary to simulate high gravity conditions. Again like with microgravity experiments there are associated complexities with the hypergravity experiments. One being that any furnaces must be made of suitably strong material to withstand the increased weight they will experience during the experiment but at the same time have a small footprint so that they can fit within the experimental gondola or rocket section.

As such a series of experiments is needed to undertake examinations on *PDAS* across a variety of gravity levels for a number of different materials. Single crystal nickel superalloy is of particular importance to the scientific community for study as controlling the *PDAS* is the primary means of controlling the strength of the final material [22, 171]. However the material is very difficult to work with due to its high melting point which is greater than a safe working temperature for aerogel, and its compositional complexity. Therefore a suitable model alloy is chosen for analysis in many instances of *PDAS* research. The most common of which is an

aluminium-copper alloy (Al with between 4-20 wt% Cu) [10, 15, 31, 168]. Not only is it a well established alloy with many years of research behind it, it is also very simplistic, and most important for the present work has a relatively low melting temperature. Therefore there is the need for simulation of the experiments using Al-Cu binary alloys and to obtain temperatures needed for the top and bottom heaters which will give constant solidification parameters within the furnace itself.

To obtain the cool down regimes needed for this a simulation of a moving boundary problem taking into consideration conduction, radiation and composition is put forward and coupled with a source based method for correcting the temperature field in the mushy zone by taking into account the effect of latent heat[172, 173]. This model is validated using the experimental method found in Cahoon *et al* [15]. An experiment was conducted on an Al-4 wt%Cu alloy under microgravity conditions[15]. A summary and implementation in the model for the experimental work is described below.

Subsequently the simulation is used to derive cool down regimes required for the solidification of an Al-20 wt%Cu alloy under μg, $1g$, and greater than $1g$. The average λ_{1g} and minimum and maximum values will then be calculated using parameters obtained during the simulation. Subsequently a calculation for λ_{flow} as a function of g will be made between 0 and $20g$ using eq. (9.3). This estimation will be used in future work to compare with experimental work undertaken on the large diameter centrifuge at the European Space Agency in Noordwijk and microgravity experiments conducted by the German Space Agency.

9.2 Methodology

An explicit cell-centred finite difference heat conduction equation in an axi-symmetrical cylindrical coordinate system was coupled to radiation from the surface of the

metal sample along with the composition of each cell. The simulation was coded in Matlab 2016b and ran on 1 core of an Intel i7 of a Windows 7 machine.

9.2.1 Governing Equations

The energy equation (eq. (9.4)) was used to calculate changes in temperature throughout two phase (solid and liquid) simulated sample taking into account both radiative and conductive effects (eq. (9.4)). The solidification is assumed to occur under Scheil conditions, with no remelting of the solid. Therefore it is assumed that the liquid phase is completely mixed therefore no information on fluid flow can be obtained within the melt as it is perfectly mixed and immobile. Radiation only occurs from the curved surface of the sample to the heat shield (see fig. 9.1) which is kept at constant room temperature. The crucible is assumed to be a perfect insulator and optically transparent.

To take into account the phase change present in the moving solid-liquid boundary across the mushy zone the 'enthalpy' method is employed. The technique is outlined in the paper by Swaminathan and Voller [172] to which the reader is referred to for greater detail. The 'apparent heat capacity method' [172] has been employed which uses a post iterative correction to the engthalpy adjusting the calculated temperature. The correction is achieved by taking into account the energy contribution of latent heat which is released during phase change.

Outlined in eqs. (9.4) to (9.12) are the governing equations for the heat transfer that takes place within the simulation.

The conservation of energy within the system is described by:

$$\frac{\partial \rho H}{\partial t} = \nabla \cdot (\kappa \nabla T) + S_{rad} \tag{9.4}$$

with the enthalpy described by:

$$H = H_{ref} + \int_{T}^{T_{ref}} c_p T dT + f_l L \tag{9.5}$$

And the radiation source term given by:

$$S_{rad} = \frac{\sigma A_{r_s,i}(T^4 - T_{atm}^4)}{\frac{1}{\epsilon} + \frac{1-\epsilon_{HS}}{\epsilon_{HS}} \frac{r}{r_{HS}}} \tag{9.6}$$

Radiation was coupled along the outer most edge of the sample to the heat shield surrounding the crucible. It was assumed that the radiation from each surface grid point can be described by the radiation between two infinitely long concentric cylinders which are both grey and diffuse[174]. This assumption was made as the top and bottom of the sample would be in contact with the aerogel and therefore only radiation would occur from the curved surface. Moreover the authors made the assumption that the aerogel is optically transparent and therefore would act as if it were a vacuum.

For a numerically stable simulation the finite difference form of the Fourier number for eq. (9.4), Fo must be less than $\frac{1}{4}$ for each node within the array [174].

$$Fo = \frac{\rho c_p}{\kappa} \frac{\Delta t}{\Delta A^2} \tag{9.7}$$

The fraction solid and thus fraction liquid at any temperature is given by the following set of rules from using the Scheil equation:

$$f_s(T) = \begin{cases} 0, & \text{if T} \geq T_m \\ 1 - \left(\frac{T - T_m}{T_{Al} - T_m}\right)^{\frac{1}{k-1}}, & \text{if } T_s < T < T_{Al} \\ 1, & \text{if } T \leq T_s \end{cases} \tag{9.8}$$

and therefore f_l is given by:

$$f_l(T) = \begin{cases} 1, & \text{if T} \geq T_m \\ 1 - f_s, & \text{if } T_s < T < T_{Al} \\ 0, & \text{if } T \leq T_s \end{cases} \tag{9.9}$$

The conservation of the solute is described by:

$$\frac{\partial \bar{C}}{\partial t} = \nabla \cdot (D_l f_l \nabla C_l) \tag{9.10}$$

Where the liquid concentration is given by:

$$C_l = \frac{\bar{C} - f_s C_s}{f_l} \tag{9.11}$$

The assumptions of the Scheil equation are used and as there is no diffusion within the solid, the solid composition is related to the liquid composition by:

$$C_s = kC_l \tag{9.12}$$

The equations were all discretised and integrated with respect to time by using a cell-centred finite difference scheme and solved for each time step in an axi-symmetrical cylindrical coordinate system. A temperature was imposed on the top and bottom of the grid and the temperature of the heat shield was assumed to be constant and equal to atmospheric conditions (see the schematic for the validation simulation in fig. 9.2).

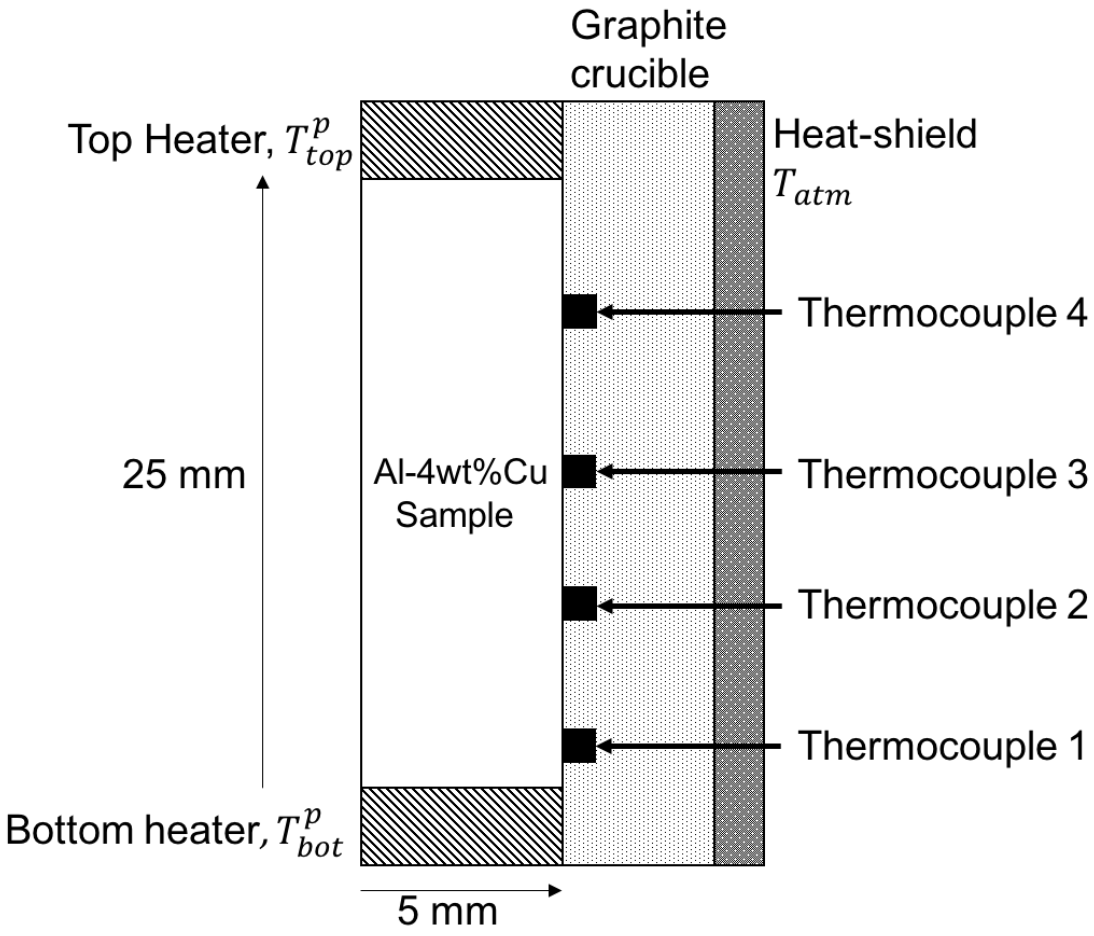


FIGURE 9.2: Schematic of the simulated furnace volume (not to scale).

9.2.2 Maintaining a Constant v^* and d

In order to maintain a constant v^* and d (and therefore ∇T) the following set of equations and associated rules are used at each time step in order to alter the cool down of the top and bottom heaters. For each time step the top and bottom heaters are decreased in temperatures by:

$$T^p_{top} = T^{p-1}_{top} - \dot{T}_{top}\Delta t \tag{9.13a}$$

$$T^p_{bot} = T^{p-1}_{bot} - \dot{T}_{bot}\Delta t \tag{9.13b}$$

These two values are then moderated at each time step if the following conditions are met:

$$T^p_{adj,top}(v^*) \begin{cases} T^{p-1}_{adj,top} + 0, & \text{if } v^* = v_{req} \\ T^{p-1}_{adj,top} + \frac{\dot{T}}{c\Delta t^{-1}}, & \text{if } v^* > v_{req} \\ T^{p-1}_{adj,top} - \frac{\dot{T}}{c\Delta t^{-1}}, & \text{if } v^* < v_{req} \end{cases} \tag{9.14}$$

$$T^p_{adj,bot}(d) = \begin{cases} T^{p-1}_{adj,top} + 0, & \text{if } d = d_{req} \\ T^{p-1}_{adj,top} + \frac{\dot{T}}{c\Delta t^{-1}}, & \text{if } d > d_{req} \\ T^{p-1}_{adj,top} - \frac{\dot{T}}{c\Delta t^{-1}}, & \text{if } d < d_{req} \end{cases} \tag{9.15}$$

Where, at the initial time step, $p = 0$ both $T^{p=0}_{adj,top}$ and $T^{p=0}_{adj,bot}$ are 0 K. The temperature adjustment scaling parameter, c, was set to $0.1\Delta t^{-1}$ so as to prevent

any large changes in the cooling rate each time step. Therefore eq. (9.13) can be rewritten as:

$$T_{top}^{p} = T_{top}^{p-1} - \dot{T}_{top} + T_{adj,top}^{p} \tag{9.16a}$$

$$T_{bot}^{p} = T_{bot}^{p-1} - \dot{T}_{bot} + T_{adj,bot}^{p} \tag{9.16b}$$

The values of v^* and d were obtained at each time step by tracking the approximate locations of the top and bottom of the mushy zone, *i.e.* the points along the length of the sample where f_s first reaches 0 ($T = T_m$) and 1 ($T = T_e$) respectively. The mushy depth, d is simply the distance between these two points. Then v^* is the displacement in the location of the solidification front between two time steps divided by Δt.

9.3 Model Validation

In order to ascertain the validity of the underlying equations in the simulation it was trialled using previous experimental work by Cahoon [15]. The areas of the experiment pertinent to the current work are briefly summarised here. A more in-depth explanation can be obtained from the paper itself [15].

9.3.1 Model Methodology

A cylindrical graphite crucible with a height of 25 mm and inner diameter of 10 mm containing an Al-4 $wt\%$ Cu alloy was initially melted and held at 1060 K. Subsequently it was then directionally solidified using a chill plate attached to the bottom of the sample. Four thermocouples in the wall of the graphite crucible

were used to give temperature readings with time, see table 9.1 for their locations. A schematic diagram (not to scale) is provided in fig. 9.2.

TABLE 9.1: Thermocouple location in the graphite crucible wall [15]

Thermocouple	**Height from base,** mm
1	1
2	7.4
3	13.7
4	20.1

As such, temperature time information is available to compare with the simulation from 1 mm into the sample until 20.1 mm. Therefore, in the interest of replicating the experiments as closely as possible (and as values for the cooling rate applied to the sample are not available) the temperature-time profiles for the top and bottom heaters, T^p_{bot} and T^p_{top} used in the simulation were taken as the temperature-time profiles of the thermocouples 1 (1 mm) and 4 (20.1 mm) respectively.

The simulation and materials parameters are given in tables 9.2 and 9.3 respectively. The location of the solidus and liquidus was tracked as mentioned above and compared with the experimental data.

The sensitivity of the mesh to numerical instability was analysed by examining the effect of the node density in terms of elements per unit area on the final composition of the solid. This was achieved by increasing the mesh density and measuring it's effect upon the maximum and minimum composition at the end of the simulation. Moreover the sensitivity of the simulation to solute depletion was also examined.

Due to copper being a grain boundary segregator and as the microgravity experiments in Cahoon *et al*[15] show large porosities with increasing copper content in areas where there are porosity (higher up the samples) the effect of solute depletion was also examined. This was achieved by decreasing the bulk composition in the simulations from 4 wt% Cu in steps of 0.01 wt% Cu down to a minimum of 3.5 wt% Cu.

TABLE 9.2: Simulation parameters for the model validation.
† h is the distance between the top and bottom thermocouple rather than the entire casting as explained in the model validation methodology.

Parameter	**Value**
$h^{\dagger}$[15]	19.1×10^{-3} m
r[15]	10×10^{-3} m
Δr	1×10^{-3} m
T_{atm}	300 K
$T_{bot}^{p=0}$[15]	1050 K
$T_{top}^{p=0}$[15]	1050 K
$T_{i,j}^{p=0}$[15]	1050 K
Δt	2×10^{-4} s
Δz	0.191×10^{-3} m

TABLE 9.3: Materials Parameters for Al-4 $wt\%$Cu[15]

Parameter	**Value**
a	1.265×10^{-5} K$^{\frac{1}{2}} m^{-\frac{1}{2}}$
C_0	4 wt%
c_p	1070 Jkg$^{-1}K^{-1}$
D_l	1.5×10^{-9} m$^2 s^{-1}$
ρ	2570 kgm^{-3}
ΔT_0	56.4 K
k	0.03
L	3.66×10^5 Jkg^{-1}
T_{Al}	933 K
T_e	843 K
$T_m^{p=0}$	923 K
X_{Cu}	0.017
ϵ_{Al}	0.05 [174]
γ_{sl}	0.1634
κ	0.4 Wm$^{-1}K^{-1}$

9.3.2 Validation Results

The simulation took a total of 2900 s to run until the final thermocouple reading from the experimental data had been reached.

The temperature-time curves for the thermocouples are given in fig. 9.3. The data from the simulation are the continuous lines and the thermocouple readings from the experiment are the points. The simulation shows a similar trend to the experiments. However for thermocouple 2 and 3 (table 9.1) the experimental values are consistently 5-10 K below the simulated values. This deviation begins at approximately 70 s for thermocouple at 13.7 mm and 160 s for the thermocouple at 7.4 mm. Subsequently the discrepancy between the simulation and experimental results remains constant throughout the rest of the simulation.

The composition profile of the solidified alloy is given in fig. 9.4 in terms of percentage error in the composition from the bulk composition of Al-4wt%Cu. The experimentally obtained values are overlain for ease of reading along with the calculated profile.

The λ was calculated by eq. (9.2) at using the conditions of the simulation in the mushy zone at a time of $142s$, which corresponded to the the time the solidification front passed through $h = 12mm$ in the sample. This height corresponds to the height at which a λ of $120\mu m$ was measured by Cahoon *et al.* [15]. A value of $128\mu m$ was calculated using the parameters given in table 9.5. At this time there was a thermal gradient of $2290Km^{-1}$ and a solidification front velocity of $382\mu ms^{-1}$.

The results of the mesh sensitivity analysis are given in fig. 9.5. The graph shows that once approximately 1000 elements/m^2 is reached there is no substantial change in the resultant composition in either the maximum or minimum wt%Cu.

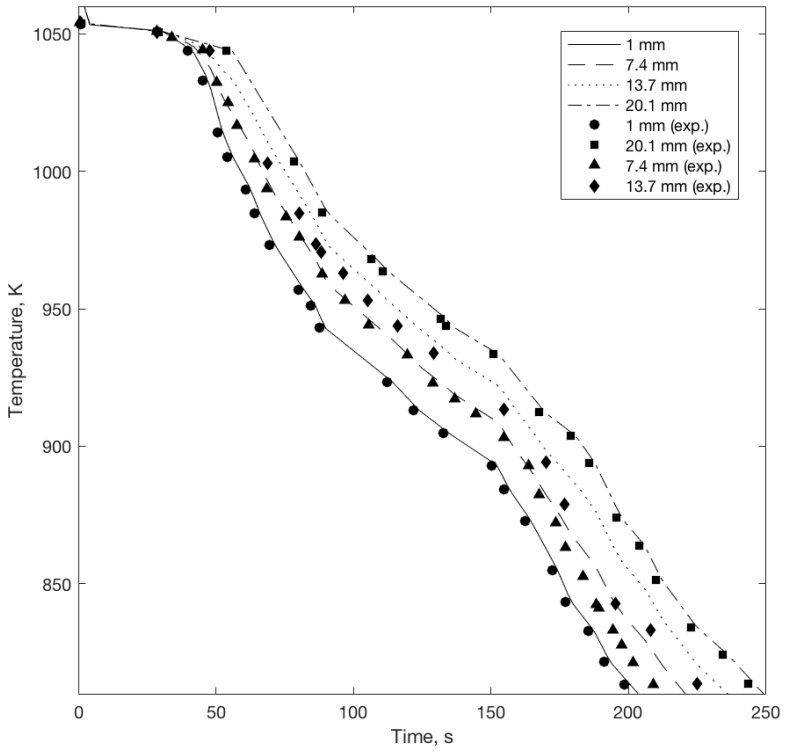


FIGURE 9.3: Temperature-time profiles for the validation simulation of the cool down of an Al-4 wt%Cu alloy in microgravity. The markers are temperatures taken from the experimental work and the lines are temperature readings obtained from the simulation.

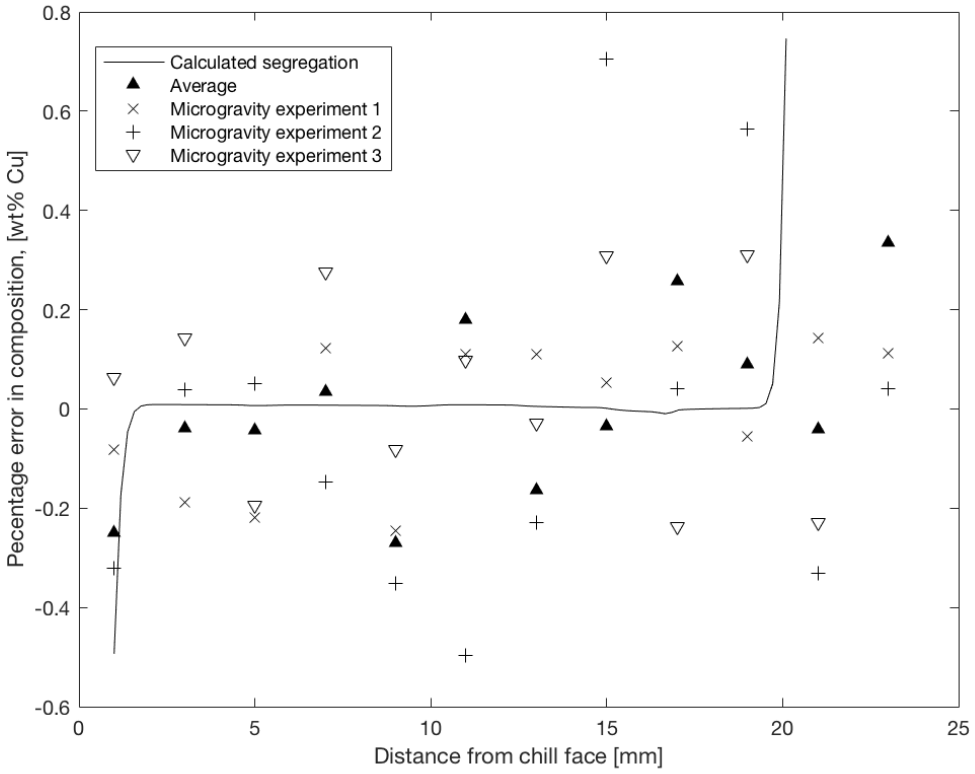


FIGURE 9.4: Relative error in composition against sample length for the simulated alloy compared to the composition readings obtained by Cahoon et al [15] for an Al-4wt% Cu alloy in microgravity.

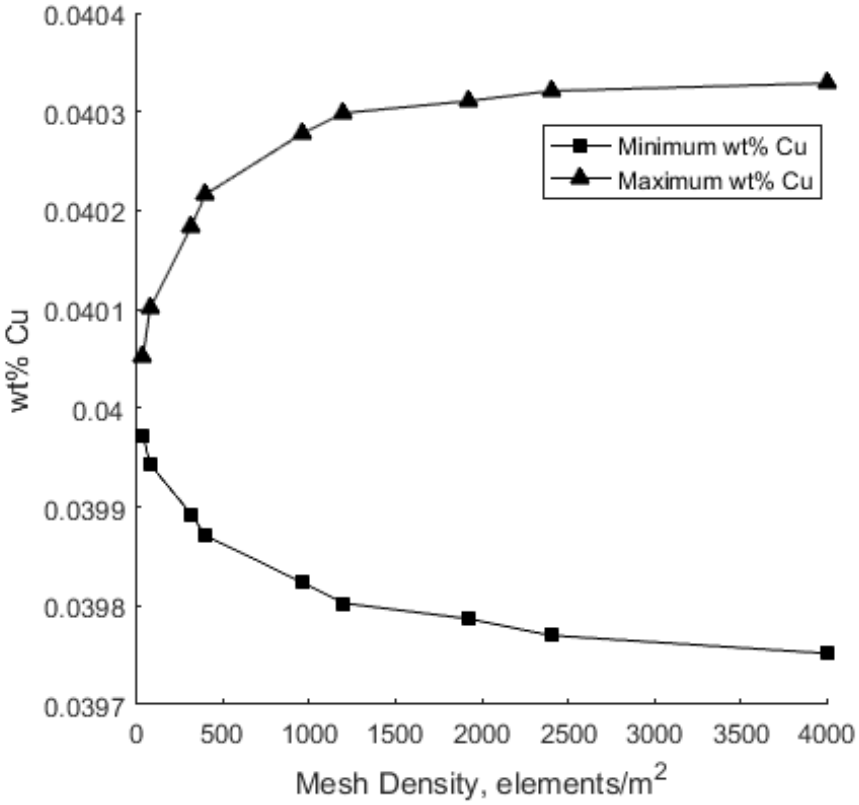


FIGURE 9.5: Composition of the minimum and maximum composition at the end of the experiment against the mesh density.

9.3.3 Validation Discussion

The model was able to accurately describe the experimental results presented in [15] as show by fig. 9.3.

There is a small variation of around $5 - 10\ K$ in the thermocouple temperature readings between the simulated results and those found in Cahoon *et al.* [15] as seen in fig. 9.3. This, as was mentioned in the paper[15], may be due to the readings measuring the temperature of the graphite crucible rather than the alloy itself. As a result they are more of an estimation of the true temperature readings than a completely accurate one. However the discrepancy is most likely due to conduction not being considered through the graphite crucible but only radiation from the sample surface outwards.

The composition was calculated during the simulation using the equations described above (eqs. (9.10) to (9.12)) at each time step. The final composition of the solid along the length of the sample shown in fig. 9.4 falls within the scatter of the experimental data. However the simulated composition is largely constant whereas increasing composition along the length of the sample is reported[15]. One possible error was that the simulation only considered two phases, liquid and solid, whereas in reality three are present, liquid solid and eutectic. Moreover shrinkage, porosity and sample cracks may have caused this scatter. This as Cahoon *et al.* mentions decreases the accuracy of the scanning electron microprobe[15]. As the simulation assumed volume was conserved and there was no porosity present this trend was not reflected within the simulation results. However neither of the above explanations give an adequate reason for the increasing trend in the average composition value of Cu as shown in fig. 9.4.

One possible explanation is the enrichment of copper at the edges of large pores present within the microstructure[175, 176] due to surface segregation of Cu in the Al-based alloy. The pores which form in microgravity are much larger than the

finely dispersed micropores present within unit gravity experiments. Due to the size they can in the absence of convection, agglomerate and be pushed ahead of the solidification interface until they become trapped within the mushy zone itself[15]. The pores represent higher Cu concentrations associated with their surfaces and as they are swept along the solidyfying sample accomplish transfer of Cu from start (Cu-depleted) to the final solidification regions where the pores are trapped leading to Cu enrichment. Fluid flow is not considered in the current simulation but, as the simulation compositions fall within the scatter of experimental data, it is unlikely to significantly change the solidification modes and the design of experiments using the aerogel furnace.

In order to analyse how the model coped with copper depletion due to porosity sensitivity simulations were undertaken by decreasing the bulk composition from 4 wt% Cu down to 3.5 wt% Cu. It was found there was little to no change in the results of the simulation due to decreasing the bulk composition. As such for the purposes of this work the authors believe it would not be applicable to include the modelling of porosity within the simulation. However it should be something to be considered in further work on modelling of solidification under microgravity of aluminium-copper alloys.

The variation from the experimental and calculated curve at $20mm$ was due to the previously mentioned fact the simulation occurred from $1mm$ to $20.1mm$ rather than the full length of the sample. This was due to the availability of only thermocouple data in these locations.

The calculation of λ using eq. (9.2) of 128 μm was within 6% of the λ reported by Cahoon *et al.* From destructive metallurgical analysis [15]. The calculated value of the λ is therefore in good agreement with the reported value. The difference between the calculated and simulated values for the primary dendrite arm spacing are most likely due to the effect of convection within the liquid which causes the λ

to decrease. As this has not been taken into consideration it is therefore reflected in the value obtained from the simulation.

Using equation eq. (9.3) a value for λ can be obtained at $g/g_1 = 0.05$ which was the reported microgravity level when a λ of 170 μm was produced in the sample by [15]. The calculated value is 175 μm which gives a percentage error of 3% from the reported value. This is well within an acceptable range.

Moreover the calculated value of v^* reported by [15] of 386 $\mu m s^{-1}$ has a percentage difference of -0.5% compared to the value obtained by tracking the liquidus interface as it progresses through the simulation. The simulated value of the thermal gradient at this time was within 12% of the value given in Cahoon *et al.* [15].

These calculated values for the v^*, ∇T and λ were all within a reasonable error of the experimental results. As the methodology outlined above–along with the technique to maintain a constant v^* and d–will be used to simulate the solidification of an Al$-$20 $wt\%$Cu rod using a carefully controlled power down experiment as described previously. As such it can be concluded that the mesh density used here of 1000 elements per m^2 was adequate to simulate this experiment. Therefore a mesh density of the same or greater are used in the following experiments.

With the mesh sensitivity analysis there was only a small difference between increasing the mesh density from 1000 elements/m^2 (as in the simulation) to the maximum analysed density of 4000 elements/m^2, as shown in fig. 9.5. This difference corresponded to a 0.18% and a 0.074% difference in the minimum and maximum composition. Due to this small difference, it is reasonable to say that the mesh is not sensitive to large compositional changes with large increases in the mesh density. As such a mesh density of greater than or equal to 1000 elements/m^2 should be used for following simulations.

9.4 Simulation of Al-20wt%Cu Temperature Profiles for Sounding Rocket Experiments

As the model has successfully been able to reproduce previous work by Cahoon *et al.* [15] it was used to simulate the temperature profiles for a directionally cast Al-20wt%Cu alloy. These temperature profiles will be used in a series of experiments to be conducted as part of the Microstructure Formation in Casting of Technical Alloys under Diffusive and Magnetically Controlled Conditions (*MICAST*) project [177] to study solidification in challenging environments. A schematic design of the aerogel furnace designed and manufactured by the German Space Agency[14] is given in fig. 9.1.

9.4.1 Materials and Simulation Parameters

In order to simulate a more realistic scenario equations were fitted to materials parameters with respect to temperature. The equations for density (ρ), heat capacity (c_p) and thermal conductivity (κ) are given below:

$$\rho(T_{i,j}^p) = \begin{cases} -7.26 \times 10^{-5}(T_{i,j}^p)^2 - 0.149T_{i,j}^p + 2.93 \times 10^3, & \text{if } T_{i,j}^p < T_e \\ -3.69T_{i,j}^p + 5790, & \text{if } T_e \geq T_{i,j}^p < T_m \\ -0.230T_{i,j}^p + 2.76 \times 10^3, & \text{if } T_{i,j}^p \geq T_m \end{cases} \tag{9.17}$$

$$c_p(T^p_{i,j}) = \frac{100}{3.43}\begin{cases} 1.03\times10^{-7}(T^p_{i,j})^3 - 1.41\times10^{-4}(T^p_{i,j})^2 & \\ +7.72\times10^{-2}T^p_{i,j} + 12.0, & \text{if } T^p_{i,j} < T_e \\ 0.0706(T^p_{i,j})^2 - 116T^p_{i,j} + 4.80\times10^4, & \text{if } T_e \geq T^p_{i,j} < T_m \\ 31.2T^p_{i,j}, & \text{if } T^p_{i,j} \geq T_m \end{cases} \tag{9.18}$$

These equations for ρ and c_p were fitted to data obtained using the TCAL5 data base in Thermo-calc.

$$\kappa = 100\big(-1.4\times10^{-7}(T^p_{i,j})^2 + 2.12\times10^{-3}T^p_{i,j} + 1.15\big) \tag{9.19}$$

The values of thermal conductivity with time were extracted manually from graphs produced by NIST for an Al20wt%Cu alloy[178].

The other materials parameters are given in table 9.4.

TABLE 9.4: Materials parameters for Al 20 wt% Cu. An approximate value for latent heat was used, in this instance for a Al 6.2wt% Cu alloy.[21]

Parameter	**Value**
a	1.265×10^{-5} K$^{\frac{1}{2}}m^{-\frac{1}{2}}$
C_0	20 wt%
D_l	3×10^{-9} m$^2s^{-1}$
k	0.14
L[21]	4×10^6 JK^{-1}
ΔT_0	54 K
T_{Al}	933 K
T_m	875 K
T_e[21]	821 K
X_{Cu}	0.0850
ϵ	0.05

The finite difference scheme parameters are given below in table 9.5. The elements per unit area for the finite difference scheme were chosen to have a greater density

than for the simulation of the reference experiment (1000 elements per m^2) so as to decrease further the possibility of numerical instability due to mesh size. The aerogel simulations had a mesh density of 1800 elements per m^2.

TABLE 9.5: Simulation parameters

Parameter	**Value**
d_{req}	7.2×10^{-3} m
h	60×10^{-3} m
r	3×10^{-3} m
$r_{H.S}$	1×10^{-2} m
Δr	1×10^{-3} m
T_{atm}	300 K
$T_{bot}^{p=0}$	821 K
$T_{top}^{p=0}$	1199 K
$T_{i,j}^{p=0}$	300 K
$\dot{T}_{bot}$	2.5 Ks^{-1}
$\dot{T}_{top}$	2.5 Ks^{-1}
Δt	5×10^{-4} s
v_{req}	12×10^{-5} ms^{-1}
Δz	1×10^{-4} m
ϵ_{HS}	0.195
γ_{sl}	0.1634 Jm^{-2}

9.5 Results

A series of simulations were undertaken using the parameters outlined above with only the required solidification rate (v_{req}) and mushy depth (d_{req}) changing. The results of which are outlined in table 9.6. The averages were taken from after the initial transient phase until the solidification front reached the top of the sample in each simulation. Run 6 was chosen for further analysis due to the mean λ that was given at the end of it and also due to the time taken for the complete solidification of the simulated sample falling within the constraining 360s required by the microgravity experiments.

Each simulation was run a total of three times and the results were averaged to give the data shown in table 9.6.

The mushy zone depth was calculated every 2.5 s. The relative error for the mushy depth as a function of d_{req} was calculated for every 2.5 s the results of which are shown in fig. 9.6. There is very little variation in the magnitude of the mushy depth with time. The spread in the data after the initial transient region is at its greatest 1% error from the input value of $d = 7.2\ mm$ which corresponds to a value of 7.27 mm. The thermal gradient was calculated using eq. (9.1) and the results given in fig. 9.7. The thermal gradient shows a similar trend to the mushy depth which is to be expected as they are inversely proportional to each other as shown by eq. (9.1).

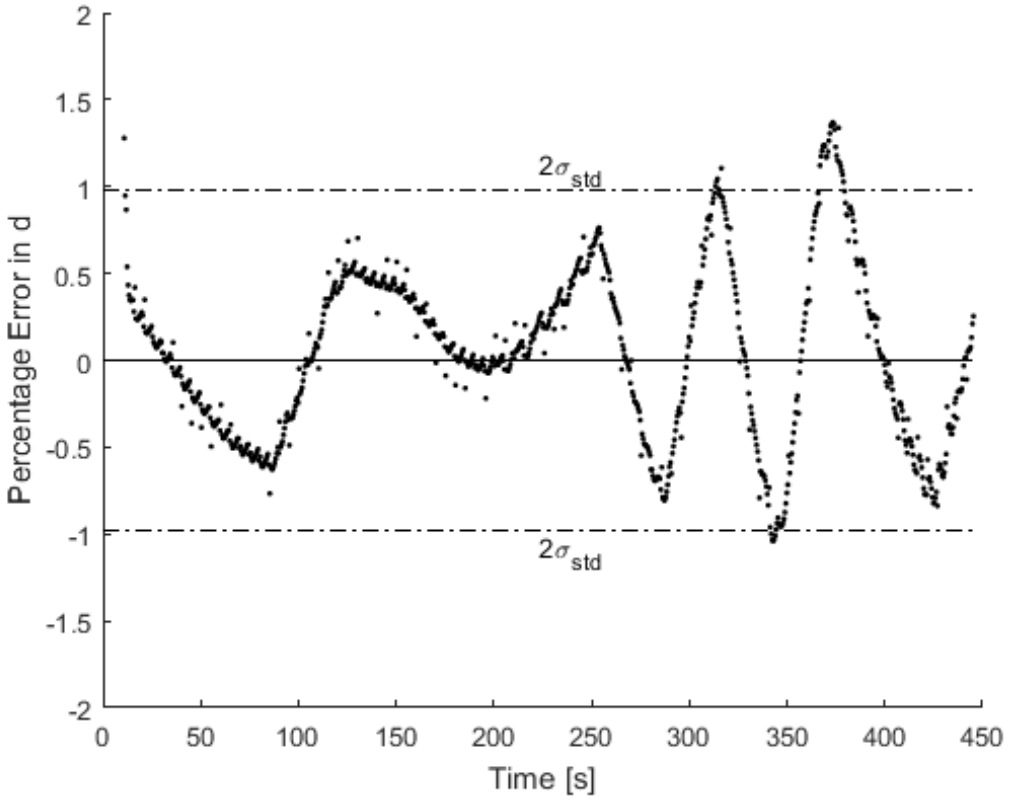


FIGURE 9.6: Relative error of the mushy depth with time obtained from the simulation of the aerogel furnace. The initial transient ended at 15 s. The standard deviation was calculated from the complete data set.

The velocity of the front was also calculated every 2.5 s and output as shown in fig. 9.8. The figure shows a greater spread in the data as compared to fig. 9.6,which shows an average percentage error of approximately 7%.

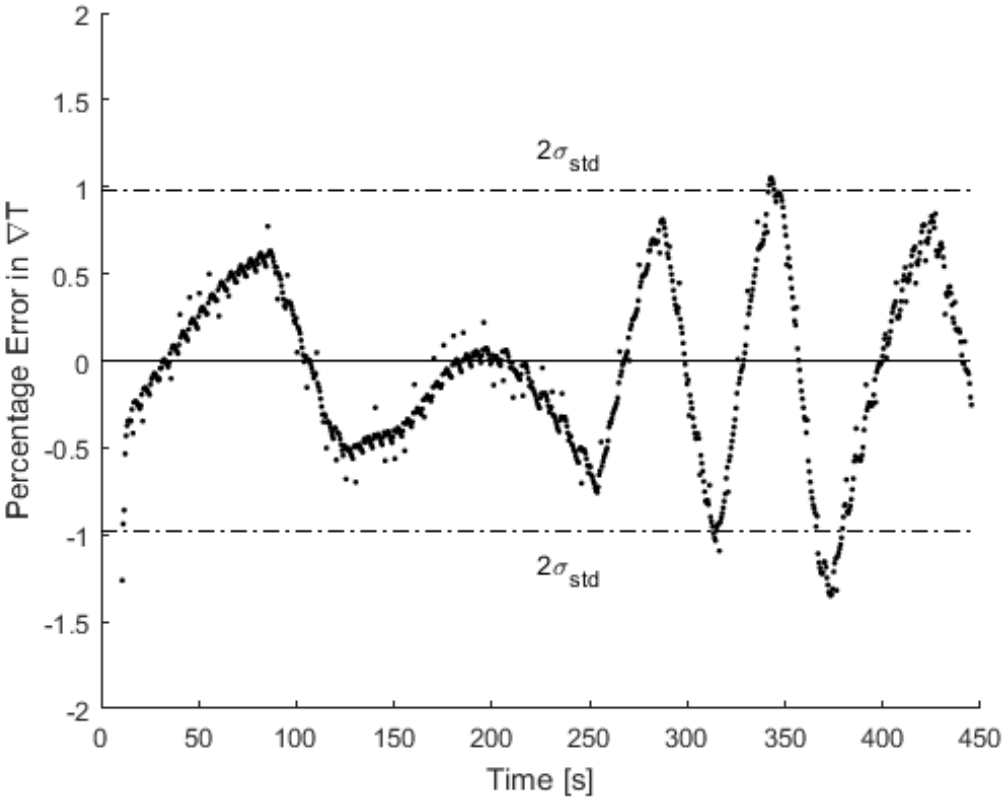


FIGURE 9.7: Relative error in thermal gradient with time calculated using the values given in fig. 9.6, the ΔT_0 from table 9.4 and eq. (9.1). The initial transient ended at 15 s. The standard deviation was calculated from the complete data set.

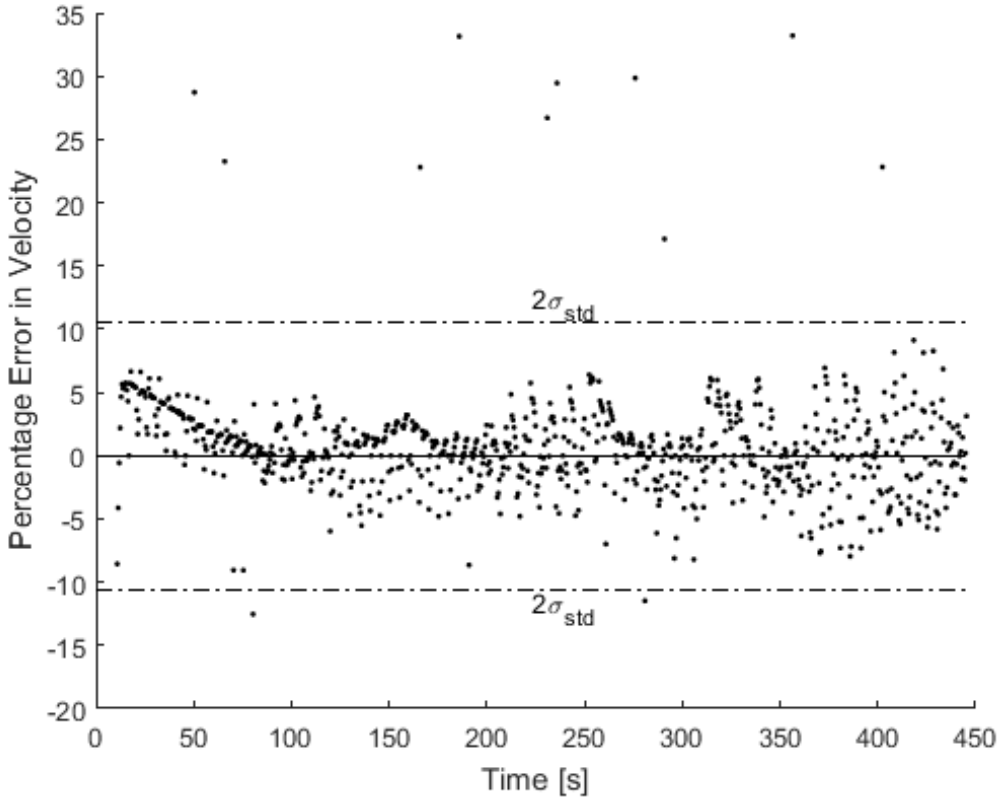


FIGURE 9.8: Relative error in solidification front velocity with time obtained from the simulation of the aerogel furnace in terms of percentage area from the input value of 12×10^{-5}. The initial transient ended at 15 s. The standard deviation was calculated from the complete data set.

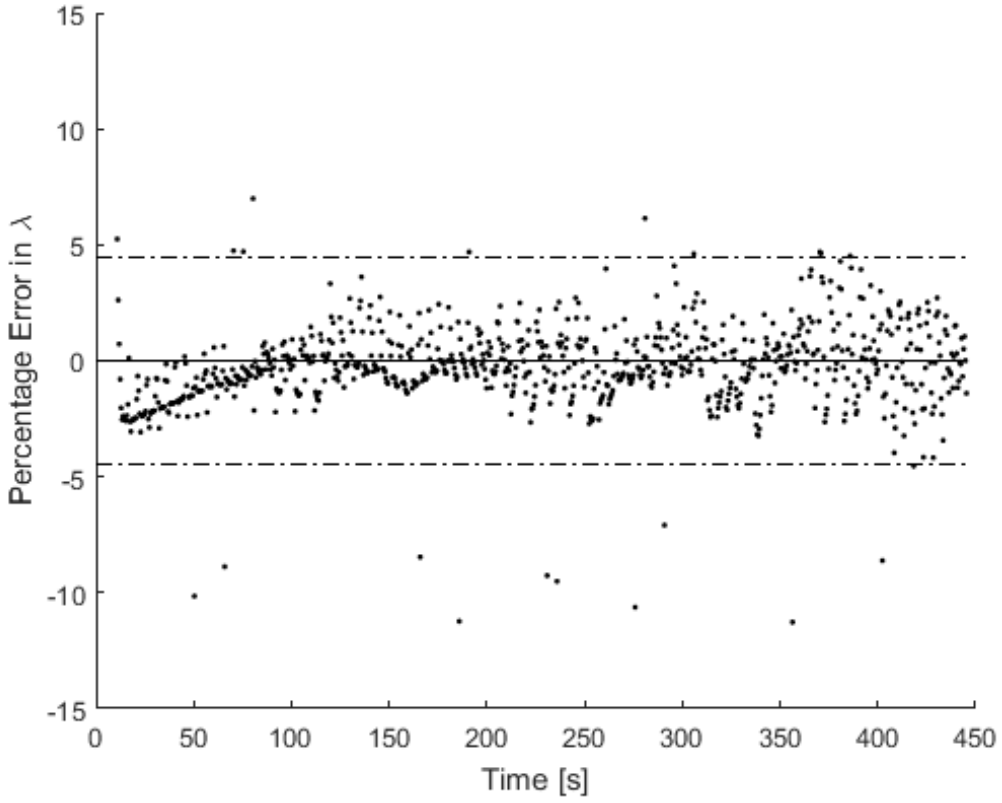


FIGURE 9.9: Relative error in primary dendrite arm spacing ($PDAS$) with time. The initial transient ended at 15 s. The standard deviation was calculated from the complete data set.

The calculated average λ was 245 μm with a deviation in the mean of 9 μm which is well within processing parameters. The minimum and maximum calculated λ values were 222 μm and 268μm respectively therefore a spread of 46 μm across the entirety of the simulation. The calculated value for λ using eq. (9.2) was 258 μm for the input values of d_{req} and v_{req}.

The mean primary dendrite arm spacing from the simulation was calculated under terrestrial ($1g$) conditions using eq. (9.3), along with the standard deviation of the mean, see fig. 9.9. The effect of the primary dendrite arm spacing λ as a function of the acceleration due to gravity, g, was then calculated using eq. (9.3). This dependence of which is also given fig. 9.11 with the error bars corresponding to the minimum and maximum λ calculated in the simulation scaled using fig. 9.11.

Given in figure fig. 9.10 are the top and bottom heater temperatures as well as the temperature along the rod at 10 mm intervals against time. The solidus and nominal liquidus temperatures given in table 9.4 are overlain on the graph. The liquidus temperature will change as a function of the local composition in the mushy zone as explained previously. At approximately 400s the solidus front reaches the top of the sample and the top and bottom heaters begin to cool much more rapidly at a rate of approximately $5Ks^{-1}$.

9.6 Discussion

A series of simulated experiments were conducted as outlined in table 9.6. These simulations all gave results within an appropriate error of less than 5 % between each of the input and output parameter as can be seen by comparing the columns in table 9.6. Moreover the average *PDAS* obtained in the simulation was in each instance within a small margin of error to the steady state calculated λ_{req} using eq. (9.2) and the values of v_{req} and d_{req}.

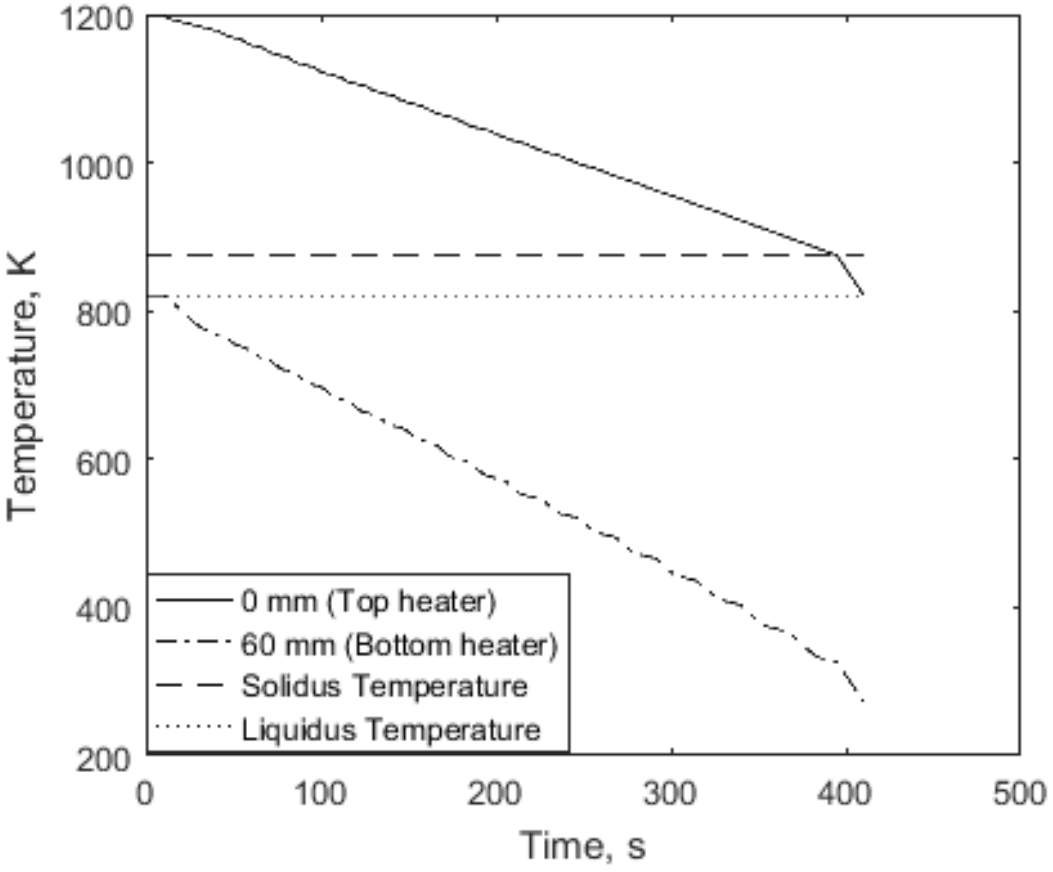


FIGURE 9.10: Temperature time profiles for the top and bottom heaters.

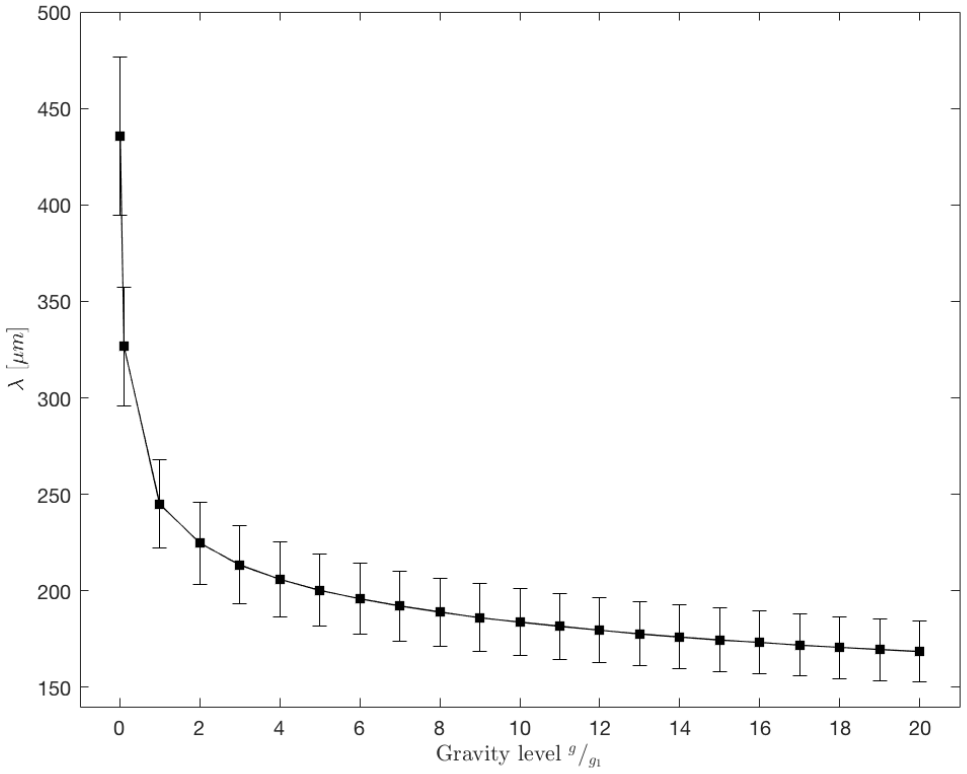


FIGURE 9.11: Calculated effect of the primary dendrite arm spacing λ as a function of the acceleration due to gravity, g, calculated using eqs. (9.2) and (9.3). The results of the simulation at $0g$ or when there was no flow are used in eq. (9.3). The standard deviation of the mean is overlain on the graph for the calculated λ at $0g$.

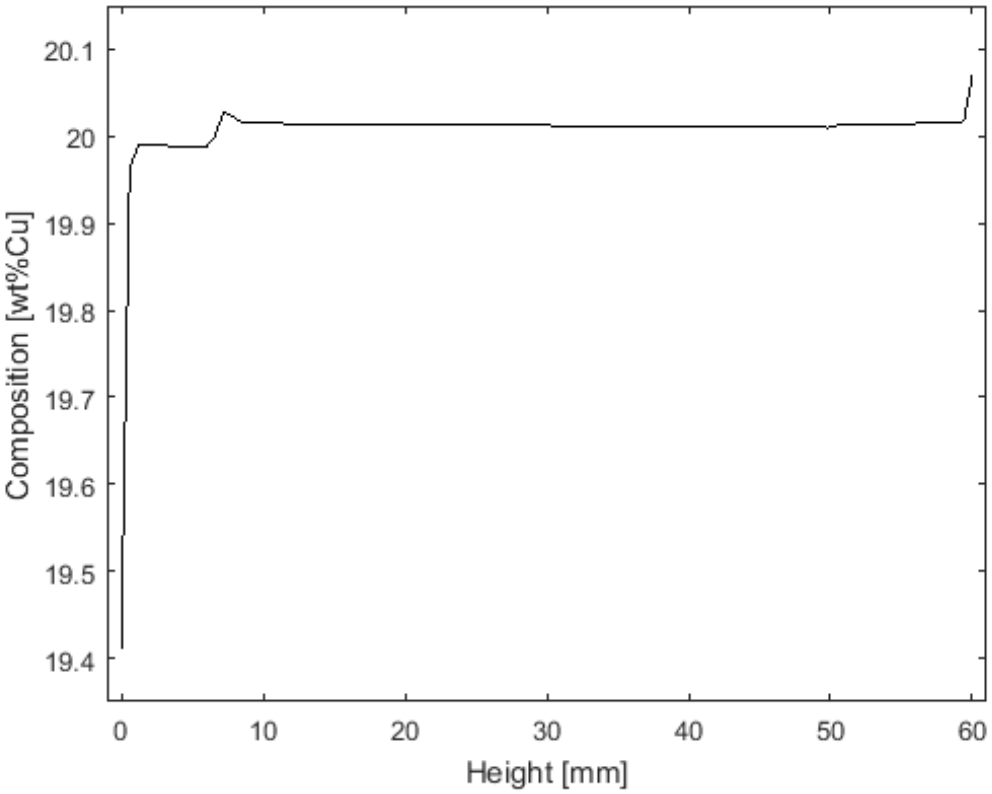


FIGURE 9.12: Composition profile for the Al-20wt%Cu rod after solidification

Run six ($v_{req} = 12\mu ms^{-1}, d_{req} = 7.2mm$) was chosen for further analysis due to the parameters being ideal for the microgravity experiment. The length of the mushy zone would give an equivalent thermal gradient of $7500Km^{-1}$. With a velocity of $12\mu ms^{-1}$ the experiment would allow for around 400-500s of time for the solidification to occur, which would allow for the investigation of a columnar to equiaxed transition after the microgravity phase of the experiment finishes and the rocket begins to accelerate back down towards earth.

The method described above was able to obtain a relatively constant mushy zone depth and therefore thermal gradient throughout the simulation–with a variation of less than 1% from the input value–during the steady state region as shown in figs. 9.6 and 9.7. As the spread in the values of d and therefore ∇T was very small, on the order of 1% over the entirety of the simulation they would have little to no measurable effect on the primary dendrite arm spacing in a real experiment.

Moreover the spread in the v^* data with time shown in fig. 9.8 can be explained as the simulation slightly overcorrecting itself cyclicly. As v^* dips below the required value the magnitude of $\dot{T}^p_{adj,top}$ begins to increase and it takes a while for the system to overcome the inertia of the changing heater and as such change v^*. The value of $T^p_{adj,top}$ can therefore run away causing a sudden increase or decrease in v^* which is unwanted. Sudden spikes seen in the graph of v^* fig. 9.8 can be explained by this phenomenon.

Comparing the magnitude of error in d and v^* (figs. 9.6 and 9.8) it is clear to see that the error is much larger in the v^* graph. d is approximately two orders of magnitude larger than v^* and on a similar scale to the grid spacing along the length. To decrease the grid spacing to a similar magnitude to the velocity would most likely remove this problem, or very likely lessen the effect of it.

Moreover the temperature variation applied to the bottom heater $\dot{T}^p_{adj,bot}$ also influences the v^* and conversely $\dot{T}^p_{adj,top}$ influences d. This leads to the unwanted effect

of each parameter, v^* and d, being influenced by the temperature moderation factor of the other, $\dot{T}^p_{adj,bot}$ and $\dot{T}^p_{adj,top}$. This overcorrection could be compensated by decreasing the time step. As the magnitude of the corrections are time dependent decreasing the Δt would allow for a smaller adjustment which would be easier to compensate as described in eq. (9.14). However decreasing the Δt would increase the computational time for the simulation to run dramatically, as such a balance between accuracy and total simulation time needs to be struck.

In both cases the value of d and v^* oscillating with time is to be expected. Due to the nature of the simulation the cooling rate of the top and bottom heater are adjusted each time step depending upon both of these parameters. This results in an unsteady temperature field which is constantly changing rather than steadily cooling down. The variation caused by this oscillation would be within processing parameters and would not affect the magnitude of the λ too greatly. The calculated variation in λ is approximately 4%. However the system must overcome an energy barrier in order to change the λ, either by a large enough variation in the v^* or ∇T. Moreover any new λ shows a large dependence upon the previous microstructure as has been shown previously within the literature[12, 144, 167, 168, 169]. It is therefore reasonable to assume that any variation in v^* or ∇T would have a negligible effect in the final microstructure of the casting.

The calculated λ as a function of gravity using the method put forward by Diepers and Steinbach [62] was used to give an estimation for the future experiments to be conducted in the large diameter centrifuge. It is important to note that whilst eq. (9.3) and fig. 9.11 would imply that as the acceleration due to gravity approaches zero so the λ would approach infinity, this however is most likely not the case. It is much more likely that there is a theoretical limit to the size of the λ which is governed by purely diffusive solidification as has been described as far back as Ivanstov's model in the 1940s and has been built upon ever since [25]. As such the calculated value of the λ approaching $0g$ may not be completely accurate.

But as mentioned previously it will be acting as a guide for future experiments conducted under microgravity conditions.

9.7 Conclusions

A method for simulating the cool down within a two heater aerogel furnace has been proposed which is able to give values for the front velocity and mushy depth (v^* and d respectively) within acceptable percentage errors. The technique couples the effect of latent heat and composition upon the evolution of the microstructure within a cell centred finite difference heat conduction and radiation scheme.

The underlying equations used in the simulation have been validated using previous experimental work by Cahoon *et al.* [15]. It was shown that the thermal fields calculated were within a reasonable tolerance to those obtained by thermocouples embedded within the graphite crucible during the experiment. Moreover the value obtained for the λ of $128\mu m$ was within an acceptable margin of error of 6%. The value of $175\mu m$ calculated for the λ under μg conditions using the equation proposed by Diepers and Steinbach [62] was also well within an acceptable margin of error of 3% from the reported value.

Subsequently the simulation was used to produce temperature time profiles for experimental work to be undertaken upon the Large Diameter Centrifuge and within sounding rockets for hyper and microgravity respectively. The simulations were able to produce temperature time profiles which gave relatively constant mushy depth (therefore thermal gradient) and velocity with time which as a result gives a stable primary dendrite arm spacing evolution.

Values for λ have been calculated under $1g$ conditions and have then been used with an analytical expression to calculate changing the primary dendrite arm spacing as a function of gravity (λ_g). The calculated values range from microgravity

to $20g$. The analytical expression is based upon previous work within the literature and warrants further exploration due to the lack of literature on the subject [33, 62, 170].

9.8 Further Work

Further work is presented below which was undertaken in addition to that presented in the text preceding. This work is added as whilst not essential to the above text is needed to give wider background to the thesis.

The work for this Chapter was undertaken on an Al 20 wt% Cu alloy rather than a Al 10 wt% Cu for subsequent parts of this thesis. Al 20 wt% Cu was chosen due to it having a smaller mushy zone at a ∇T available for use in the aerogel furnace.

An Al 10 wt% Cu alloy was chosen as it could more easily imaged using the available **CT** scanner at the University of Birmingham. Initial tests in the **CT** scanner on both alloys showed that the Al 10 wt% alloy had the greater degree of x-ray penetration allowing more of the internal structure of the sample to be imaged. The Al 20 wt% Cu sample was too dense for accurate imaging when using a sample diameter of 6 mm.

9.8.1 Fluid flow in the melt

The Boussinesq equation and thermosolutal convection was coupled in order to ascertain what the effect of buoyancy driven flow in the simulation:

$$\Delta\rho = \frac{\rho}{\rho_{ref}} = 1 - \beta_T(T - T_{ref}) - \beta_C(C_{liq} - C_{ref}) \tag{9.20}$$

This equation gives information on the density differences within the liquid of the solidifying material. As such eq. (9.20) was only evaluated when the fraction of liquid f_l is greater than 0, *i.e.* not within the solid region, when $f_l = 0$. Conversely when $f_s = 1$ is set to density should be equivalent to the reference temperature T_{ref} and therefore the density difference $\Delta\rho$ should be unity. In order to achieve this the reference temperature, composition and density is taken at the solidus temperature for a uniformly mixed material. The values of which are presented below in table 9.7.

As β_C is negative it indicates that the solute is much denser than the solvent. Therefore regions with a higher concentration of Cu will be much denser and will sink to the bottom of the liquid region. Conversely the Cu depleted regions will be more buoyant and as a result rise upwards. In the simulation described here in this Chapter it was assumed that there would be no fluid flow within the liquid. As a result simulations were purely diffusive with no convection in the liquid. In reality thermosolutal convection would occur within the liquid as the solid front advances for gravity levels greater than μg. The acceleration due to gravity provides the buoyancy force required for the movement of discrete volumes of liquid to travel upwards or downwards leading to bulk fluid movement. The effect of the convection would only increase with increasing gravity level resulting in greater convectional instabilities such as dendrite fragmentations[179]. This effect is something which needs to be analysed in greater detail.

The fluid flow within the melt can be described by the single phase momentum equation given by Kumar and Dutta [179]:

$$\frac{\partial}{\partial t}(\rho\vec{u}) + \rho\vec{u}\cdot(\nabla\vec{u}) = \nabla\cdot\left(\mu\frac{\rho}{\rho_{ref}}\nabla\vec{u}\right) - \nabla P + S_b - S_{\vec{u}} \tag{9.21}$$

Where the buoyancy source term, S_b is described by:

$$S_b = \rho\vec{g}[\beta_T(T - T_{ref}) + \beta_C(C_l - C_{ref})] \tag{9.22}$$

and the source term giving the frictional resistance to fluid flow, $S_{\vec{u}}$, is given by:

$$S_{\vec{u}} = \frac{\mu\rho\vec{u}}{K\rho_l} \tag{9.23}$$

The buoyancy source term eq. (9.22) gives the baseline momentum change per second for the system which goes from 0 when the acceleration due to gravity is 0 and increases either positively or negatively depending upon how the alloy segregates. In this instance with an aluminium 20 wt% copper alloy the copper solute is much denser than the aluminium solvent, so as gravity increases it becomes heavier thus the source term S_b will decrease as shown in fig. 9.13. This effect of gravity on the denser copper pulls it towards the bottom of the mould and increases the effect that macrosegregation will have upon the solidifying material.

The magnitude of the velocity within the mushy zone v_{mush} can be obtained by assuming that flow through these regions follows Darcy's law. As a result the flow can be expressed by:

$$v_{mush} = \frac{\Delta\rho g K}{\nu f_l} \tag{9.24}$$

Where the permeability, K, is given by[180]:

$$K = 6 \times 10^{-4} \frac{f_l^3}{1 - f_l^2}\lambda_1^2 \tag{9.25}$$

Which as shown above λ is a function of gravity level can be rewritten as:

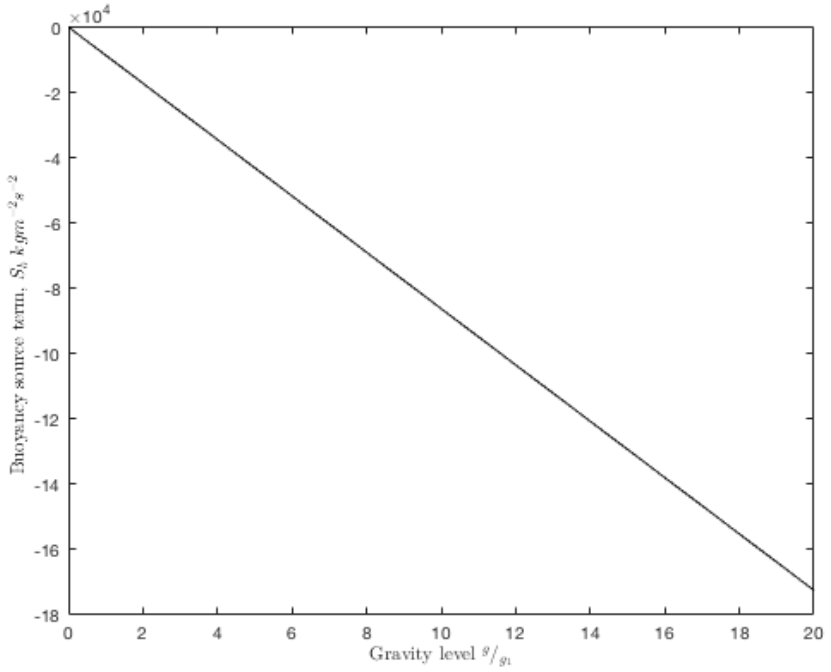


FIGURE 9.13: The affect of gravity on the buoyancy source term described in eq. (9.23)

$$K = 6 \times 10^{-4} \frac{f_l^3}{1 - f_l^2} \left(\lambda_1 \left(\frac{g}{g_1} \right)^{\frac{1}{8}} \right)^2 \tag{9.26}$$

where λ_1 is the primary dendrite arm spacing under $1g$ conditions, *i.e.* nominal gravity. eq. (9.23) shows the effect of v_{mush} calculated using eq. (9.24) for a $f_l = 0.5$. An $f_l = 0.5$ corresponds to the mid-point of the mushy zone.

9.8.2 Rayleigh number based fragmentation

As the acceleration due to gravity increases it will increase the fluid flow due to buoyancy forces. The result of this increase is the greater likelihood of convectional instabilities such as dendrite fragmentation. Fragmentation occurs due to the remelting of secondary arms at their base causing them to break off and float away into the melt and out of the mushy zone. The fluid flow present in the solidifying material allows for the transport of the detached dendrite arms and for their transport into undercooled regions of the melt. It is in the undercooled regions that they can stabilise and grow forming equiaxed crystal [179].

$$Ra = \frac{\Delta \rho g K}{\nu f_l v^*} > 1 \tag{9.27}$$

where:

- g is acceleration due to gravity
- K is the permeability [m^{-2}]
- v^* is the velocity at the tip of the dendrite
- ν is the kinematic viscosity [$\mathrm{m}^2\mathrm{s}^{-1}$]
- f_l is the fraction liquid

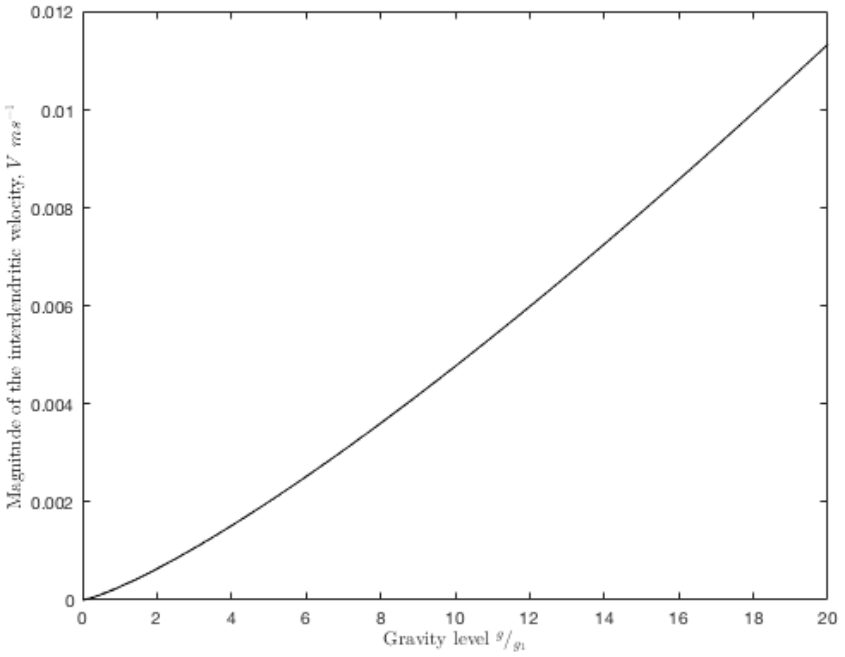


FIGURE 9.14: The effect of gravity on the interdendritic velocity where λ_1 is also a function of g as described in the text above.

It is clear from eq. (9.27) that as g increases so too does the chance that fragmentation will occur. The effect of buoyancy and Rayleigh based fragmentation can be easily coupled into the simulation described above in this Chapter. By coupling them into the simulation an idea of when and if fragmentation of dendrites will occur during the directional casting of Al-10 wt% Cu in a centrifuge.

However as the scope of this work was limited to purely ground based experiments this effect will need to be analysed in greater detail in future work following this thesis within the **MICAST** project. This limitation was due in part to the aerogel furnaces being produced by the **DLR** not being manufactured in time for work to be undertaken using them.

TABLE 9.6: Results of the simulations with differing solidification rates and mushy depth requirements and the average values obtained.

Run	v_{req}, $\mu m s^{-1}$	d_{req}, mm	λ_{req}, μm	$\bar{v}$, $\mu m s^{-1}$	$\bar{d}$, mm	$\bar{\lambda}$, μm	t_f, s
1	100	7.00	278	104	7.00	262	577
2	120	7.00	254	122	7.00	245	492
3	150	7.00	227	151	7.00	222	397
4	200	7.00	196	197	7.04	197	305
5	100	7.20	282	104	7.18	262	577
6	120	7.20	258	121	7.20	245	496
7	150	7.20	230	151	7.20	225	397
8	200	7.20	199	200	7.20	203	300
9	100	7.50	288	102	7.49	272	588
10	120	7.50	263	120	7.49	253	500
11	150	7.50	235	147	7.50	225	408
12	200	7.50	203	197	7.51	204	305
13	100	7.75	293	102	7.73	283	588
14	120	7.75	267	121	7.73	256	496
15	150	7.75	239	153	7.75	234	392
16	200	7.75	207	201	7.76	206	299
17	100	8.00	297	98.2	8.00	300	611
18	120	8.00	272	123	7.95	261	488
19	150	8.00	242	150	8.01	243	400
20	200	8.00	210	201	8.01	210	299

Parameter	**Value**
C_{ref}	20 wt%Cu
T_{ref}	821 K
β_C	-0.032 $kgm^{-3}wt\%^{-1}$
β_T	5×10^{-4} $kgm^{-3}wt\%^{-1}$
ρ_{ref}	2250 kgm^{-3}

TABLE 9.7: Parameters used to evaluate the $\Delta\rho$ during the Aerogel furnace simulation using the Boussinesq equation in eq. (9.20)

Chapter 10

Appendix B

Skeletonisation to Find the Centre of Dendrites Traced from a 2D Microstructural Image

Title:

Skeletonisation to Find the Centre of Dendrites Traced from a 2D Microstructural Image

Authors:

Joshua Miller, Martin Strangwood, Sonja Steinbach and Nils Warnken

Creation of algorithm, implementation, analysis and writing undertaken by Joshua Miller. Supervision of work from Nils Warnken. Final editing of paper by Nils Warnken, Sonja Steinbach and Martin Strangwood.

Publication:

Published in Solidification Processing 2017 Conference Proceedings and presented there.

Synopsis:

A novel method is proposed for finding the centre of a dendrite using a skeletonisation based technique. By finding the medial transform or skeleton of a binarised image the dendrite can be reduced down into a series of lines which describe the shape of the original dendrite. The centre of the dendrite can then be found by locating the intersection of two of the lines making up the skeleton. The centre corresponds to the intersection of the two longest of these lines. The method was tested against the centre of gravity technique and was shown to work better for shapes which did not show tertiary arm growth.

Paper length:

2593 words.

Skeletonisation to Find the Centre of Dendrites Traced from a 2D Microstructural Image

J. E. Miller[1], M. Strangwood[1], S. Steinbach[2] and N. Warnken[1]
[1] School of Metallurgy and Materials, University of Birmingham, U.K.
[2] Institut für Materialphysik im Weltraum, Deutsches Zentrum für Luft- und Raumfahrt (DLR), 51170 Köln, Germany

Abstract

As three-dimensional analysis of dendritic microstructures (such as Ni-superalloys) has become more prevalent with the use of techniques such as Robo-Met 3D®, synchrotron and computerised tomography, there has been a greater need for accurate and efficient methods to characterise dendrites in three dimensions. One parameter which is needed for a variety of further calculations is the primary dendrite arm spacing (λ_1). This parameter can be calculated by finding the distances between all of the centres of the dendrites on a single plane. However before this can be computed the locations of all these centres must be obtained. One technique which has often been used in the literature is the centre of geometry method, which simply determines the centre of gravity of each dendrite as seen in a micrograph. However, this method has some major drawbacks. For instance it can assign the centre outside of a dendrite, which often applies to irregular shaped dendrites. As a result another technique shall be presented using skeletonisation. It is shown here that this technique represents good improvement over the centre of geometry method; however it also has drawbacks in certain specific conditions. Combined use of all these methods however shows promise in the search for a reliable method to identify the centres of differently shaped dendrites.

Keywords: Dendrite Centre, Skeletonisation, Image Analysis, Microscopy, Primary Dendrite Arm Spacin.g.

1. Introduction

The centre of a dendrite is a useful point to obtain when analysing images of as-cast microstructures, as it can be used to calculate the primary dendrite arm spacing (PDAS, λ_1) of materials which exhibit dendritic morphology. Usually given as a range of values, the PDAS is the average spacing between all the dendrite centres in a single slice or plane of a dendritic microstructure. This parameter controls many properties of the final material including the fatigue and wear resistance, tensile strength [1], and microporosity formation [2]. As such it is important to accurately obtain the PDAS where these material properties are of paramount importance, for example in gas turbine applications. The classical method of obtaining this parameter is by using the equation:

$$\lambda_1 = c\sqrt{\frac{A}{N}} \qquad (1)$$

Where A is the total area of the sample, N is the total number of dendrites and c is a coefficient which is dependent upon the microstructure [4]. This method however only gives an average value for the PDAS of a whole sample rather than a PDAS for each individual dendrite which would allow for statistical analysis of a sample. However techniques are available that can achieve this (e.g. the Warnken-Reed method [3-5]).

Therefore in order to calculate an accurate value for the PDAS (using eq. (1), minimum spanning tree, Warnken-Reed, Voronoi, Warnken-Reed-Voronoi or any other method [3–5]) it is necessary first to accurately find the centre of the dendrite.

The centre of the dendrite is here defined to be the point on a plane whereby the dendrite tip first passed through whilst it was growing (in a direction approximately perpendicular to the plane). However due to any microsctructural analysis occurring after solidification, the location of the dendrite centre is not immediately clear. The centre can be found using techniques such as Wave Dispersive X-ray Spectroscopy (*WDS*) or Energy Dispersive X-ray Spectroscopy (*EDX*) mapping, [6] and by knowing how microsegregation affected the composition during solidification. One example is Ni-superalloys containing tungsten, this element segregates towards the centre of the dendrite, so it is merely necessary to find the regions of highest tungsten concentration which correspond to the centre. However *WDS* and *EDX* mapping are very time intensive techniques, especially when studying large microstructural areas, which are needed to calculate a PDAS.

Hence, a technique is needed to accurately obtain the centres of dendrites within a large area image such as from optical micrographs or a slice of a reconstructed tomography volume. One technique that could be used is finding the centre of geometry of a dendrite. This technique is very easy to implement and also very quick to run. However as it works by finding the average point in a binary shape it can often assign the centre in an incorrect point if the shape of the dendrite is not regular. Another technique that is put forward and compared in this paper is a skeletonisation-based technique which relies upon the shape of the dendrite itself in order to find the centre. This technique has seen a lot of use in medical imaging [7–9] and will be customised here to obtain the centre of a dendrite. The two techniques will be compared using a variety of test cases, both simple shapes and also traced dendrites taken from real microstructures.

2. Methodology

Two methods will be compared, the centre of geometry and the skeleton centre method. The details of each are described below. In order to test both of these methods they will be trialled on a number of test cases. These test cases are a series of regular and irregular binary shapes, either created in MATLAB or traced from micrographs of a directionally cast polycrystalline Ni-superalloy sample (figs. 3 to 4). All of the work has been coded in and undertaken in MATLAB.

2.1 Centre of Geometry

The centre of gravity method, like manually assigning the centre of a dendrite, is rather simplistic. It works on the principle of finding the 'average' position of all the points within a shape whilst assuming that the shape has uniform density and is within a uniform 'gravitational' field. The result is the average position which can be within the shape or outside of it.

2.2 Centre Skeletonisation

Skeletonisation is a technique whereby a binary image is eroded step by step away until the skeleton of the image is obtained. This skeleton is the thinnest version of a shape, consisting of a one pixel thick line which is equidistant from the original edges of the binary shape. If the skeleton is dilated back using the same number of iterations it took to produce it, the original shape will be reformed. For a more rigorous mathematical explanation of skeletisation refer to reference number [7]. Once this skeleton is obtained the shape is pruned to remove any spurious skeleton lines which are brought about by local inhomogeneities on the edges of the binary shape.

Skeletisation can be achieved in 3D and has been used substantially in medical imaging [8, 9]. It has to a lesser extent seen use in materials science [10, 11], however it has not yet become as prevalent due to 3D microstructural imaging being currently more of a novelty. For the purposes of this paper only 2D skeletonisation will be examined.

This skeletonisation technique takes advantage of the resulting shape of the skeleton. For a dendrite this will be a cross due to the skeleton forming along the centre line of each of the secondary arms. It is hypothesised by the authors that the centre of cross will in fact be the centre of the dendrite. As a result the centre of the dendrite can be found at the point where the two lines of the cross intersect. This can be done quickly and easily by finding the cross shape in the matrix of binary pixels, i.e. in locations where the binary matrices

$$\begin{bmatrix} 0 & 1 & 0 \\ 1 & 1 & 1 \\ 0 & 1 & 0 \end{bmatrix} \text{ or } \begin{bmatrix} 1 & 0 & 1 \\ 0 & 1 & 0 \\ 1 & 0 & 1 \end{bmatrix}$$

occur.

These binary crosses are known as branching points and are the regions from which the arms of the skeleton extend. These intersections are possible centres of the dendrite, but before the realistic centre of the dendrite can be assigned the lengths of the arms connected to these branch points are measured and compared. It is hypothesised by the authors that the location on the branch point which can be considered the centre of the dendrite will have the longest arms attached to it. This is because from the original centre of the dendrite the arms have had the largest growth from this point to the ends of the secondary arms, and any tertiary arms associated with branching point will be much shorter. Therefore taking this into consideration the group of arms connected to each branch point are measured and the mean taken. The average values for each group are then compared and the branch point with the largest mean value is then assigned as the centre of the dendrite. For this work the inbuilt skeletonisation function in MATLAB [12] is used along with some custom functions developed by the authors.

3. Results

The two methods were trialled on two sets of test cases (figs. 1 to 4). Two ideal shapes (figs. 1 and 2) a regular square and a cross (signifying an idealised dendrite), and dendrites traced from a Ni-superalloy micrograph (figs. 3 and 4). The traced images of dendrites consist of two regular dendrites (fig. 3) and an irregular dendrite (fig. 4) which shows tertiary arm growth. In each case the skeleton formed is overlain on the original binary image and the centre of geometry and skeleton centre are superimposed.

In the ideal test cases (figs. 1 and 2) the assigned centre of geometry and skeleton centre are essentially identical. However in the dendritic test cases there is a difference of at least 100µm between the skeleton and centre of geometry (figs. 3 and 4). Furthermore in fig 3 the centre of the dendrite has been assigned correctly, that is at the correct branching point. However in figure 4 the skeleton centre has been assigned some distance from where the authors believe it to be (as indicated on the figure).

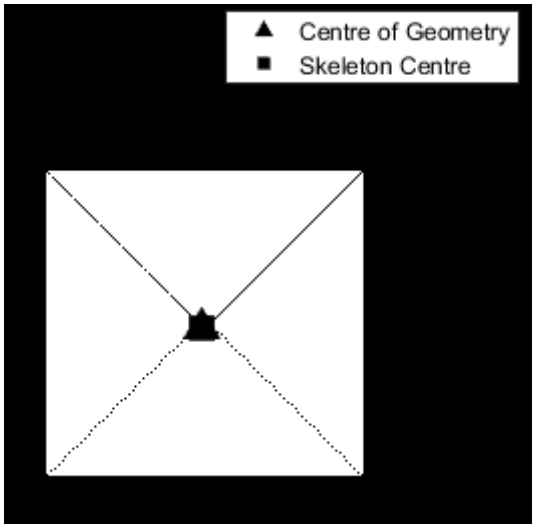


Figure 1. The square test case with its skeleton superimposed upon it. The centre of geometry and skeleton centre are also superimposed. The square has a side length of 400 pixels.

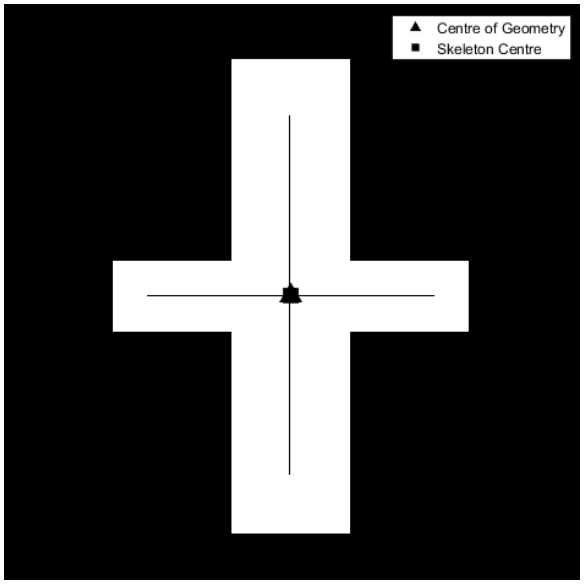


Figure 2. The cross test case which represents a dendrite with four secondary arms. The skeleton lines have been superimposed onto the image.

4. Discussion

As can be seen in figs. 1 and 2 the centre of geometry and the skeleton centre are almost identical. This shows that at least for simple symmetrical geometries the skeleton centre method can find the 'true' geometrical centre of a shape.

The methods were also compared using two dendrites, one regular and the other irregular as shown in figs. 3 and 4. In fig. 3 the skeleton assigned centre is an improvement to the centre of geometry as it is much closer to the true centre of the dendrite, and in the authors opinion it lies on top of it. In this example the distance between the skeleton and geometry assigned centres is ~100 μm. This difference can be explained easily as the centre of geometry is simply taking an average of every point in a binary image to find the mean x and y coordinates. Thus if there is an excess of points in one direction, such as if there is an elongated secondary arm as shown in figure 3, then the centre of geometry will be shifted in that direction.

Despite the skeletonisation technique being much better than the centre of geometry method it does have its limitations, for example in the case represented in fig. 4. As this dendrite shows tertiary arm growth it leads to a new branch of the skeleton forming along the tertiary arms. As a result there are many more branching points and associated skeleton arms between them. This can lead to issues where an incorrect centre is chosen which has occurred here. In this case there is a large distance between the skeleton centre and the author assigned centre of the dendrite of several hundred micrometres.

It is therefore obvious to see that even though the technique works very well for more regular dendrites (as in fig. 3) it falls down when analysing more complicated morphologies such as this one. Therefore a technique is needed to identify these more irregular dendrites as it has become clear to the authors that a "one-size-fits-all" approach is not reasonable. One possible method could be achieved by taking into account the aspect ratio or the perimeter to area ratio to separate more regular and more irregular dendrites as from observation it is clear to see that dendrites with more tertiary arms would have a greater perimeter and therefore a larger perimeter to area ratio. Subsequently a different method specifically designed for these complex morphologies could be used to find the centre. One possible avenue of exploration is the fitting of splines to the skeleton lines and finding the centre by means of algebraic manipulation.

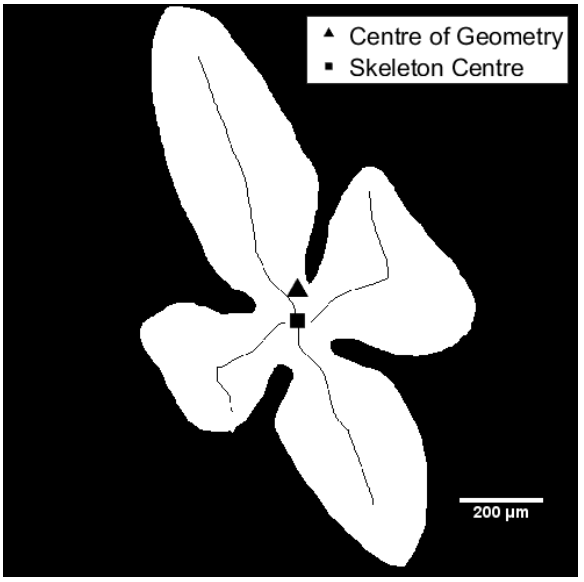


Figure 3. A regular dendrite with its skeleton superimposed along with the centre of geometry and skeleton centre.

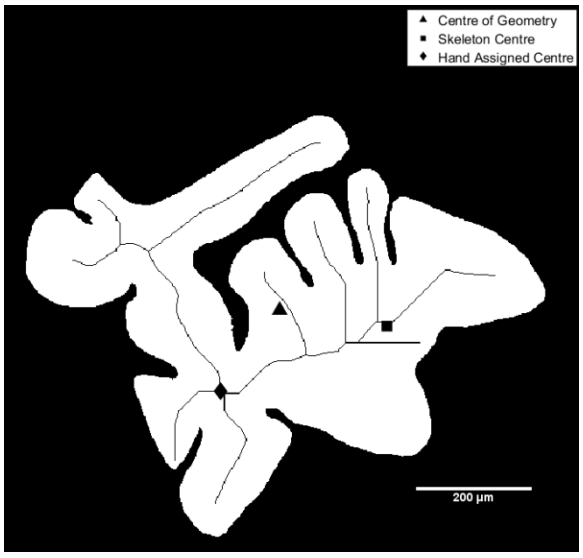


Figure 4. An irregular traced dendrite with its skeleton superimposed along with the centre of geometry and skeleton centre.

5. Conclusions

A new method using skeletonisation has been outlined to find the centre of dendrites from binary images. The technique has been trialled on both ideal test cases of simple shapes and more complicated traced dendrites. The method shows good improvement over the traditional centre of gravity method for regular dendrites. However the technique falls down when analysing more complex dendrites which show tertiary arm growth. As a result more work is needed to explore ways to accurately obtain the centre of these complicated morphologies, possibly by fitting splines to the skeleton lines.

Acknowledgements

The authors would like to thank the European Space Agency and the MICAST team (ESA-MAP programme MICAST', contract 14347/01/NL/SH) for both funding the research and the invaluable help they have given.

References

1. K.S. Cruz, E. S. Meza, F.A.P. Fernandes, J.M.V. Quaresma, L.C. Casteletti, and A. Garcia, *Metallurgical and Materials Transactions*, 2010, **A41**: 972.
2. Melo, M., Rizzo, E. & Santos, R. *J Mater Sci* ,2005, **40**: 1599.
3. M.A. Tschopp, J.D. Miller, A.L. Oppedal, and K.N. Solanki. *Metallurgical and Materials Transactions A*, 2015, **46A**:4610.
4. M.A. Tschopp, J.D. Miller, A.L. Oppedal, and K.N. Solanki, *Metallurgical and Materials Transactions A* , 2014, **42**:426.
5. N. Warnken and R.C Reed, *Metallurgical and Materials Transactions A*, 2011, **45**: 1675.
6. D.G. Eskin and L. Katgerman, *Aluminium Alloys: The Physical and Mechanical Propertiers*, 2008, chap 37.
7. R.C. Gonzalez and R.E. Woods, *Digital Image Processing*, 2008, 1st Ed.
8. P.K. Saha, G. Borgefors, and G. Sanniti di Baja, *Pattern Recognition Letters*, 2016, **76:**3
9. B. Zhou, Z. Zhang, J. Wang, Y.E. Yu, X.S. Liu, K.K. Nishiyama, M.R. Rubin, E. Shane, J.P. Bilezikian, and X.E. Guo. *Pattern Recognition Letters, 2016*, **76:**83
10. M. Talukdar, O. Torsaeter, M.A. Ioannidis, and J.J. Howard, *Journal of Petroleum Science and Engineering*, 2002, **35**:1.
11. E. Plougonven and D. Bernard, *Advances in Water Resources*, 2011, **34**:731.
12. Matlab, *Image Processing Toolbox: User's Guide*, 2016, URL https://uk.mathworks.com/help/images/ref/bwmorph.html.

Chapter 11

Appendix C

A Large-Scale 3D Computer Tomography Analysis of Primary Dendrite Arm Spacing Response to Withdrawal Velocity Change Using Dendrite Centre Tracking

Title:

A Large-Scale 3D Computer Tomography Analysis of Primary Dendrite Arm Spacing Response to Withdrawal Velocity Change Using Dendrite Centre Tracking

Authors:

Joshua Miller, Laszlo Sturz, Sonja Steinbach, Gerhard Zimmermann and Nils Warnken

Experimentation undertaken by Joshua Miller. Computerised tomography analysis undertaken by both Josh Miller and Sonja Steinbach. Analysis of tomography

data undertaken by Josh Miller. Supervision of work from Nils Warnken. Final editing of paper by Nils Warnken, Sonja Steinbach, Laszlo Sturz and Gerhard Zimmerman.

Publication:

Published in the SG18 proceedings and delivered as a keynote presentation by Nils Warnken.

Synopsis:

Directional solidification of a aluminium 10 wt% Cu rod was undertaken in a Bridgman furnace under varying a withdrawal rate. The sample was initially solidified at a withdrawal rate of 40 μms^{-1} and changed instantaneously to 80 μms^{-1}. The aluminium copper rod was then imaged using a **CT** machine and the volume binarised. Subsequently the **PDAS** was calculated for each slice along the length of the rod and there was a change in the primary dendrite arm spacing which occurred over 2500 μm until it destabilised. Further more the number of nearest neighbours were tracked along the length of the sample. Finally the locations of newly initiated dendrites and ones that have been out competed are also found along the length of the sample.

Paper length:

2822 words.

A Large-Scale 3D Computer Tomography analysis of Primary Dendrite Arm Spacing Response to Withdrawal Velocity Change Using Dendrite Centre Tracking

J. E. Miller[1], L. Sturz[2], S. Steinbach[3], G. Zimmermann[2], and N. Warnken[1]

[1]Department of Metallurgy and Materials, University of Birmingham, United Kingdom, B15 2TT

[2] ACCESS e.V., Intzestr. 5, 52072 Aachen, Germany

[3] Institut für Materialphysik im Weltraum, Deutsches Zentrum für Luft- und Raumfahrt (DLR), 51170 Köln, Germany

Email of corresponding author: N.Warnken@bham.ac.uk

Keywords: Directional Solidification; Computerised Tomography; Primary Dendrite Arm Spacing; Changing Withdrawal Velocities; 3D Metallography; Dendrite Centre Tracking; Aluminium 10 wt% Copper

Abstract. Directional solidification of alloys is an extremely important process to understand due to the many high value products that are produced in this manner, *e.g.* turbine blades. Controlling how the columnar dendrites grow and pack together is an important aspect of increasing the strength and longevity of these components. As such 3D examination of a 200 mm in length and 6 mm diameter aluminium 10 wt % copper rod solidified under varying withdrawal rates (40 μm/s then a jump to 80 μm/s) has been undertaken in a lab based computerised tomography (*CT*) machine. Novel image analysis techniques involving active contours and skeletonisation have been used to track the dendrites through the sample itself. Sites of dendrite initiation and termination have been identified automatically within the dataset. These points of dendrite creation or deletion where found to be most prevalent after a step change in the withdrawal rate. Information on the array packing and primary dendrite arm spacing (*PDAS*, λ) for each grain within the sample has been obtained. The results show that there is a distance delay after the withdrawal rate change and the onset of a *PDAS* restructuring.

Introduction

With the advent of lab based computerised tomography (*CT)* scanners there has been an increase in the options available for 3D metallography that researchers can undertake. *CT* scanners allow for the non-destructive analysis of components and castings and can build up a 3D virtual view of the internal microstructure of a component. This has allowed for the quick and relatively easy evaluation of microstructures in three dimensions where previously the only avenue available to researchers was the use of tedious serial sectioning.

Moreover with the increase of computation power available greater volumes of data can be now analysed swiftly and cost effectively. As such now is the first time that the large volumes associated with *CT* analysis can be effectively analysed and giving a greater understanding of how a dendritic array evolves in a directionally solidified sample giving a stable *PDAS.*

Many equations for *PDAS* calculation have been put forward including the Trivedi equation which takes account of the marginal stability criterion [1]:

$$\lambda = 2.83\, m(k-1)D\Gamma L C^{0.25} v^{-0.25} G^{-0.5} \qquad (1)$$

Where: m is the liquidus slope [K/wt%]; k is the partition coefficient; D is the diffusivity of solute in the liquid [m^2s^{-1}]; Γ is the Gibbs-Thomson coefficient [mK]; L is a constant which depends upon the harmonic perturbations which is set to 28 [1]; C is the bulk composition [wt%]; v is the solidification front velocity; and G is the thermal gradient [K/m].

Eq. 1 has proven adapt in producing predictions for the *PDAS* in steady state solidification. However not quite as adapt in the unsteady state. In this type of situation, the dendritic array restructures to compensate for changing solidification conditions resulting in either the creation or termination of primary dendrite arms [2-5]. Ma [2 & 3] set the stable limit for the *PDAS* to λ_{min} = 2/3 λ to λ_{max} = 4/3 λ. If the *PDAS* becomes too small a dendrite is outcompeted and killed off and the microstructure readjusts increasing the *PDAS.* Conversely if the *PDAS* is too large then a new primary dendrite arm will fill a gap in the array formed from the growth of a tertiary arm from one of the surrounding dendrites.

This array restructuring is easy to see in two dimensional samples especially in transparent model alloys [2-4]. However, it is much more difficult in 3D. When calculating the *PDAS* in a solidified sample it must first be sectioned and the number of individual dendrites (N) counted, then using the equation:

$$\lambda_B = \sqrt{\frac{A}{N}} \qquad (2)$$

the bulk *PDAS* can be calculated for that transverse section of the sample if the area of the slice, A, is known [6-8]. The drawback of this method is that it only gives an average value for the *PDAS* so no statistical analysis can be undertaken using it. Methods such as the Warnken-Reed and Voronoi *PDAS* calculations can however be used to find the local *PDAS* across a sample [6-8].

Therefore, in order to test how microstructures readapt in 3D to changing solidification conditions, an Al-10 wt% Cu sample was directionally solidified under a constant *G* of 10 K/m with an instantaneous velocity jump from 40 μm/s to 80 μm/s. It was then imaged in a *CT* and examined using custom algorithms developed by the authors in Matlab to calculate the local and bulk *PDAS* and find instances where new dendrites are created.

Methodology

An Al-10wt% Cu master alloy billet was cast from commercially pure aluminium and copper at the University of Birmingham Casting lab. It was then *EDM*ed into a 200 mm length rod with a 6 mm diameter in the Netshape Laboratory, Birmingham. The sample was then directionally solidified in the lab-scale CARLO Bridgman furnace at ACCESS e.V. Germany under a constant withdrawal of 40 μm/s for 60 mm with an instantaneous velocity jump to 80 μm/s which was then constant for 30 mm. The bottom 90 mm of the sample was used to hold the sample in place and top 20 mm was assumed to be unusable. These lengths for the 40 and 80 μm/s sections were chosen to give each section an equal number of diffusion lengths ($800L_d$ in each instance) for the usable 90 mm of sample where: $L_d = D/v$. Which is an L_d of 75 μm and 37.5 μm respectively (using parameters in Table 1).

The sample was then *CT*ed at the Institut für Materialphysik im Weltraum at the German Aerospace Centre (DLR), using a GE Phoenix nanotom microCT scanner with an acceleration voltage of 100 kV and a current of 110 μA. The resulting voxel size was 2 μm^3. The images were then analysed using a series of author written applications within Matlab to: binarise and segment the images using active contours; then find the centre of each dendrite using the skeleton centre method [9]. The dendrite centres of each slice were then joined up forming lines that followed the primary arm of a dendrite producing a “forest” of separate dendrite trunks. The coordinates of a newly initiated dendrite were found by locating where these traced lines branched. This branching indicates a situation where a tertiary arm from the original primary trunk has become stable and formed a new primary trunk.

The bulk *PDAS* for each slice in the sample was calculated using equation 2 above. The local *PDAS* along the length was also calculated using the Voronoi and Warnken-Reed methods which are described by Tschopp et al. [6 & 7] and Warnken and Reed [8]. The average number of nearest neighbours for these two methods was also calculated. In the Warnken-Reed method the authors used an α value of 1.5. The results of this were compared with calculations for the *PDAS* using Eq. 1 and the parameters given in Table 1.

Table 1: Table of parameters used in Eq. 1 to calculate the PDAS [10]

Parameter	Value
C	10 [wt% Cu]
D	$3x10^{-9}$ [m^2s^{-1}]
G	10 000 [Km^{-1}]
k	0.14
L	28
m	-3.37 [$Kwt\%^{-1}$]
v_1	40 [μms^{-1}]
v_2	80 [μms^{-1}]
Γ	2.41 [Km]

Results

The *PDAS* was determined along the length of the manipulated and binarised *CT* volume (Fig. 1, with two of the *CT* slices before and after the transition shown in Fig. 2) using each of the different methods described above *i.e.* the bulk, Warnken-Reed, and Voronoi. As can be seen in Figure 1 the bulk *PDAS* method gives the highest value for the *PDAS* along the sample with the Voronoi and then Warnken-Reed below that. The evolving dendrite array takes approximately 2500 µm (equivalent to 66 L_d) until the *PDAS* stabilises and does not decrease further. After which it remains relatively constant. The minimum and maximum stable *PDAS* has also been calculated and shown on Fig. 1. These values were calculated for each slice using $\lambda_{min} = 2/3\ \lambda$ to $\lambda_{max} = 4/3\ \lambda$.

Fig. 3 shows that along the length of the sample there was a slight increase in the number of nearest neighbours in the Warnken-Reed method on the order of 0.05 neighbours. Whereas the Voronoi method shows an increase of approximately 0.2 new neighbours. In both instances there is a steady increase after the velocity change until it plateaus after 2500 µm.

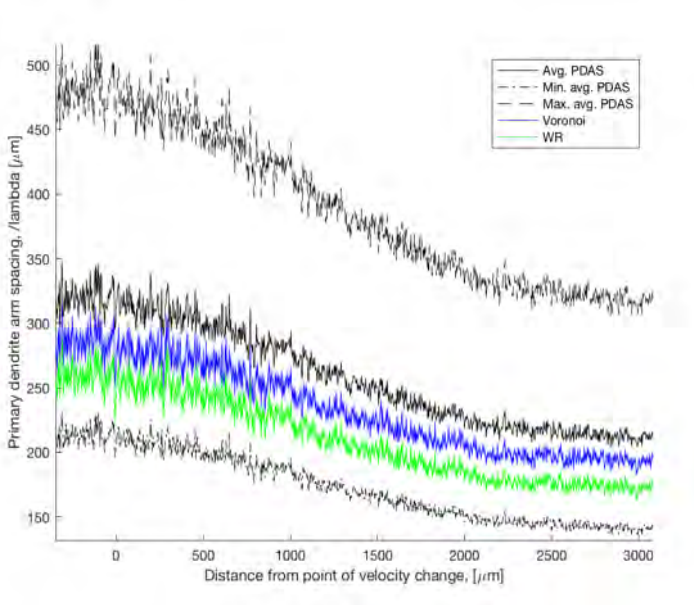


Figure 1: PDAS along the length of the sample from the velocity change

Fig. 4 shows the cumulative number of created or outcompeted dendrites along the length of the sample. As can be seen there is a relatively constant rise in the number of new dendrites being formed after the velocity change. Whereas after 1000 µm there begins to be dendrites which are eliminated.

The calculated values for the *PDAS* using Eq. 1 and the parameters in Table 1 were 310 µm and 260 µm at 40 µm/s and 80 µm/s respectively. The former value shows good agreement with the results in Fig. 1 prior to the velocity change (distance < 0 µm). Whereas the calculated value for the PDAS of 260 µm at 80 µm/s (distance > 2500 µm) is incorrect by 40 µm as

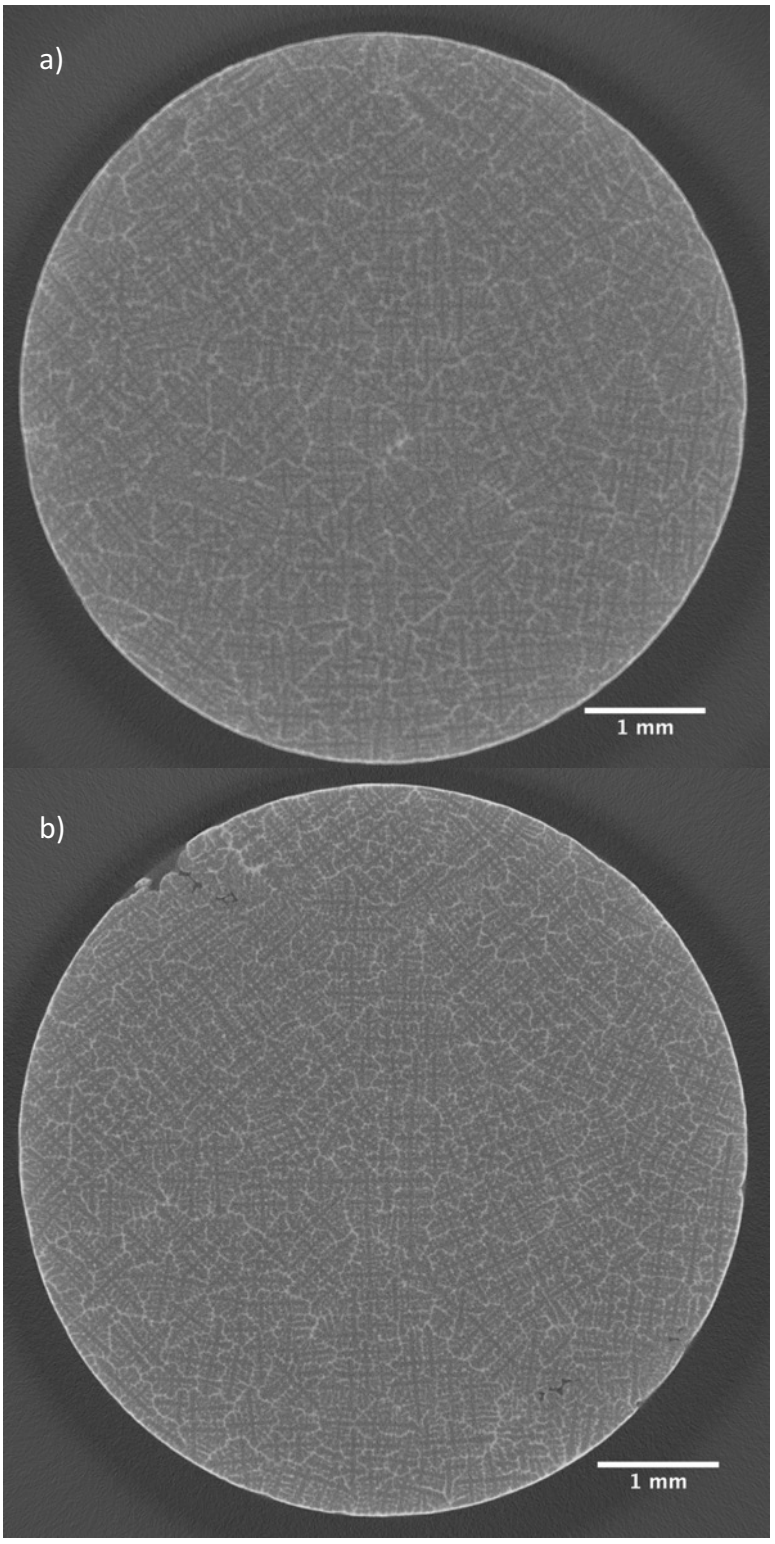


Figure 2: CT micrographs of the sample 1 mm before the velocity change (a) and 3 mm after the transition (b)

the stabilised PDAS in this region is 220 µm. However Eq. 1 is just one of many *PDAS* calculation models.

Using information from Fig. 4 the location of the initiations and deletions was found. Fig. 5 shows the stabilisation and deletion of dendrites within the array after 1700 µm and every 200 µm afterwards until 2300 µm. In both cases of stabilisation and deletion the dendritic array readjusts itself around the new or removed dendrite.

Discussion

The results of the experiment show that the microstructural array rearranges itself with changing solidification conditions. In this instance, an increase in the velocity from 40 to 80 µm/s. The *PDAS* decreased when calculated using Eq. 2, and with the Voronoi and Warnken-Reed methods for each slice along the length of the sample. This reduction in *PDAS* was expected due to the expectation that the evolving microstructural array would adapt to a lower value (as shown by comparing Fig. 2a and 2b). This re-adaption was achieved by means of a production of new primary dendrite trunks which formed from the stabilisation of tertiary dendrite arms (Fig. 5). As can be seen in Fig. 4 there is a continual increase in the number of new primary dendrite arms after the velocity change. Including after this graph shows that the dendrite array restructuring was not due to a columnar to equiaxed transition (*CET*) but rather a gradual restructuring as new tertiary dendrite arms fill gaps within the dendritic array.

Moreover Fig. 4 and 5 show that there are some instances of dendrites being out competed and "killed off". The last such instance of a dendrite being out competed coincides with the levelling off in the number of nearest neighbours seen in Fig. 3. After this levelling of the *PDAS* remains constant and so too does the approximate number of total dendrites.

Fig. 5 also implies that the missorientation between the dendrites may play a role in the deletion of the dendrites. The outcompeted dendrite is missorientated by 45^{o} to all the surrounding nearest neighbours.

A clear feature of Fig. 1 is that the *PDAS* adjustment is not an instantaneous process but takes place over several mm. In this instance, approximately 2.5 mm. This distance corresponds to approximately 70 times the diffusion length in the 80 µm/s regime. It is possible that the diffusion length L_d plays an intrinsic part in the restructuring of a dendritic microstructure. As it may be possible that a certain number of L_d need to be reached before the array reaches a stable and unchanging *PDAS* after a velocity change. However more experiments will need to be undertaken to see if this or another parameter plays a role in the time taken for a dendritic array to re-stabilise.

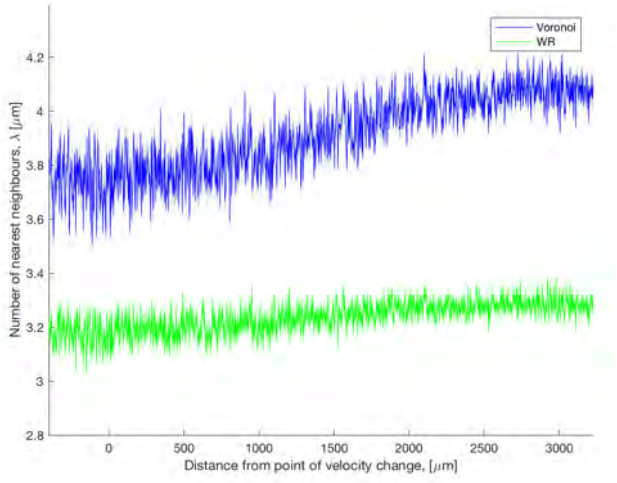


Figure 3: Change in nearest neighbour number along the length of the sample

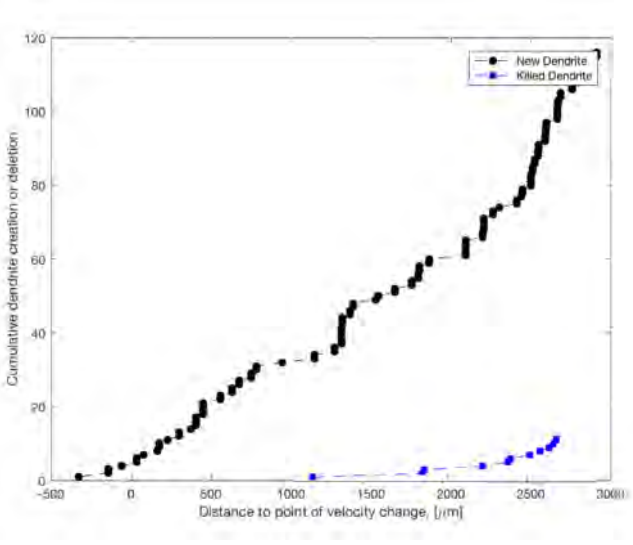


Figure 4: Cumulative dendrite creation or deletion along the length of the sample

Conclusions

A directionally solidified Al-10 wt% Cu rod was solidified under a 40 µm/s withdrawal rate which was instantaneously changed to 80 µm/s after 60 mm. This was achieved to promote dendritic array restructuring by the promotion of tertiary arms stabilising into primary arms.

The solidified rod was *CT*ed and analysed using image analysis algorithms written by the authors to trace the centre of the dendrites using the Skeleton Centre method [9]. The *PDAS* was calculated along the length of the sample using the bulk, Voronoi, and Warnken-Reed methods showing in each case that it took approximately 2.5 mm for the array structure to return to steady state with a continuous *PDAS*.

During this transition, new dendrites were created via the promotion of tertiary arm growth and tracked within the 3D *CT* volume. The creation of these new primary arms gives credence to the extension of 2D dendrite array restructuring [2-5] in 3D. Moreover, sites where primary trunks were out competed were also found along the length of the sample showing that the microstructure is continuously adjusting the array to bring it into a stable configuration.

The authors tentatively put forward that the diffusion length L_d may in some way be used to predict the length that the array adjustment occurs over until a new stable *PDAS* is reached. For this sample, approximately 66 L_d at 80 µm/s were reached before the array stabilised at a *PDAS* of 230 µm.

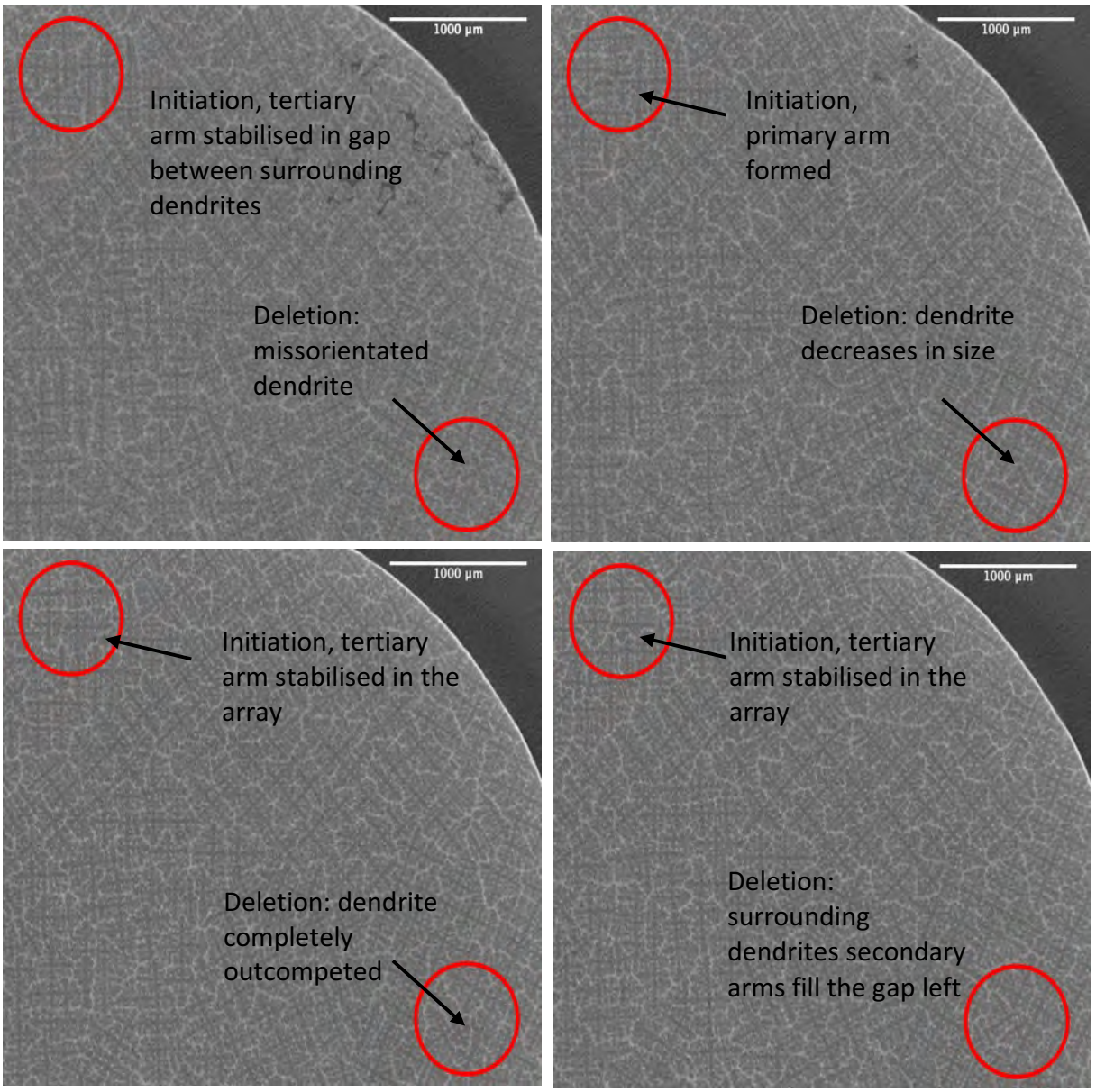


Figure 5: Sites of dendrite initiation and deletion. The images are a) 1700 µm b) 1900 µm, c) 2100 µm and d) 2300 µm from the velocity change.

Acknowledgments

This work forms part of the Microstructure Formation in Casting of Technical Alloys under Diffusive and Magnetically Controlled Conditions (MICAST) project. The authors would like to thank the ESA for funding as part of the MICAST project and support with this work. With special thanks to Adrian Caden and Peter Cranmer for help casting the master alloy; Amanda Field and Sam Crutchely for the help with EDMing the sample; Christoph Pickmann at Acces e.V. for running the Bridgman furnace; and Vanessa Indrizzi for help with the Matlab code.

References

[1] R. Trivedi. Interdendritic spacing: Part ii. a comparison of theory and experiment. Metallurgical and Materials Transactions A, 15(6):977–982, Jun 1984.

[2] D. Ma. Development of dendrite array growth during alternately changing solidificaton condition. Journal of Crystal Growth, 260:580–589, 2004.

[3] D. Ma. Response of primary dendrite spacing to varying temperature gradient during directional solidification. Metallurgical and Materials Transactions B, 35B:735–742, 2004.

[4] E. Üstün, E. Çadirli, and H. Kaya. Dendritic solidification and characterization of a succinonitrile–acetone alloy. Journal of Physics: Condensed Matter, 18(32):7825, 2006.

[5] V. Indrizzi, N. Warnken, and D. Putman. Computational study of spacing selection in directionally growing dendritic arrays. In SP17, 07 2017.

[6] M. A. Tschopp, J. D. Miller, A. L. Oppedal, and K. N. Solanki. Characterizing the local primary dendrite arm spacing in directionally solidified dendritic microstructures. Metallurgical and Materials Transactions A, 45(1):426–437, 2014.

[7] M. A. Tschopp, J. D. Miller, A. L. Oppedal, and K. N. Solanki. Evaluating local primary dendrite arm spacing characterization techniques using synthetic evaluating local primary dendrite arm spacing characterization techniques using synthetic directionally solidified dendritic microstructures. Metallurgical and Materials Transactions A, 46A:4610–4628, October 2015.

[8] N. Warnken and R. C. Reed. On the characterization of directionally solidified dendritic microstructures. Metallurgical and Materials Transactions A, 42(6):1675–1683, 2011.

[9] J. E. Miller, M. Strangwood, S. Steinbach, and N. Warnken. Skeletonisation to find the centre of dendrites traced from a 2d microstructural image. In Z. Fan, editor, Solidification Processing 2017, 2017.

[10] M. Gündüz and E. Çadrli. Directional solidification of aluminium–copper alloys. Materials Science and Engineering: A, 327(2):167 – 185, 2002.

Bibliography

[1] J. E. Miller, L. Sturz, G. Zimmermann, S. Steinbach, and N. Warnken. A large-scale 3d computer tomography analysis of primary dendrite arm spacing response to withdrawal velocity change using dendrite centre tracking. In *Solidification and Gravity 2018*, 2018.

[2] J. E. Miller, M. Strangwood, S. Steinbach, and N. Warnken. Skeletonisation to find the centre of dendrites traced from a 2d microstructural image. In Z. Fan, editor, *Solidification Processing 2017*, 2017.

[3] S. Steinbach, J. Drescher, J. E. Miller, N. Warnken, L. Sturz, and G. Zimmermann. Furnace technology for experiments on sounding rockets: Directional solidification of al-cast alloys in artex. In J. J. W. A. van Loon, editor, *Hypergravity Workshop January 2018*, 2018.

[4] J. E. Miller, V. Indrizzi, M. Strangwood, and N. Warnken. Simulation and design for directional solidification experiments of al-20wt *To be submitted*, TBC.

[5] J. E. Miller and N. Warnken. Grain orientation from optical images. *To be submitted*, TBC.

[6] Geralt. Ice crystal. Published under CC0 public domain, November 2014.

[7] ESA, October 2014.

[8] Wikipedia. Binary phase diagram of alcu, May 2012.

[9] Nils Warnken. Jmak and avrami graphs. JMAK Graphs, 2015.

[10] Dominique Bouchard and John S. Kirkaldy. Prediction of dendrite arm spacings in unsteady-and steady-state heat flow of unidirectionally solidified binary alloys. *Metallurgical and Materials Transactions B*, 28(4):651–663, Aug 1997.

[11] Jake Brooks. Mri brain scan. MRI scan of Jake Brooks' brain, 2017.

[12] Dexin Ma. Development of dendrite array growth during alternately changing solidification condition. *Journal of Crystal Growth*, 260(3):580 – 589, 2004.

[13] D. Ma. Development of dendrite array growth during alternately changing solidificaton condition. *Journal of Crystal Growth*, 260:580–589, 2004.

[14] S. Steinbach and J. Drescher. DLR aerogel frunace technical drawings, December 2016.

[15] J. R. Cahoon, M. C. Chaturvedi, and K. N. Tandon. The unidirectional solidification of Al-4 wt pct Cu ingots in microgravity. *Metallurgical and Materials Transactions A*, 29(13):1101–1111, Mar 1998.

[16] Melvin Avrami. Kinetics of phase change. i general theory. *The Journal of Chemical Physics*, 7(12):1103–1112, 1939.

[17] Melvin Avrami. Kinetics of phase change. ii transformationtime relations for random distribution of nuclei. *The Journal of Chemical Physics*, 8(2): 212–224, 1940.

[18] D. A. Porter, K. E. Easterling, and M. Y. Sherif. *Phase Transformations in Metals and Alloys*. CRC Press, third edition, 2009.

[19] Pere Bruna, Daniel Crespo, Ricard González-Cinca, and Eloi Pineda. On the validity of avrami formalism in primary crystallization. *Journal of Applied Physics*, 100(5):054907, 2006.

[20] J.J. Li, J.C. Wang, Q. Xu, and G.C. Yang. Comparison of johnson–mehl–avrami–kologoromov (jmak) kinetics with a phase field simulation for polycrystalline solidification. *Acta Materialia*, 55(3):825 – 832, 2007.

[21] Alexandre P. Boeira, Ivaldo L. Ferreira, and Amauri Garcia. Modeling of macrosegregation and microporosity formation during transient directional solidification of aluminum alloys. *Materials Science and Engineering: A*, 435:150 – 157, 2006.

[22] R. C. Reed. *The Superalloys: Fundamentals and Applications*. Caimbridge University Press, 1st edition, 2006.

[23] M. S. A. Karunaratne, D. C. Cox, P. Carter, and R. C. Reed. Modelling of the microsegregation in cmsx-4 superalloy and its homogenisation during heat treatment. *Superalloys*, pages 263–273, 2000.

[24] W. Kurz and D. J. Fisher. *Fundamentals of Solidification*. Trans Tech Publications, fourth edition, 1998.

[25] R. Trivedi and W. Kurz. Dendritic growth. *International Materials Reviews*, 39(2):49–74, 1994.

[26] M. C. Flemings. *Solidification Processing*. McGraw-Hill, 1974.

[27] W Kurz. Solidification microstructureprocessing maps: Theory and application. *Advanced Engineering Materials*, 3:443 – 452, 07 2001.

[28] S Sakane, T Takaki, M Ohno, T Shimokawabe, and T Aoki. Gpu-accelerated 3d phase-field simulations of dendrite competitive growth during directional

solidification of binary alloy. *IOP Conference Series: Materials Science and Engineering*, 84(1):012063, 2015.

[29] G. Zimmermann, L. Sturz, H. Nguyen-Thi, N. Mangelinck-Noel, Y. Z. Li, C.-A. Gandin, R. Fleurisson, G. Guillemot, S. McFadden, R. P. Mooney, P. Voorhees, A. Roosz, A. Ronaföldi, C. Beckermann, A. Karma, C.-H. Chen, N. Warnken, A. Saad, G.-U. Grün, M. Grohn, I. Poitrault, T. Pehl, I. Nagy, D. Todt, O. Minster, and W. Sillekens. Columnar and equiaxed solidification of al-7 wt.% si alloys in reduced gravity in the framework of the cetsol project. *JOM*, 69(8):1269–1279, Aug 2017.

[30] Sonja Steinbach and Lorenz Ratke. The influence of fluid flow on the microstructure of directionally solidified alsi-base alloys. In *ASM International 2007*, volume 2, pages 1388–1394, 12 2005.

[31] M Gündüz and E Çadrl. Directional solidification of aluminium–copper alloys. *Materials Science and Engineering: A*, 327(2):167 – 185, 2002.

[32] M. A. Tschopp, J. D. Miller, A. L. Oppedal, and K. N. Solanki. Evaluating local primary dendrite arm spacing characterization techniques using synthetic evaluating local primary dendrite arm spacing characterization techniques using synthetic directionally solidified dendritic microstructures. *Metallurgical and Materials Transactions A*, 46A:4610–4628, October 2015.

[33] Corbett C. Battaile, R. N. Grungel, A. B. Hmelo, and T. G. Wang. The effect of enhanced gravity levels on microstructural development in pb-50 wt pct sn alloys during controlled directional solidification. *Metallurgical and Materials Transactions A*, 25A:865–870, April 1994.

[34] M.A. Tschopp, M.A. Groeber, R. Fahringer, J.P. Simmons, A.H. Rosenberger, and C. Woodward. Symmetry-based automated extraction of microstructural features: Application to dendritic cores in single-crystal ni-based superalloys. *Scripta Materialia*, 62(6):357 – 360, 2010.

[35] M A Tschopp, M A Groeber, R Fahringer, J P Simmons, A H Rosenberger, and C Woodward. Automated detection and characterization of microstructural features: application to eutectic particles in single crystal ni-based superalloys. *Modelling and Simulation in Materials Science and Engineering*, 18(2):025014, 2010.

[36] M.A. Tschopp, M.A. Groeber, J.P. Simmons, A.H. Rosenberger, and C. Woodward. Automated extraction of symmetric microstructure features in serial sectioning images. *Materials Characterization*, 61(12):1406 – 1417, 2010.

[37] J. Alkemper, S. Sous, C. Stöcker, and L. Ratke. Directional solidification in an aerogel furnace with high resolution optical temperature measurements. *Journal of Crystal Growth*, 191(1):252 – 260, 1998.

[38] N.J. Humphreys, D. McBride, D.M. Shevchenko, T.N. Croft, P. Withey, N.R. Green, and M. Cross. Modelling and validation: Casting of al and tial alloys in gravity and centrifugal casting processes. *Applied Mathematical Modelling*, 37(14–15):7633 – 7643, 2013.

[39] D.G. McCartney and J.D. Hunt. Measurements of cell and primary dendrite arm spacings in directionally solidified aluminium alloys. *Acta Metallurgica*, 29(11):1851 – 1863, 1981.

[40] T. Schenk, H. Nguyen Thi, J. Gastaldi, G. Reinhart, V. Cristiglio, N. Mangelinck-Noël, H. Klein, J. Härtwig, B. Grushko, B. Billia, and J. Baruchel. Application of synchrotron x-ray imaging to the study of directional solidification of aluminium-based alloys. *Journal of Crystal Growth*, 275(1–2):201 – 208, 2005. Proceedings of the 14th International Conference on Crystal Growth and the 12th International Conference on Vapor Growth and Epitaxy.

[41] José E. Spinelli, Noé Cheung, Pedro R. Goulart, José M.V. Quaresma, and Amauri Garcia. Design of mechanical properties of al-alloys chill castings based on the metal/mold interfacial heat transfer coefficient. *International Journal of Thermal Sciences*, 51:145 – 154, 2012.

[42] P. A. Curreri, J. E. Lee, and D. M. Stefanescu. Dendritic solidification of alloys in low gravity. *Metallurgical Transactions A*, 19(11):2671–2676, 1988.

[43] A.J. Clarke, D. Tourret, Y. Song, S.D. Imhoff, P.J. Gibbs, J.W. Gibbs, K. Fezzaa, and A. Karma. Microstructure selection in thin-sample directional solidification of an al-cu alloy: In situ x-ray imaging and phase-field simulations. *Acta Materialia*, 129:203 – 216, 2017.

[44] L. Abou-Khalil, G. Salloum-Abou-Jaoude, G. Reinhart, C. Pickmann, G. Zimmermann, and H. Nguyen-Thi. Influence of gravity level on columnar-to-equiaxed transition during directional solidification of al-20 wt. *Acta Materialia*, 110:44–52, 2016.

[45] R. H. Mathiesen, L. Arnberg, Y. Li, V. Meier, P. L. Schaffer, I. Snigireva, A. Sngigirev, and A. K. Dahle. X-ray videomicroscopy studies of eutectic al-si solidification in al-si-cu. *Metallurgical and Materials Transactions A*, 42(1):170–180, January 2011.

[46] Robin P. Mooney, Laszlo Sturz, Gerhard Zimmermann, and Shaun McFadden. Thermal characterisation with modelling for a microgravity experiment into polycrystalline equiaxed dendritic solidification with in-situ observation. *International Journal of Thermal Sciences*, 125:283 – 292, 2018.

[47] Brian M. Patterson, Kevin C. Henderson, Paul J. Gibbs, Seth Imhoff, and Amy J. Clarke. Multi-scale imaging of al-7at.%cu eutectics using micro- and nano-scale x-ray computed tomography. In *Microscopy and Microanalysis*, volume 20 S3, pages 780–781. Cambridge University Press, 2014.

[48] M. Ahmadein, M. Wu, G. Reinhart, H. Nguyen-Thi, and A. Ludwig. Modelling al-4wt.parameters deduced from in-situ synchrotron x-ray radiography. In *IOP Conf. Series: Materials Science and Engineering*, volume 117. 4th International Conference on Advances in Solidification Processes (ICASP-4), IOP Publishing, 2016.

[49] Qingyu Zhang, Dongke Sun, Shiyan Pan, and Mingfang Zhu. Microporosity formation and dendrite growth during solidification of aluminum alloys: Modeling and experiment. *International Journal of Heat and Mass Transfer*, 146:118838, 2020.

[50] G. P. Ivanstov. Temperature field around spherical, cylindrical and needle-shaped crystals which grow in super cooled melt. *Dokl. Akad. Nauk USSR*, 58:1113, 1947.

[51] G. Horvay and J. W. Cahn. Dendritic and speroidal growth. *Acta Materialia*, 9, July 1961.

[52] D. E. Temkin. Growth velocity of a needle crystal in a supercooled melt. *Dokl. Akad. Nauk. SSSR*, 132:1307–1310, 1960.

[53] J. A Dantzig and Michel Rappaz. *Solidification*. Lausanne : EPFL Press ; London : Taylor Francis [distributor], 1st ed edition, 2009.

[54] G. E. Nash and M. E. Glicksman. Capillarity limited steady-state growth 1. theoretical development. *Acta Materialia*, 22(10):1283–1290, 1974.

[55] N. Shevchenko, O. Roshchupkina, O. Sokolova, and S. Eckert. The effect of natural and forced melt convection on dendritic solidification in ga-in alloys. *Journal of Crystal Growth*, 417:1–8, 2015.

[56] X. Hu, S. Li, S. Gao, L. Liu, and H. Fu. Effect of melt convection on primary dendrite arm spacing in directionally solidified pb-26 *Trans. Nonferrous Met. Soc. China*, 21:65–71, 2011.

[57] M. E. Glicksman and M. B. Koss. Dendritic growth velocities in microgravity. *Physical review letters*, 73(4):573–576, July 1994.

[58] J. D. Hunt. Solidification and casting of metals. *The Metal Society*, pages 3–9, 1979.

[59] R. Trivedi. Interdendritic spacing: Part ii. a comparison of theory and experiment. *Metallurgical and Materials Transactions A*, 15(6):977–982, Jun 1984.

[60] Erkan Üstün, Emin Çadirli, and Hasan Kaya. Dendritic solidification and characterization of a succinonitrile–acetone alloy. *Journal of Physics: Condensed Matter*, 18(32):7825, 2006.

[61] Y. A. Chen, I. N. Bandeira, A. H. Franzan, S. Eleutério Filho, and M. R. Slomka. *Materials Processing in High Gravity*. Springer US, Boston, MA, 1994.

[62] Herman-Josef Diepers and Ingo Steinbach. Interaction of interdendritic convection and dendritic primary spacing: Phase-field simulation and analytical modeling. *Materials Science Forum*, 508:145–150, March 2006.

[63] K. G. Libbrecht. The physics of snow crystals. *Reports on Progress in Physics*, 68(4):855, 2005.

[64] E. Ben-Jacob, N. Goldenfeld, J. S. Langer, and G. Schön. Boundary-layer model of pattern formation in solidification. *Physical Review A*, 29(1):330–340, January 1984.

[65] A. Dathe, A. M. Tarquis, and E. Perrier. Multifractal analysis of the pore- and solid-phases in binary two dimensional images of natural porous structures. *Geoderma*, 134(3-4):318–326, October 2006.

[66] N. Warnken, D. Ma, A. Drevermann, R. C. Reed, S. G. Fries, and I. Steinbach. Phase-field modelling of as-cast microstructure evolution in nickel based superalloys. *Acta Materialia*, 57:5862–5875, 2009.

[67] H. Kaya, E. Çadrl, and M. Gündüz. Dendritic growth in an aluminum-silicon alloy. *Journal of Materials Engineering and Performance*, 16(1):12–21, February 2007.

[68] A. Papapetrou. Untersuchungen über dendritisches wachstum von kristallen (investigations on the dendritic growth of crystals). *Zeitschrift für Kristallographie*, 92(1):89–129, 1935.

[69] M. Asta, C. Beckerman, A. Karma, W. Kurz, R. Napolitano, M. Plapp, G. Purdy, M. Rappaz, and R. Trivedi. Solidification microstructures and solid-state parallels: Recent developments, future directions. *Acta Materialia*, 57(4):941–971, February 2009.

[70] J. A. Dantzig and M. Rappaz. *Solidification*, chapter 8. EPFL Press, 1st edition, 2009.

[71] J.S Langer and H Müller-Krumbhaar. Theory of dendritic growth—i. elements of a stability analysis. *Acta Metallurgica*, 26(11):1681 – 1687, 1978.

[72] J.S. Langer and J. Müller-Krumbhaar. Stability effects in dendritic crystal growth. *Journal of Crystal Growth*, 42:11 – 14, 1977.

[73] Daniel I. Meiron. Selection of steady states in the two-dimensional symmetric model of dendritic growth. *Phys. Rev. A*, 33:2704–2715, Apr 1986.

[74] Kumio Okaichi, Miwa Ide, Aya Usui, and Yutaka Okumura. Hypergravity induces phosphorylation of p53 at serine 15, but not an expression of p53-downstream genes. *Journal of radiation research*, 45:399–403, 10 2004.

[75] J.J.W.A. Van Loon, Jutta Krause, H Cunha, J Goncalves, H Almeida, and Peter Schiller. The large diameter centrifuge, ldc, for life and physical sciences and technology. *European Space Agency, (Special Publication) ESA SP*, 663, 01 2008.

[76] A J Flikweert, T Nimalasuriya, G.M.W. Kroesen, and W W Stoffels. Imaging laser absorption spectroscopy of the metal-halide lamp in a centrifuge (1–10g). *Plasma Sources Science and Technology*, 16:606, 07 2007.

[77] Walter Federle, K Rohrseitz, and B Hölldobler. Attachment forces of ants measured with a centrifuge: Better 'wax-runners' have a poorer attachment to a smooth surface. *The Journal of experimental biology*, 203:505–12, 03 2000.

[78] Sara Battaglioli, Anthony Robinson, and Shaun Mcfadden. Influence of natural and forced gravity conditions during directional columnar solidification. *International Journal of Heat and Mass Transfer*, 126, 05 2018.

[79] Alexandre Viardin, L Sturz, Markus Apel, and Ulrike Hecht. Phase field modeling of (ti) solidification in ti-45at.Columnar dendrite growth at various gravity levels. *Materials Science Forum*, 790-91:34, 05 2014.

[80] Gerhard Zimmermann, M Hamacher, and L Sturz. Effect of zero, normal and hyper-gravity on columnar dendritic solidification and the columnar-to-equiaxed transition in neopentylglycol-(d)camphor alloy. *Journal of Crystal Growth*, 01 2019.

[81] Wajira Mirihanage, David Browne, L Sturz, and Gerhard Zimmermann. Numerical modelling of the material science lab - low gradient furnace (msl-lgf) microgravity directional solidification experiments on the columnar to equiaxed transition. *IOP Conference Series: Materials Science and Engineering*, 27:012010, 01 2012.

[82] T. Duffar. *Alloy Physics: A Comprehensive Reference*, chapter 3. Wiley-VCH, 2007.

[83] M. E. Glicksman. *Principles of Solidification: An Introduction to Modern Casting and Crystal Growth Concepts*. Springer New York, 2011.

[84] Enzo Liotti, Carlos Arteta, Andrew Zisserman, Andrew Lui, Victor Lempitsky, and Patrick S. Grant. Crystal nucleation in metallic alloys using x-ray radiography and machine learning. *Science Advances*, 4(4), 2018.

[85] R. Trivedi and W. Kurz. Solidification microstructures: A conceptual approach. *Acta Metallurgica et Materialia*, 42(1):15 – 23, 1994.

[86] W. Kurz, C. Bezençon, and M. Gäumann. Columnar to equiaxed transition in solidification processing. *Science and Technology of Advanced Materials*, 2(1):185–191, 2001.

[87] M. Ahmadein, M. Wu, and A. Ludwig. Analysis of macrosegregation formation and columnar-to-equiaxed transition during solidification of al-4wt. *Journal of Crystal Growth*, 417:65 – 74, 2015. Effect of natural and forced convection in materials crystallization.

[88] J.D. Hunt. Steady state columnar and equiaxed growth of dendrites and eutectic. *Materials Science and Engineering*, 65(1):75 – 83, 1984. Solidification Microstructure: 30 Years after Constitutional Supercooling.

[89] Melvin Avrami. Kinetics of phase change. i general theory. *The Journal of Chemical Physics*, 7(12):1103–1112, 1939.

[90] S C. Gill and W Kurz. Rapidly solidified alcu alloys—ii. calculation of the microstructure selection map. *Acta Metallurgica Et Materialia*, 43:139–151, 01 1995.

[91] S.C. Gill and W Kurz. Rapidly solidified alcu alloys—i. experimental determination of the microstructure selection map. *Acta Metallurgica et Materialia*, 41:3563–3573, 12 1993.

[92] Eli Vandersluis and Comondore Ravindran. Comparison of measurement methods for secondary dendrite arm spacing. *Metallography, Microstructure, and Analysis*, 6(1):89–94, Feb 2017.

[93] R. P. Mooney, S. McFadden, M. Reboq, and D. J. Browne. A front tracking model for transient solidification of al-7wtbridgman furnace. *Transactions of Indian Institute of Metallurgy*, 65(6):527–530, December 2012.

[94] Sara Battaglioli, Shaun Mcfadden, and Anthony Robinson. Front tracking model for bridgman solidification of gamma-tial alloys. In *SP17, 6th Decennial International Conference on Solidification Processing*, 07 2017.

[95] Gerhard Zimmermann, L Sturz, Li Yuze, H Nguyen-Thi, N Mangelinck-Noël, R Fleurisson, Gildas Guillemot, Shaun Mcfadden, Robin Mooney, Peter Voorhees, András Roósz, C Beckermann, Alain Karma, Nils Warnken, E Perchat, M Grohn, I Poitrault, D Toth, and W.H. Sillekens. Columnar and equiaxed solidification within the framework of the esa map project cetsol. In *Seventh International Conference on Solidification and GravityAt: Miskolc-Lillafüred, Hungary*, 09 2018.

[96] S. Steinbach and L. Ratke. The influence of fluid flow on the microstructure of directionally solidified alsi-base alloys. *Metallurgical and Materials Transactions A*, 38A:1388–1394, July 2007.

[97] S. Steinbach and L. Ratke. Furnace technology for experiments on sounding rockets: Directional solidification on al-cast alloys in artex. *International Journal of Microgravity Science and Application*, page 467, 2008.

[98] W. Kurz and D.J. Fisher. Dendrite growth at the limit of stability: tip radius and spacing. *Acta Metallurgica*, 29(1):11 – 20, 1981.

[99] G. A. Santos, P. R. Goulart, A. A. Couto, and A. Garcia. *Primary Dendrite ARM Spacing Effects upon Mechanical Properties of an AL–3Wt%CU–1Wt%LI Alloy*, pages 215–229. Springer Singapore, Singapore, 2017.

[100] M. L. N. M. Melo, E. M. S. Rizzo, and R. G. Santos. Predicting dendrite arm spacing and their effect on microporosity formation in directionally solidified al-cu alloy. *Journal of Materials Science*, 40(7):1599–1609, Apr 2005.

[101] ANGELA J. VASCONCELOS, RAFAEL H. KIKUCHI, ANDRÃâ S. BARROS, THIAGO A. COSTA, MARCELINO DIAS, ANTONIO L. MOREIRA, ADRINA P. SILVA, and OTÃÅVIO L. ROCHA. Interconnection between microstructure and microhardness of directionally solidified binary Al-6wt.Al-6wt. *Anais da Academia Brasileira de CiÃ*, 88:1099 – 1111, 06 2016.

[102] N. Warnken. *Simulation of Microstructure Formation During Solidification and Solution Heat Treatment of a Novel Single Crystal Superalloy*. Deutsche Nationalbibliothek, 2007.

[103] Gao Sifeng, Liu Lin, Xu Yiku, Yang Chubin, Zhang Jun, , and Fu Hengzhi. In uences of processing parameters on microstructure during investment casting of nickel-base single crystal superalloy dd3. *China Foundry*, 9(2):159–164, May 2012.

[104] J.S. Kirkaldy and D. Venugopalan. Pattern selection relations for deep-rooted binary alloy cells. *Scripta Metallurgica*, 23(9):1603 – 1608, 1989.

[105] Manuel V. Canté, José E. Spinelli, Ivaldo L. Ferreira, Noé Cheung, and Amauri Garcia. Microstructural development in al-ni alloys directionally solidified under unsteady-state conditions. *Metallurgical and Materials Transactions A*, 39(7):1712, April 2008.

[106] Otávio L. Rocha, Cláudio A. Siqueira, and Amauri Garcia. Heat flow parameters affecting dendrite spacings during unsteady-state solidification of sn-pb and al-cu alloys. *Metallurgical and Materials Transactions A*, 34(4): 995–1006, Apr 2003.

[107] Nils Warnken and Roger C. Reed. On the characterization of directionally solidified dendritic microstructures. *Metallurgical and Materials Transactions A*, 42(6):1675–1683, 2011.

[108] Vanessa Indrizzi, Nils Warnken, and Duncan Putman. Computational study of spacing selection in directionally growing dendritic arrays. In *SP17*, 07 2017.

[109] S.H. Han and R. Trivedi. Primary spacing selection in directionally solidified alloys. *Acta Metallurgica et Materialia*, 42(1):25 – 41, 1994.

[110] Wislei R. Osório, José E. Spinelli, Noé Cheung, and Amauri Garcia. Secondary dendrite arm spacing and solute redistribution effects on the corrosion resistance of al–10wt *Materials Science and Engineering: A*, 420(1):179 – 186, 2006.

[111] R. Trivedi and K. Somboonsuk. Constrained dendritic growth and spacing. *Materials Science and Engineering*, 65(1):65 – 74, 1984. Solidification Microstructure: 30 Years after Constitutional Supercooling.

[112] Miao-Miao Fang, Hong Yan, Xian-Chen Song, and Yong-Hui Sun. Effect of (pr+ce) additions on microstructure and mechanical properties of alsi5cu1mg alloy. *Applied Sciences*, 9(9), 2019.

[113] Emine Acer, Emin Çadırlı, Harun Erol, Hasan Kaya, and Mehmet Gündüz. Effects of growth rates and compositions on dendrite arm spacings in directionally solidified al-zn alloys. *Metallurgical and Materials Transactions A*, 48(12):5911–5923, Dec 2017.

[114] Emine Acer, Emin Çadırlı, Harun Erol, and Mehmet Gündüz. Effect of growth rate on the microstructure and microhardness in a directionally solidified al-zn-mg alloy. *Metallurgical and Materials Transactions A*, 47(6): 3040–3051, Jun 2016.

[115] S. Boden, S. Eckert, and G. Gerbeth. Visualization of freckle formation induced by forced melt convection in solidifying gain alloys. *Materials Letters*, 64(12):1340 – 1343, 2010.

[116] F.X. Lin, A. Godfrey, D. Juul Jensen, and G. Winther. 3d ebsd characterization of deformation structures in commercial purity aluminum. *Materials Characterization*, 61(11):1203 – 1210, 2010.

[117] G. Spanos, D.J. Rowenhorst, A.C. Lewis, and A.B. Geltmacher. Combining serial sectioning, ebsd analysis, and image-based finite element modeling. *MRS Bulletin*, 33(6):597–602, 2008.

[118] Armin Zankel, Julian Wagner, and Peter Poelt. Serial sectioning methods for 3d investigations in materials science. *Micron*, 62:66 – 78, 2014.

[119] J. D. Madison, O. D. Underwood, G. A. Poulter, and E. M. Huffman. Acquisition of real-time operation analytics for an automated serial sectioning system. *Integrating Materials and Manufacturing Innovation*, 6(2):135–146, Jun 2017.

[120] Jonathan Madison, J.E. Spowart, D.J. Rowenhorst, J Fiedler, and T.M. Pollock. Characterization of three-dimensional dendritic structures in nickel-base single crystals for investigation of defect formation. In *Superalloys 2008*, pages 881–888, 09 2008.

[121] Jakub Jaroszewicz, Hubert Matysiak, Jakub Michalski, Kamil Matuszewski, Krzysztof Kubiak, and Krzysztof Jan Kurzydlowski. Characterization of single-crystal dendrite structure and porosity in nickel-based superalloys using x-ray micro-computed tomography. In *Euro Superalloys 2010*, volume 278 of *Advanced Materials Research*, pages 66–71. Trans Tech Publications, 9 2011.

[122] A. J. Kubis, G. J. Shiflet, D. N. Dunn, and R. Hull. Focused ion-beam tomography. *Metallurgical and Materials Transactions A*, 35A:1935–1934, 2004.

[123] M. D. Uchic, L. Holzer, B. J. Inkson, E. L. Principe, and P. Munroe. Three-dimensional microstructural characterisation using focused ion beam tomography. *MRS Bulletin*, 32:408–416, May 2007.

[124] Wajira Mirihanage, Ken Falch, Daniele Casari, Shaun Mcfadden, David Browne, Irina Snigireva, A Snigirev, Yanjun Li, and Ragnvald Mathiesen. Non-steady 3d dendrite tip growth under diffusive and weakly convective conditions. *Materialia*, 5:100215, 03 2019.

[125] Thermo Scientific. *Thermo Scientific^{TM} Avizo^{TM} Software 9 User Guide*. Thermo Scientific^{TM}, 2018.

[126] Rafael C. Gonzalez and Richard E. Woods. *Digital Image Processing (3rd Edition)*. Prentice-Hall, Inc., Upper Saddle River, NJ, USA, 2006.

[127] Li Wang, Lei He, Arabinda Mishra, and Chunming Li. Active contours driven by local gaussian distribution fitting energy. *Signal Processing*, 89

(12):2435 – 2447, 2009. Special Section: Visual Information Analysis for Security.

[128] Hongjiang Wei, Luke Xie, Russell Dibb, Wei Li, Kyle Decker, Yuyao Zhang, G. Allan Johnson, and Chunlei Liu. Imaging whole-brain cytoarchitecture of mouse with mri-based quantitative susceptibility mapping. *NeuroImage*, pages –, 2016.

[129] Bin Zhou, Zhendong Zhang, Ji Wang, Y. Eric Yu, X. Sherry Liu, Kyle K. Nishiyama, Mishaela R. Rubin, Elizabeth Shane, John P. Bilezikian, and X. Edward Guo. In vivo precision of digital topological skeletonization based individual trabecula segmentation (its) analysis of trabecular microstructure at the distal radius and tibia by hr-pqct. *Pattern Recognition Letters*, 76:83 – 89, 2016. Special Issue on Skeletonization and its Application.

[130] L. Yang, O. Tuzel, P. Meer, and D. J. Foran. Automatic image analysis of histopathology specimens using concave vertex graph: Miccai. *International Conference on Medical Image Computing and Computer-Assisted Intervention*, 11(01):833–841, 2008.

[131] N. Ayache and J. S. Duncan. Medical image analysis. *Medical Image Analysis*, 31, 2016.

[132] Laszlo Sturz, Gerhard Zimmermann, Stephan Rex, Michael Mathes, and Bernd Kauerauf. Analysis of diffusive cellular patterns in directional solidification of bulk samples. *Metallurgical and Materials Transactions A*, 35(1): 239–246, Jan 2004.

[133] Mark A. Tschopp, Jon D. Miller, Andrew L. Oppedal, and Kiran N. Solanki. Characterizing the local primary dendrite arm spacing in directionally solidified dendritic microstructures. *Metallurgical and Materials Transactions A*, 45(1):426–437, 2014.

[134] A. Viardin, L. Sturz, G. Zimmermann, and M. Apel. Phase-field modeling of the columnar-to-equiaxed transition in neopentylglycol-camphor alloy solidification. *Journal of Physics: Conference Series*, 327:1–8, 2011.

[135] L. Sturz, M. Hamacher, and G. Zimmermann. Results from low-gravity and normal gravity experiment "trace+" on dendritic growth and the columnar-equiaxed transition in the the transparent alloy system npg-dc. In *21st ESA Symposium on European Rocket and Ballon Programmes and Related Research*. ESA, June 2013.

[136] Alfredo Rodriguez, Douglas B. Ehlenberger, Dara L. Dickstein, Patrick R. Hof, and Susan L. Wearne. Automated three-dimensional detection and shape classification of dendritic spines from fluorescence microscopy images. *PLOS ONE*, 3(4):1–12, 04 2008.

[137] R.C. Buckingham, C. Argyrakis, M.C. Hardy, and S. Birosca. The effect of strain distribution on microstructural developments during forging in a newly developed nickel base superalloy. *Materials Science and Engineering: A*, 654(Supplement C):317 – 328, 2016.

[138] S. Gardner, W. Li, M. Coleman, and R. Johnston. The effects of thermo-mechanical history on the microstructure of a nickel-base superalloy during forging. *Materials Science and Engineering: A*, 668(Supplement C):263 – 270, 2016.

[139] Matteo Seita, Michael M. Nimerfroh, and Michael J. Demkowicz. Acquisition of partial grain orientation information using optical microscopy. *Acta Materialia*, 123(Supplement C):70 – 81, 2017.

[140] Y.C. Lin, Xian-Yang Wu, Chen Xiao-Min, Jian Chen, Dong-Xu Wen, Jin-Long Zhang, and Lei-Ting Li. Ebsd study of a hot deformed nickel-based superalloy. *Journal of Alloys and Compounds*, 640:101–113, 08 2015.

[141] Y.Z. Zhou, A. Volek, and N.R. Green. Mechanism of competitive grain growth in directional solidification of a nickel-base superalloy. *Acta Materialia*, 56(11):2631 – 2637, 2008.

[142] J. Guo, S. Amira, P. Gougeon, and X.-G. Chen. Effect of the surface preparation techniques on the ebsd analysis of a friction stir welded aa1100-b4c metal matrix composite. *Materials Characterization*, 62(9):865 – 877, 2011.

[143] Peter J. Szabo and I. Kardos. Correlation between grain orientation and the shade of color etching. *Materials Characterization*, 61(8):814 – 817, 2010.

[144] X. Lin, W. Huang, J. Feng, T. Li, and Y. Zhou. History-dependent selection of primary cellular/dendritic spacing during unidirectional solidification in aluminum alloys. *Acta Materialia*, 47(11):3271 – 3280, 1999.

[145] Dazhuang Kang, Jinghua Liu, Chengbao Jiang, and Huibin Xu. Control of solid–liquid interface morphology and radial composition distribution: Tb-dyfe single crystal growth. *Journal of Alloys and Compounds*, 621:331 – 338, 2015.

[146] Ta-Wei Fu and William R. Wilcox. Influence of insulation on stability of interface shape and position in the vertical bridgman-stockbarger technique. *Journal of Crystal Growth*, 48(3):416 – 424, 1980.

[147] Robin P. Mooney, Shaun McFadden, Zuzana Gabalcová, and Juraj Lapin. An experimental–numerical method for estimating heat transfer in a bridgman furnace. *Applied Thermal Engineering*, 67(1):61 – 71, 2014.

[148] L. Liu, T. Hang, M. Zou, W. Zhang, J. Zhang, and H. Fu. The effects of withdrawal and melt overheating histories on the microstructure of a nicked-based single crystal superalloy. In R. C. Reed, editor, *Superalloys 2008*. TMS, 2008.

[149] Mark Ballico, Khaled Chahine, John Reizes, and Jafar Madadnia. Thermal conductivity of graphite felt at high temperatures. In *8th Australasian Heat and Mass Transfer Conference*, pages 1–4, 01 2005.

[150] M. A. Tschopp. Symmetry-based filter for feature extraction - example, July 2014.

[151] R. C. Gonzalez and R. E. Woods. *Digital Image Processing*. Pearson Prentice Hall, 1st edition, 2008.

[152] M. A. Tschopp, J. P. Simmons M. A. Groeber, A. H. Rosenberger, and C. Woodward. Technique for automated extraction of symmetric microstructural features: Application to dendritic cores in single crystal ni-based superalloys. Technical report, United States Air-Force Reasearch Laboratory, 2011.

[153] Mark Tschopp, M A. Groeber, J P. Simmons, A H. Rosenberger, and C Woodward. Technique for automated extraction of symmetric microstructural features: Application to dendritic cores in single crystal ni-based superalloys. Technical report, United States Air-Force Reasearch Laboratory, 06 2010.

[154] Brandan Walters, Tatiana Uynuk-Ool, Miriam Rothdiener, Julian Palm, Melanie L. Hart, Jan P. Stegemann, and Bernd Rolauffs. Engineering the geometrical shape of mesenchymal stromal cells through defined cyclic stretch regimens. *Scientific Reports*, 7(1):6640, 2017.

[155] Rohit Trivedi, Prantik Mazumder, and Surendra Tewari. The effect of convection on disorder in primary cellular and dendritic arrays. *Metallurgical and Materials Transactions A*, 33:3763–3775, 12 2002.

[156] C Dussert, G Rasigni, M Rasigni, J Palmari, and Antoine Llebaria. Minimal spanning tree: A new approach for studying order and disorder. *Physical review. B, Condensed matter*, 34:3528–3531, 10 1986.

[157] R. C. Prim. Shortest connection networks and some generalizations. *Bell System Technical Journal*, 36(6):1389–1401, 1957.

[158] Richard Hoffman and Anil K Jain. A test of randomness based on the minimal spanning tree. *Pattern Recognition Letters*, 1(3):175 – 180, 1983.

[159] David Freedman and Persi Diaconis. On the histogram as a density estimator:l2 theory. *Zeitschrift für Wahrscheinlichkeitstheorie und Verwandte Gebiete*, 57(4):453–476, Dec 1981.

[160] Martin Ester, Hans-Peter Kriegel, Jörg Sander, and Xiaowei Xu. A density-based algorithm for discovering clusters a density-based algorithm for discovering clusters in large spatial databases with noise. In *Proceedings of the Second International Conference on Knowledge Discovery and Data Mining*, KDD'96, pages 226–231. AAAI Press, 1996.

[161] A. Pineau, G. Guillemot, D. Tourret, A. Karma, and Ch.-A. Gandin. Growth competition between columnar dendritic grains – cellular automaton versus phase field modeling. *Acta Materialia*, 155:286 – 301, 2018.

[162] D. Tourret and A. Karma. Growth competition of columnar dendritic grains: A phase-field study. *Acta Materialia*, 82:64 – 83, 2015.

[163] Tomohiro Takaki, Shinji Sakane, Munekazu Ohno, Yasushi Shibuta, Takashi Shimokawabe, and Takayuki Aoki. Primary arm array during directional solidification of a single-crystal binary alloy: Large-scale phase-field study. *Acta Materialia*, 118:230 – 243, 2016.

[164] Chunwen Guo, Junjie Li, Zhijun Wang, and Jincheng Wang. Non-uniplanar competitive growth of columnar dendritic grains during directional solidification in quasi-2d and 3d configurations. *Materials Design*, 151:141 – 153, 2018.

[165] Huang Weidong, Geng Xingguo, and Zhou Yaohe. Primary spacing selection of constrained dendritic growth. *Journal of Crystal Growth*, 134(1):105 – 115, 1993.

[166] S. Steinbach and L. Ratke. Artex — in situ observation of directional solidification of binary aluminium alloys on texus. *Microgravity - Science and Technology*, 16(1):111–115, Mar 2005.

[167] Myung-Jin Suk, Young-Min Park, and Young-Do Kim. Dendrite spacing and microstructure evolution dependent on specimen history. *Scripta Materialia*, 57(11):985–987, 2007.

[168] Morteza Amoorezaei, Sebastian Gurevich, and Nikolas Provatas. Spacing characterization in al–cu alloys directionally solidified under transient growth conditions. *Acta Materialia*, 58(18):6115–6124, 2010.

[169] Peng Peng, Xinzhong Li, Yanqing Su, and Jingjie Guo. Response of primary dendrite distribution to deceleration growth conditions in a snni peritectic alloy. *Materials Chemistry and Physics*, 177(Supplement C):496 – 504, 2016.

[170] P. Lehmann, R. Moreau, D. Camel, and R. Bolcato. A simple analysis of the effect of convection on the structure of the mushy zone in the case of horizontal bridgman solidification. comparison with experimental results. *Journal of Crystal Growth*, 183(4):690 – 704, 1998.

[171] Nils Warnken. Studies on the solidification path of single crystal superalloys. *Journal of Phase Equilibria and Diffusion*, 37(1):100–107, Feb 2016.

[172] C.R. Swaminathan and V.R. Voller. On the enthalpy method. *International Journal of Numerical Methods for Heat and Fluid Flow*, 3(3):233–244, 1993.

[173] S.D. Felicelli, J.C. Heinrich, and D.R. Poirier. Three-dimensional simulations of freckles in binary alloys. *Journal of Crystal Growth*, 191(4):879 – 888, 1998.

[174] F. P. Incropera, D. P. Dewitt, T. L. Bergman, and A. S. Lavine. *Principles of heat and mass transfer*, chapter 13, page 886. John Wiley Sons, Singapore, 7th edition, 2013.

[175] S J García Vergara, C E Blanco Pinzon, and P Skeldon. Enriched alloy layer on an al-cu alloy studied by cyclic voltammetry. *Journal of Physics: Conference Series*, 786(1):012031, 2017.

[176] T. Hashimoto, X. Zhou, P. Skeldon, and G.E. Thompson. Structure of the copper–enriched layer introduced by anodic oxidation of copper-containing aluminium alloy. *Electrochimica Acta*, 179:394 – 401, 2015. Ubiquitus Electrochemistry.

[177] S. Steinbach, L. Ratke, G. Zimmerman, L. Sturz, A. Roosz, J. Kovács, Y. Fautrelle, O. Budenkova na J. Lacaze, S. Dost, G.-U. Grün, N. Warnken, M. Wu, and W. Sillekens. Investigation of the effect of fluid flowon microstructure evolution in al-si-fe alloys: The micast project. In Z. Fan, editor, *SP17*, volume 6th, pages 267–271. Brunel University, BCAST, July 2017.

[178] C. Y. Ho, M. W. Ackerman, K. Y. Wu, S. G. Oh, and T. N. Havill. Thermal conductivity of ten selected binary alloy systems. *Journal of Physical and Chemical Reference Data*, 7(3):959–1178, 1978.

[179] Arvind Kumar and Pradip Dutta. A rayleigh number based dendrite fragmentation criterion for detachment of solid crystals during solidification. *Journal of Physics D: Applied Physics*, 41(15):155501, 2008.

[180] M. Wu, A. Vakhrushev, G. Nummer, C. Pfeiler, A. Kharicha, and A. Ludwig. Importance of melt flow in solidifying mushy zone. *The Open Conservation Biology Journal*, 2:16–23, 2010.